



HAL
open science

Dynamic Interplay between Magnetization and Surface Acoustic Waves in Magnetostrictive $\text{Fe}(1-x)\text{Ga}(x)$ Thin Films

Carolyna Hepburn

► **To cite this version:**

Carolyna Hepburn. Dynamic Interplay between Magnetization and Surface Acoustic Waves in Magnetostrictive $\text{Fe}(1-x)\text{Ga}(x)$ Thin Films. Materials Science [cond-mat.mtrl-sci]. Paris Institute of Nanosciences (INSP), 2017. English. NNT: . tel-02411563v1

HAL Id: tel-02411563

<https://theses.hal.science/tel-02411563v1>

Submitted on 17 Nov 2018 (v1), last revised 15 Dec 2019 (v2)

HAL is a multi-disciplinary open access archive for the deposit and dissemination of scientific research documents, whether they are published or not. The documents may come from teaching and research institutions in France or abroad, or from public or private research centers.

L'archive ouverte pluridisciplinaire **HAL**, est destinée au dépôt et à la diffusion de documents scientifiques de niveau recherche, publiés ou non, émanant des établissements d'enseignement et de recherche français ou étrangers, des laboratoires publics ou privés.



UNIVERSITE PIERRE ET MARIE CURIE
École doctorale 397: physique et chimie des matériaux

Thèse de DOCTORAT
Spécialité Physique

présentée par Mme Hepburn Carolyn
Pour obtenir le grade de Docteur de l'Université Pierre et Marie Curie VI

Sujet de la thèse

Dynamic Interplay between Magnetization and
Surface Acoustic Waves
in Magnetostrictive $\text{Fe}_{1-x}\text{Ga}_x$ Thin Films

Devant le jury composé de:

Rapporteur	André THIAVILLE	Directeur de recherche - LPS
Rapporteur	Ferran MACIA	Research scientist - UB, Espagne
Examineur	Olivier FRUCHART	Directeur de recherche - SPINTEC
Examineur	Liza HERRERA-DIEZ	Chargée de recherche - C2N
Examineur	Andrea GAUZZI	Professeur - UPMC
Co-directeur de thèse	Massimiliano MARANGOLO	Professeur - UPMC
Directeur de thèse	Jean-Yves DUQUESNE	Chargé de recherche - INSP

Préparée à l'Institut des Nanosciences de Paris
Soutenue le 13/12/2017

Résumé

Récemment, beaucoup d'efforts ont été consacrés au contrôle de l'aimantation dans les nanostructures par d'autres moyens qu'un champ magnétique externe. En effet, le but est de miniaturiser les dispositifs et il est difficile d'imposer un champ magnétique présentant de faibles dimensions latérales. D'autre part, les ondes de spin ouvrent actuellement de nouvelles perspectives dans le traitement de l'information. Les avantages qu'elles présentent sont les suivants: longueurs d'onde nanométriques, à comparer à celles des ondes électromagnétiques dans la même gamme de fréquences (GHz-THz), et absence de chauffage par effet Joule.

Une possibilité de contrôle réside dans l'utilisation d'ondes acoustiques de surface pour induire la dynamique de l'aimantation ou pour contrôler les ondes de spin. En d'autres termes le contrôle de l'aimantation s'exerce alors via une déformation dynamique. Ceci est rendu possible grâce à une propriété fondamentale des corps magnétiques, le couplage magnéto-élastique, c'est-à-dire le couplage entre aimantation et déformation.

Cette thèse porte sur la phénoménologie de l'interaction magnéto-élastique dans les couches minces épitaxiées magnétostrictives de $\text{Fe}_{0.8}\text{Ga}_{0.2}$. Nous avons effectué une étude expérimentale systématique des interactions magnéto-élastiques dans des films minces de différentes épaisseurs et structures magnétiques. Nous avons aussi développé deux modèles phénoménologiques, pour interpréter nos expériences. Nous obtenons le résultat important suivant: il est possible d'extraire, d'une étude acoustique, les constantes magnéto-élastiques ainsi que les constantes d'anisotropie magnétique.

La thèse a aussi une forte composante technologique. Un des buts était d'exciter efficacement des ondes acoustiques de surface dans la gamme de fréquences de quelques GHz (1-5 GHz) sur substrat piézoélectrique de GaAs dans le but d'observer l'interaction résonante avec les ondes de spin thermiques. Nous avons aussi cherché à exciter des ondes de spin, dans des couches minces épitaxiées, avec des antennes RF afin d'observer l'interaction résonante. Nous présentons des expériences préliminaires sur cette interaction, qui ont été réalisées en diffusion Brillouin (BLS) et en diffusion micro Brillouin, en collaboration avec le laboratoire GHOST à Pérouse, en Italie.

Abstract

Recently, lot of efforts have been devoted to control the magnetization in nanostructures by means other than external magnetic field to achieve device miniaturization, as it is difficult to handle the magnetic field at low lateral dimensions. On the other hand, a new road emerged towards the wave based computing by employing spin waves (SWs). The advantages, that SWs offer for the data processing are nm wavelength as compared to the electromagnetic waves in the same frequency range (GHz-THz) and the absence of Joule heating.

A possibility exists to use Surface Acoustic Waves (SAWs), in other words, dynamic strain, to induce magnetization dynamics or to control spin waves. This is possible due to a very fundamental property of magnetic bodies, the magneto-elastic coupling, that is when magnetization orientation and strain are coupled.

This thesis focuses on the phenomenology of the magneto-elastic interaction in thin epitaxied films of magnetostrictive $\text{Fe}_{0.8}\text{Ga}_{0.2}$. We performed a systematic experimental study of the magneto-elastic interactions in thin films of different thicknesses and magnetic structures. We also developed two phenomenological models in order to interpret our results. An important result of this study is that we are able to extract the magneto-elastic and the magnetic anisotropy constants by acoustic means.

The thesis has also a strong technological component. One aim was to efficiently excite surface acoustic waves in GHz frequency range (1-5 GHz) on GaAs piezoelectric substrates in order to observe the resonant interaction with thermal spin waves. We also managed to excite spin waves in thin epitaxied magnetostrictive layers, using RF antennas. We report preliminary measurements on this interaction that were performed with Brillouin light scattering (BLS) and micro BLS techniques in collaboration with the GHOST laboratory in Perugia, Italy.

“ ... So they took it as a working hypothesis that happiness lay in gaining perpetually new insights into the unknown and the meaning of life was to be found in the same process. Every man is a magus in his inner soul, but he becomes one only when he begins to think less about himself and more about others, when it becomes more interesting for him to work than to recreate himself in the ancient meaning of the word. ”

“Monday begins on Saturday”

A. & B. Strougazki

Introduction

The properties and the physics of magnetic materials comprise a formidably rich area of research where subtle effects emerging from quantum mechanics and relativity, such as spin-orbit effect and crystal field, merge with macroscopic and classical phenomena, like shape induced magnetic anisotropy, remanent magnetization and dipolar spin waves. This richness has also led to a number of applications that followed fundamental discoveries within a remarkably short span of time. This is particularly true in the field of modern magnetism, called spintronics, whose commonly accepted beginning is the independent discovery by Albert Fert and Peter Grünberg of the Giant Magnetoresistance (GMR) in 1988 ([1], [2]). Few years later, millions of GMR-based spin valves were flying few nanometers above magnetic hard disks exploiting subtle quantum transport phenomena. The electrical resistance of these devices, constituted of two ferromagnetic (FM) layers separated by a non-FM thin metallic layer, is strongly affected by the stray field produced by granular media, possessing an overall magnetization corresponding to a bit. A similar success was found in the fundamental research concerning TMR (Tunnel Magnetoresistance). Here, very thin ‘quantum’ tunnel barrier filters selectively majority and minority spin conduction channels leading, similar to the GMR spin valves, to a high susceptibility with respect to the local magnetic field. The applications in data storage and magnetic field sensing have been immediate. This rapid development of spintronic devices led to *the first challenge* for today’s magnetic community that we would mention in this introduction: the drastic miniaturization of the size of bits in magnetic recording media led to problems in handling with magnetic field at low lateral dimensions, especially in the ‘writing’ operation in hard disks. Nevertheless, the spintronic community took up the challenge and understood that other ways to reverse magnetizations, avoiding direct application of the field, were needed. Today there exist many new tools to trigger magnetization dynamics. An in-exhaustive list of examples is given in the figure below.

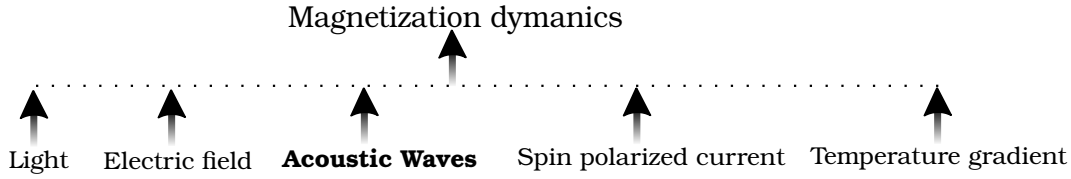


Figure 1: Available methods to trigger magnetization dynamics.

In this context, it's worthwhile to report that E. Beaurepaire *et al.* first demonstrated in 1996 the ultrafast demagnetization in Ni thin films by a femtosecond (fs) laser pulse [3]. Since then ultra-fast magnetization dynamics became an intense research field, for example, the fs laser pulses were used to generate phonons to induce magnetization precession in Ni [4] and in $\text{Fe}_{0.81}\text{Ga}_{0.19}$ alloys [5]. In 2007, an all optical magnetization switching (AOS) was realized for the first time in rare-earth ferrimagnetic alloys GdFeCo [6], followed by experimental investigations in other materials, such as rare-earth orthoferrite $(\text{SmPr})\text{FeO}_3$ [7], ferrimagnetic alloys of different compositions $\text{Tb}_x\text{Co}_{1-x}$ [8], ferromagnetic FePt [9]. Using a femtosecond pulse of circularly polarized light, AOS makes it possible to induce magnetization reversal at a picosecond time scale.

Other examples include magnetization reversal by spin-polarized current in magnetic tunnel junctions or pillar structures via spin-transfer-torque [10], generation of pure spin current via temperature gradient (spin Seebeck effect) [11], electric field assisted magnetization switching in Mn-doped III-IV ferromagnetic semiconductors ($(\text{In,Mn})\text{As}$, $(\text{Ga,Mn})\text{As}$, $(\text{Ga,Mn})(\text{As,P})$) via modulation of magnetic anisotropy [12],[13], voltage-dependent domain wall motion in ferromagnetic junctions with perpendicular magnetic anisotropy, Co/AlOx and CoB/TaOx [14] and etc.

Recently, lot of efforts have been devoted to control of magnetization in nanostructures by external stress and acoustic means. This is the so-called domain of **straintronics** [15]. Indeed, it was claimed that spintronics devices whose magnetization is switched by strain rather than by inductive means may lead to significant reduction in energy dissipation, [15], [16]. In particular, the possibility to control magnetization via **Surface Acoustic Waves** (SAWs) has been reported, for example: elastically driven ferromagnetic resonance [17], [18], irreversible [19] and precessional magnetization switching [20], strong reduction of coercivity [21], acoustically assisted magnetic recording [22], domain wall propagation [23] and etc.

All these examples are possible because of a very fundamental property of ferromagnetic bodies, namely **magneto-elastic coupling**, meaning that magnetization orientation and strain are *coupled*. This can be seen from the examples of direct and inverse magnetostriction [24]. In the first case, under applied magnetic field magnetostrictive materials change their shape or dimension (Joule effect (1842)). Vice versa, an external stress can cause magnetization reorientation (Villari effect (1865)). A beautiful experimental manifestation of the magneto-

elastic interaction is the SAWs' coupling *to* the ferromagnetic resonance (FMR) mode to induce precessional switching [20] on one hand, and generation *of* SAWs *by* induced FMR [25], on the other.

It should be stressed, that this research topic spans already about six decades. It dates back to 1950s, when C. Kittel [26], A.I. Akhiezer *et al.* [27] studied theoretically the coupling between magnons and phonons. The elastically driven FMR, or *magneto acoustic resonance* (MAR) as it was referred to in the past, was already experimentally observed by E.G. Spencer and R.C. LeCraw [28] (1958), H. Bömmel and K. Dransfeld [29] (1959), M. Pomerantz [30] (1961), R.J. Ikola [31] (1965) etc.

The *second challenge* for the magnetism community that we would like to mention concerns data processing assisted by magnetic tools. For a long period, CMOS electronics did not have any magnetic device in proximity. Nowadays, STT-MRAM (Spin Transfer Torque Magnetic RAM) is considered to be well suited for many mainstream applications, such as storage technology. Magnetism could be useful even for logic operations as attested by recent advances in magnonics with a goal to control and manipulate collective magnetization excitations, i.e. spin waves or magnons. Interestingly, logic operations could be performed by waves rather than by electron transport. Since these are waves, any phenomenon inherent to the waves of different origins, will also be inherent to SWs. The fundamental wave properties such as, the excitation and propagation, reflection and refraction, interference and diffraction etc. can be exploited [32], [33]. For example, Mach-Zehnder interferometer can be realized, basically using any type of waves: light, magnons or matter waves. The advantages, that SWs can offer for the data processing are nm wavelength as compared to the electromagnetic waves in the same frequency range, GHz-THz frequency range and the absence of Joule heating [34]. This opens up the possibilities for device miniaturization, increase in data transfer rate, decrease in power dissipation and the **wave based computing**, where the information can be encoded or processed, employing both wave amplitude and phase [35], [36]. However, one should be sure, that the SW attenuation length, that is the product of its life-time and the group velocity, is large enough for technological purposes [37]. For example, attenuation length in pure Fe is about $10\mu m$ at 10 GHz.

A control “unit” for spin waves is a medium, in which the magnetic properties are modulated *periodically* in space and time. Such a medium is referred to as “magnonic” crystal and is a magnetic analog of a photonic crystal. In magnonic crystals SW propagation is affected due to Bragg scattering and as a result, band gaps arise in the wave dispersion. An excellent review on the magnonic crystals can be found in [38]. In *static* magnonic crystals modulation of the parameters such as film thickness, saturation magnetization etc. are constant in time as a result of geometric structuring or patterning. An example of a *reconfigurable* magnonic crystal is an assembly of magnetic nanowires, magnetized parallel or anti-parallel with respect to one another, the magnetization alignment can be externally controlled with a magnetic field, yielding the reconfigurability [39]. In *dynamic* magnonic crystal periodic modulation

of the magnetic properties occurs at a timescale shorter than the characteristic time of SWs propagation through the crystal. A first realization of such crystal was done, using a metallic meander structure, which allows to create spatially periodic magnetic field via current [40]. Once again acoustics, and in particular its intrinsic wave nature, could play an important role. Dynamic Bragg grating can be naturally created via *standing* SAWs. In such a case, the strain control can be implemented locally or globally in a continuous-wave or pulsed configuration. The periodic SAW induced modulation of the magnetic properties can be then easily tuned, by controlling the emission of SAWs. To realize this idea, we need to have a ferromagnetic medium with a strong magneto-elastic coupling. A good candidate for such purposes is, developed in 1999, iron gallium or *galfenol* alloys, that exhibits enhanced magnetostriction and is ferromagnetic below 675°C [41]. This material will be at the heart of this PhD thesis. So far we discussed spintronics, magnonics and how acoustics enters this global context via magneto-elasticity. Keeping the potential applications in mind, we first turn our attention to the fundamental questions.

The goal of this thesis is, first to understand the phenomenology of the magneto-elastic interactions in thin films. In particular, we focus on Fe and FeGa epitaxied on a technologically relevant semiconductor, GaAs. To the best of our knowledge, studies performed so far are either purely experimental or involve heavy theoretical approaches, that do not really give a clear insight into the physics behind the interaction. We thus combined both a systematic experimental study of the magneto-elastic interactions and developing of two phenomenological models, based on previous theoretical investigations, in order to interpret our results. It turns out that we are able to extract the magneto-elastic and the magnetic anisotropies coefficients of epitaxied thin films by acoustic means.

Secondly, based on our understanding of the interaction, we direct ourselves towards the potential applications. Consequently, the “deuxième volet” of this thesis has a strong technological component, as in order to manipulate spin waves via acoustics waves, we need to be able to excite and detect both. The challenge is to efficiently excite surface acoustic waves in GHz frequency range (1-5 GHz) on GaAs piezoelectric substrate to match the spin wave frequencies in Fe_{0.8}Ga_{0.2} alloy, the latter is chosen as an investigation material due to its enhanced magnetostrictive properties, as mentioned above. This opens the possibility to study *resonant* interaction, both with thermal SWs and SWs, excited by induction via RF antennas. Preliminary measurements to study SWs-SAWs resonant interaction were performed towards the end of this thesis by Brillouin light scattering (BLS) and micro BLS technique in collaboration with the GHOST laboratory in Perugia, Italy.

Thesis Outline

Here we give a brief description of the content in each chapter.

Chapter 1 introduces the theoretical background. We present the basic concepts of linear acoustics and ferromagnetism. In particular, we consider the propagation of surface acoustic waves in a semi-infinite elastic medium in order to compute the particle displacement and strain components, present in the wave.

In the section on ferromagnetism we discuss the different contributions to the total energy of a ferromagnet. These notions will be used later in the chapter 2 and chapter 6.

Chapter 2 presents an analytical and numerical treatment of SAW-induced magnetization dynamics. We compute the SAW-induced torque on the magnetization, considering different magneto-crystalline anisotropy systems: biaxial, uniaxial and biaxial-uniaxial. These results give a simple description of the physical system and permit to partially interpret our experimental findings and the physics behind the magneto-elastic interaction. Furthermore, we can deduce how to optimize the effect of a propagating SAW on the magnetization.

Chapter 3 focuses on the presentation of the material, used for the study in this thesis. We describe the sample growth, the structural and magnetic peculiarities, such as the enhanced magnetostriction and presence of additional contributions to the MCA, namely uniaxial and perpendicular MCA. The understanding of different contributions of MCA is crucial to analyze and fit the experimental data.

Chapter 4 is devoted to the experimental setup, used to perform the RF measurements, and the sample fabrication process. The main technological advancements in this thesis are the excitation of harmonic frequencies (up to 9th) and high frequencies (up to 5GHz) of SAWs on the piezoelectric GaAs substrate via inter-digital transducers (IDTs). For this we used different IDT designs, described in the literature. Preliminary trials to excite spin waves (SWs) with RF antennas were successfully performed.

Chapter 5 presents *some* of the experimental results. To avoid redundancy we focus only on few samples with the in-plane MCA. We give a description of the experimental observations, that distinguishes several features. These features are analyzed in the chapter 6. We conclude the chapter with the discussion of the preliminary measurements, performed to check the resonant SAWs-SWs interaction in a 4 nm thick film of $\text{Fe}_{0.8}\text{Ga}_{0.2}$ by conventional BLS in collaboration with the GHOST laboratory, Perugia, Italy.

Chapter 6 is the core chapter of this thesis. We present two analytical models, that permit to interpret, altogether with the notions of SAW-induced torque (chapter 2), our experimental findings and *to extract the material constants*, namely magneto-elastic coefficient, B_2 and the MCA constants, K_1 , K_{ip} , biaxial and uniaxial, respectively. We thus propose a new method to extract the material parameters, using surface acoustic waves.

Each chapter is in turn summarized with a conclusion to facilitate the reading.

Contents

Résumé	ii
Abstract	iv
Introduction	viii
Thesis Outline	xiii
1 Basic Concepts	1
1.1 Rayleigh Waves	1
1.1.1 Concepts of linear acoustics	3
1.1.2 Propagation in a semi-infinite elastic solid	8
1.1.3 Propagation along [100] in the (100) plane	10
1.1.4 Propagation along [110] in the (100) plane	12
1.2 Ferromagnetism	14
1.2.1 Energy density of a ferromagnet	17
1.2.2 Zeeman energy density	17
1.2.3 Shape anisotropy energy or magnetostatic self-energy	17
1.2.4 Magneto-crystalline anisotropy energy (MCA)	18
1.2.5 Discussion on the origin of MCA	20
1.2.6 Elastic energy density	21
1.2.7 Magneto-elastic energy (MEL): phenomenology	21
1.2.8 Expressions for the magneto-elastic energy	24
1.3 Magnetization dynamics	25
1.3.1 Equation of motion	25
1.4 Conclusion	27
2 SAW-induced Magnetization Dynamics	29
2.1 Expression of Torque Density	31
2.2 Calculation steps	32
2.3 SAW along [100]	35

2.3.1	Neglecting e_{13}	36
2.3.2	Taking e_{13} into account	37
2.4	SAW along [110]	39
2.5	Numerical Analysis	40
2.5.1	Uniaxial MCA	41
2.5.2	Biaxial MCA	45
2.5.3	Biaxial MCA with uniaxial contribution	47
2.6	Conclusion	50
3	Galfenol $\text{Fe}_{1-x}\text{Ga}_x$ Alloys	53
3.1	Structural and Magnetostrictive Properties of Bulk FeGa	54
3.2	Origin of Magnetostriction in FeGa Alloys: extrinsic vs. intrinsic	56
3.2.1	<i>Ab initio</i> approach	57
3.3	Interplay of Anisotropies in Thin Films	58
3.3.1	UMA & PMA	60
3.4	Sample Growth	61
3.5	Conclusion	64
4	Sample Fabrication and Experimental Setup	65
4.1	Excitation and detection of SAWs. RF experimental setup	66
4.2	Fabrication procedure	70
4.2.1	Wet etching	70
4.2.2	Electron beam lithography	72
4.3	Excitation of harmonics	74
4.4	High frequency range, 4-5 GHz: synchronous IDTs	75
4.5	Excitation of spin waves with RF antennas	77
4.6	Sample connection	78
4.7	Conclusion	79
5	RF measurements: Experimental Results	81
5.1	General remarks	82
5.2	32m0206 $\text{Fe}_{0.8}\text{Ga}_{0.2}$ 58nm	84
5.2.1	High field region	85
5.2.2	Low field region	88
5.2.3	Effect of frequency	92
5.3	Preliminary BLS measurements: 32m0279 $\text{Fe}_{0.8}\text{Ga}_{0.2}$ 4nm	93
5.4	Conclusion	97

6 Modeling the System	99
6.1 State of art of Theoretical Approaches	99
6.2 Anelastic approach	104
6.2.1 Expressions for $\frac{\Delta V}{V}$	111
6.3 Film-on-Substrate Approach	112
6.3.1 Ferromagnetic Film: Transverse Wave Velocity, \hat{v}_T	115
6.3.2 Ferromagnetic Film: Longitudinal Wave Velocity, \hat{v}_L	117
6.3.3 Longitudinal velocity, \hat{v}_L vs transverse velocity, \hat{v}_T	118
6.4 Interpretation and Fits of the Experimental Data	119
6.4.1 32m0215 Fe 67nm	123
6.4.2 32m0206 Fe _{0.8} Ga _{0.2} 58nm	127
6.5 Conclusion	128
Conclusion & Perspectives	130
A Local rotations	135
B Propagation along [100] direction: detailed calculation	136
C Expression for free energy density	142
D Expressions for angular variations $\delta\theta(t)$, $\delta\varphi(t)$	143
E First and second order derivatives of free energy density	146
F Strain and magnetization orientation at equilibrium	148
G Kappa, κ_i, κ_{ij} and zeta, ζ_i, ζ_{ij} terms	152
H Relative change in velocity $\frac{\Delta V}{V}$ and change in attenuation $\Delta\Gamma$	153
Bibliography	155

Chapter 1

Basic Concepts

This chapter focuses on the basic principles of linear acoustics and ferro-magnetism. In the section 1.1 we give basic concepts of the theory of elasticity, that is the definition of a deformation, strain and stress tensors, followed by a description of Rayleigh waves. A detailed analytical treatment of a Rayleigh wave, propagating in a semi-infinite elastic solid, along [100] direction, is given in the appendix B, while a summary for SAW propagation along [100] and [110] is presented in the main text. As a result we obtain analytical expressions for the strain tensor, ε_{ij} and particle displacement components, u_i . In the section 1.2 we give a description of the energy density terms of a ferromagnet and the phenomenological equation of motion for a precessing magnetization (Landau-Lifshitz-Gilbert equation). The basic concepts, described in this chapter are then employed in the analytical treatment of magnetization dynamics, triggered by surface acoustic waves (chapter 2), as well as in the chapter 6, which is devoted to the modeling of the physical system, studied in this thesis.

1.1 Rayleigh Waves

“If you want to find the secrets of the universe, think in terms of energy, frequency and vibration.”

N. Tesla

Acoustics studies time-varying vibrations in the material media, in other words, the propagation of sound. The name acoustics derives from a Greek word *akouein*, meaning “to hear”. People began to study sound already in the antiquity, as example, Pythagoras investigated vibrating strings and musical sounds [42] (ch.2).

The first mathematical treatment of sound propagation was given by Isaac Newton in his treatise “Principia Mathematica Philosophiae Naturalis” (1686), where he interpreted sound as “pressure pulses” transmitted through a fluid medium [43] (ch.1). In 1787 a remarkable experiment was performed by E.F.F. Chladni, in which he used sprinkled sand on vibrating plates to show different vibration modes (fig. 1.1).

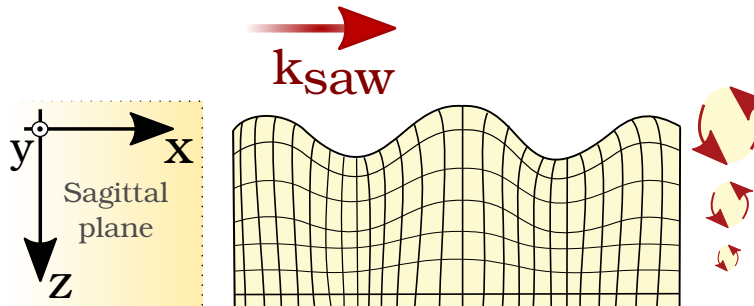
Figure 1.1: Cladni patterns on vibrating circular plates, from [42].



Lord Rayleigh gave a mathematical treatment of vibrating membranes and plates in his “Theory of sound” and in 1885 discovered surface elastic waves, that can propagate in a semi-infinite isotropic solid [44]. He also explained the phenomenon of a “whispering gallery” in St. Paul’s cathedral, in which a sound wave bounces from a concave surface, as it propagates [45] (1910).

The characteristic features of the Rayleigh waves is that they are localized at the surface, as the wave amplitude decays with depth quasi-exponentially at about one wavelength. In the case of a wave propagating along high symmetry directions, its polarization is elliptical and it is confined to the sagittal plane, that contains surface normal and propagation directions, as represented on the figure below, fig. 1.2.

Figure 1.2: Graphical representation of the Rayleigh wave, adapted from [46]. Propagating wave along high symmetry directions, is elliptically polarized in the sagittal plane and decays quasi-exponentially with depth.



Rayleigh wave is one of the several discovered types of Surface Acoustic Waves (SAWs). When a solid is considered to be infinite, three plane waves can propagate in a given direction at different velocities, with quasi-longitudinal and quasi-transverse (shear) polarizations¹. For a *finite* solid a boundary imposes mechanical conditions (and electrical for piezoelectric materials) and the wave is said to be *guided* [47] (ch.5). Other examples include Sezawa² [48],

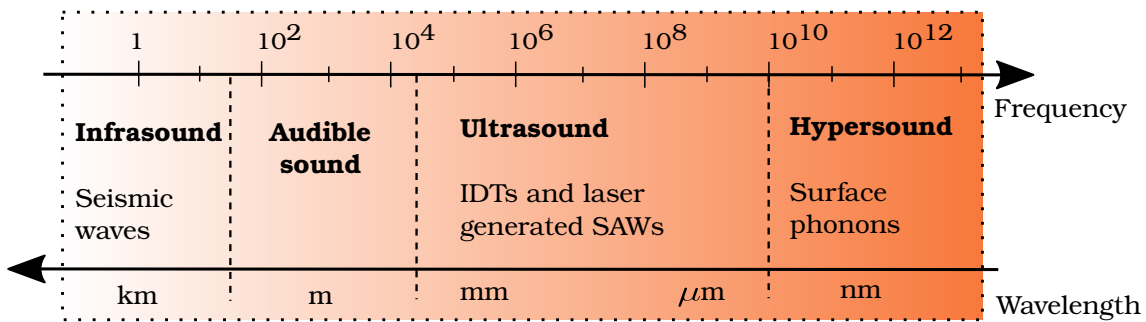
¹Unless the propagation is along high symmetry direction [47], ch. 4.

²This is a type of high-order *Rayleigh modes*, that arise in the piezoelectric film-on-substrate structure, as example ZnO/GaAs, due to smaller sound velocity in the film, than in the substrate. These modes are guided in the over-layer.

Love³, Bleustein-Gulyaev-Shimizu⁴ [49], Lamb⁵, Stoneley⁶ [46], Scholte⁷ [46] waves etc. It should be noted that the surface waves exist over a large range of frequencies [46], as sketched in fig. 1.3. The surface waves, studied in this thesis are excited by the interdigital transducers (IDTs) (chapter 4, section 4.1) and are thus in the ultrasonic region. We focus only on the Rayleigh waves and from now on we simply refer to as SAWs.

In what follows we give general concepts of linear acoustics and treat the propagation of SAWs in a semi-infinite elastic solid with a cubic symmetry.

Figure 1.3: Frequency range of Surface Acoustic Waves (taken from [46]).



1.1.1 Concepts of linear acoustics

Before discussing the propagation of elastic waves in solids, we remind the notions of **strain** and **stress**. The following description is based on the references [50] (ch.1,2), [51] (p.1-6), [47] (ch.3-4). Note that, since the minimal wavelengths of the SAWs in the ultrasonic region scale from μm - down to hundreds of nm, the elastic medium can be considered as **continuous**. Thus, when we discuss a particle displacement in the SAW, we rather refer to *a collection of atoms*, moving in unison.

Under the action of applied forces, a solid body undergoes a deformation. If the body returns to its original form after the external forces were removed, the deformation is said to be *elastic*. Ideal elastic behavior is characterized by an instantaneous response to an applied stress and a unique equilibrium position, towards which the system returns [52] (p.2-4). Consider a point in a solid body, for which equilibrium position is given by a position vector \mathbf{r} *before* a deformation and a position vector \mathbf{r}' *after* the deformation, as represented in the fig. 1.4a. The **displacement vector field** is defined as

$$\mathbf{u}(\mathbf{r}, t) = \mathbf{r}'(\mathbf{r}, t) - \mathbf{r} \quad (1.1)$$

³Shear horizontal (SH) waves with only a transverse displacement, that exist in a film-on-substrate structure, when the velocity of the SH wave is smaller in the film, than in the substrate.

⁴Shear horizontal wave, existing in a piezoelectric semi-infinite solid.

⁵These waves propagate in a medium, bounded by two surfaces, i.e. a free plate.

⁶An “interface” wave between two semi-infinite solids, that decays into both solids.

⁷An “interface” wave, propagating between fluid and an elastic medium.

or $u_i(\mathbf{r}, t) = x'_i(\mathbf{r}, t) - x_i$ in vector component notation (in the standard basis, $i \in [1, 2, 3] \Leftrightarrow [x, y, z]$). Both \mathbf{r}' and \mathbf{u} are functions of the initial coordinates and are time-varying quantities. Deformation implies that points within the solid body are displaced *relative to each other*, therefore rigid translations and rotations (fig. 1.4b, fig. 1.4c), for which the distance between two points before and after deformation remains unchanged, must be excluded from the mathematical description, as we shall see.

To describe the deformation we use differential form of eq. (1.1) at some time t_0 :

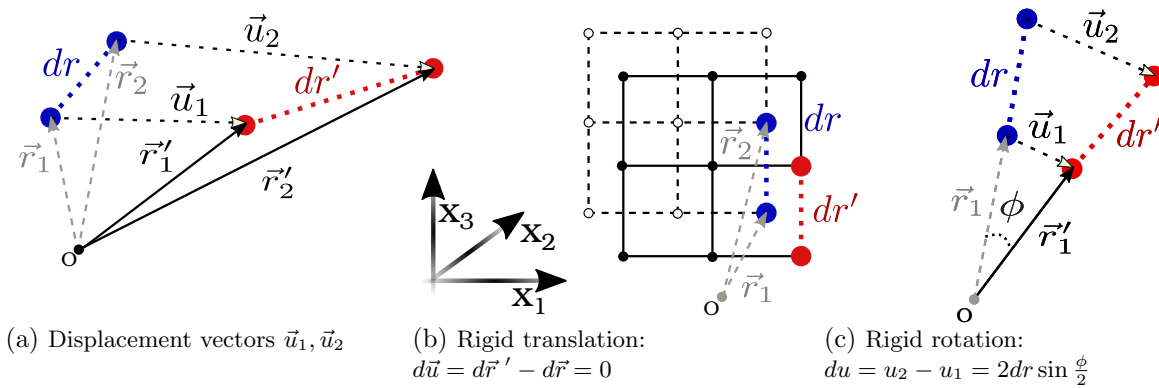
$$d\mathbf{u}(\mathbf{r}, t_0) = \frac{\partial \mathbf{u}}{\partial x_1} dx_1 + \frac{\partial \mathbf{u}}{\partial x_2} dx_2 + \frac{\partial \mathbf{u}}{\partial x_3} dx_3 = \sum_{ij} \frac{\partial u_i}{\partial x_j} dx_j \mathbf{x}_i = d\mathbf{r}' - d\mathbf{r} \quad (1.2)$$

or in matrix notation, where $\xi(\mathbf{r}, t_0)$ is defined as *displacement gradient matrix*:

$$\begin{pmatrix} du_1 \\ du_2 \\ du_3 \end{pmatrix} = \underbrace{\begin{pmatrix} \frac{\partial u_1}{\partial x_1} & \frac{\partial u_1}{\partial x_2} & \frac{\partial u_1}{\partial x_3} \\ \frac{\partial u_2}{\partial x_1} & \frac{\partial u_2}{\partial x_2} & \frac{\partial u_2}{\partial x_3} \\ \frac{\partial u_3}{\partial x_1} & \frac{\partial u_3}{\partial x_2} & \frac{\partial u_3}{\partial x_3} \end{pmatrix}}_{\xi(\mathbf{r}, t_0)} \begin{pmatrix} dx_1 \\ dx_2 \\ dx_3 \end{pmatrix} \quad (1.3)$$

Given the above relation, one could compute the differential displacement of any two points in a deformed solid. For rigid translations differential displacement du is zero (fig. 1.4b), as it must, in the absence of a deformation. However, $du \neq 0$ for rigid rotations as can be seen in the fig. 1.4c.

Figure 1.4: Two points in the solid *before* a deformation (blue color) and *after* the deformation (red color), dr and dr' represent the distance between two points before and after the deformation, respectively. Differential displacement vector is defined as $d\vec{u} = \vec{u}_2 - \vec{u}_1 = d\vec{r}' - d\vec{r}$, adapted from [50].



We thus need a quantity, that cancels out both for rigid translations and rotations. Such quantity is a scalar $dr' - dr$, that represents the difference in distance between two points before and after the deformation. Mathematically it is more convenient to define:

$$\Delta = dr'^2 - dr^2, \quad (1.4)$$

eq. (1.4) thus represents *a measure of deformation*. Applying eq. (1.2) and making use of dummy indices, we can express dr'^2 in terms of dr^2 :

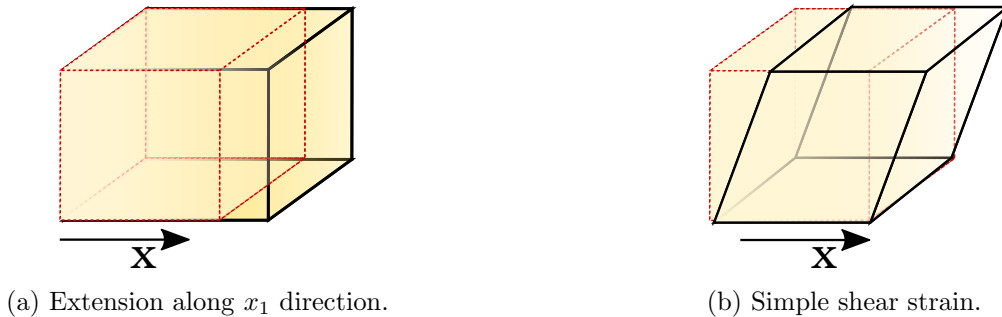
$$\begin{aligned} dr'^2 &= \sum_i dx_i'^2 = \sum_i (dx_i + du_i)^2 = \sum_i dx_i^2 + \sum_i du_i du_i + 2 \sum_i du_i dx_i = \\ &dr^2 + \sum_{ijk} \frac{\partial u_i}{\partial x_j} \frac{\partial u_i}{\partial x_k} dx_j dx_k + 2 \sum_{ij} \frac{\partial u_i}{\partial x_j} dx_j dx_i = \\ &dr^2 + \sum_{ijk} \frac{\partial u_k}{\partial x_j} \frac{\partial u_k}{\partial x_i} dx_j dx_i + \sum_{ij} \left(\frac{\partial u_i}{\partial x_j} + \frac{\partial u_j}{\partial x_i} \right) dx_i dx_j = \\ &dr^2 + \sum_{ij} \left(\frac{\partial u_i}{\partial x_j} + \frac{\partial u_j}{\partial x_i} + \sum_k \frac{\partial u_k}{\partial x_i} \frac{\partial u_k}{\partial x_j} \right) dx_i dx_j \end{aligned}$$

For small deformations, i.e. $\frac{\partial u_k}{\partial x_i} \ll 1$, quadratic terms above in the equation can be neglected. Plugging the expression for dr'^2 into the eq. (1.4), we obtain:

$$\begin{aligned} \Delta &= \sum_{ij} 2\varepsilon_{ij} dx_i dx_j, \\ \varepsilon_{ij} &= \frac{1}{2} \left(\frac{\partial u_i}{\partial x_j} + \frac{\partial u_j}{\partial x_i} \right) \end{aligned} \quad (1.5)$$

with ε_{ij} defined as components of the **strain tensor** for *small* deformations. It follows immediately, that the strain tensor is symmetric and dimensionless. Physically the strain components represent relative change in length: ε_{ii} represent simple expansion or compression in a given direction (fig. 1.5a), while ε_{ij} represent a shear strain as depicted in the fig. 1.5b.

Figure 1.5: Graphical representation of strain components, longitudinal, ε_{11} and shear, ε_{13} .



There exists a relation between the displacement gradient matrix eq. (1.3), $\xi(\mathbf{r}, t_0)$ and strain matrix eq. (1.5), (ε_{ij}) , we can express:

$$\xi(\mathbf{r}, t_0) = \frac{1}{2} \left(\xi(\mathbf{r}, t_0) + \xi^t(\mathbf{r}, t_0) \right) + \frac{1}{2} \left(\xi(\mathbf{r}, t_0) - \xi^t(\mathbf{r}, t_0) \right),$$

where ξ^t is a transpose of ξ . We thus have:

$$\xi(\mathbf{r}, t_0) = \frac{1}{2} \begin{pmatrix} 2\frac{\partial u_1}{\partial x_1} & \frac{\partial u_1}{\partial x_2} + \frac{\partial u_2}{\partial x_1} & \frac{\partial u_1}{\partial x_3} + \frac{\partial u_3}{\partial x_1} \\ \frac{\partial u_2}{\partial x_1} + \frac{\partial u_1}{\partial x_2} & 2\frac{\partial u_2}{\partial x_2} & \frac{\partial u_2}{\partial x_3} + \frac{\partial u_3}{\partial x_2} \\ \frac{\partial u_3}{\partial x_1} + \frac{\partial u_1}{\partial x_3} & \frac{\partial u_3}{\partial x_2} + \frac{\partial u_2}{\partial x_3} & 2\frac{\partial u_3}{\partial x_3} \end{pmatrix} + \frac{1}{2} \begin{pmatrix} 0 & \frac{\partial u_1}{\partial x_2} - \frac{\partial u_2}{\partial x_1} & \frac{\partial u_1}{\partial x_3} - \frac{\partial u_3}{\partial x_1} \\ \frac{\partial u_2}{\partial x_1} - \frac{\partial u_1}{\partial x_2} & 0 & \frac{\partial u_2}{\partial x_3} - \frac{\partial u_3}{\partial x_2} \\ \frac{\partial u_3}{\partial x_1} - \frac{\partial u_1}{\partial x_3} & \frac{\partial u_3}{\partial x_2} - \frac{\partial u_2}{\partial x_3} & 0 \end{pmatrix} = \varepsilon + \Omega$$

It is thus can be seen that the displacement gradient matrix can be decomposed into two parts, *symmetric* strain and *antisymmetric* part:

$$\Omega_{ij} = \frac{1}{2} \left(\frac{\partial u_i}{\partial x_j} - \frac{\partial u_j}{\partial x_i} \right) \quad (1.6)$$

It can be shown (appendix A), that the asymmetric strain physically represents an infinitesimal *local rotation*, as depicted in the fig. 1.6. Local rotations, however, do not enter the equations of motion for particle displacement (eq. (1.9)) due to their negligible moment of inertia, as discussed in [50] (p. 46-47).

A deformation on a microscopic scale is the change in the atomic arrangement. Consequently internal stresses (inter-atomic forces) arise to push the system to its mechanical equilibrium. In a freely vibrating system only internal stresses are present.

Let us consider a volume element ΔV of a solid body. We are interested in the total internal force, that is exerted by the surrounding volume elements on ΔV . The total force is thus the sum of forces of all volume elements in the body, that act on ΔV . Hence, we can represent the total force by a volume integral:

$$\int \mathbf{F}(\mathbf{r}) dV$$

where $\mathbf{F}(\mathbf{r})$ is the force per unit volume or force density.

Since the inter-atomic forces are short range, the total force on ΔV acts on its surface. We can then represent the above integral as the integral over the surface. By means of divergence theorem, ($\int \nabla \cdot \mathbf{A} dV = \oint \mathbf{A} \cdot d\mathbf{s}$), each component F_i of the force density $\mathbf{F}(\mathbf{r})$ should be divergence of a vector, since we look for a function that depends on the coordinates (x_1, x_2, x_3) . It must also reflect the direction of the force component, so $F_i = F_i(x_1, x_2, x_3)$. Necessarily, the component F_i of the force is divergence of a second rank tensor, defined as $F_i \equiv \sum_j \frac{\partial \sigma_{ij}}{\partial x_j}$. Thus, we have:

$$\int F_i dV = \sum_j \int \frac{\partial \sigma_{ij}}{\partial x_j} dV = \sum_j \oint \sigma_{ij} ds_j$$

where ds_j are the components of the surface element vector \mathbf{ds} directed outward and normal to the surface element. The tensor σ_{ij} is referred to as **stress tensor** and it is symmetric, as can be shown [50] (p. 46-47). $\sigma_{ij} ds_j$ represents the i th component of the force on the surface element ds_j , perpendicular to the x_j axis, or vice versa, since the tensor is symmetric (fig. 1.7). It is expressed in the units of force per unit area, i.e. in Pascal or in J/m^3 .

Figure 1.6: Local rotation: dashed lines (gray) represent the undeformed solid, solid lines (red) after the deformation, adapted from [50].

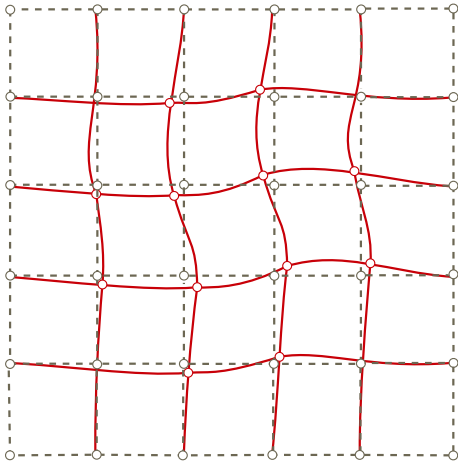
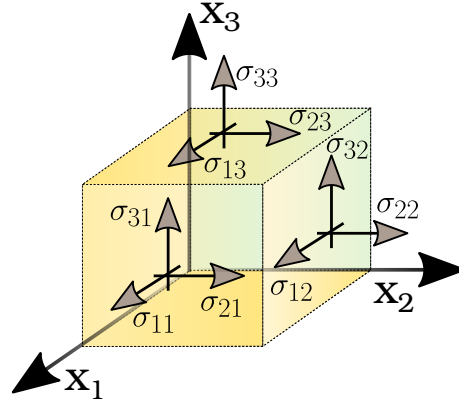


Figure 1.7: Graphic representation of the stress tensor components.



We next can express stress in terms of strain to reformulate **the Hooke's law** in three dimensions. For elastic solids, assuming small deformations, Taylor-expansion of the stress around a zero strain yields: (here we use the Einstein's summation convention, sum is over $j, k \in [1, 2, 3]$.)

$$\sigma_{ij}(\varepsilon_{kl}) = \sigma_{ij}(0) + \left. \frac{\partial \sigma_{ij}(\varepsilon_{ij})}{\partial \varepsilon_{kl}} \right|_{\varepsilon_{kl}=0} \varepsilon_{kl} + \frac{1}{2} \left. \frac{\partial^2 \sigma_{ij}(\varepsilon_{ij})}{\partial \varepsilon_{kl} \partial \varepsilon_{mn}} \right|_{\varepsilon_{kl}=0, \varepsilon_{mn}=0} \varepsilon_{kl} \varepsilon_{mn} + \dots$$

The first term vanishes, since there is no stress when strain is zero (absence of a deformation) and neglecting the second order terms we obtain:

$$\sigma_{ij} = \sum_{kl} \left. \frac{\partial \sigma_{ij}(\varepsilon_{ij})}{\partial \varepsilon_{kl}} \right|_{\varepsilon_{kl}=0} \varepsilon_{kl} = \sum_{kl} c_{ijkl} \varepsilon_{kl} \quad (1.7)$$

where the proportionality constants are the components of the **elastic tensor**, which describes material constants. As can be seen from eq. (1.7), $[\sigma_{ij}] = [c_{ijkl}] = [Pa]$. The elastic tensor has $3^4 = 81$ components, which are reduced to 21 due to symmetry of the strain and stress tensors, that is $c_{ijkl} = c_{jikl} = c_{ijlk}$. The components can be represented in a contracted form, referred to as Voigt notation [53]: $c_{\alpha\beta} = c_{ijkl}$, where α corresponds to (ij) and β to

(kl) , respectively:

$$(11) \leftrightarrow 1, (22) \leftrightarrow 2, (33) \leftrightarrow 3 \\ (23) = (32) \leftrightarrow 4, (13) = (31) \leftrightarrow 5, (12) = (21) \leftrightarrow 6$$

Using eq. (1.5) and the symmetry property, the above expression can be re-written in terms of a displacement:

$$\sigma_{ij} = \frac{1}{2} \sum_{kl} c_{ijkl} \left(\frac{\partial u_k}{\partial x_l} + \frac{\partial u_l}{\partial x_k} \right) = \sum_{kl} c_{ijkl} \frac{\partial u_k}{\partial x_l} \quad (1.8)$$

It should be noted that, since stress a tensor field and its components assume spacial dependence, one should consider the volume element ΔV to be **infinitesimally small**, i.e. the limit as ΔV tends to zero, in order to properly define stress at a point \mathbf{r} .

1.1.2 Propagation in a semi-infinite elastic solid

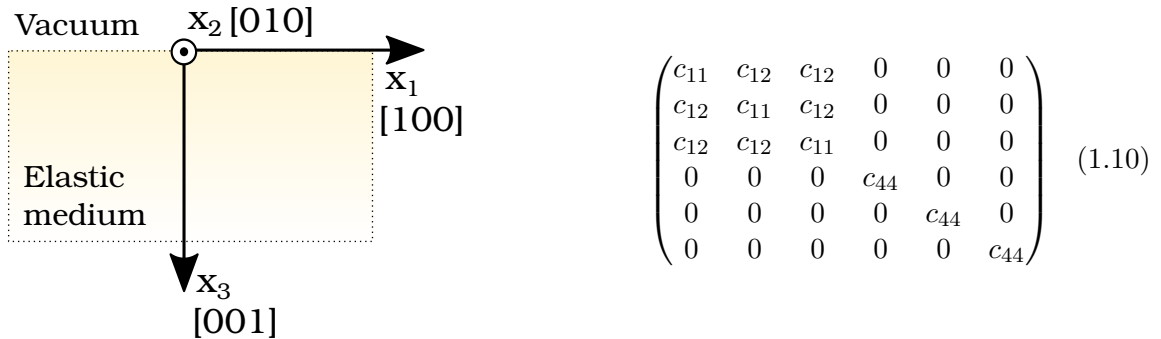
Consider a semi-infinite elastic solid of a cubic symmetry, as represented in the fig. 1.8. Taking into account the Hooke's law given by eq. (1.7), eq. (1.8), the second Newton's law for a free vibration is expressed as:

$$\rho \frac{\partial^2 u_i}{\partial t^2} = \sum_{jkl} c_{ijkl} \frac{\partial^2 u_k}{\partial x_j \partial x_l} \quad (1.9)$$

where ρ is the mass density of a considered medium. The eq. (1.9) represents the equation of motion for a free vibration and is a starting point for the description of elastic wave propagation in crystalline media.

Cubic symmetry of the lattice simplifies the elastic tensor by reducing the number of constants to 3, [47] (p.141). It is expressed in the standard basis (four fold axis) by the eq. (1.10). Given the equation of motion and the expression for the elastic tensor, we can now consider the propagation of the elastic wave in the semi-infinite elastic solid.

Figure 1.8: Solid half-space.



Note that, in this approach several assumptions are made.

Assumption №1
Piezoelectricity is not taken into account

In general, for a piezoelectric solid, the equation of motion and the constitutive equations for the stress and dielectric displacement, \mathbf{D} are of the form [47] (p.216, p.154):

$$\rho \frac{\partial^2 u_i}{\partial t^2} = c_{ijkl} \frac{\partial^2 u_l}{\partial x_j \partial x_k} + \underbrace{e_{kij} \frac{\partial^2 \phi}{\partial x_j \partial x_k}}_{\text{piezoelectric term}} \quad \begin{cases} \bar{\sigma} &= \bar{c} \cdot \bar{\varepsilon} - \bar{e} \cdot \mathbf{E} \\ \mathbf{D} &= \bar{d} \cdot \bar{E} + \bar{e} \cdot \bar{\varepsilon} \end{cases}$$

where \bar{e} , \bar{d} , \mathbf{E} , ϕ are piezoelectric, dielectric tensors, electric field and electric potential, respectively. A piezoelectric wave, would possess three components: two mechanical displacements, u_1 , u_3 and the associated electric potential due to piezoelectricity. Taking into account the latter significantly increases the complexity of the problem, such that at some points no analytical calculation is possible, and one has to resort to a numerical solution. Simplification of the problem is justified in case of *weak* piezoelectric materials, such as GaAs, for which the character of the Rayleigh wave is not affected by piezoelectricity to a significant extent ([47], p.290). Intuitively speaking, introducing the latter is equivalent to introducing effective elastic constants of the medium. The Rayleigh velocity, as we shall see, depends on the elastic constants and thus, its absolute value will be affected. A posteriori, we can justify our assumption by comparing numerical values of the computed Rayleigh velocity with the experimental values, for the propagation along [110] (or [1 $\bar{1}$ 0]) directions. Comparison yields **2853 m/s**, theoretical value vs **2710 m/s**, experimental value (within the measurement error of $\simeq 5\%$), which translates to $\simeq 5.3\%$ of error with respect to the experimental value. It is thus a reasonable compromise between the simplification and the corresponding error.

Assumption №2
Attenuation is not taken into account

To simplify further, we do not take into account the attenuation, since we are interested in the dependence of the displacement components, u_i and strain components, ε_{ij} on the depth, z , while the attenuation results in a decrease of the wave amplitude with the propagation distance, i.e. x-dependence.

1.1.3 Propagation along [100] in the (100) plane

We consider a wave, propagating along $x_1 \parallel [100]$ direction of a cubic system, as represented in the fig. 1.8. Taking into account the expression for the elastic tensor in the standard [100] basis and assuming no dependency⁸ on x_2 in the Rayleigh wave, i.e. $\frac{\partial}{\partial x_2} = 0$, summation over non-zero elastic constants yields, eq. (1.9):

$$\begin{cases} \rho \frac{\partial u_1^2}{\partial t^2} = c_{11} \frac{\partial^2 u_1}{\partial x_1^2} + c_{12} \frac{\partial^2 u_3}{\partial x_1 \partial x_3} + c_{44} \left(\frac{\partial^2 u_1}{\partial x_3^2} + \frac{\partial^2 u_3}{\partial x_1 \partial x_3} \right) \\ \rho \frac{\partial u_2^2}{\partial t^2} = c_{44} \left(\frac{\partial^2 u_2}{\partial x_1^2} + \frac{\partial^2 u_2}{\partial x_3^2} \right) \\ \rho \frac{\partial u_3^2}{\partial t^2} = c_{12} \frac{\partial^2 u_1}{\partial x_1 \partial x_3} + c_{11} \frac{\partial^2 u_3}{\partial x_3^2} + c_{44} \left(\frac{\partial^2 u_1}{\partial x_1 \partial x_3} + \frac{\partial^2 u_3}{\partial x_1^2} \right) \end{cases} \quad (1.11)$$

Analytical expression, describing a particle displacement in a surface wave would be of the form of a plane wave, that decays exponentially with depth, as it propagates:

$$u_i = U_i e^{-\alpha x_3} e^{-\gamma x_1} e^{i(\omega t - k x_1)} \quad (1.12)$$

where U_i is the amplitude of the displacement or polarization, α penetration depth (m^{-1}), reflecting the fact that the wave amplitude is decreasing with depth, γ stands for attenuation (m^{-1}) and is a characteristic of a material. Following the assumption №2, we neglect the attenuation. A detailed calculation can be found in the appendix B, here we present only the main steps and conclusions.

1. We assume solutions of the form of eq. (1.12) and look for the unknown penetration depth, α , wave vector, k and angular frequency, ω , the latter two are related by $k = \frac{\omega}{V_r}$, where V_r is the Rayleigh velocity.
2. Plugging the solutions into the system of equations, eq. (1.11) we obtain a quadratic equation in q^2 , where q is defined as $q = \frac{\alpha}{k}$. It yields thus two solutions q_1^2 and q_2^2 :

$$q^4 + q^2 \frac{(c_{12} + c_{44})^2 - c_{11}^2 - c_{44}^2 + (c_{11} + c_{44})\rho V_r^2}{c_{11}c_{44}} + \frac{(c_{11} - \rho V_r^2)(c_{44} - \rho V_r^2)}{c_{11}c_{44}} = 0 \quad (1.13)$$

3. Since the solid is finite, the obtained solutions should satisfy boundary conditions, relating the mechanical variables at the interface between two media. In our case the second medium is vacuum, this implies that normal stresses are zero at the surface, $\sigma_{i3} = 0$. We find that separately, the solutions do not satisfy the boundary conditions, $\sigma_{i3} = 0$ and thus, a linear combination of the solutions should be taken:

⁸Since the particle displacement in the Rayleigh wave is polarized in the $x_1 x_3$ sagittal plane, thus a priori, is independent of x_2 coordinate.

$$\begin{cases} u_1 &= (U_1 e^{-\alpha_1 x_3} + U_2 e^{-\alpha_2 x_3}) e^{i(\omega t - kx_1)} \\ u_2 &= 0 \\ u_3 &= (W_1 e^{-\alpha_1 x_3} + W_2 e^{-\alpha_2 x_3}) e^{i(\omega t - kx_1)} \end{cases}$$

4. From the above equations it follows that the boundary conditions are satisfied if there exists some V_r , satisfying

$$(c_{44} - \rho V_r^2)(c_{11}^2 - c_{12}^2 - c_{11} \rho V_r^2)^2 = c_{11} c_{44} (c_{11} - \rho V_r^2)(\rho V_r^2)^2 \quad (1.14)$$

which is the equation for the Rayleigh velocity, V_r .

5. Solving eq. (1.14) and then eq. (1.13) numerically, we can obtain the analytical expressions for the normalized displacements, eq. (1.15) (**real part**) and strain components, eq. (1.16) (**complex notation**). The computed Rayleigh velocity is $\mathbf{V}_r = 2711 \text{ m/s}$ along the [100] direction.

$$\begin{cases} u_x &= 2 \cos\left(\frac{\phi}{2} + \omega t - kx_1\right) \cos\left(q_I x'_3 + \frac{\phi}{2}\right) e^{-q_R x'_3} \\ u_y &= 0 \\ u_z &= 2r \sin\left(\frac{\phi}{2} + \omega t - kx_1\right) \sin\left(q_I x'_3 - \psi + \frac{\phi}{2}\right) e^{-q_R x'_3} \end{cases} \quad (1.15)$$

$$\begin{cases} \frac{1}{kU_1} \varepsilon_{11} &= 2 e^{i(\frac{\phi-\pi}{2})} e^{-q_R x'_3} \cos\left(q_I x'_3 + \frac{\phi}{2}\right) e^{i(\omega t - kx_1)} \\ \frac{1}{kU_1} \varepsilon_{13} &= e^{i(\pi + \frac{\phi}{2})} e^{-q_R x'_3} \left\{ q_R \cos\left(q_I x'_3 + \frac{\phi}{2}\right) + q_I \sin\left(q_I x'_3 + \frac{\phi}{2}\right) + r \sin\left(q_I x'_3 - \psi + \frac{\phi}{2}\right) \right\} e^{i(\omega t - kx_1)} \\ \frac{1}{kU_1} \varepsilon_{33} &= 2r e^{i(\frac{\phi-\pi}{2})} e^{-q_R x'_3} \left\{ -q_R \sin\left(q_I x'_3 - \psi + \frac{\phi}{2}\right) + q_I \cos\left(q_I x'_3 - \psi + \frac{\phi}{2}\right) \right\} e^{i(\omega t - kx_1)} \end{cases} \quad (1.16)$$

where $x'_3 = kx_3$ is the normalized depth, ϕ and ψ are phase constants, that appear in the calculation due to the displacements amplitude ratios, $\frac{U_2}{U_1}$ and $r = \frac{W_1}{U_1}$, respectively. The obtained solution for penetration depth, α and wave vector, k , $q = \frac{\alpha}{k}$ is a complex number, q_R and q_I being the real and imaginary parts, respectively.

As can be seen in the figures below, Rayleigh wave penetrates the solid at about its wavelength, λ_{saw} in depth, x_3 . We will need, in what follows, the complex expressions of the strain components, ε_{11} and ε_{13} , marked in blue for clarity. Furthermore, it is important to note that the shear strain component ε_{13} is *vanishingly small near the surface*. We discuss this point in the chapter 2 and chapter 6.

Figure 1.9: Normalized displacements vs normalized depth, eq. (1.15), evaluated at $t = 0$, $x_1 = 0$.

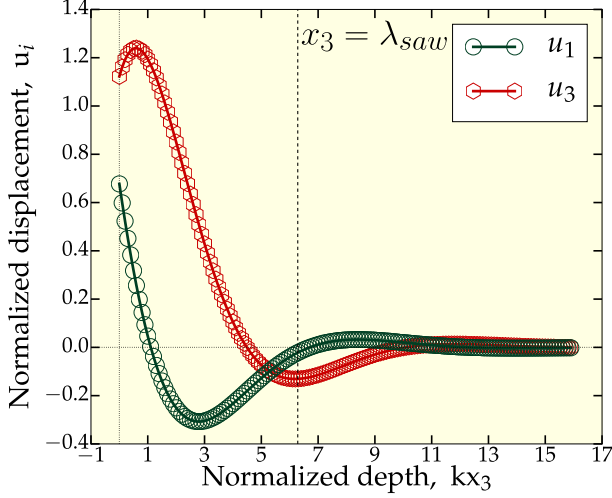
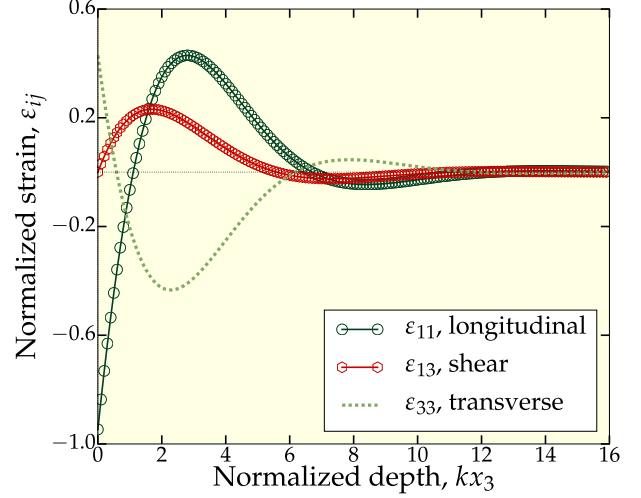


Figure 1.10: Normalized strain components (**real part**) vs normalized depth, eq. (1.16), evaluated at $t = 0$, $x_1 = 0$.



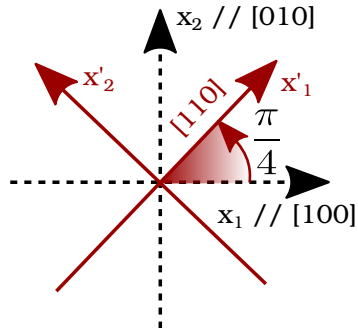
1.1.4 Propagation along $[110]$ in the (100) plane

Since the propagation is along $[110]$, we need to express the elastic constants in the new basis: $x'_1 = [110]$, $x'_2 = [\bar{1}10]$, $x'_3 = [001]$. The coordinate transformation is represented in the fig. 1.11. The elastic components in the new basis can be found using the transformation rule: $c'_{ijkl} = \gamma_{i\alpha} \gamma_{j\beta} \gamma_{k\gamma} \gamma_{l\delta} c_{\alpha\beta\gamma\delta}$, where γ is the transformation matrix⁹:

$$\gamma = \begin{pmatrix} \frac{1}{\sqrt{2}} & \frac{1}{\sqrt{2}} & 0 \\ -\frac{1}{\sqrt{2}} & \frac{1}{\sqrt{2}} & 0 \\ 0 & 0 & 1 \end{pmatrix} \quad (1.17)$$

and results in eq. (1.18):

Figure 1.11: New coordinate system is obtained by $\pi/4$ rotation around $[001]$ direction.



$$\begin{cases} c'_{11} = \frac{c_{11}}{2} + \frac{c_{12}}{2} + c_{44} \\ c'_{12} = \frac{c_{11}}{2} + \frac{c_{12}}{2} - c_{44} \\ c'_{13} = c_{12} \\ c'_{33} = c_{11} \\ c'_{44} = c_{44} \\ c'_{66} = \frac{c_{11}}{2} - \frac{c_{12}}{2} \end{cases} \quad (1.18)$$

⁹Each row represents the coordinates in the old basis.

The calculation is carried out in the same way as in the previous section, yielding the equation for the Rayleigh velocity, expressed in terms of the elastic constants in the new basis:

$$(c'_{44} - \rho V_r^2) \left[c'_{11} c'_{33} - c'^2_{13} - c'_{33} \rho V_r^2 \right]^2 = c'_{33} c'_{44} (c'_{11} - \rho V_r^2) (\rho V_r^2)^2$$

The analytical expressions for the normalized displacements and strain components are the same as given in the previous section. The only difference is in the calculated Rayleigh velocity, reflecting the anisotropy of the media: $\mathbf{V}_r = \mathbf{2853m/s}$ along [110].

1.2 Ferromagnetism

*“Now sing my muse, for ’tis a weighty cause.
Explain the Magnet, why it strongly draws,
And brings rough Iron to its fond embrace.”*
Lucretius Carus, 99-55 B.C.

The first mentioning of lodestone, or magnetite, appears in the Greek writings at about 800 B.C. [54]-[55]. The term *lodestone* dates back to 15th century and it originates from the old English "lode", meaning "to guide" or to "lead". First compasses were made from lodestones, as commonly believed in China in around 2700 B.C., and used in navigation. It is through them the ancient people discovered magnetism. The fig. 1.12 grasps very briefly some important events in its history. On the course of time our understanding evolved from the idea that the lodestone had a divine origin and possessed a soul, through united theory of electricity, magnetism and light, to the formulation of quantum mechanical exchange interaction, that is responsible for the magnetic ordering.

Figure 1.12: following references [54]-[55], some important events in the history of magnetism.

1269 A.D.

Petrus Peregrinus

observed and documented several properties of magnets: existence of magnetic poles, their attraction and repulsion, showed how magnetize an iron needle with a lodestone.

1600 treatise "De Magnete"

William Gilbert

discovered that the earth is itself a giant magnet, realized a loadstone would lose its magnetic properties if incandescent and beating wrought iron with a hammer would induce magnetism.

1824-1831

Michael Faraday

introduced the concept of a field, discovered magnetic induction, including a new parameter in the theory of electromagnetism - time. In 1845 discovered magneto-optic effect, bearing his name, making link between magnetism and light.

1581

Robert Norman

observed that a magnetized needle would tilt with respect to horizontal (magnetic inclination).

1820

Hans Christian Oesterd

observed deflection of a compass needle by current carrying wire (driven by voltaic cell), showing for the first time the existing connection between electricity and magnetism.

1864

James Clerk Maxwell

unified the theory of electricity, magnetism and light, giving it a mathematical frame.

1644

René Descartes

proposed his theory of magnetism, described the iron-filling method for magnetic field mapping.

1820-1827

André Marie Ampère

founded the science of electrodynamics. He showed that magnetism is produced by "electricity in motion", invented galvanometer to measure current.

1888

Heinrich Herz

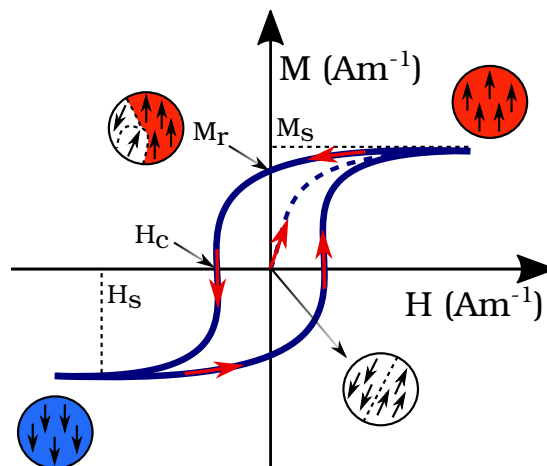
Was the first to send and receive radio waves.

Today we can distinguish between several types of magnetism, based on the magnetic order, response to the applied field, i.e. magnetic susceptibility, and dependence of the magnetic order on temperature (for example, the textbooks [56] (ch.5) or [57], p.13 gives magnetic “family tree”). In this thesis we focus on ferromagnetism in metals.

Ferromagnets exhibit magnetic ordering, i.e. magnetic moments within the solid are aligned even in the absence of an external magnetic field. This *spontaneous* magnetization¹⁰ occurs at temperatures below *Curie* temperature, above which thermal vibrations hinder the alignment, the magnetic order is destroyed and the material becomes paramagnetic. The magnetization orientation is not constant, but varies throughout the material, which manifests itself in the existence of *magnetic domains*, separated by domain walls. The fingerprint of a ferromagnet is its irreversible non-linear response to the applied field, i.e. ferromagnetic hysteresis, as represented in the figure below (fig. 1.13).

The question why certain materials exhibit permanent magnetism was there for a long time. A. M. Ampère thought that the magnetism of solid bodies originates from tiny currents, existing inside of matter. Pierre Weiss in 1907 proposed a theory of ferromagnetism, suggesting that the alignment of magnetic moments occurs due to an internal “molecular field”, proportional to magnetization, $\mathbf{H}_W = \lambda\mathbf{M}$, though of an unknown origin.

Figure 1.13: A sketch of a ferromagnetic hysteresis. The dashed curve represents the first magnetization process, initially a ferromagnet is in a *demagnetized* state. Sample is saturated, when magnetization reaches a constant value, M_s . At remanence^a, i.e. zero field, ferromagnet retains some of its magnetization, M_r and coercive field, H_c is necessary field to reverse it.



^aNote that magnetization orientation along a certain preferable direction is energetically equivalent for both senses. Application of a magnetic field increases the probability to be directed in certain sense, resulting in a remanent magnetization, as opposed to the initially demagnetized state.

¹⁰The term spontaneous magnetization was coined by James Ewing in 1881, who studied the phenomena [57] (p.8).

For example, an estimation of this field at the transition (Curie) temperature of 10^3 K, as example, yields a field¹¹ of around 1500T [56] (p.88), which indicates an enormous strength of interaction. In 1928 Werner Heisenberg in his famous paper could explain the origin of Weiss' "molecular field" and thus, of ferromagnetism [59], using quantum mechanics to treat a many-body problem. It originates from the quantum mechanical *exchange interaction*, as a result of electron-electron interaction (the Coulomb repulsion) and Pauli exclusion principle. Two descriptions of the exchange interaction (apart from the original paper) can be found in the literature. First is very simplified, as it considers a pair of interacting electrons, for example, described in [56] (ch.4), [60] (ch.6). A concrete many-body problem, much more elaborated, is considered in [61] (ch. 17, pp. 330-334). In essence, the interaction between spins of the ions can be described in terms of Heisenberg Hamiltonian:

$$H_{Heis} = - \sum_{i < j} J_{ij} \vec{S}_i \cdot \vec{S}_j,$$

where subscripts i, j represent spins on different atomic sites and the term J_{ij} is defined as the *exchange* integral. It is caused by the fermionic nature of electrons, in particular the Pauli exclusion principle, and has no classical analogue. Exchange couplings (the coefficients J_{ij}) are called ferromagnetic (resp. antiferromagnetic), when they are positive (resp. negatives) and favor preferential parallel (resp. anti-parallel) alignment of interacting spins.

What it is important for us to note is that, considering the exchange interaction implies a discrete medium, that is every atomic site possesses a magnetic moment. In what follows, the energy density terms of a ferromagnet are presented, considering a *continuous* medium: the magnetization is a vector field, $\vec{M}(\vec{r})$ defined at every point in space within the body, that is, in a volume larger than the lattice unit cell. Furthermore, all corresponding calculations are carried out under **single domain approximation**, which implies *no exchange energy penalty* as all spins are aligned, in other words magnetization is *uniform*. Thus in what follows, exchange energy term does not appear.

¹¹The highest magnetic field ever reached in the laboratory for the moment is of 100T, while strongest magnetic fields are produced by neutron stars (magnetars), of about 10^{10-11} T [58] !

1.2.1 Energy density of a ferromagnet

As discussed, the magnetic order of a ferromagnet comes from the pure quantum mechanical phenomena, exchange interaction. However, magnetization of a ferromagnet is not uniform in the solid, the latter is divided into magnetic domains, that is regions with different orientation of a net magnetic moment, as schematically represented in fig. 1.13. The origin of domains formation was first pointed out by L. Landau and E. Lifshitz in 1935 [62]. They made an assumption, that the magnetic moments in a ferromagnetic crystal orient so as to *minimize* its total energy. Under this assumption they determined the orientation distribution of magnetic moments, as well as the domain and domain wall width and postulated the origin of its formation. In 1959, Charles Kittel gave a review on this subject [63] and an excellent source on magnetic domain theory can be found in [64]. In what follows we discuss different contributions to the total energy density of a ferromagnet. The analytical expressions, presented here, will be used to derive the expression for the “effective” magnetic field, that plays a leading role in the magnetization dynamics.

1.2.2 Zeeman energy density

Zeeman energy is the energy of a magnetic moment in an external field. For a solid ferromagnet its density is defined as:

$$f_z = -\mu_0 \mathbf{M} \cdot \mathbf{H}_{ext} \quad (1.19)$$

It is clear, that if magnetization is anti-parallel to the external field, it would cost an energy penalty $2\mu_0 M H_{ext}$, thus a parallel alignment with the field is energetically favorable.

1.2.3 Shape anisotropy energy or magnetostatic self-energy

This energy is of Zeeman type, but originates from magnetic field, produced by a magnetized object itself. A graphic representation is given in the fig. 1.14: field produced by magnetization acts against it and is referred to as *demagnetizing field*, H_d inside the object and *stray field*, H_{stray} outside.

The magnetostatic energy, also referred as stray field energy or demagnetizing energy, is given by:

$$E_d = -\frac{1}{2}\mu_0 \int_{sample} \mathbf{M} \cdot \mathbf{H}_d dV$$

Calculation of demagnetizing field is, in general, complicated, as it is related to the shape of a magnetized body (from which “shape anisotropy” stems) and to its magnetic homogeneity. The demagnetizing field can be expressed by the formula:

$$\mathbf{H}_d = -\bar{N}\mathbf{M},$$

where \bar{N} is a demagnetizing tensor. Analytical expressions can be found in literature for uniformly magnetized ellipsoids [64] (ch.3): general, disc-shaped, nearly spherical, etc. For a thin film it can be show [65], that the magnetostatic energy is expressed as:

$$E_d = \frac{1}{2} \mu_0 M_s^2 \cos^2 \theta \quad (1.20)$$

where θ is defined as the angle between the magnetization and the normal to the sample surface. It is immediately clear, that in thin films the in-plane magnetization orientation, $\theta = \frac{\pi}{2}$ is favorable, since the energy vanishes.

1.2.4 Magneto-crystalline anisotropy energy (MCA)

In a crystal certain crystallographic directions are energetically favorable for the magnetization orientation at remanence. Such preference of the magnetization to lie in a specific direction is called *magneto-crystalline anisotropy*.

The expression for the anisotropy energy density ($\frac{J}{m^3}$) can be obtained phenomenologically by an expansion in power series of directional cosines [66] ch.7, since this energy term depends on the magnetization orientation and hence should be the function of its components (fig. 1.15):

$$f_{mca} = b_0 + \sum_i b_i m_i + \sum_{ij} b_{ij} m_i m_j + \sum_{ijk} b_{ijk} m_i m_j m_k + \sum_{ijkl} b_{ijkl} m_i m_j m_k m_l + O(m^5)$$

Figure 1.14: Graphic representation of the demagnetizing field, \mathbf{H}_d inside of the ferromagnet and \mathbf{H}_{stray} outside.

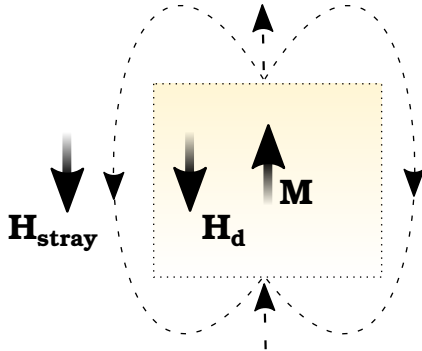
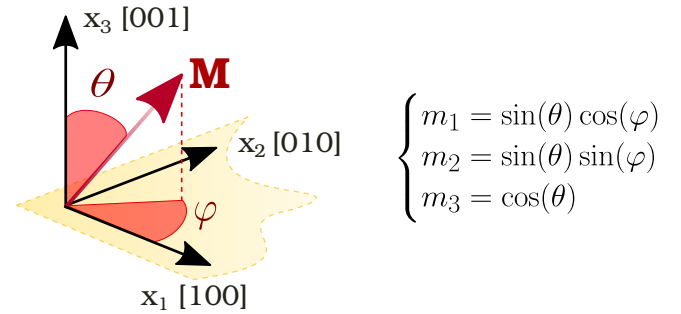


Figure 1.15: Directional cosines of magnetization.



Since there should be no difference in energy for opposite magnetization directions, the above function is symmetric, i.e. $f_{mca}(m_i) = f_{mca}(-m_i)$, and thus the *odd terms* are *excluded* from the expression. The b_{ij} coefficient vanishes unless $i = j$ as $m_i^2 = (-m_i)^2$. Taking into account the symmetries of different crystallographic systems, one can obtain the corresponding expressions. For example:

- ▷ **Cubic system** posses 3-fold rotational symmetry¹², i.e. rotation by $2\pi/3$ about the diagonal leaves the crystal unchanged and yields a cyclic permutation of the axes, hence the indices $i = 1, 2, 3$ are indistinguishable. Thus, $b_{11} = b_{22} = b_{33}$. Under the condition $\sum_i m_i^2 = 1$, $\sum_{ij} b_{ij} m_i m_j$ is a constant and the following expression is obtained, as described in details in [66]:

$$f_{mca}^{cubic} = K_0 + K_1 (m_1^2 m_2^2 + m_2^2 m_3^2 + m_1^2 m_3^2) + K_2 m_1^2 m_2^2 m_3^2 + \dots =$$

$$K_0 + \frac{K_1}{4} \left(\sin^4 \theta \sin^2(2\varphi) + \sin^2(2\theta) \right) + \frac{K_2}{4} \sin^2 \theta \sin^2(2\theta) \sin^2(2\varphi) + \dots \quad (1.21)$$

where K_i the magneto-crystalline anisotropy constants are functions of $b_{..}$ -coefficients.

- ▷ **Uniaxial anisotropy** implies the presence of only one hard axis. The expression is given by expansion in power series of the form [65] (p.184):

$$f_{mca}^{uni} = \sum_n K_{un} \sin^{2n} \theta \simeq K_{u0} + K_{u1} \sin^2 \theta + K_{u2} \sin^4 \theta + \dots \quad (1.22)$$

Note that, the sign of the anisotropy constants affects “the choice” of the easy and hard axes. This can be seen directly from the expression. For example, consider the eq. (1.21) for the in-plane magnetization, i.e. $\theta = \frac{\pi}{2}$ and so the expression reduces to $K_0 + \frac{K_1}{4} \sin^2(2\varphi)$. If $K_1 < 0$, then a way to minimize the energy is to maximize the $\sin(2\varphi)$ term, that is $\varphi = \frac{\pi}{4}$. Thus, for the negative MCA constant, the easy axes are the (110) directions family¹³.

In contrast, if $K_1 > 0$, the way to minimize the energy is to set this term to zero, which implies $\varphi = \frac{\pi}{2}$ and thus, the easy axes are the (100) family.

In the case of the uniaxial MCA only one easy axis is preferred. As it follows from eq. (1.22), positive value of the MCA constant would result in the in-plane (IP) magnetization orientation, while negative, for out-of-plane (OP). For in-plane magnetization orientation, as in the case of thin films¹⁴, the role of the uniaxial MCA is to promote one hard axis. The expression

¹²As can be seen from [47] p.90, all classes of cubic symmetry possess triad axis, A_3 .

¹³The φ angle is defined **with respect to [100] axis** (fig. 1.15).

¹⁴For thin films, another type of anisotropy can be present, referred to as perpendicular magnetic anisotropy, that leads in some of our samples to the formation of stripe-like magnetic domains, as will be discussed in chapter 3.

for the energy density is given by [67]:

$$f_{mca}^{uni} = K_u \sin^2 \theta \cos^2 \left(\varphi - \frac{\pi}{4} \right) \quad (1.23)$$

As an order of magnitude, the anisotropy constants for **bulk** iron, Fe and nickel, Ni are listed in the table below. Note that, at saturation magnetization, the anisotropy constants are temperature dependent.

Table 1.1: Anisotropy constants for **bulk** systems at different temperatures from [65] (p.192).

Element	K_1 (J/m^3) at 4.2K	K_2 (J/m^3) at 4.2K	K_1 (J/m^3) at T_{room}	K_1 (J/m^3) at T_{room}
Fe	$5.2 \cdot 10^4$	$-1.8 \cdot 10^4$	$4.8 \cdot 10^4$	$-1.0 \cdot 10^4$
Ni	$-12 \cdot 10^4$	$3.0 \cdot 10^4$	$-4.5 \cdot 10^4$	$-2.3 \cdot 10^4$

1.2.5 Discussion on the origin of MCA

The physical origin of the MCA lies in the spin orbit coupling (SOC) and crystal field: the spin of the electron interacts with its orbital motion, which in turn, is coupled to the crystal lattice by means of electrostatic fields. In other words, if crystal field has low symmetry and if valence electrons of an atom have non-zero orbital moment, meaning asymmetric charge distribution, then the orbitals interact anisotropically with the crystal field. That is, certain orientations for the molecular orbitals are energetically preferred.

The contribution of the SOC energy to the MCA energy is derived using time-independent perturbation theory [68]. The perturbative analysis is applicable in the case of transition metals (TM), since the SOC energy in the case of latter is very weak¹⁵, as compared to the electron binding energies and the crystal field (about 10^{-6} eV/atom for highly symmetric cubic crystals). The relativistic SOC perturbed Hamiltonian for a *single* electron is expressed by:

$$H = H_0 + H_{soc} = H_0 + \xi(r) \vec{\sigma} \cdot \vec{L},$$

where $\xi(r) = \frac{1}{4c^2 r} \frac{\partial V}{\partial r}$.

The magnetism of TM, like iron, comes from the $3d$ electrons¹⁶. These are conduction electrons, that are well described in the frame of Stoner model of itinerant ferromagnetism. Considering such system, the correction to the total energy due to the SOC will come from the second order term:

$$E_{soc} = \sum_o \sum_i \frac{|\langle o | H_{soc} | i \rangle|^2}{\varepsilon_o - \varepsilon_i} = \sum_o \sum_i \xi^2(r) \frac{|\langle o | \vec{\sigma} \cdot \vec{L} | i \rangle|^2}{\varepsilon_o - \varepsilon_i}, \quad (1.24)$$

¹⁵as can be seen from the expression above, $\xi \propto \frac{\partial V}{\partial r}$. The Coulomb potential in turn is proportional to the atomic number, hence the SOC has a stronger effect in heavy atoms like rare earth elements as Y, Gd etc.;

¹⁶since the $3d$ shell is not closed and $4s^2$ electrons participate in bonding;

where first sum runs over all occupied states, i.e. over the total number of electrons, while i is summed over all possible states¹⁷ and $\varepsilon_o, \varepsilon_i$ single-state energies. When $i = o$, the matrix element $|\langle o|H_{soc}|o\rangle|$ vanishes, and hence the correction to the total energy comes from the interaction between the occupied o and unoccupied states u :

$$E_{soc} = \sum_{o,u} \xi^2(r) \frac{|\langle o|\vec{\sigma} \cdot \vec{L}|u\rangle|^2}{\varepsilon_o - \varepsilon_u} \quad (1.25)$$

The eq. (1.25) represents a quantum mechanical approach. This approach is important for *ab initio* calculations, as will be seen in the chapter 3.

1.2.6 Elastic energy density

The elastic energy density is given by [53]:

$$f_{el} = \frac{1}{2} \sum_{i,j,k,l} c_{ijkl} \varepsilon_{ij} \varepsilon_{kl}$$

For a cubic symmetry with only three independent elastic constants (eq. (1.10)), the above expression reduces to:

$$f_{el}^{cubic} = \frac{1}{2} c_{11} (\varepsilon_{11}^2 + \varepsilon_{22}^2 + \varepsilon_{33}^2) + 2c_{44} (\varepsilon_{12}^2 + \varepsilon_{23}^2 + \varepsilon_{31}^2) + c_{12} (\varepsilon_{22}\varepsilon_{33} + \varepsilon_{11}\varepsilon_{33} + \varepsilon_{11}\varepsilon_{22})$$

1.2.7 Magneto-elastic energy (MEL): phenomenology

Magneto-elastic energy arises as a result of the coupling between magnetization direction and mechanical strain. At equilibrium a ferromagnetic crystal, possessing a spontaneous magnetization, is strained, strain being dependent on the direction of the equilibrium magnetization with respect to the crystal axes.

In what follows, we describe the phenomenological approaches, used to derive the expression for the magneto-elastic energy density. The reader might skip this part, if not interested, the final expressions are given in the section 1.2.8.

To our knowledge, there exist several approaches to derive the expression for the magneto-elastic energy density: (1) energy expansion in power series in directional cosines of magnetization and strain components, (2) pair interaction model ([24], ch.2, section V) and (3) symmetry formalism ([24], ch.2, section III). Symmetry formalism is based on energy invariance with bulk translations, rotations, time reversal and symmetry operations, i.e. corresponding elements of a point group of the considered crystal. This approach is more rigorous, as it

¹⁷note, that $|o\rangle, |i\rangle$ are not the eigenstates of the H_{soc} , since spin and orbital character do not mix for the unperturbed Hamiltonian eigenstates;

includes higher order magneto-elastic coefficients in the energy terms. Although being mathematically rigorous, it leads to cumbersome expressions, we thus focus on simpler methods.

1. Expansion in power series

Following C. Kittel [63], E.W. Lee proposed the following expansion of the magneto-elastic energy density [69]:

$$f_{mel}^{cubic} = \sum_{ijk} B_{ijk} m_i \varepsilon_{jk} + \sum_{ijkl} B_{ijkl} m_i m_j \varepsilon_{kl} + O(m^4, \varepsilon^2)$$

where B_{ijk} , B_{ijkl} are magneto-elastic constants of the material, expressed in $[J/m^3]$. As in the case of magneto-crystalline energy, the function should be symmetric with respect to m_i , i.e. opposite magnetization directions produce the same strain [24]. Thus, B_{ijk} should vanish. Following symmetry arguments for a cubic system, one can derive the final expression¹⁸:

$$f_{mel} = B_1 (\varepsilon_{11} m_1^2 + \varepsilon_{22} m_2^2 + \varepsilon_{33} m_3^2) + 2B_2 (\varepsilon_{12} m_1 m_2 + \varepsilon_{23} m_2 m_3 + \varepsilon_{13} m_1 m_3) \quad (1.26)$$

The energy of a physical system is defined at equilibrium. In a deformed ferromagnet, the strain components are the functions of the equilibrium directional cosines. The equilibrium values for strain components¹⁹ are found by minimizing the total energy with respect to strain (appendix F), $\bar{\varepsilon}_{ij} = -\frac{B_2}{4c_{44}} \bar{m}_i \bar{m}_j$, where c_{44} is the elastic constant of the material. It is thus clear, that at equilibrium the B_2 -term is quadratic in m_i and the above function is even.

2. Atomic pair model

Pair interaction model was originally proposed by Louis Néel [70] (1954) to explain the microscopic origin of magneto-crystalline anisotropy and magneto-elasticity in terms of interactions, both isotropic and anisotropic, between atomic pairs as opposed to already existing "classical theory" (referred to C. Kittel [63], 1949). We follow the derivation, presented by Lacheisserie in [71] (pp. 351-357), [24] (pp. 3).

Consider a pair of atoms, separated by a distance r , ψ being the angle between the atomic magnetic moment (parallel to the spontaneous magnetization) and the distance vector \mathbf{r} (fig. 1.16a). The interaction energy *between two atoms*, f_{ij} should be a function of the distance and the angle ψ to reflect the coupling between the magnetization orientation and inter-atomic position. It is expanded in Legendre polynomial basis

¹⁸Note that in [63] the 2-factor of B_2 is missing.

¹⁹The "-" sign stands for equilibrium value.

as:

$$f_{ij}(r, \psi) = A_0(r) + A_2(r) \left(\cos^2 \psi - \frac{1}{3} \right) + A_4(r) \left(\cos^4 \psi - \frac{6}{7} \cos^2 \psi + \frac{3}{35} \right) + \dots \quad (1.27)$$

where the $A_i(r)$ coefficients depend only on the inter-atomic distance and thus indicate the strength of interaction with the distance. The total magneto-elastic energy of a ferromagnet can be obtained by summing up the interactions in a *deformed* crystal²⁰. However, the interactions can be both long and short-ranged. Long-range implies the dipolar interactions and thus, summation should be carried out over all the atomic pairs. The result in such a case depends on the actual shape of the ferromagnet, in other words represents the shape anisotropy energy. If only the interaction between nearest neighbors is considered, then the summation will lead to magneto-crystalline and magneto-elastic energy terms.

To do so, first we re-write the $\cos \psi$ in terms of directional cosines of the magnetization, m_i and distance vector components, w_i . From fig. 1.16a it follows that $\cos \psi = \frac{\mathbf{M} \cdot \mathbf{r}}{\|\mathbf{M} \cdot \mathbf{r}\|} = \sum_i m_i w_i$.

Secondly, it should be noted, that the first term, $A_0(r)$ in the above expression does not depend on the angle between the magnetization and distance vector. Thus, this term includes isotropic effects, such as the exchange energy²¹.

The magneto-elastic energy to the first order is obtained by summing the $A_2(r)$ -term over nearest neighbors in a deformed crystal. Using expression for $\cos \psi$, the eq. (1.27) can be re-written up to the first order:

$$f_{ij} = \underbrace{A_0(r)}_{\text{isotropic effects}} + \underbrace{A_2(r) \left[(m_1 w_1 + m_2 w_2 + m_3 w_3)^2 - \frac{1}{3} \right]}_{\text{MEL effects to 1st order}} + \underbrace{\dots}_{\text{higher orders}}$$

The next step is to consider an elongation, as represented in fig. 1.16b, with $r = r_0 + \delta r$, where r_0 , r is the distance between two atoms in undeformed and deformed crystal, respectively. For small elongation we thus can Taylor expand the distance dependent coefficient $A_2(r)$ to obtain:

$$f_{ij}^{mel} = \left[A_2(r_0) + \frac{dA_2(r)}{dr} \Big|_{r_0} \delta r + \frac{1}{2} \frac{d^2 A_2(r)}{dr^2} \Big|_{r_0} \delta r^2 + O(\delta r^3) \right] \left[(m_1 w_1 + m_2 w_2 + m_3 w_3)^2 - \frac{1}{3} \right]$$

The δr , δr^2 should be then expanded in terms of strain ε_{ij} up to the second order. The expansion is cumbersome and the exact expressions can be found in [24] (pp. 97-98).

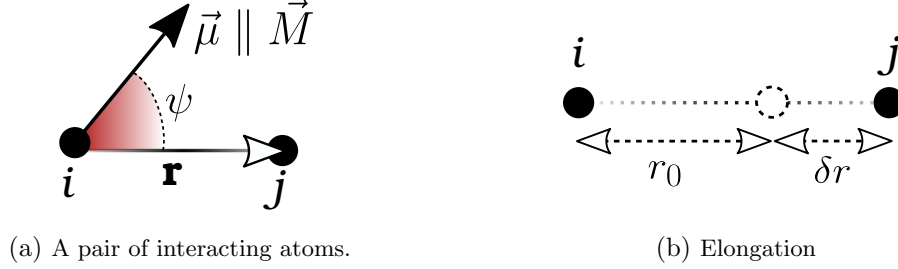
²⁰Since the magneto-elastic energy is the result of a deformation.

²¹The exchange energy does not lead to anisotropy, as it depends only on the angle between the adjacent spins, but not on the angle between the magnetization and specific crystallographic axis.

We accept and refer to the final result in the case of cubic symmetry:

$$f_{mel}^{cubic} = B_1 \left(\varepsilon_{11} \left(\alpha_1^2 - \frac{1}{3} \right) + \varepsilon_{22} \left(\alpha_2^2 - \frac{1}{3} \right) + \varepsilon_{33} \left(\alpha_3^2 - \frac{1}{3} \right) \right) + 2B_2 \left(\varepsilon_{12} \alpha_1 \alpha_2 + \varepsilon_{23} \alpha_2 \alpha_3 + \varepsilon_{13} \alpha_1 \alpha_3 \right) \quad (1.28)$$

Figure 1.16: Graphic representation of atomic pair model.



1.2.8 Expressions for the magneto-elastic energy

From the two phenomenological approaches, discussed above, one arrives to the following expressions for the magneto-elastic energy density:

$$\begin{cases} f_{mel}^{cubic} = B_1 \left(\varepsilon_{11} m_1^2 + \varepsilon_{22} m_2^2 + \varepsilon_{33} m_3^2 \right) + 2B_2 \left(\varepsilon_{12} m_1 m_2 + \varepsilon_{23} m_2 m_3 + \varepsilon_{13} m_1 m_3 \right) \\ f_{mel}^{cubic} = B_1 \left(\varepsilon_{11} \left(\alpha_1^2 - \frac{1}{3} \right) + \varepsilon_{22} \left(\alpha_2^2 - \frac{1}{3} \right) + \varepsilon_{33} \left(\alpha_3^2 - \frac{1}{3} \right) \right) + 2B_2 \left(\varepsilon_{12} \alpha_1 \alpha_2 + \varepsilon_{23} \alpha_2 \alpha_3 + \varepsilon_{13} \alpha_1 \alpha_3 \right) \end{cases}$$

the expressions differ by “ $-\frac{1}{3}$ ” term. This point is rather confusing in the literature, for both expressions are used, without specification. To discuss this, recall that there are two types of magnetostriction, **volume** and **Joule magnetostriction**, as described in [71] (ch. 12). The first implies *change* in volume, while the latter is *volume conservative*. Mathematically, the volume conservation is expressed in terms of strain, that is a relative volume change, $\frac{dV' - dV}{dV}$ is given by the trace of the strain matrix [51] (p.3). It can be shown (see appendix F), that at equilibrium the strain values can be expressed as:

$$\bar{\varepsilon}_{ii} = -\frac{B_1}{2c'_{66}} \bar{m}_i^2 + \beta, \quad \beta = \begin{cases} \frac{B_1 c_{12}}{c'_{66} (c_{11} + 2c_{12})} & \text{from eq. (1.26)} \\ \frac{B_1}{6c'_{66}} & \text{from eq. (1.28)} \end{cases}$$

From eq. (1.28) it follows immediately, that $\text{tr}(\bar{\varepsilon}) = \sum_i \bar{\varepsilon}_{ii} = 0$. Thus, to account for the volume conservation, the eq. (1.28) should be used.

1.3 Magnetization dynamics

1.3.1 Equation of motion

Consider a free electron spin under time-dependent magnetic field $\mathbf{B}(t)$. Time evolution of the mean value of spin operator, $\langle \mathbf{S} \rangle$ can be derived from Schrödinger equation [72] (pp. 2-6):

$$\frac{d}{dt} \langle \mathbf{S} \rangle (t) = -\frac{g\mu_B}{\hbar} \langle \mathbf{S} \rangle (t) \times \mathbf{B}(t) \quad (1.29)$$

where g is Landé factor and $\mu_B = \frac{|q_e|\hbar}{2m_e} = 9.274 \cdot 10^{-24}$ (Am²) is Bohr magneton, q_e, m_e being electron charge and mass, respectively. Magnetic moment, associated with electron spin, comes from analogy with classical mechanics. Under the action of an external field torque on the magnetic moment is expressed as:

$$\boldsymbol{\tau} = -\frac{\mu_B}{\hbar} \mathbf{l} \times \mathbf{B} = \boldsymbol{\mu}_l \times \mathbf{B}$$

where $\mathbf{l}, \boldsymbol{\mu}_l$ [Am²] are orbital angular momentum and the associated magnetic moment, respectively. The difference with the quantum mechanical orbital magnetic moment is the well known Landé factor, g , i.e. $\boldsymbol{\mu}_l = g\frac{\mu_B}{\hbar}$. Thus, we associate a magnetic moment to orbital angular momentum. By this analogy, a magnetic moment is associated to a spin angular momentum and the quantum mechanical expression takes the form:

$$\boldsymbol{\mu}_s = -g\frac{\mu_B}{\hbar} \langle \mathbf{S} \rangle = \gamma \langle \mathbf{S} \rangle \quad (1.30)$$

with γ being the electron *gyromagnetic ratio*, $\gamma = -\frac{g\mu_B}{\hbar} = g\frac{q_e}{2m_e} < 0$ ($\gamma/2\pi = 28$ GHz/T). Thus, multiplying eq. (1.29) by this ratio, we obtain:

$$\frac{d\boldsymbol{\mu}_s(t)}{dt} = \mu_0\gamma \boldsymbol{\mu}_s(t) \times \mathbf{H}(t)$$

Volume magnetization of a magnetized object is defined as sum over spin magnetic moments per unit volume (due to quenching of orbital magnetic moments), i.e. $\mathbf{M} = \sum \boldsymbol{\mu}_s/V$ [Am⁻¹], hence:

$$\frac{d\mathbf{M}(t)}{dt} = \gamma_0\mathbf{M}(t) \times \mathbf{H}(t) \quad (1.31)$$

with

$$\gamma_0 = \mu_0\gamma < 0 \quad \left(\frac{m}{A \cdot s} \right) \quad (1.32)$$

The eq. (1.31) is known as Landau-Lifshitz equation and it describes a precessional motion of magnetization around the applied field. If we assume time-independent field, multiplying

eq. (1.31) by $\mathbf{M}(t)$ and \mathbf{H} successively, gives:

$$\begin{cases} \frac{d|\mathbf{M}(t)|^2}{dt} = 0 \\ \frac{d\mathbf{M}(t)}{dt} \cdot \mathbf{H} = 0 \end{cases} \quad (1.33)$$

This implies that the modulus of $\mathbf{M}(t)$ and the angle between the magnetization and the applied field are conserved in time. Thus, according to eq. (1.31), once a static field is applied, magnetization would precess forever. The damping term is introduced in eq. (1.31) phenomenologically in terms of an *effective field* $\mathbf{H}_{eff} = \mathbf{H} + \frac{\alpha}{\gamma_0 M_s} \frac{d\mathbf{M}(t)}{dt}$, so that:

$$\frac{d\mathbf{M}(t)}{dt} = \gamma_0 \mathbf{M}(t) \times \mathbf{H}(t) + \frac{\alpha}{M_s} \mathbf{M}(t) \times \frac{d\mathbf{M}(t)}{dt}$$

where α is Gilbert damping parameter and M_s is the saturation value of the magnetization. This equation is referred to as Landau-Lifshitz-Gilbert equation. It is convenient to normalize the above equation by M_s :

$$\frac{d\mathbf{m}(t)}{dt} = \gamma_0 \mathbf{m}(t) \times \mathbf{H}(t) + \alpha \mathbf{m}(t) \times \frac{d\mathbf{m}(t)}{dt} \quad (1.34)$$

Study of different mechanisms, responsible for damping, is an intense research field. For a review the reader is referred to [73] (ch.5), which focuses on intrinsic and extrinsic damping mechanisms in metallic ferromagnetic thin films and multi-layered structures, and [74] (ch.11-14), which deals with different relaxation mechanisms in general, including higher order scattering (three or four magnon scattering), providing theoretical treatment, a good summary is given in the thesis [75] (pp. 30-37).

The damping mechanisms can be direct and indirect. Direct mechanisms imply spin-lattice relaxation, i.e. the energy transfer from a uniform mode (ferromagnetic resonance, $k = 0$) to the lattice motion (phonons). Energy transfer from uniform mode into a non-uniform mode (spin waves, $k \neq 0$) is referred to as spin-spin relaxation and is an indirect process, as energy of non-uniform modes would dissipate into lattice [76]. Furthermore, damping mechanisms are classified as intrinsic and extrinsic. Intrinsic in the sense, that the mechanisms cannot be avoided, as electron scattering with magnons and phonons. Extrinsic mechanisms are related to the structural defects and geometrical peculiarities, as defined by B. Heinrich [73]. The damping processes strongly depend on the nature of the material, i.e. whether it is a magnetic insulator²² [77], semiconductor²³ [78] (pp.74-87) or a metallic ferromagnet.

²²A study of temperature dependence of the damping parameter of a yttrium iron garnet sphere in the 5-300 K temperature range.

²³A review on spin dynamics in semiconductors. The most efficient spin relaxation mechanisms in semiconductors are summarized.

In case of the latter following mechanisms were found to contribute to damping: eddy currents²⁴ [79], incoherent scattering of itinerant electrons by phonons and magnons [80], two-magnon scattering.

The contributions to the damping of magnetic system have different fingerprints: one is linear in frequency, the other, for example two-magnon scattering, assumes non-linear response. The viscous damping of magnetization that appears in eq. (1.34), leads to the direct processes, i.e. lattice relaxation [81].

1.4 Conclusion

This chapter introduced the basic concepts of acoustics and ferromagnetism, the notions of which will be used throughout the thesis. We summarize with the following conclusions:

1. In the chapter 1 we considered the propagation of a Rayleigh wave in a semi-infinite elastic solid along [100] and [110] directions. Rayleigh wave is a particular type of Surface Acoustic Waves (SAWs), that is localized at the surface and decays with depth quasi-exponentially at about one wavelength. It contains two (particle) displacement components²⁵, u_1 and u_3 , yielding three non-zero strain components ε_{11} (longitudinal), ε_{13} (shear) and ε_{33} (transverse). The computed displacement and strain components as a function of the normalized depth, kx_3 are represented in the figures below:

Figure 1.17: Normalized displacements vs normalized depth, eq. (1.15), evaluated at $t = 0$, $x_1 = 0$.

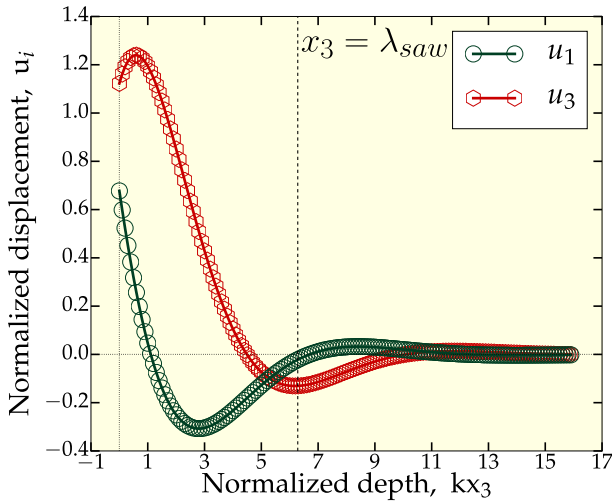
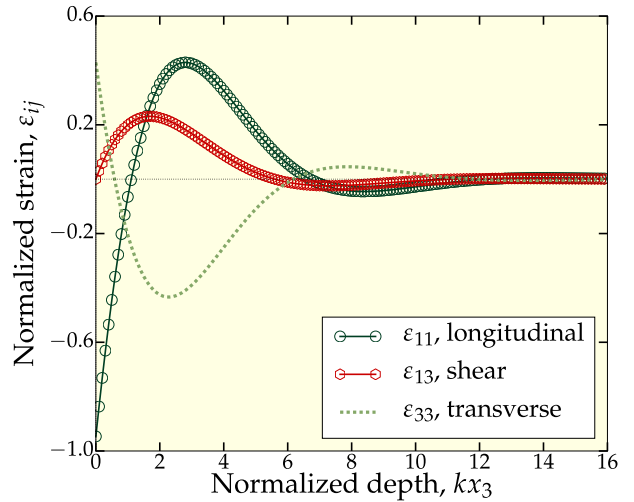


Figure 1.18: Normalized strain components vs normalized depth, eq. (1.16) **real part**, evaluated at $t = 0$, $x_1 = 0$.



²⁴The authors consider the influence of eddy currents on dipolar spin waves, that are dominated by dipolar interaction, and hence, the neglect the exchange.

²⁵In the standard [100] basis: $\mathbf{x}_1 \parallel [100]$, $\mathbf{x}_2 \parallel [010]$ and $\mathbf{x}_3 \parallel [001]$.

It is important to note that the shear component *vanishes* at the surface, i.e. for $x_3 = 0$. The obtained expressions for longitudinal and shear strain components will be used in the next chapter: ($x'_3 = kx_3$ is the normalized depth, ϕ and ψ are phase constants, r displacements amplitude ratio. The solution, $q = \frac{\alpha}{k}$ for penetration depth, α and wave vector, k is a complex number with real, q_R and imaginary, q_I parts.)

$$\begin{cases} \frac{1}{kU_1}\varepsilon_{11} &= 2 e^{i(\frac{\phi-\pi}{2})} e^{-q_R x'_3} \cos\left(q_I x'_3 + \frac{\phi}{2}\right) e^{i(\omega t - kx_1)} \\ \frac{1}{kU_1}\varepsilon_{13} &= e^{i(\pi + \frac{\phi}{2})} e^{-q_R x'_3} \left\{ q_R \cos\left(q_I x'_3 + \frac{\phi}{2}\right) + q_I \sin\left(q_I x'_3 + \frac{\phi}{2}\right) + r \sin\left(q_I x'_3 - \psi + \frac{\phi}{2}\right) \right\} e^{i(\omega t - kx_1)} \end{cases}$$

2. In the section 1.2 we focused on the energy density of a ferromagnet and the Landau-Lifshitz-Gilbert equation, describing magnetization dynamics: ($\gamma_0 = \mu_0\gamma < 0$)

$$\frac{d\mathbf{m}(t)}{dt} = \gamma_0 \mathbf{m}(t) \times \mathbf{H}(t) + \alpha \mathbf{m}(t) \times \frac{d\mathbf{m}(t)}{dt}$$

Free energy density of a ferromagnet is the sum of several contributions, namely: Zeeman, demagnetizing, magneto-crystalline anisotropy (MCA), magneto-elastic and elastic energy densities. Note that, the samples, studied in this thesis, exhibit both biaxial (cubic) and uniaxial in-plane MCA. The final expression is given in appendix C. The equation of motion and the expression for the total energy density will be used in the chapter 2 and chapter 6.

Chapter 2

SAW-induced Magnetization Dynamics

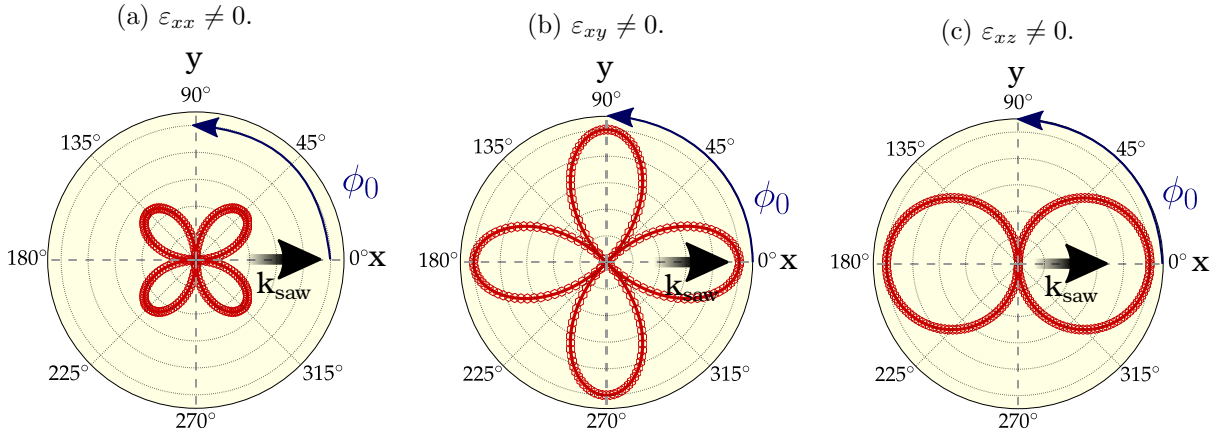
In the previous chapter we discussed surface acoustic waves and ferromagnetism separately. But the phonon system is coupled to the spin system via magneto-elastic coupling and thus, affecting one would affect another and vice versa, as we can see from the examples of direct or inverse magnetostriction. Although this thesis mostly focuses on the effects of magnetization dynamics *on* SAW propagation, let us first consider how this dynamics is triggered by a propagating SAW.

The mechanism of strain-induced magnetization precession was already discussed in the literature in the framework of a phenomenological approach, based on the LLG equation [82]. In this work the magnetization dynamics is induced by a picosecond acoustic pulse (all optical excitation) in a ferromagnetic semiconductor (Ga,Mn)As, the work is preceded by the experimental investigations, reported in [83]. The interaction mechanism can be seen as follows. Imposing strain on a ferromagnetic film modifies its total energy density (section 1.2.1) and thus, changes the internal effective field, \mathbf{H}_{eff} felt by magnetization. As a consequence, magnetization experiences a torque, exerted by the effective field, and is set into a precessional motion. In what follows, we employ the phenomenological approach, proposed in [82], to compute the SAW-induced torque. This permits us to have a simple physical picture of the interaction between SAW and magnetization and partially interpret our experimental results, presented in the chapter 5.

The last point to mention before proceeding further is the dependence of magneto-elastic coupling on the direction of the applied magnetic field, that is, and let us coin the term, its *directionality*. Reports on the latter can be found in the literature. For example, experimentally this was observed by several authors [84] (1975), [85] (1977), [86] (1988), [87] (2002), [88] (2012). To be more precise, in [84] - [86] change in SAW velocity and attenuation were measured as a function of few field directions, revealing different acoustic behaviour. In [87] A. Clark *et al.* showed angular dependence of magnetostrictive constant in iron gallium (see

chapter 3). M. Weiler *et al.* [88] attribute the angular dependence of measured SAW transmission to the elastically driven ferromagnetic resonance. From a theoretical point of view the directionality was discussed by L. Dreher *et al.* [17]. Authors have estimated the SAW-induced effective field, that triggers magnetization dynamics (via torque) under the single domain approximation. They assumed that the film experiences the same strain, that exists in SAW, when the latter propagates in a semi-infinite elastic solid. Two types of SAWs are considered: Rayleigh waves and Love waves, meaning different strain components, existing in the wave, that is ε_{xx} , ε_{xz} (shear transverse), ε_{zz} for the first and ε_{xy} (shear horizontal) for the latter. The expression for the SAW-induced effective field is given as a function of the strain components and the in-plane saturation magnetization angle, ϕ_0 with respect to the SAW wave vector. By considering only one strain component, the authors can distinguish which component contributes to the coupling, as represented in the figure below. As can be seen, in case of the longitudinal component, ε_{xx} the effective field vanishes, if saturation magnetization is parallel, $\vec{M}_s \parallel \vec{k}_{\text{SAW}}$ or perpendicular, $\vec{M}_s \perp \vec{k}_{\text{SAW}}$ to the SAW wave vector, fig. 2.1a. The situation is inversed, if one compares the case with longitudinal, ε_{xx} (fig. 2.1a) and shear horizontal strain, ε_{xy} (fig. 2.1b). Importantly, there is non-zero coupling for the parallel configuration, $\vec{M}_s \parallel \vec{k}_{\text{SAW}}$ in case of the transverse shear, ε_{xz} (fig. 2.1c).

Figure 2.1: Polar plot of the SAW-induced effective field magnitude for different non-zero strain components at saturation, adapted from [17].



In what follows we extend this computation and present the SAW-induced torque density versus the applied field angle and intensity. Note that in the article [17], the final result was to compute the absorbed radio-frequency power and to compare it with the measured results versus field intensity and angle for a system, exhibiting in-plane uniaxial MCA.

We consider a ferromagnetic film, magnetized in-plane up to saturation and this justifies the single domain approximation. The piezoelectric substrate imposes strain on the film and we *assume*, that the film experiences strain identical to that, existing in a propagating SAW in a semi-infinite elastic solid (see the section 1.1.2). Here we consider the [110] and [100]

SAW propagation directions. The film posses cubic symmetry and exhibits both biaxial and uniaxial magneto-crystalline anisotropies.

It is important to distinguish between static and dynamic variables of our system. That is, at equilibrium magnetization has a certain orientation, $(\bar{\theta}, \bar{\varphi})$ and the ferromagnet is spontaneously strained. We thus define **the equilibrium** of the system by $(\bar{\theta}, \bar{\varphi}, \bar{\varepsilon}_{ij})$ and assume small time-dependent excursions about this position, that is:

$$\begin{cases} \theta &= \bar{\theta} + \delta\theta(t) \\ \varphi &= \bar{\varphi} + \delta\varphi(t) \\ \varepsilon_{ij} &= \bar{\varepsilon}_{ij} + \delta\varepsilon_{ij}(t) \end{cases} \quad (2.1)$$

The dynamic quantities vary periodically with time (i.e. $\propto e^{i\omega t}$).

2.1 Expression of Torque Density

As described in the section 1.3, torque (Nm) on a spin magnetic moment due time-dependent effective magnetic H-field can be expressed as:

$$\boldsymbol{\tau}(t) = \mu_0 \boldsymbol{\mu}_s(t) \times \mathbf{H}_{eff}(t)$$

Multiplying by electron gyromagnetic ratio, γ and summing over spin magnetic moments per unit volume, we obtain:

$$\begin{cases} \gamma \mathbf{T} = \frac{d\mathbf{M}(t)}{dt} = \mu_0 \gamma \mathbf{M}(t) \times \mathbf{H}_{eff}(t) & or \\ \mathbf{T} = \frac{M_s}{\gamma} \frac{d\mathbf{m}(t)}{dt} \left(\frac{J}{m^3} \right) \end{cases} \quad (2.2)$$

where \mathbf{T} is defined as the **net torque density**, while time-variation of normalized magnetization is given by Landau-Lifshitz equation and if, damping is taken into account, by the equation of Landau-Lifshitz-Gilbert, as was discussed in the previous chapter: $\gamma_0 = \mu_0 \gamma < 0$

$$\frac{d\mathbf{m}(t)}{dt} = \gamma_0 \mathbf{m}(t) \times \mathbf{H}_{eff}(t) + \alpha \mathbf{m}(t) \times \frac{d\mathbf{m}(t)}{dt}$$

The \mathbf{m} is a unit vector expressed in the Cartesian, eq. (2.3) and spherical, eq. (2.4) basis. It is convenient to work with spherical coordinates.

$$\mathbf{m} = \begin{pmatrix} m_1 \\ m_2 \\ m_3 \end{pmatrix} = \begin{pmatrix} \sin \theta \cos \varphi \\ \sin \theta \sin \varphi \\ \cos \theta \end{pmatrix} \quad (2.3) \quad \mathbf{m} = \begin{pmatrix} m_r \\ m_\theta \\ m_\varphi \end{pmatrix} = \begin{pmatrix} 1 \\ 0 \\ 0 \end{pmatrix} \quad (2.4)$$

We thus need to express the $\frac{d\mathbf{m}(t)}{dt}$ term in order to calculate the torque. We assume small

excursions of magnetization about the equilibrium position and this implies the *norm conservation*, that is $m_r \approx 1 = e_r$. Time-dependent variation of \mathbf{m} -vector in spherical coordinates is expressed as $d\mathbf{m} = d\theta \mathbf{e}_\theta + \sin\theta d\varphi \mathbf{e}_\varphi$ (taking into account the norm conservation), then

$$\frac{d\mathbf{m}}{dt} = \frac{d\theta}{dt} \mathbf{e}_\theta + \sin\theta \frac{d\varphi}{dt} \mathbf{e}_\varphi \quad (2.5)$$

Plugging eq. (2.5) into eq. (2.2), we obtain:

$$\mathbf{T} = i\omega \frac{M_s}{\gamma} \left(\delta\theta \mathbf{e}_\theta + \sin\theta \delta\varphi \mathbf{e}_\varphi \right) \quad (2.6)$$

which is the expression to evaluate the torque.

2.2 Calculation steps

The calculations are rather lengthy to be presented in the main text, we thus refer to the appendix D-appendix G. The section 2.5 summarizes the calculation with a numerical analysis. The reader is invited to the section 2.5, if prefers to skip the preceding parts. The main steps of the search procedure are the following:

- (i) First, we express time-dependent angular variations $\delta\theta(t)$, $\delta\varphi(t)$ by exploiting the LLG equation, as explained in the appendix D. The effective field, \mathbf{H}_{eff} is obtained from the gradient of the total energy density with respect to magnetization [89]:

$$\begin{cases} \mathbf{H}_{eff} = -\frac{1}{\mu_0 M_s} \nabla_m F \\ F = F_Z + F_d + F_{biax} + F_{uni} + F_{mel} + F_{el} \end{cases}$$

the energy, F is the sum of different contributions (see appendix C).

The obtained expressions for $\delta\theta(t)$, $\delta\varphi(t)$ are proportional to the κ_i , ζ_i , κ_{ij} , ζ_{ij} terms, which are combinations of second order derivatives of the free energy density¹, $F_{\theta\theta}$, $F_{\varphi\varphi}$, $F_{\theta\varphi}$, $F_{\theta\varepsilon_{ij}}$, $F_{\varphi\varepsilon_{ij}}$, evaluated **at equilibrium**, that is at $(\bar{\theta}, \bar{\varphi}, \bar{\varepsilon}_{ij})$.

The expressions for the first and second order derivatives of energy density are given in the appendix E, while the obtained angular variations are of the form:

$$\begin{cases} \delta\theta = \sum_{i \leq j} \frac{(\kappa_2 \zeta_{ij} - \zeta_2 \kappa_{ij} - i\omega \zeta_{ij}) \delta\varepsilon_{ij}}{\zeta_2 \kappa_1 - \zeta_1 \kappa_2 + \omega^2 + i\omega(\zeta_1 + \kappa_2)} \\ \delta\varphi = \sum_{i \leq j} \frac{(\zeta_1 \kappa_{ij} - \kappa_1 \zeta_{ij} - i\omega \kappa_{ij}) \delta\varepsilon_{ij}}{\zeta_2 \kappa_1 - \zeta_1 \kappa_2 + \omega^2 + i\omega(\zeta_1 + \kappa_2)} \end{cases} \quad (2.7)$$

¹Here we use a compact notation, $\frac{\partial^2 h}{\partial x \partial y} = h_{xy}$.

with

$$\left\{ \begin{array}{l} \zeta_1 = -\alpha|\eta| F_{\theta\theta} \Big|_{eq} - \frac{|\eta|}{\sin\theta} F_{\theta\varphi} \Big|_{eq} \\ \zeta_2 = -\alpha|\eta| F_{\theta\varphi} \Big|_{eq} - \frac{|\eta|}{\sin\theta} F_{\varphi\varphi} \Big|_{eq} \\ \zeta_{ij} = -\alpha|\eta| F_{\theta\varepsilon_{ij}} \Big|_{eq} - \frac{|\eta|}{\sin\theta} F_{\varphi\varepsilon_{ij}} \Big|_{eq} \end{array} \right. \left\{ \begin{array}{l} \kappa_1 = \frac{|\eta|}{\sin\theta} F_{\theta\theta} \Big|_{eq} - \frac{\alpha|\eta|}{\sin^2\theta} F_{\theta\varphi} \Big|_{eq} \\ \kappa_2 = \frac{|\eta|}{\sin\theta} F_{\theta\varphi} \Big|_{eq} - \frac{\alpha|\eta|}{\sin^2\theta} F_{\varphi\varphi} \Big|_{eq} \\ \kappa_{ij} = \frac{|\eta|}{\sin\theta} F_{\theta\varepsilon_{ij}} \Big|_{eq} - \frac{\alpha|\eta|}{\sin^2\theta} F_{\varphi\varepsilon_{ij}} \Big|_{eq} \end{array} \right. \quad (2.8)$$

where, for the sake of compactness, we define a constant, η as:

$$\eta = \frac{\gamma}{1 + \alpha^2} \frac{1}{M_s} \quad \frac{rad}{s} \left(\frac{J}{m^3} \right)^{-1} \quad (2.9)$$

Note that, for a small damping parameter, as in our case $\alpha \simeq 0.01$ (measured by FMR), this constant reduces to $\simeq \frac{\gamma}{M_s}$.

- (ii) We need to evaluate the second order derivatives, that appear in the expressions for the angular variations. Since we evaluate the derivatives at equilibrium, the equilibrium orientation and strain components should be defined. This can be done by minimizing the total energy density with respect to the angles and strain components, that is we look for $(\bar{\theta}, \bar{\varphi}, \bar{\varepsilon}_{ij})$, such that the first order derivative of the energy vanishes (and the second order derivatives are positive):

$$\frac{\partial F}{\partial \theta} \Big|_{eq} = \frac{\partial F}{\partial \varphi} \Big|_{eq} = \frac{\partial F}{\partial \varepsilon_{ij}} \Big|_{eq} = 0$$

The results, obtained in the appendix F, yield the following expressions for the equilibrium strain components, represented here in terms of directional cosines, \bar{m}_i for short notation (in the standard basis), note $c'_{66} = \frac{(c_{11} - c_{12})}{2}$:

$$\bar{\varepsilon}_{ii} = -\frac{B_1}{2c'_{66}} \bar{m}_i^2 + \frac{B_1}{6c'_{66}}, \quad \bar{\varepsilon}_{ij} = -\frac{B_2}{4c_{44}} \bar{m}_i \bar{m}_j \quad i \neq j \quad (2.10)$$

We also deduce that the magnetization is in-plane, i.e. $\bar{\theta} = \frac{\pi}{2}$, both at **zero or in-plane** applied magnetic field. Given this and equilibrium strain values, we can finally express

the second order derivatives only in terms of the in-plane angle, $\bar{\varphi}$:

$$\left\{ \begin{array}{l} F_{\theta\theta} \Big|_{eq} = \mu_0 H M_s \cos(\bar{\varphi} - \varphi_H) + \mu_0 M_s^2 + K_1 [2 - \sin^2(2\bar{\varphi})] - 2K_{ip} \cos^2(\bar{\varphi} - \frac{\pi}{4}) + \\ \quad \frac{B_1^2}{c_{66}'} (\cos^4 \bar{\varphi} + \sin^4 \bar{\varphi}) + \frac{B_2^2}{8c_{44}} \sin^2(2\bar{\varphi}) \\ F_{\varphi\varphi} \Big|_{eq} = \mu_0 H M_s \cos(\bar{\varphi} - \varphi_H) + 2K_1 \cos(4\bar{\varphi}) - 2K_{ip} \cos\left(2\bar{\varphi} - \frac{\pi}{2}\right) + \\ \quad \frac{B_1^2}{c_{66}'} \cos^2(2\bar{\varphi}) + \frac{B_2^2}{4c_{44}} \sin^2(2\bar{\varphi}) \\ F_{\theta\varphi} \Big|_{eq} = 0 \end{array} \right. \quad (2.11)$$

The only non-zero $F_{\theta\varepsilon_{ij}}$, $F_{\varphi\varepsilon_{ij}}$ terms are:

$$\left\{ \begin{array}{l} F_{\theta\varepsilon_{13}} \Big|_{eq} = -B_2 \cos \bar{\varphi} \\ F_{\theta\varepsilon_{23}} \Big|_{eq} = -B_2 \sin \bar{\varphi} \end{array} \right. \quad \left\{ \begin{array}{l} F_{\varphi\varepsilon_{11}} \Big|_{eq} = -B_1 \sin(2\bar{\varphi}) \\ F_{\varphi\varepsilon_{22}} \Big|_{eq} = B_1 \sin(2\bar{\varphi}) \\ F_{\varphi\varepsilon_{12}} \Big|_{eq} = B_2 \cos(2\bar{\varphi}) \end{array} \right. \quad (2.12)$$

With this, we can simplify the κ_i , ζ_i , κ_{ij} , ζ_{ij} terms of the eq. (2.7) (angular variations), as given in the appendix G.

- (iii) The next step is to consider the SAW propagation direction. The convenience of the eq. (2.7) is that it represents the generalized equations for time-varying $\delta\theta$ and $\delta\varphi$. Taking the corresponding form of the energy density, we can consider arbitrary symmetry of the system, for example cubic or tetragonal. Furthermore time-varying strain components $\delta\varepsilon_{ij}$ are those of SAW, which can be chosen to propagate in any direction.

2.3 SAW along [100]

SAW is taken to propagate along [100] direction, the strain components can be expressed in the standard basis as: ($\delta\varepsilon_{ij}(t) = e_{ij}(t)$, change of notation)

$$(\varepsilon_{ij}) = \underbrace{\begin{pmatrix} \bar{\varepsilon}_{11} & \bar{\varepsilon}_{12} & \bar{\varepsilon}_{13} \\ \bar{\varepsilon}_{12} & \bar{\varepsilon}_{22} & \bar{\varepsilon}_{23} \\ \bar{\varepsilon}_{13} & \bar{\varepsilon}_{23} & \bar{\varepsilon}_{33} \end{pmatrix}}_{\text{static strain}} + \underbrace{\begin{pmatrix} e_{11}(t) & 0 & e_{13}(t) \\ 0 & 0 & 0 \\ e_{13}(t) & 0 & e_{33}(t) \end{pmatrix}}_{\text{SAW-imposed strain}}$$

In what follows we assume:

Assumption

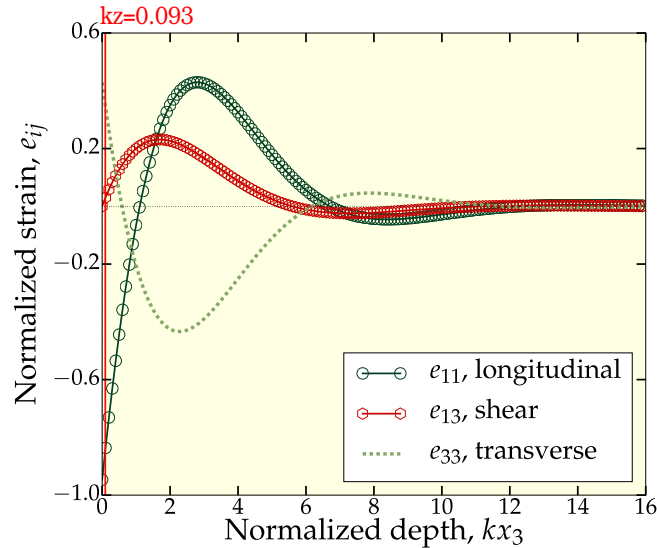
A film experiences the SAW-imposed strain, identical to that, produced at the surface of the substrate.

For a film thickness of 50nm and a SAW wave length of $3.4\mu\text{m}$ (833 MHz), the normalized depth is about 0.093. At this value, the shear component, e_{13} is very small, compared to the longitudinal, e_{11} , that is $\frac{e_{11}}{e_{13}} \simeq 30$ (fig. 2.2). Nevertheless, we will show that we can detect shear component induced effects in the experimental measurements.

Also, following the appendix G, for the in-plane magnetization the terms ζ_{33} , κ_{33} , that appear in the expressions for angular variations, vanish and thus, the transverse component, e_{33} does not play a role in the calculation.

Let us first consider a simpler case, when the shear component is neglected, as described in the next section.

Figure 2.2: Computed strain components. Red vertical solid line represents the normalized depth, $kx_3=0.093$, which corresponds to the wavelength of $3.4\mu\text{m}$ and the depth of 50nm.



2.3.1 Neglecting e_{13}

In the considered case, we are sensitive only to the longitudinal strain component. The corresponding expressions for angular variations (eq. (2.7)) reduce to:

$$\begin{cases} \delta\theta = -i \frac{\omega|\eta|B_1 \sin(2\bar{\varphi})}{\omega^2 - \omega_0^2} e_{11}(t) \\ \delta\varphi = -\frac{\eta^2 F_{\theta\theta} B_1 \sin(2\bar{\varphi})}{\omega^2 - \omega_0^2} e_{11}(t) \end{cases} \quad (2.13)$$

where the ω_0 is **the eigenfrequency** of the system for negligible damping, more precisely for $\alpha^2 \ll 1$ [19]:

$$\omega_0^2 = \eta^2 F_{\theta\theta} F_{\varphi\varphi} \quad (2.14)$$

In section 1.1.3 we found an analytical expression for the longitudinal strain component, $e_{11}(t)$ (eq. (1.16)). We can evaluate this expression at the surface, $x_3 = 0$ and for $x_1 = 0$, $t = 0$, the latter thus reduces to: (ϕ is the phase constant, arising from the calculation)

$$e_{11} = A(0) \cos(\phi/2) e^{i(\frac{\phi-\pi}{2})} \quad (2.15)$$

where $A(x_3)$ [-] is the strain amplitude². In general, SAW-induced strain is of the order of $10^{-6} - 10^{-4}$ in magnitude, we choose to take the value of $A(0) = 10^{-5}$. It does not affect the torque dependence on the direction of the applied field, in what we are interested, but *does* affect the torque amplitude (the amplitude is larger for larger strain). Finally, using eq. (2.6) (torque expression), eq. (2.13) and eq. (2.15), we can express the torque density ($\bar{\theta} = \frac{\pi}{2}$):

$$\mathbf{T} = \frac{B_1 \sin(2\bar{\varphi})}{\omega^2 - \omega_0^2} \begin{pmatrix} 0 \\ \omega^2 A(0) \cos\left(\frac{\phi}{2}\right) e^{i(\frac{\phi-\pi}{2})} \\ -\omega|\eta|F_{\theta\theta}A(0) \cos\left(\frac{\phi}{2}\right) e^{i\frac{\phi}{2}} \end{pmatrix}$$

Taking the real part yields:

$$\text{Re}(\mathbf{T}) = \frac{B_1 \sin(2\bar{\varphi})}{\omega^2 - \omega_0^2} \begin{pmatrix} 0 \\ A_\theta \\ A_\varphi \end{pmatrix}$$

²The strain amplitude depends on the excitation power of the inter-digital transducers, that are used to generate SAW (see chapter 4).

where we define

$$\begin{cases} A_\theta &= \omega^2 A(0) \frac{\sin(\phi)}{2} \\ A_\varphi &= -\omega|\eta|F_{\theta\theta}A(0) \cos^2(\phi/2) = A_\varphi(H, \bar{\varphi}) \end{cases} \quad (2.16)$$

and the norm is expressed as:

$$\boxed{\|\text{Re}(\mathbf{T})\|_{[100]} = \left| \frac{B_1 \sin(2\bar{\varphi})}{\omega^2 - \omega_0^2} \right| \sqrt{A_\theta^2 + A_\varphi^2}} \quad (2.17)$$

The [100] subscript denotes the SAW propagation direction. In this case the expression indicates the acoustic sensitivity towards **B₁ magneto-elastic constant**.

Note that among A_θ and A_φ terms, only the latter depends on the field intensity and the magnetization equilibrium angle. This term is proportional to the second order derivative of the free energy density, $F_{\theta\theta}$, given by eq. (2.11). However, the expression is dominated by the demagnetizing term, $\mu_0 M_s^2 \propto 10^6$, while the Zeeman term, $\mu_0 H M_s$ becomes compatible to the latter for the field intensity above 100mT (i.e. beyond saturation). The angle-dependent terms, containing anisotropy constants are of the order 10^4 J/m^3 and magneto-elastic (squared) / elastic constants ratio of the order $10^2 - 10^3 \text{ J/m}^3$, and thus, are negligible. It follows that, the dependence on the field direction comes from $\sin(2\bar{\varphi})$ and $1/(\omega^2 - \omega_0^2)$ terms, as will be shown later. The term $\sqrt{A_\theta^2 + A_\varphi^2}$ rather contributes to the amplitude and does not reflect its directionality (A_θ is constant and A_φ is proportional to $F_{\theta\theta}$, dominated by the constant demagnetizing term at low and Zeeman term at high fields).

Note also, that the eigenfrequency, $\omega_0^2 = \eta^2 F_{\theta\theta} F_{\varphi\varphi}$ contains the B_2 magneto-elastic constant via second order derivatives. However, as discussed above, $F_{\theta\theta}$ is dominated by the demagnetizing term and $F_{\varphi\varphi}$ by the MCA terms, or Zeeman term at high fields. Thus, ω_0 does not contribute to the “ B_2 -sensitivity”.

2.3.2 Taking e_{13} into account

From the eq. (2.7) we obtain the following expressions for angular variations in terms of shear and longitudinal strain components:

$$\begin{cases} \delta\theta(t) = \frac{-i\omega|\eta|B_1 \sin(2\bar{\varphi}) \mathbf{e}_{11}(t) - |\eta|B_2 \cos \bar{\varphi} [|\eta|F_{\varphi\varphi} + i\alpha\omega] \mathbf{e}_{13}(t)}{\omega^2 - \omega_0^2 - i\alpha\omega|\eta|(F_{\theta\theta} + F_{\varphi\varphi})} \\ \delta\varphi(t) = \frac{-|\eta|B_1 \sin(2\bar{\varphi}) [|\eta|F_{\theta\theta} + i\alpha\omega] \mathbf{e}_{11}(t) + i\omega|\eta|B_2 \cos \bar{\varphi} \mathbf{e}_{13}(t)}{\omega^2 - \omega_0^2 - i\alpha\omega|\eta|(F_{\theta\theta} + F_{\varphi\varphi})} \end{cases} \quad (2.18)$$

It will be useful to note (also for later chapter 6, section 6.2), that the terms, containing damping (marked in blue) can be neglected. This can be seen from the figures below, that show the comparison between the terms of the eq. (2.18), plotted versus angle for two values of the applied field (fig. 2.3 - fig. 2.4).

Figure 2.3: Real part and imaginary parts of the denominator in the eq. (2.18) vs applied field angle at different field intensities.

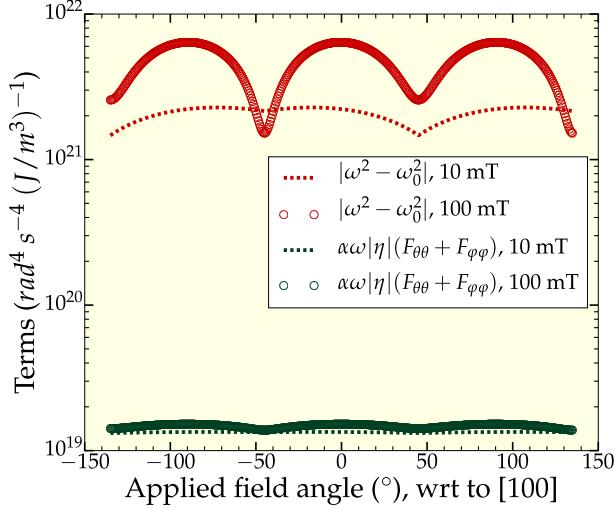
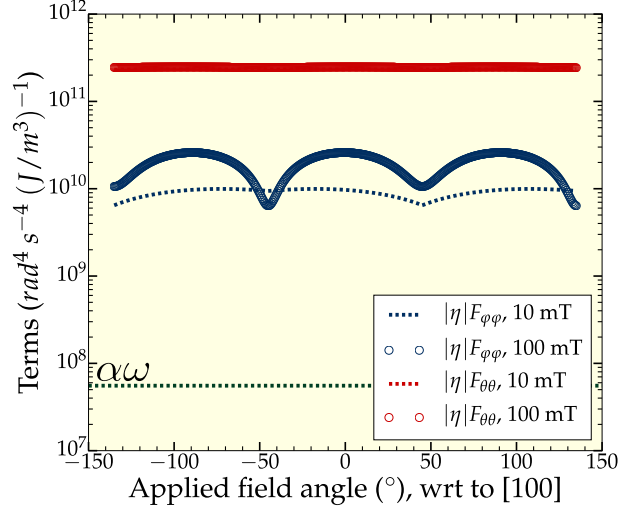


Figure 2.4: $|\eta|F_{\varphi\varphi}$ and $|\eta|F_{\theta\theta}$ terms vs applied field angle at different field intensities. Dashed green line represents the $\alpha\omega$ term.



We can evaluate the expressions for e_{11} and e_{13} , given by eq. (1.16), at $x_1 = 0, t = 0$, but now taking a variable depth: ($x'_3 = kx_3$ is the normalized depth, ϕ and ψ are phase constants, r displacements amplitude ratio. The solution, $q = \frac{\alpha}{k}$ for penetration depth, α and wave vector, k is a complex number with real, q_R and imaginary, q_I parts.)

$$\left\{ \begin{array}{l} e_{11} = \underbrace{A(x_3) e^{-q_R x'_3} \cos(q_I x'_3 + \phi/2)}_{A_{11}(x_3)} e^{i(\frac{\phi-\pi}{2})} = A_{11}(x_3) e^{i(\frac{\phi-\pi}{2})} \\ e_{13} = A(x_3) e^{-q_R x'_3} \underbrace{\left\{ q_R \cos\left(q_I x'_3 + \frac{\phi}{2}\right) + q_I \sin\left(q_I x'_3 + \frac{\phi}{2}\right) + r \sin\left(q_I x'_3 - \psi + \frac{\phi}{2}\right) \right\}}_{A_{13}(x_3)} e^{i(\pi + \frac{\phi}{2})} \\ = A_{13}(x_3) e^{i(\pi + \frac{\phi}{2})} \end{array} \right.$$

Plugging the above expressions into the eq. (2.18) (damping is neglected) and using the eq. (2.6) (torque expression), the torque density norm is given by:

$$\|\text{Re}(\mathbf{T})\| = \left| \frac{1}{\omega^2 - \omega_0^2} \right| \sqrt{A_\theta^2(x_3) + A_\varphi^2(x_3)}$$

with

$$\left\{ \begin{array}{l} A_\theta(x_3) = \left(\omega^2 B_1 \sin(2\bar{\varphi}) A_{11}(x_3) - \omega |\eta| F_{\varphi\varphi} B_2 \cos \bar{\varphi} A_{13}(x_3) \right) \sin \frac{\phi}{2} \\ A_\varphi(x_3) = \left(-\omega |\eta| F_{\theta\theta} B_1 \sin(2\bar{\varphi}) A_{11}(x_3) + \omega^2 B_2 \cos \bar{\varphi} A_{13}(x_3) \right) \cos \frac{\phi}{2} \end{array} \right. \quad (2.19)$$

An important conclusion can be drawn directly from the expressions for $A_\theta(x_3)$ and $A_\varphi(x_3)$. For $\bar{\varphi} = \varphi_B$ (saturation), it follows immediately, that torque cancels out if the field is applied perpendicularly to the SAW wave vector, $\vec{k}_{saw} \perp \vec{B}$, that is for $\varphi_B = \frac{\pi}{2}$.

However, in contrast to the previous case (section 2.3.1), torque does not vanish, when the field (or saturation magnetization) is parallel to the SAW wave vector, $\vec{k}_{saw} \parallel \vec{B}$, that is for $\varphi_B = 0$. Furthermore, only shear component, e_{13} triggers the magnetization dynamics in this configuration.

Numerical solution of $kx_3 = 0$ shows, that the maximal value of the torque norm due to the shear component ($\vec{k}_{saw} \parallel \vec{B}$ configuration) is only about 2% of the maximal value of the norm, when both components contribute ($\angle(\vec{B}, \vec{k}_{saw}) = 45^\circ$ configuration). Indeed the contribution of the shear strain is negligible with respect to the longitudinal strain. However, as will be shown in the chapter 6, it is the shear strain that results in small variations of the SAW velocity, when the field and the SAW wave vector are parallel.

For simplicity, in what follows, we assume the shear strain to vanish at the surface and we do not take it into account. As a result of this reasonable approximation, there will be two field directions, in which torque vanishes. Furthermore, it permits to avoid “mixing” of the magneto-elastic constants, B_1 and B_2 in the analytical expressions, eq. (2.19).

2.4 SAW along [110]

We now consider SAW, propagating along [110] direction. Note that, in our experiments SAWs propagate both in [110] and $[1\bar{1}0]$ directions, the two being equivalent for the expressions of the torque density norm. In such a case we need to express the SAW components in the same basis as the magnetization.

In the [110], $[1\bar{1}0]$, [001] basis

$$(\varepsilon'_{ij}) = (\bar{\varepsilon}'_{ij}) + \begin{pmatrix} e'_{11}(t) & 0 & e'_{13}(t) \\ 0 & 0 & 0 \\ e'_{13}(t) & 0 & e'_{33}(t) \end{pmatrix}$$

In the standard basis

$$(e_{ij}(t)) = \begin{pmatrix} \frac{1}{2}e'_{11} & \frac{1}{2}e'_{11} & \frac{1}{\sqrt{2}}e'_{13} \\ \frac{1}{2}e'_{11} & \frac{1}{2}e'_{11} & \frac{1}{\sqrt{2}}e'_{13} \\ \frac{1}{\sqrt{2}}e'_{13} & \frac{1}{\sqrt{2}}e'_{13} & e'_{33} \end{pmatrix}$$

As previously seen, we can suppose the shear strain to vanish at the surface, $e'_{13} \approx 0$, thus in the standard basis we have:

$$(\varepsilon_{ij}) = (\bar{\varepsilon}_{ij}) + \frac{1}{2} \begin{pmatrix} e'_{11}(t) & e'_{11}(t) & 0 \\ e'_{11}(t) & e'_{11}(t) & 0 \\ 0 & 0 & 2e'_{33}(t) \end{pmatrix}$$

Following the same procedure, described in the sections above, we obtain:

$$\|\text{Re}(\mathbf{T})\|_{[110]} = \left| \frac{B_2 \cos(2\bar{\varphi})}{2(\omega^2 - \omega_0^2)} \right| \sqrt{A_\theta^2 + A_\varphi^2} \quad (2.20)$$

Note that, if SAW propagates along [110] direction, we are sensitive to the **B₂ magneto-elastic coupling constant**. Also, the [110] and [$\bar{1}\bar{1}0$] directions are equivalent for SAW propagation and we obtain the same analytical expressions for the norm of the torque density.

2.5 Numerical Analysis

This section is devoted to the analysis of the previously derived expressions for the torque density norm. The latter is computed and represented to show its dependence both on the field direction and intensity. The constants, used in computations, namely MCA anisotropy, magneto-elastic coefficients etc., are listed in the table below. To distinguish between the contributions of biaxial and uniaxial MCA, let us first consider a **uniaxial** system that shows one hard (one easy) axis, then a biaxial MCA and to complete we include both contributions.

Table 2.1: Parameters, typical for Fe_{0.8}Ga_{0.2}, used in computation, and their source.

Parameter	Value	Source
Saturation magnetization, M_s ($\frac{A}{m}$)	10^6	VSM measurements
Biaxial anisotropy constant, K_1 ($\frac{J}{m^3}$)	2.4×10^4	FMR measurements (58nm film)
Uniaxial anisotropy constant, K_{ip} ($\frac{J}{m^3}$)	-0.6×10^4	FMR measurements (58nm film)
Magneto-elastic constant, B_1 ($\frac{J}{m^3}$)	-10^7	[90]
Magneto-elastic constant, B_2 ($\frac{J}{m^3}$)	-10^7	[90]
Elastic constants, c_{ij} (GPa)	$c_{11} = 196.0$ $c_{12} = 156.0$ $c_{44} = 123.1$	[91]
Acoustic frequency, ω (MHz)	833	experimental value
Strain amplitude, A (-)	10^{-5}	arbitrary value

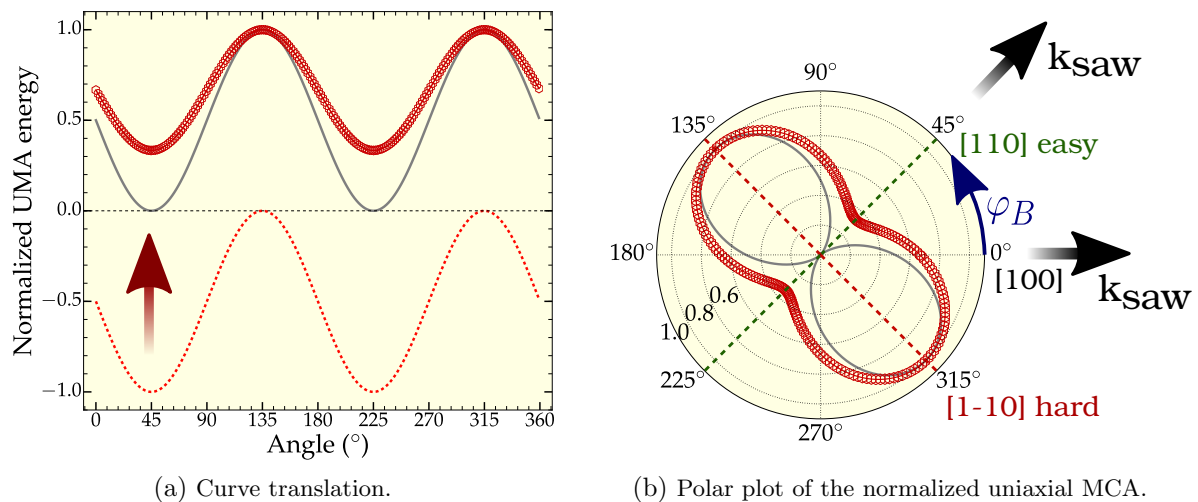
2.5.1 Uniaxial MCA

We start with a polar plot of the uniaxial magneto-crystalline anisotropy energy density to give a graphical representation of the easy and hard axes, as represented in the fig. 2.5b. Note that the anisotropy constant, K_{ip} is negative so we translate the curve (fig. 2.5a) to be able to make a polar plot, which is defined only for positive real numbers. This implies introducing a constant, which is legitimate, as the energy of a physical system is defined up to a constant³. The effect of the uniaxial contribution can be clearly seen from the computation of the proper frequency, as will be discussed further.

We consider both $[100]$ and $[110]$ SAW propagation directions in the (100) plane, the latter being equivalent to the propagation along $[1\bar{1}0]$ in the sense, that it yields the same analytical expression for the norm of the torque density. The applied field angle, φ_B and the equilibrium magnetization orientation, $\bar{\varphi}$ are defined **with respect to $[100]$ direction**.

The fig. 2.6 - fig. 2.7 represent computed norm of the torque density for SAW, propagating along $[100]$ and the easy, $[110]$ directions, respectively. Note that **the scale** in the color plots is **different** for better visibility.

Figure 2.5: Normalized uniaxial anisotropy energy density vs angle (a). The curve (dashed line) is first translated such that the energy minima correspond to zero energy (solid gray line), followed by another translation (and *normalization*) (line with markers). Polar plot (b). The color code represents the hard (red) and easy (green) axes. SAW is considered to propagate both along the $[100]$ and easy, $[110]$ directions.



To discuss the obtained results, we first discuss the magnetization equilibrium orientation. As stated in the section 1.2, we work under single domain approximation, that is the

³Note that, this translation can have a misleading representation for a constant is arbitrary. As a result, the polar plot represents a system strongly or weakly anisotropic, depending on the additive constant, as can be seen from the fig. 2.5b. In what follows we use a polar graphical representation, that more realistically represents the physical system.

Figure 2.6: Norm,

$$\|\text{Re}(\mathbf{T})\|_{[100]} = \left| \frac{B_1 \sin(2\bar{\varphi})}{\omega^2 - \omega_0^2} \right| \sqrt{A_\theta^2 + A_\varphi^2}$$

vs intensity and direction of the magnetic field.

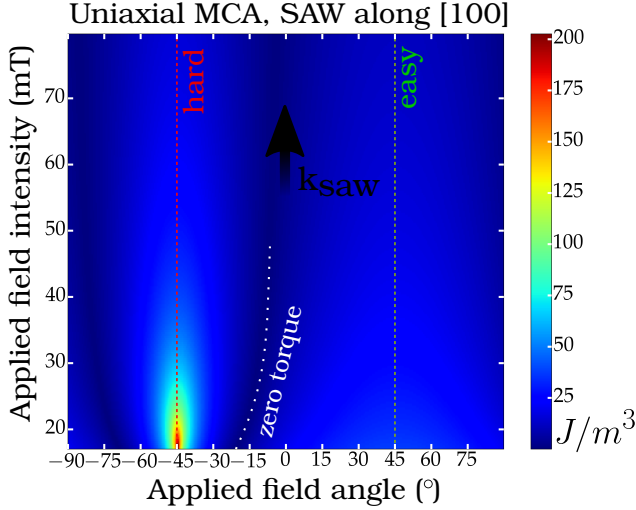
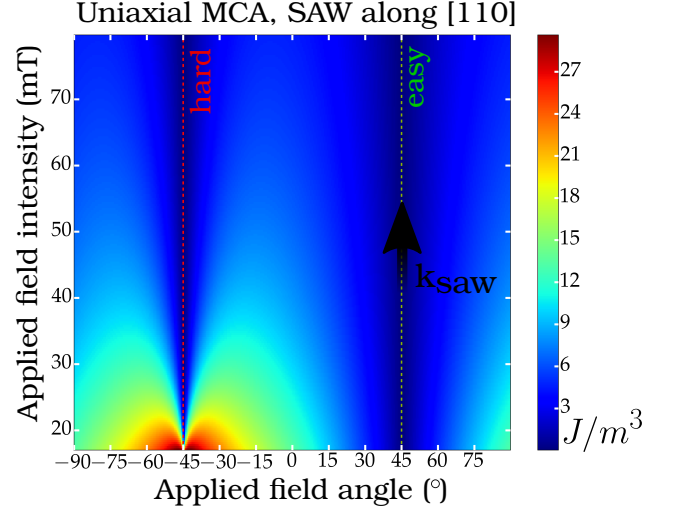


Figure 2.7: Norm,

$$\|\text{Re}(\mathbf{T})\|_{[110]} = \left| \frac{B_2 \cos(2\bar{\varphi})}{2(\omega^2 - \omega_0^2)} \right| \sqrt{A_\theta^2 + A_\varphi^2}$$

vs intensity and direction of the magnetic field.



magnetization is uniform. However, depending on the field direction, the equilibrium magnetization may or may not be aligned with the external field of fixed intensity. Within our phenomenological model, we compute the magnetization equilibrium angle, $\bar{\varphi}$ (as described in details in the appendix F) and also the projection of the magnetization on the applied field axis. The latter is equivalent to the experiment, performed with the vibrating sample magnetometer (VSM) technique, in which projection of the magnetization on the applied field is measured. The results are presented in the figures below for field, applied along the hard axis, $\varphi_B = 134.9^\circ$ and at 60° with respect to the [100] direction. Note that the computed curves reflect the experimental protocol, that we follow for the acoustical measurements, i.e. we start with a high field and reduce it progressively to zero. In such a case magnetization will rotate towards the closest easy axis. Since the field is applied at 134.9° , the closest easy axis is [110] direction, i.e. perpendicular to the direction of the applied field (see fig. 2.5b). Thus at zero field, the projection assumes zero value.

It is important to note, that the saturation rates depend on the field direction. For example, compare the field, applied along the hard axes and at 60° with respect to [100] (fig. 2.8). However the projection of magnetization along the field is larger in the latter case (fig. 2.9). Following this, we compute the norm of the torque density, while taking the equilibrium magnetization orientation into account. That is, for every point in the colorplot, (B, φ_B) we compute the corresponding $\bar{\varphi}$. The starting field for the computation is set by the saturation field along the hard axis, that is above the shaded region in the fig. 2.8 - fig. 2.9.

Figure 2.8: Equilibrium angle vs field intensity, applied along the hard axis and at 60° with respect to $[100]$ direction. Shaded region represents the region below saturation, when the field is applied along the hard axis.

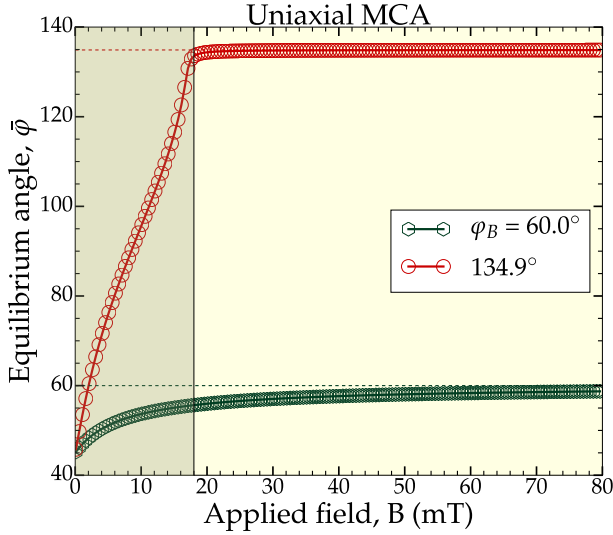
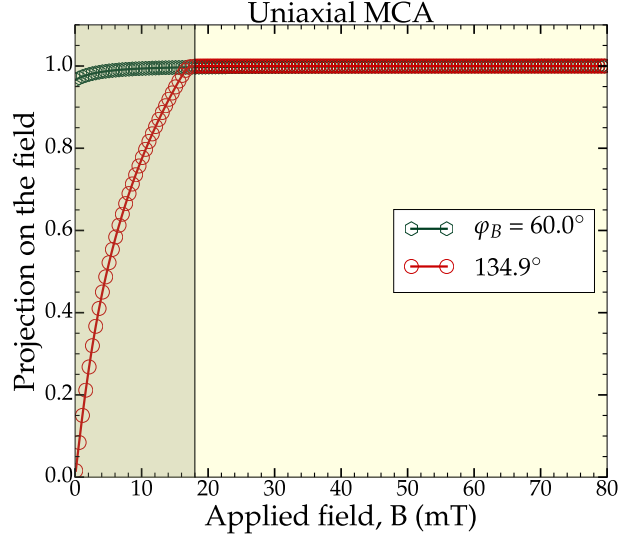


Figure 2.9: Projection of normalized magnetization on the applied field vs field intensity. Field applied along the hard axis and at 60° with respect to $[100]$ direction.



From the fig. 2.6 - fig. 2.7 the following conclusions can be made.

- (i) First, it is clear from the obtained expressions (eq. (2.17), eq. (2.20)), that due to the torque dependence on $\sin(2\bar{\varphi})$ and $\cos(2\bar{\varphi})$ (in the case of $[100]$ and $[110]$ SAW propagation, respectively) **it vanishes, if equilibrium magnetization is parallel or perpendicular to the SAW wave vector, \mathbf{k}_{saw}** . However, as discussed in the section 2.3.2, the zero norm for parallel configuration is a consequence of the neglected shear strain component. In reality, we expect a contribution, although vanishingly small. **Consequently torque is larger (but not maximal), when magnetization is at $\frac{n\pi}{4}$ with respect to the SAW wave vector, where n is an odd integer.** This results from maximization of the $\sin(2\bar{\varphi})$ and $\cos(2\bar{\varphi})$ functions.
- (ii) In the case of the propagation along $[100]$, **the torque norm assumes maximum value if the field is applied along the hard axis, at -45° in contrast with the easy axis, at 45°** . The norm is zero for certain angles, as partially represented in the colorplot with a white dashed line.

To better resume these points we plot the equilibrium angle, $\bar{\varphi}$ vs field intensity, applied at -15° , -45.1° and -75° , fig. 2.10. As can be seen in the fig. 2.11, magnetization rotates from its easy axes toward the applied field and passes 0° , 90° orientation. This results in parallel, $\mathbf{m} \parallel \mathbf{k}_{saw}$ and perpendicular, $\mathbf{m} \perp \mathbf{k}_{saw}$ configuration, for which torque vanishes.

Figure 2.10: Equilibrium angle vs field intensity at different field directions. The dashed lines represent 0° and -90° angles.

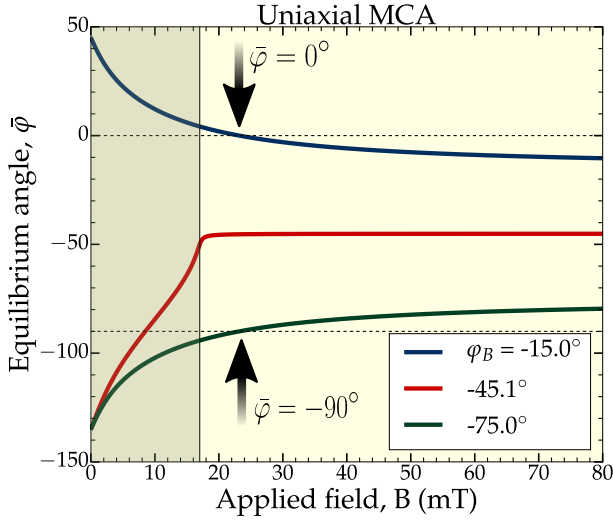
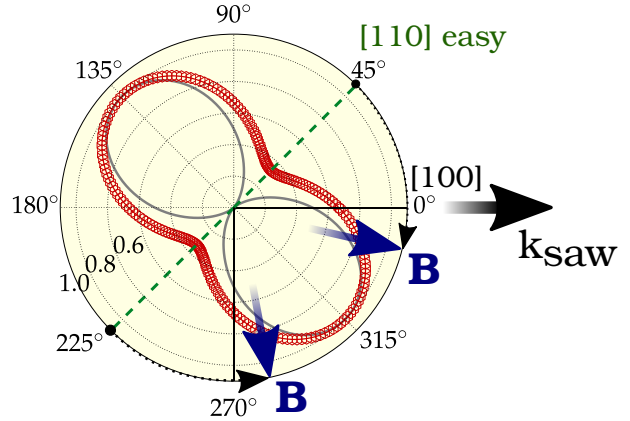


Figure 2.11: Polar plot of the uniaxial MCA. Applied field and SAW propagation directions are schematically represented with arrows.



On the other hand, when field is applied along the hard axis, -45.1° , torque is maximal. This maximum value is a consequence of two contributions. First, as discussed above, related to the maximal value of the $\sin(2\bar{\varphi})$ term. The second is related to the denominator in the expression of the norm, containing the SAW and its eigenfrequencies, $1/(\omega^2 - \omega_0^2)$. We represent the computed torque norm and the eigenfrequency, $\omega_0/2\pi$ versus field intensity for different directions in the fig. 2.12 and fig. 2.13, respectively. **It is clear that, applying the field along the hard axis results in a drop of eigenfrequency**, as in contrast with the easy axis, the difference in frequencies is about 3.1 GHz. Reducing the eigenfrequency, will decrease the $\omega^2 - \omega_0^2$ term, resulting in a larger norm, as follows from the eq. (2.17).

- (iii) In the case of the **propagation along [110]** (fig. 2.5b), the situation is reversed, that is **torque vanishes, if the field is applied both along the hard and easy axes, due to perpendicular and parallel configurations, respectively**. Torque assumes maximal values at around -45° , i.e. the energy barrier, due to the drop in frequency. However, if we compare the maximal numerical values of the norm for [100] and [110] propagation directions, the latter is about 7 times smaller. This is related to the product of $\cos(2\bar{\varphi})$ and $1/(\omega^2 - \omega_0^2)$ terms. For the [110] propagation it is not “optimized”. When SAW is directed along [100], saturating the system along the hard axis results both in the frequency drop and maximal value of $\sin(2\bar{\varphi})$ term. For the [110] propagation, saturation along the hard axis results in the perpendicular configuration, where the torque vanishes.

Thus, if one wants to maximize the effect of SAW on the magnetization, the choice of [100] as the propagation direction is more appropriate. Note that, the larger is the anisotropy, the larger will be the decrease in frequency and hence, the SAW effect will be more pronounced.

Figure 2.12: Torque norm vs field intensity for different field directions.

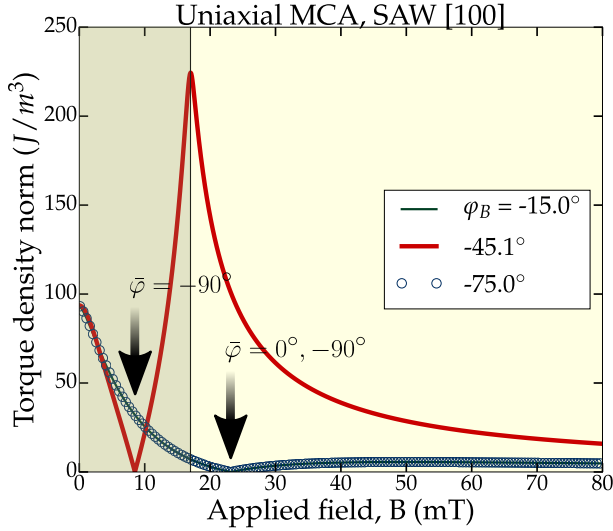
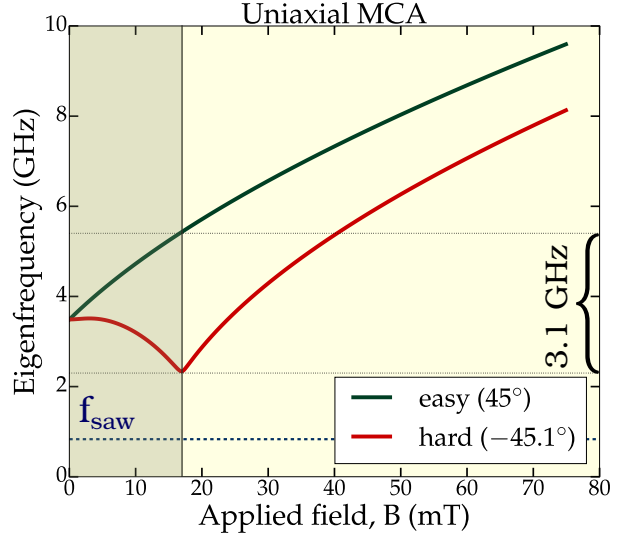


Figure 2.13: Eigenfrequency, $\omega_0/2\pi$ vs field, applied along the hard and easy axes.



- (iv) From the fig. 2.13 it follows, that the eigenfrequency increases with the field. As a consequence the torque norm vanishes at high fields. **This implies that, stronger the field is, lesser is the effect of SAW on the magnetization.**

2.5.2 Biaxial MCA

In the case of biaxial MCA the system possesses in the (001) plane two hard and two easy axes, as represented in the polar plot⁴, fig. 2.14. The corresponding eigenfrequency is represented in the fig. 2.15. In such case, a larger MCA will require larger saturation field and a larger frequency drop, as compared to the uniaxial system. As can be seen, the difference in eigenfrequency for the field, applied along the easy and hard axes can go up to 8.3 GHz. The computed torque density norm is represented in fig. 2.16 - fig. 2.17 for both [100] and [110] SAW propagation directions. We stress that **the scale** in the plots **is different** for better visibility. In comparison with the uniaxial system, the [110] and $[1\bar{1}0]$ directions are equivalent due to the anisotropy of the system and thus the torque norm is symmetric with respect to [100] direction.

⁴Note that, if we compare the anisotropy constant of iron gallium thin film, $K_1 = 2.6 \cdot 10^4$ (J/m^3) with that of a pure iron thin film, $4.5 \cdot 10^4 - 6.3 \cdot 10^4$ (J/m^3) [92], the latter is about twice larger. Thus, to give a more realistic polar representation of the energy density we added an arbitrary constant, $0.5 \cdot 10^4$ (J/m^3).

Figure 2.14: Polar plot of normalized biaxial anisotropy energy. The red line with markers is the result of addition of a constant. The color code represents the hard (red) and easy (green) axes.

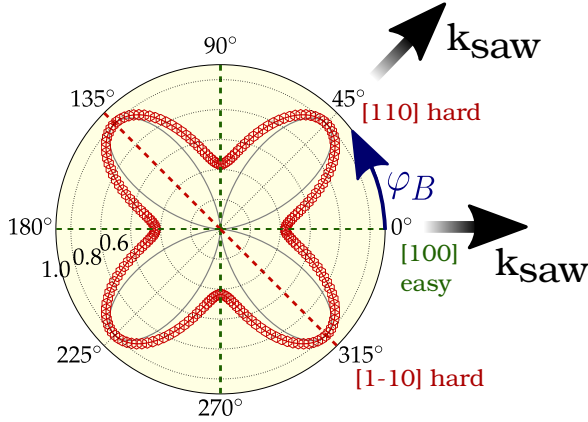


Figure 2.16: Norm, $\|\text{Re}(\mathbf{T})\|_{[100]} = \left| \frac{B_1 \sin(2\varphi)}{\omega^2 - \omega_0^2} \right| \sqrt{A_\theta^2 + A_\varphi^2}$ vs intensity and direction of the magnetic field.

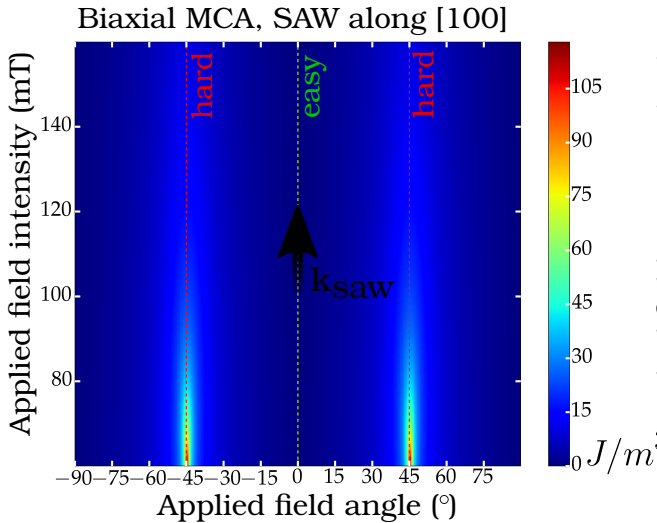


Figure 2.15: Eigenfrequency, $\omega_0/2\pi$ vs field, applied at different directions.

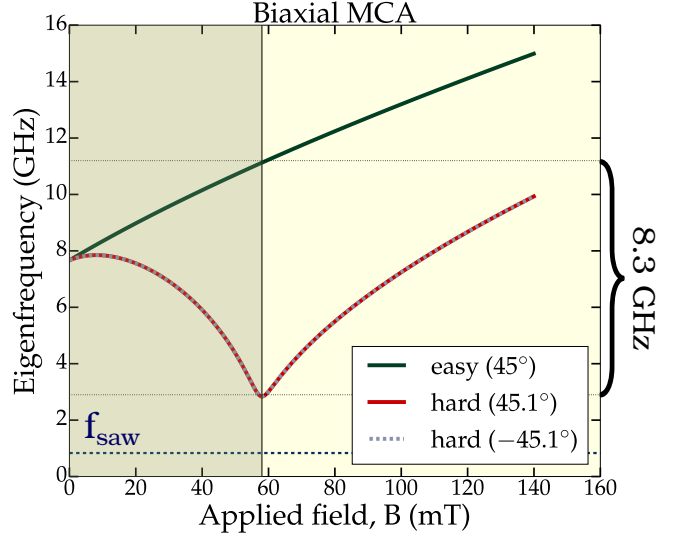
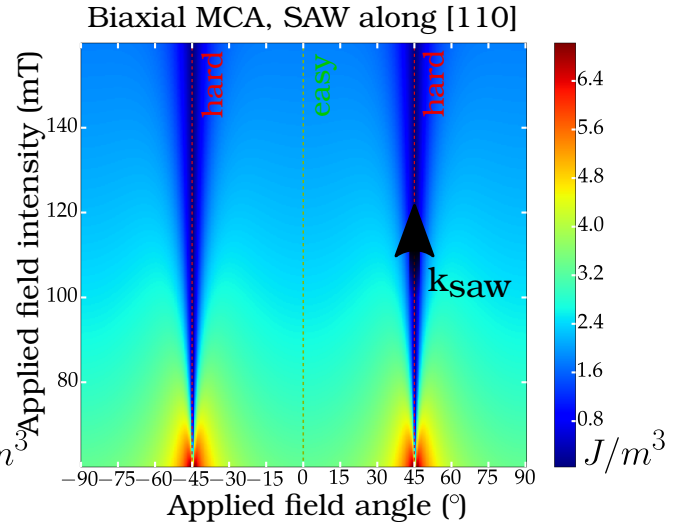


Figure 2.17: Norm, $\|\text{Re}(\mathbf{T})\|_{[110]} = \left| \frac{B_2 \cos(2\varphi)}{2(\omega^2 - \omega_0^2)} \right| \sqrt{A_\theta^2 + A_\varphi^2}$ vs intensity and direction of the magnetic field.



Note that, in the case of [100] propagation, since the easy axes are along (100) family, saturating the system along hard axes does not result in intermediate parallel or perpendicular configurations, as it was in the case of the uniaxial system (fig. 2.6).

To maximize the SAW effect on magnetization in this case the optimal configuration would be to propagate along the easy axes, (100) and apply the field along

the hard one, (110) , that is at 45° with respect to the SAW wave vector.

Note that the decrease in the torque norm, as compared to the uniaxial system, is related to the computation starting field value, we will come back to this point in the following section.

2.5.3 Biaxial MCA with uniaxial contribution

We will now consider a physical system, that exhibits biaxial MCA added to a uniaxial contribution. This can be observed in the hysteresis cycle for the sample of 55nm of $\text{Fe}_{0.8}\text{Ga}_{0.2}$ and also for the film of pure iron (chapter 6, fig. 6.14). The fig. 2.18 and fig. 2.19 show the in-plane hysteresis and polar plot of the remanent magnetization from the measurements, performed by VSM (Vibrating sample magnetometer). As discussed previously, this technique allows to measure the projection of magnetization along the applied field, that is $M_s \cos(\psi)$, where M_s is saturation magnetization and ψ is the angle between the applied field and magnetization, $\psi = \angle(\vec{B}, \vec{M})$. As can be seen, the $[1\bar{1}0]$ and $[110]$ axes are not totally equivalent as a result of the uniaxial MCA contribution. Furthermore, the hard axis, indicated by the lowest value of the magnetization at remanence, is slightly shifted with respect to the high symmetry direction, $[1\bar{1}0]$. The system is less anisotropic, as compared to the pure iron. Measured anisotropy and magneto-elastic constants are given in the table 2.1, section 2.5. The polar plot of the energy density is represented in the fig. 2.20b. From the computation, the hard axis is along the high symmetry direction, namely $[1\bar{1}0]$, medium is along $[110]$ and the easy axes are slightly shifted with respect to $[100]$ and $[010]$. The torque density norm is represented in the fig. 2.27 - fig. 2.28 for SAW along $[100]$ and $[110]$, respectively.

Figure 2.18: In-plane hysteresis cycle, measured by VSM, for $\text{Fe}_{0.8}\text{Ga}_{0.2}$ of 55nm.

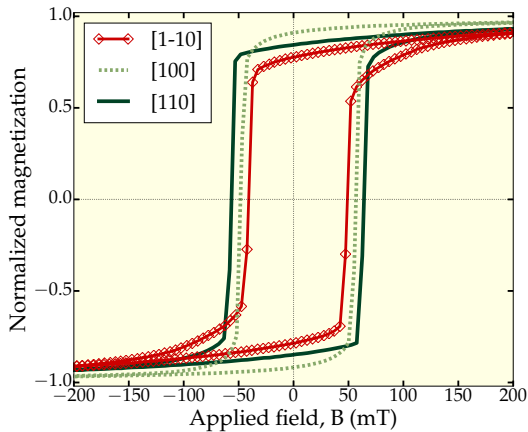


Figure 2.19: Polar plot of normalized remanent magnetization, experimental data. Field was applied with respect to $[1\bar{1}0]$ direction.

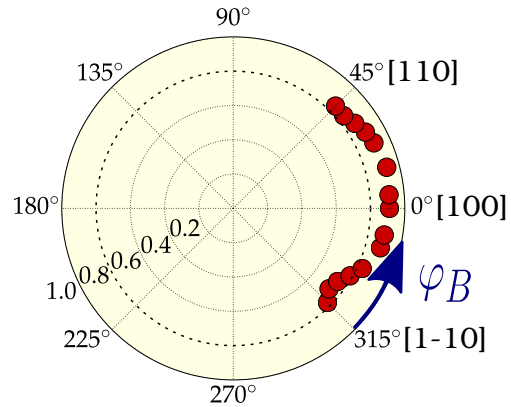
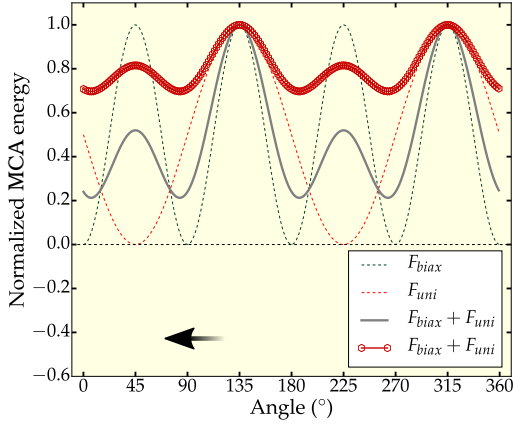
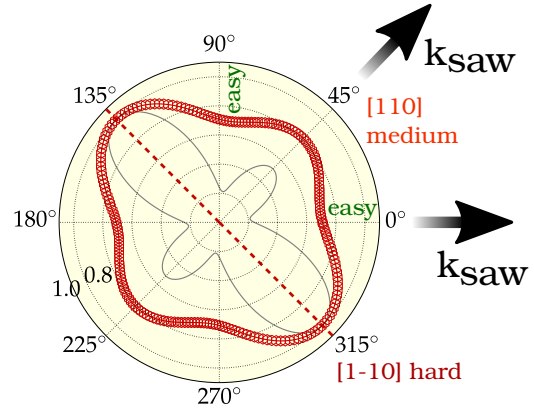


Figure 2.20: (a) Biaxial, uniaxial and total energy densities. The curve, representing the total energy, is translated as a result of addition of a constant, $2 \cdot 10^4$ (J/m^3). (b) Polar plot of the total energy density.



(a) Curve translation.



(b) Polar plot of the total MCA energy density.

Figure 2.21: Norm,
 $\|\text{Re}(\mathbf{T})\|_{[100]} = \left| \frac{B_1 \sin(2\varphi)}{\omega^2 - \omega_0^2} \right| \sqrt{A_\theta^2 + A_\varphi^2}$
 vs intensity and direction of the magnetic field.

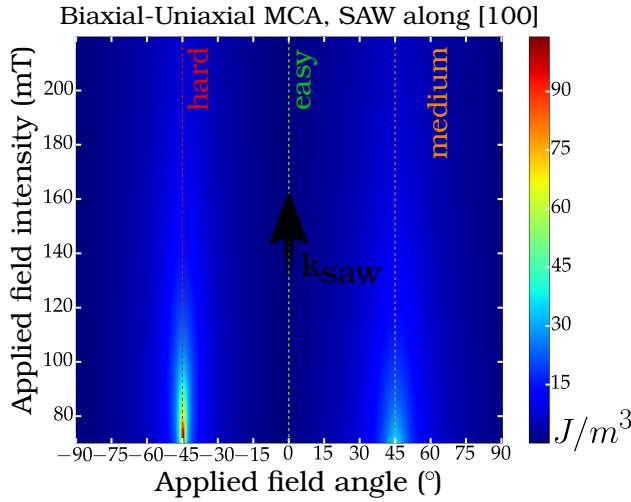
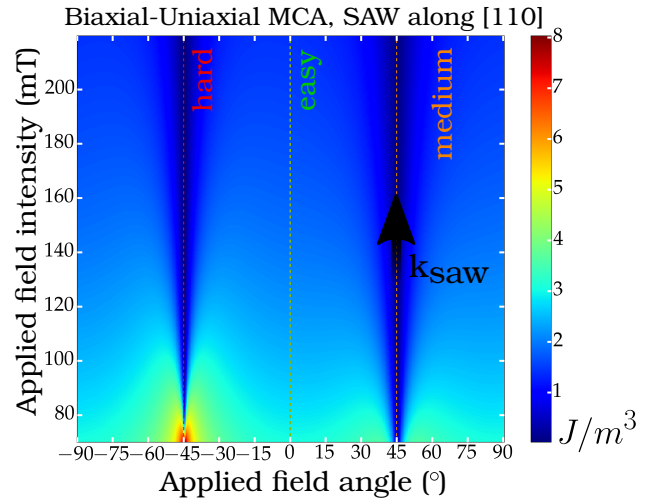
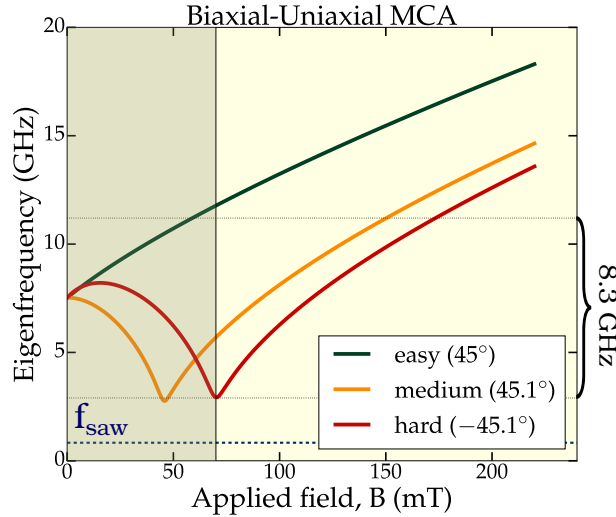


Figure 2.22: Norm,
 $\|\text{Re}(\mathbf{T})\|_{[110]} = \left| \frac{B_2 \cos(2\varphi)}{2(\omega^2 - \omega_0^2)} \right| \sqrt{A_\theta^2 + A_\varphi^2}$
 vs intensity and direction of the magnetic field.



To analyze this result, let us first notice that the contribution of the uniaxial MCA is to promote one hard axis and thus, the energy barrier is larger in the $[1\bar{1}0]$ direction. The computed eigenfrequencies vs field for different field directions are represented in fig. 2.23. As in the case of the uniaxial MCA, the $[1\bar{1}0]$ and $[110]$ are not-equivalent, the latter represents a *medium* axis. As a consequence, the torque norm will assume maximum values, if the system is saturated along the hard axis, $[1\bar{1}0]$ for $[100]$ propagation.

Figure 2.23: Computed eigenfrequencies for the real system vs field, for different field directions.



As stated previously, the torque norm is larger in the case of the uniaxial MCA, if we compare the three systems considered (uniaxial, biaxial, biaxial-uniaxial). This is related to the eigenfrequency. In the fig. 2.24 we represent the $1/(\omega^2 - \omega_0^2)$ term vs applied field angle for the MCA systems considered, at the corresponding saturating field values. The eigenfrequency of the system, ω_0 for different anisotropy systems is plotted vs field, applied along $[1\bar{1}0]$ direction, in the fig. 2.25. As can be seen, in the case of uniaxial anisotropy the frequency drop is slightly larger, resulting in a larger torque norm.

Figure 2.24: Term $1/(\omega^2 - \omega_0^2)$ vs applied field angle for different anisotropy systems at corresponding saturating fields.

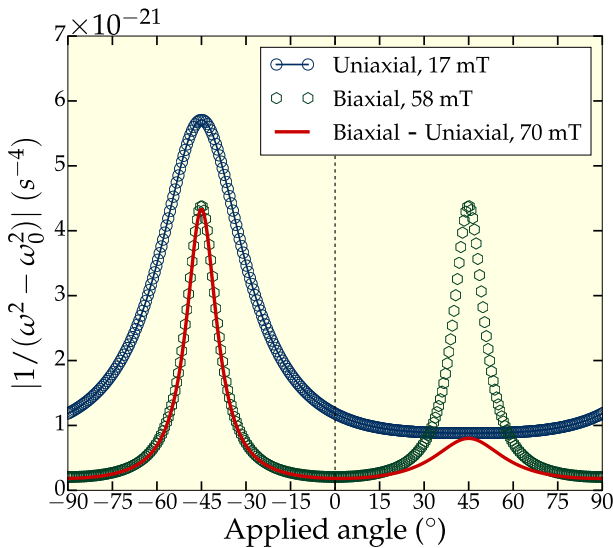
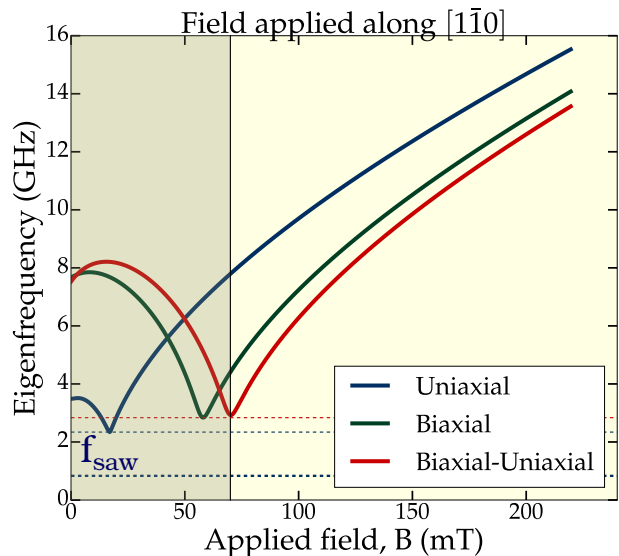


Figure 2.25: Eigenfrequency, $\omega_0/2\pi$ for field, applied at -45.1° for different anisotropies.



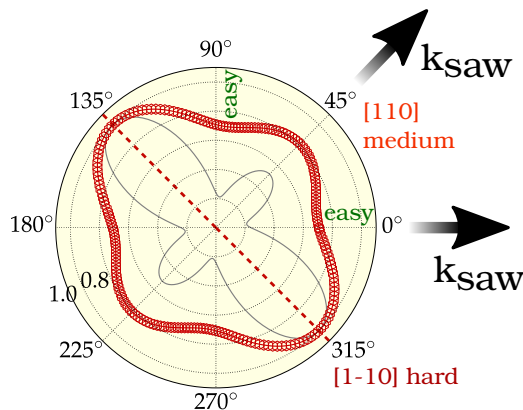
2.6 Conclusion

In this chapter we discussed SAW-induced torque density, that triggers magnetization dynamics. To summarize, a propagating SAW modifies the total energy density of a ferromagnet, resulting in modification of the effective field and thus, magnetization experiences a torque. The SAW induced torque strongly depends on the intensity and direction of the applied field with respect to the SAW wave vector and on the SAW propagation direction, [100] or [110].

To compute the norm of the torque density, we employed the LLG equation and expressed angular variations of the precessing magnetization, $\delta\theta$, $\delta\varphi$ in terms of the SAW strain components, derived in the chapter 1.

For clarity of the analysis, we considered separately three magneto-crystalline anisotropy systems: uniaxial, biaxial and biaxial-uniaxial. The real physical system exhibits the latter one, as depicted in the polar plot of the normalized MCA energy density below.

Figure 2.26: Polar plot of the MCA energy density: biaxial-uniaxial MCA.



The computed torque is given in the colorplots below, for [100] and [110] SAW propagation (the scale of the color plots is different for better visibility).

In the figures below we represent the norm of the torque density, computed for a system, exhibiting biaxial-uniaxial MCA (real physical system), for [100] and [110] SAW propagation directions. SAW induced torque presents higher values at low fields, but is still active at higher fields, well beyond the technical saturation of our samples. There are two configurations, where the resultant torque is zero or vanishingly small (if the shear SAW component is taken into account), that is when saturation magnetization is perpendicular or parallel to the SAW wave vector. There is a possibility to maximize the SAW effect on magnetization, while choosing the appropriate field directions and SAW propagations directions, depending on the magnetic anisotropy of the system. In this case, SAW propagating along the easy axis and the field, applied along the hard axis, result in a maximal torque. Note that, this is the consequence of the system's sensitivity to the magneto-crystalline anisotropy at rather small

Figure 2.27: Norm,

$$\|\text{Re}(\mathbf{T})\|_{[100]} = \left| \frac{B_1 \sin(2\varphi)}{\omega^2 - \omega_0^2} \right| \sqrt{A_\theta^2 + A_\varphi^2}$$

vs intensity and direction of the magnetic field.

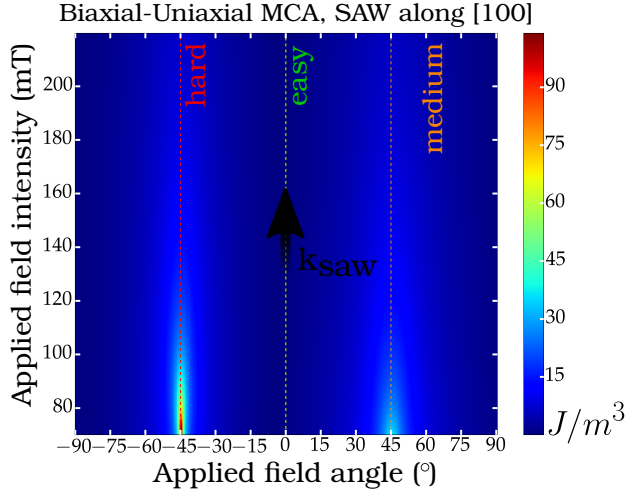
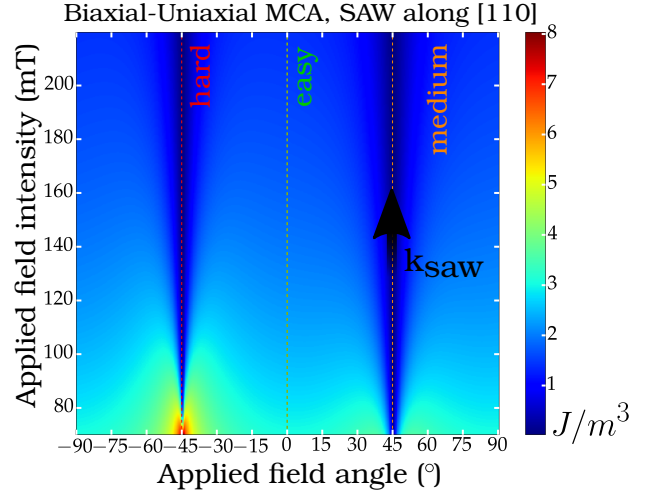


Figure 2.28: Norm,

$$\|\text{Re}(\mathbf{T})\|_{[110]} = \left| \frac{B_2 \cos(2\varphi)}{2(\omega^2 - \omega_0^2)} \right| \sqrt{A_\theta^2 + A_\varphi^2}$$

vs intensity and direction of the magnetic field.



fields, right after the saturation. Another important observation is straightforward dependence of SAW on the magneto-elastic coefficients, B_1 , B_2 . Note that the effects, described in this chapter are the effects of SAW on magnetization. In our experiments, described in chapter 5, we look at the effects of magnetization on the SAW propagation. But since both systems are coupled via magneto-elastic coupling, there is a strong interplay between the two. This rather simple and physical description permits us to partially explain our experimental results in terms of SAW-induced magnetization dynamics above saturation.

Chapter 3

Galfenol $\text{Fe}_{1-x}\text{Ga}_x$ Alloys

Even though magnetostriction was discovered by Joule in 1842, the practical usage was not immediate. During the World War II magnetostrictive Ni-based alloys were used in transducers for sonar¹ applications [41], [93]. In the 1960s A.E. Clark *et al* at *U.S. Naval Ordnance Laboratory* discovered large magnetostriction in rare earth metals terbium, Tb and dysprosium, Dy at low temperatures. In order to obtain large magnetostriction at room temperatures, they created the rare earth/3d transition metal alloys, TbFe_2 and DyFe_2 , but at a price of high magneto-crystalline anisotropy, which thus required a high saturation field. The necessity to reduce anisotropy led to the discovery of the alloy $\text{Tb}_{0.27}\text{Dy}_{0.73}\text{Fe}_{1.95}$ or terfenol-D². This alloy shows a giant magnetostriction at room temperature and low saturation field, however it is brittle. To achieve a good compromise among these properties, i.e. large magnetostriction, high Curie temperature, reasonable magneto-crystalline anisotropy and high tensile strength, $\text{Fe}_{1-x}\text{Ga}_x$ or *Galfenol*, alloys were developed in 1999 at Naval Surface Warfare Center by A. E. Clark *et al*. The table 6.1 resumes the main properties of the different bulk magnetostrictive materials.

Table 3.1: Magnetostrictive constants for different materials. As can be seen iron gallium exhibits moderate magnetostriction, but higher tensile strength as compared to Terfenol-D, from [65], [95], [96].

Single crystal (T_{room})	$\lambda_{100} \times 10^{-6}$	$\lambda_{111} \times 10^{-6}$	Tensile strength (MPa)
Fe	21	-21	~ 250
Ni	-46	-24	~ 250
$\text{Fe}_{0.8}\text{Ga}_{0.2}$	~ 400	-	~ 500
$\text{Tb}_{0.3}\text{Dy}_{0.7}\text{Fe}_2$	-	1600	~ 28

¹Sonar is derived from SOund Navigation And Ranging.

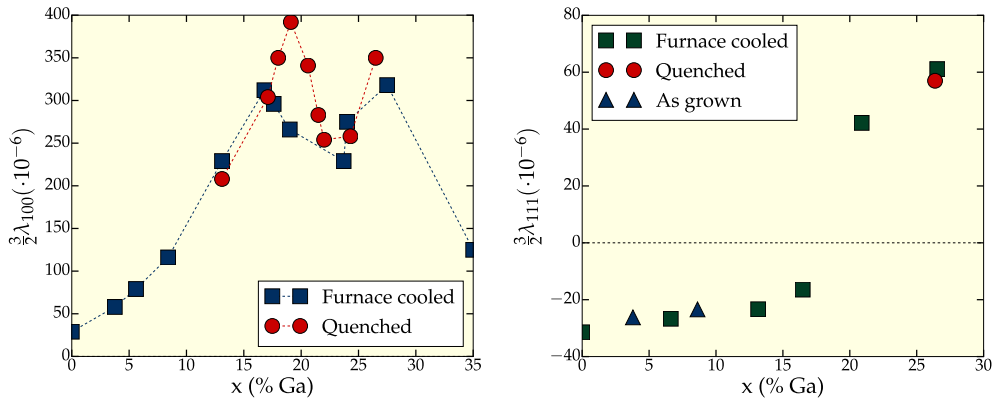
²“Ter” stands for Terbium, “Fe” for iron, “NOL” derived from Naval Ordnance Laboratory and “D” for dysprosium [94].

3.1 Structural and Magnetostrictive Properties of Bulk FeGa

The magnetic behavior of galfenol with the concentration $x\%$ is known for samples of massive material. In 2003 Clark et al. [97] presented measurements of magnetostriction and elastic constants for $\text{Fe}_{1-x}\text{Ga}_x$ monocrystals. One of the objectives was to investigate the effect of thermal history on these properties. They prepared two groups of samples with different thermal treatments. The samples prepared at 1000° experienced either a slow cooling at $10^\circ/\text{min}$ or a rapid cooling (quenching). The constants of magnetostriction $\frac{3}{2}\lambda_{100}$ and $\frac{3}{2}\lambda_{111}$ were measured using strain gauge techniques.

The results for the tetragonal magnetostriction, $\frac{3}{2}\lambda_{100}$ and $\frac{3}{2}\lambda_{111}$ are shown in the fig. 3.1. Slowly cooled samples present two maxima at around $x=17\%$ and $x=27\%$ and a strong suppression between them. Quenched samples present a stronger value of $\frac{3}{2}\lambda_{100}$ with the first peak at a slightly higher concentration $x=19\%$. It is important to notice, that $\frac{3}{2}\lambda_{111}$ exhibits lower absolute values and that the sign changes for a concentration of $x=18\%$.

Figure 3.1: Measured magnetostriction values in bulk $\text{Fe}_{1-x}\text{Ga}_x$ samples as a function of the Ga concentration, $x\%$, adapted from [97].



The dependence on the thermal treatment motivated deep structural studies of the samples. Indeed, the atomic structure of Galfenol alloys is quite complicated and the reader is referred to [98]. The fig. 3.2 shows possible crystallographic structures that may result when the alloy is formed: chemically disordered bcc A2, ordered bcc B2, disordered bcc DO_3 and fcc Ll_2 . Several ferromagnetic phases can coexist for a given gallium concentration, as can be seen in the equilibrium phase diagram (fig. 3.3).

In this thesis we will focus on samples with $x=20\%$. The phases that appear for these concentrations are A2, B2 and DO_3 . The A2 is an iron bcc network - Fe with atoms of Ga randomly distributed. Both phases B2 and DO_3 are bcc networks of Fe in which we can find Ga pairs. As shown in the fig. 3.2 in the B2 structure, Ga-pairs occupy second nearest neighbor sites along the $\langle 100 \rangle$ directions, in the DO_3 they occupy neighboring sites along the $\langle 110 \rangle$ directions. At low concentrations (lower than 20%) bulk samples are characterized by the A2 structure.

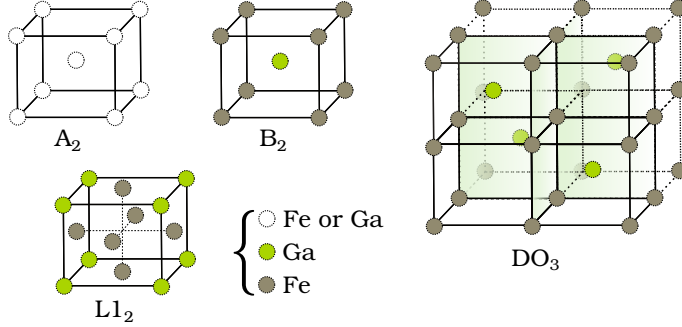
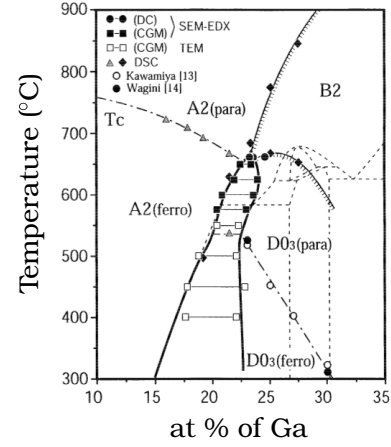
Figure 3.2: Different crystal structures of $\text{Fe}_{1-x}\text{Ga}_x$, adapted from [98].


Figure 3.3: Phase diagram from [98].



Between 20% and 23% the A2 and DO_3 structures are observed in the slowly cooled samples. In quenched samples the B2 structure is also observed.

Concerning the magneto-elastic coefficients in bulk galfenol, the B_1 and B_2 constants quantify the change in anisotropy due to an induced deformation in the sample. In the case of cubic symmetry, they related to the magnetostriction according to the equations:

$$\lambda_{100} = -\frac{2}{3} \frac{B_1}{(c_{11} - c_{12})}, \quad \lambda_{111} = -\frac{1}{3} \frac{B_2}{c_{44}}$$

This permitted Clark to extract the B_1 and B_2 parameters from magnetostriction measurements, once the elastic constants c_{11} , c_{12} and c_{44} are known:

 Table 3.2: Extracted magneto-elastic parameters by A. Clark *et al.*, from [97].

Ga content, x%	$(c_{11} - c_{12})/2$ (GPa)	$\frac{3}{2} \lambda_{100} \times 10^{-6}$	B_1 (MJ/m ³)
0	48	30	2.9
5.8	40	79	-6.3
13.2	28	210	-11.8
17	21	311	-13.1
18.7	19.7	395	-15.6
24.1	9.4	270	-5.1
27.2	6.8	350	-4.8
x%	c_{44} (GPa)	$\frac{3}{2} \lambda_{111} \times 10^{-6}$	B_2 (MJ/m ³)
0	116	-32	7.4
8.6	119	-27	6.4
13.2	~ 119	-24	5.7
20.88	~ 120	-42	-10.1
28.63	~ 120	-61	-14.6

We notice that B_1 and B_2 depend on the Ga content and do not differ significantly in amplitude for $x=20\%$ since a large part of the Ga - induced $\frac{3}{2}\lambda_{100}$ enhancement is related to a softening of the $c_{11} - c_{12}$ elastic constants term. We also notice the change of sign of the B_2 term for x close to 15%.

3.2 Origin of Magnetostriction in FeGa Alloys: extrinsic vs. intrinsic

Different theories try to explain the influence of the addition of Ga in the increase of the magnetostriction of galfenol compared to pure Fe. To solve this question, one of the first attempts was to correlate the magnetostriction with the aforementioned structural phases. Indeed, near the first maximum of magnetostriction, the phases that play the main role are A2, DO_3 and B2. Therefore, the first theoretical calculations were devoted to the understanding of the magnetostrictive contribution given by perfect crystals of each phase. These initial studies, conducted with first-principles techniques, found that phase B2 is prone to a tetragonal distortion that originates the highest λ [99]. This would be an intrinsic origin of magnetostriction. Some years later, evidence began to appear about the existence of nanoprecipitates and a new theory that includes nanocrystals was presented. This model is based on the idea that heat treatment produces a state chemically and structurally heterogeneous consisting of nanometric precipitates of the DO_3 phase into the A2 matrix [98], [100]. In this framework, it was proposed that the observed magnetostriction and the reduction of the elastic constants of these alloys can be caused either by a displacive transformation induced by a magnetic field and/or by the reorientation, induced by tension, of tetragonal micro-domains that are formed in the heterogeneous alloy. The origin would be extrinsic [101], [102]. In this context, new studies of first principles were carried out for clusters of B2 or DO_3 , immersed in a bcc Fe matrix. In this case the results showed very low and even negative λ_{100} for phase B2, as opposed to the results obtained in pure B2 crystal [103]. This article clearly shows how sensitive this magnetostriction is with respect to the atomic ordering. It's worthwhile to mention that X-ray diffraction measurements [104] could not show any evidence of an alignment of the nanoprecipitates with an external magnetic field, imposing a limit to the aforementioned extrinsic theory. Later, ab initio calculations performed on very large unit cell permitted to compare the total energies of systems with the same Ga-concentrations but with non-equivalent configurations. They succeeded in calculating the lowest energy Ga configuration in the cubic cell and the magnetostrictive coefficients that go with. The conclusion of the authors is that nanoclustering is not needed to explain enhanced magnetostriction. An intrinsic (electronic structure related) mechanism would be at the origin of the phenomenon [105]. This conclusion corroborates with the more recent large scale ab initio molecular dynamic calculations [106], which succeeded in reproducing the Ga-dependent magnetostriction curve and gave a subtle vision of the magnetostriction phenomenon (section 3.2.1).

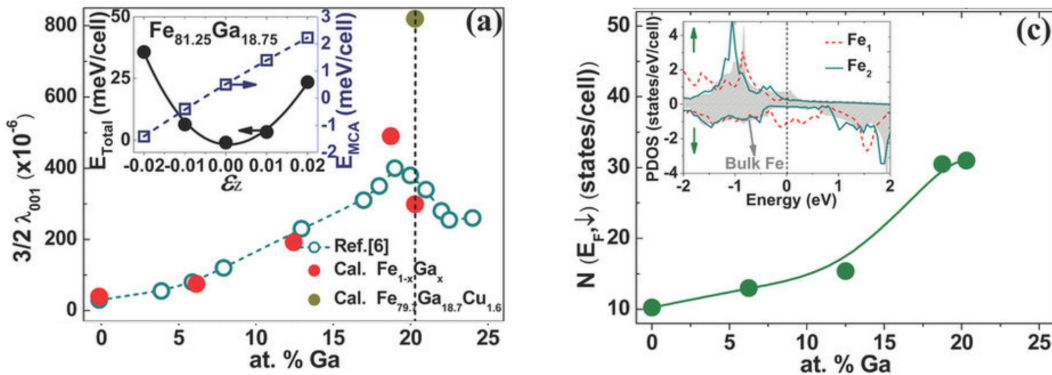
3.2.1 *Ab initio* approach

On the other hand, recent *ab initio* calculations, performed by Wang *et al.* [106], show Ga-induced changes of the electronic structure of the material³. This might be an exhaustive argument for the enhanced MS. Following the eq. (1.24) in the section 1.2.1, the contribution to the MCA energy is proportional to the spin orbit coupling. The maximum contribution comes from the interaction between the occupied states close to the Fermi level with unoccupied states, because their energy difference, i.e. denominator, is small. To determine the tetragonal MS coefficient λ_{001} the following relation was used in [106], by considering a deformed lattice cell $\varepsilon_{xx} = \varepsilon_{yy} = -\frac{1}{2}\varepsilon_{zz}$ (i.e. ε_{11} and ε_{22} should be replaced in the equations for the MCA, magneto-elastic and elastic energy densities, to yield the following relation):

$$\lambda_{001} = \frac{2}{3} \frac{df_a/d\varepsilon_{zz}}{d^2 f_{tot}/d\varepsilon_{zz}^2} = -\frac{B_1}{3c'} \quad (3.1)$$

The fig. 3.4 represents the main results. As can be seen from the inset of the fig. 3.4 (a), the MCA energy increases monotonically and the total energy has its minimum when the system is unstrained. The curve of λ_{001} , fig. 3.4 (a), obtained by *ab initio* calculations, is in a good agreement with previous experimental results: λ_{001} increases quadratically till $x \approx 19\%$ and decreases abruptly after. The inset of the fig. 3.4 (c) represents the density of occupied and unoccupied states for the first (Fe_1) and second (Fe_2) neighbors of Ga and the bulk iron. According to the eq. (3.1), strong MS is expected for a system with large MCA energy under small lattice distortion. As can be seen, the DOS of Fe_1 shows high peaks in the minority spin channel close to the Fermi level (at 0eV). This enhances the MCA energy, leading to the increase of the magnetostrictive constant. Furthermore, the number of states of minority spin channel $N(E_{F,\downarrow})$ (fig. 3.4, c) increases monotonically with Ga concentration.

Figure 3.4: The inset of the figure (a) represents the MCA and total energies as a function of strain ε_{zz} . Fig.(a) shows the MS constant λ_{001} as a function of Ga concentration. The inset of the figure (c) represents the DOS of occupied (*left*) and unoccupied (*right*) states for the first (Fe_1), second (Fe_2) neighbours of Ga and the bulk iron (shaded background). The flashes (\uparrow) and (\downarrow) represent majority and minority spin channels respectively. Fig.(c) gives the number of states within the minority spin channel $N(E_{F,\downarrow})$ vs Ga content (Ref. [106]).

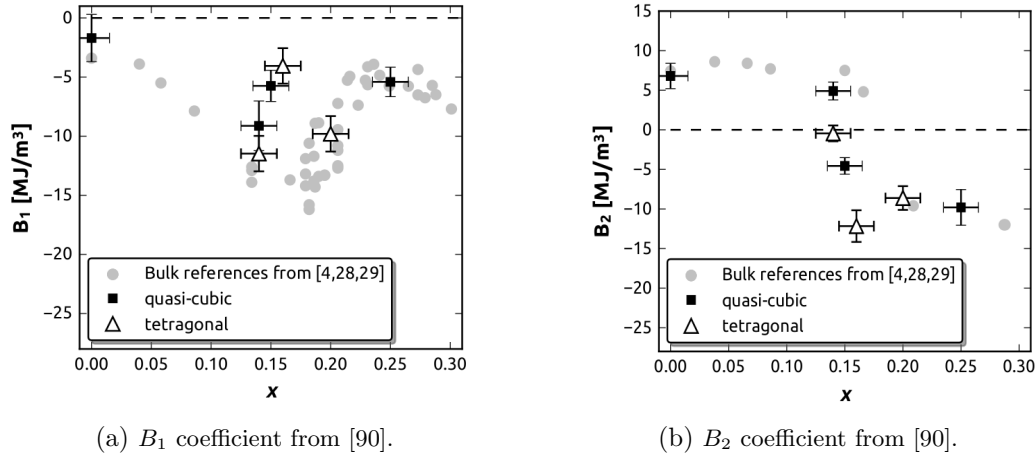


³Fe_{81.25}Ga_{18.75} is taken as an example for simulations.

What is important for our sample is that the Ga concentration reaches 19.9%, which corresponds to the first peak of the magnetostrictive constant λ_{100} as measured by Clark *et al.* (fig. 3.1). It is important to note, that our sample is a thin film of FeGa on the GaAs substrate and one should expect different properties compared to the bulk galfenol.

Systematic study of magnetic anisotropies and magneto-elastic properties of $\text{Fe}_{1-x}\text{Ga}_x$ thin films as a function of film thickness and gallium content was done by M. Barturen during her PhD research [92]. The important consequence on the magneto-elastic properties is summarized in two figures below, that present the measured magneto-elastic constants of thin films vs gallium content [90]. It is thus clear, that the bulk and thin film magneto-elastic constants B_1 and B_2 , proportional to the MS constants, do not differ much in values for the 20% Ga concentration. Furthermore, these values will be used in comparison with the computational results, presented in the chapter 6, in order to validate the theoretical model.

Figure 3.5: Measured magnet-elastic coefficients of galfenol thin films vs gallium content in samples of 50 – 100nm thick.



3.3 Interplay of Anisotropies in Thin Films

We start this section with the observation of hysteresis loop⁴ for in-plane applied field in $\text{Fe}_{0.8}\text{Ga}_{0.2}$ films of 4, 55 and 96nm and magnetic image⁵ of the latter sample. Following conclusions are made:

- (i) From fig. 3.6: the two in-plane directions $[1\bar{1}0]$ and $[110]$ are not equivalent, the remanent magnetization is reduced by 78% if sample is magnetized along $[1\bar{1}0]$ (hard axis), by 61% if along $[100]$ (intermediate) and $[110]$ is the easy axis.

⁴Measured by VSM on PPMS equipment (Quantum Design).

⁵Measured by magnetic force microscopy technique.

- (ii) From fig. 3.7: the non-equivalence of two directions is much less pronounced for 55nm film, the role of [110] and [100] axes is reversed.
- (iii) From fig. 3.8: sample is in-plane *isotropic*. The MFM (fig. 3.9) image shows the presence of stripe-like magnetic domains. This particular domain structure complicates the understanding of the magneto-elastic coupling phenomenology but introduces interesting new features in the acoustic measurements. In the following we will discuss samples without this stripe pattern.

Figure 3.6: Hysteresis of **4nm** film.

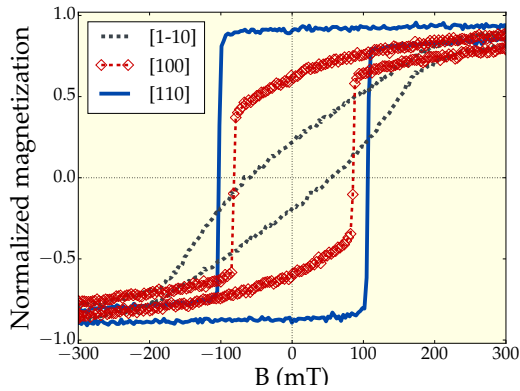


Figure 3.7: Hysteresis of **55nm** film.

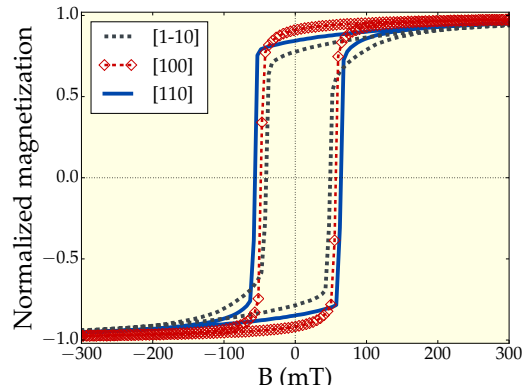


Figure 3.8: Hysteresis of **96nm** film.

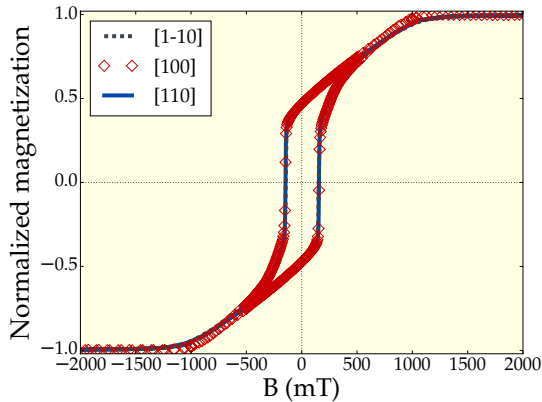
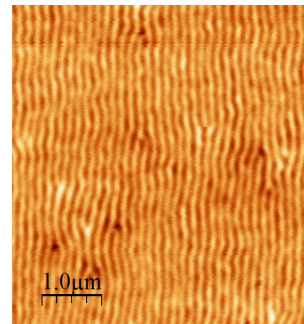


Figure 3.9: Stripe like domains in **96nm** film.



The observed features show different magneto-crystalline anisotropy, when compared to pure iron (see chapter 6, fig. 6.14). The magnetic anisotropies that arise in *film-on-substrate*, ZnSe/GaAs heterostructure are referred to as in-plane uniaxial (UMA) and perpendicular (PMA)⁶ magnetic anisotropy, the latter leads to the formation of stripe-like magnetic domains (fig. 3.9).

3.3.1 UMA & PMA

The growth of single-crystal Fe thin film on GaAs semiconductor by MBE were intensively investigated in the 80s for its potential applications in spintronics. J.J. Krebs *et al.* observed for the first time that, the expected biaxial magnetic anisotropy in a layered structure Fe/GaAs(100) was altered by the induced in-plane UMA and PMA [107]. Presence of in-plane UMA results in non-equivalence of in-plane directions, while PMA, depending on the sign of the corresponding anisotropy constant, favors the out-of-plane or in-plane magnetization. The effect of UMA was also observed in Fe/ZnSe/GaAs heterostructure [108]. *Ab initio* calculations attribute the microscopic origin of UMA to the interface effects, namely *anisotropic interface bonding* [109]. From [92] it follows is that the induced UMA depends on the sample thickness: the UMA constant reverses sign for small thicknesses (this implies easy/hard axis reversal), is present in films of around 40nm thick, 20% of Ga and vanishes for above 60nm (fig. 3.10, left).

The PMA contribution is discussed in [110] and it is shown to originate from the same interface effects, the magnitude of both contributions decreases with the increasing film thickness [111], [110]. However, there exists another source of PMA in thin $\text{Fe}_{(1-x)}\text{Ga}_x$ films. In the work, presented in [112], the authors report on tetragonally distorted samples, distortion being attributed to “the short-range ordering of Ga-Ga pairs along the [001] growth direction”. The fig. 3.10 (right) displays measured lattice parameters of single crystal gallenol films as a function of different Ga content. As a result, pristine iron in-plane lattice parameter is conserved, while the out-of-plane parameter increases with the Ga content. The tetragonal structure was found to be metastable, as it is fully released under annealing (300°C).

The PMA, observed in these films, was attributed to the tetragonal distortion of the lattice [67]. A phenomenological model was proposed, showing that a preferential alignment of Ga pairs along $\langle 100 \rangle$ results in an extra energy, that takes into account the parallel or perpendicular alignment of spins of the neighboring Fe atoms with respect to Ga-Ga pairs.

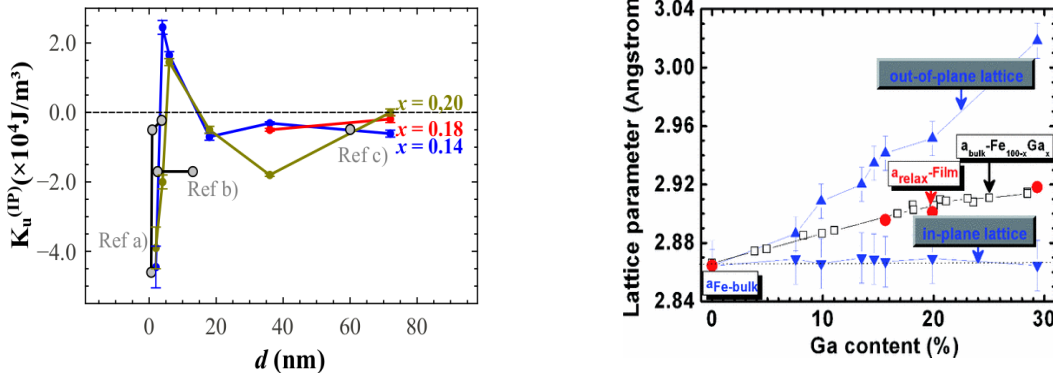
From experimental view point to support the findings, the PMA anisotropy constants were measured both in as-grown and annealed samples, the latter being cubic. A large constant was measured in tetragonally distorted samples, $K_{PMA} \sim 5 \times 10^5 \text{ J/m}^3$, while for the annealed ones the PMA contribution was vanishingly small.

Peculiarity of the PMA is that its competition with the magneto-static self-energy leads to

⁶Both terms “perpendicular magnetic anisotropy” or “out-of-plane magnetic anisotropy” are equivalent in literature.

the formation of stripe domain structure, as was observed in fig. 3.9, [113], [114]. The whole stripe pattern can be rotated and aligned parallel to the last saturating magnetic field. The minimal field, at which the pattern begins to rotate, should be above 40mT, as reported in [115].

Figure 3.10: (Left) Uniaxial magnetic anisotropy constant $K_u^{(IP)}$ vs film thickness for different gallium content, from [92]. (Right) Measured lattice parameters from [112]: out-of-plane (up triangles), in-plane (down triangles), relaxed lattice parameters (full circles) vs the Ga content. Open squares represent lattice parameters from R.A.Dunlap *et al.*, J.Magn.Magn.Mater. **305**,315 (2006), for comparison.



3.4 Sample Growth

The control of crystal structure in FeGa thin films is the necessary condition to monitor the impact of magneto-elastic coupling parameters in SAW propagation and to tailor magnonic devices, exploiting well defined SW and SAW modes. In order to obtain high quality and well oriented samples, FeGa thin films were grown by molecular beam epitaxy (MBE). The growth was performed by Mahmoud Eddrief at INSP.

Epitaxial thin films present the required texture, [001] out-of-plane orientation, if they are grown by MBE on GaAs(001) substrates. $\text{Fe}_{1-x}\text{Ga}_x$ thin films were deposited on a $c(2 \times 2)$ Zn-terminated ZnSe epilayer, grown on a GaAs substrate, a prototype of a low reactive iron/semiconductor interface [116].

A very good quality thin films are obtained if the ZnSe thin film is grown on a MBE-deposited GaAs buffer, covering the original GaAs substrate. The growth of the GaAs buffer layer was performed by Paola Atkinson in a UHV-interconnected III-V growth chamber. Details of the MBE growth of a pseudomorphic 20-nm-thick ZnSe epilayer have been previously reported in [117]. The ZnSe epilayer constitutes an efficient chemical barrier to separate galfenol from the substrate. We kept the growth temperature at 180°C, following a well established recipe, reported in [112].

At the end of the growth, the samples were covered by a protective 10-nm gold capping layer. In the same aforementioned article, the INSP team performed a study of the Ga con-

tent in thin films by XPS (X-Ray Spectroscopy), Rutherford backscattering (RBS), energy dispersive x-ray spectrometry (EDX) accompanied by X-ray diffraction (XRD) experiments. This permitted to establish a Ga content vs. lattice parameter calibration curve. The epitaxial conditions relationship were also established: $\text{FeGa}(001)//\text{ZnSe}(001)//\text{GaAs}(001)$ and $\text{FeGa}[001]//\text{ZnSe}[001]//\text{GaAs}[001]$.

In this thesis, we focused on 20% Ga-content thin films in order to maximize the magneto-elastic coupling. It is important to mention that 50 nm thick $\text{Fe}_{1-x}\text{Ga}_x$ thin films are fully relaxed in the bcc-like structure of pure iron. Of course, the larger Ga size increases the lattice parameter of pristine Fe unit cell. Nevertheless, a tetragonal distorted unit cell can be stabilized in FeGa thin films with a c/a ratio running from 1% up to 3% [112]. This is probably due to Ga ordering in the growth direction leading to Perpendicular Magnetic anisotropy (PMA) and weak magnetic stripe domains formation, as reported in M. Barturen's thesis [92]. Here, we focus on samples presenting a cubic structure in order to stabilize the in-plane magnetization equilibrium orientation.

All the films were characterized by X-ray diffraction, using a Rigaku Smartlab equipment and a $\text{Cu K}\alpha$ radiation (Mahmoud Eddrief and Sarah Hidki). This permitted to evaluate the lattice parameter and to evaluate the thin film thickness (X-Ray reflectivity oscillations). The thickness of some samples was double checked by TEM analysis (Dominique Demaille). The c/a ratio was evaluated by measuring the angles between the cubic (112) and (-1,-1,2) reflections. The magnetic characterization (hysteresis curves and magnetic moment measurements) of all the samples was done by the author on a VSM (Vibrating Sample Magnetometer) on a PPMS (Physical Properties Measurements System) equipment (table 3.4).

In the table below we summarize the main parameters of the samples studied in this thesis (table 3.3). In the following, we will focus on the measurements performed on the sample 32m0206, that presents a bcc structure. All the other samples were also employed for acoustic measurements or BLS studies. However, the results are not shown explicitly for all the samples for two reasons: redundant with respect to 32m0206 or poor acoustic signal.

The magnetization dynamics of samples was also characterized by FMR (Ferromagnetic Resonance) experiments by Julian Milano (Cetro Atomico Bariloche, Argentina), table 3.4. This permitted to extract Gilbert damping parameter and magnetic anisotropy constants, that will be employed in the modeling part of this thesis.

Table 3.3: Samples growth characteristics. Concentration of Ga \simeq 20%, $T_{Ga}=730^{\circ}\text{C}$, substrate GaAs(001)-SI. For all the samples the capping layer is **Au**, except **32m0179**, **ZnSe**.

Sample	d (nm)	C_{OP} (nm) 002	a_{IP} (nm) 200	C/a (112, 1-12)
32m0153	FeGa 92 ± 2 nm Au $7-8 \pm 0.3$ nm	$C = 0.2925 \pm 0.0005$ nm ($2\Theta = 63.57 \pm 0.1^{\circ}$)	In-plane	$C/a = 1.014 \pm 0.002$ $a = 0.2884 \pm 0.0007$ nm (112, 1-12) = $71.3 \pm 0.1^{\circ}$
32m0179 A	FeGa 25 ± 3 nm	Out-Of-Plane	In-plane	
32m0203	FeGa 26 ± 3 nm RX 26-29 nm TEM Au $9-11 \pm 0.3$ nm	$C = 0.2913 \pm 0.0005$ nm ($2Q = 63.86 \pm 0.1^{\circ}$)	In-plane	$C/a = 1.007 \pm 0.002$ $a = 0.2892 \pm 0.0007$ nm (112, 1-12) = $70.9 \pm 0.1^{\circ}$
32m0205	FeGa 44 ± 3 nm RX 36-40 nm TEM Au $9-10 \pm 0.3$ nm	$C = 0.2919 \pm 0.0005$ nm ($2Q = 63.71^{\circ} \pm 0.1^{\circ}$)	$a_{200}=0.2883$ ± 0.0005 nm ($2\Theta\gamma =$ $64.6 \pm 0.1^{\circ}$)	$C/a = 1.016 \pm 0.002$ $a = 0.2873 \pm 0.0007$ nm (112, 1-12) = $71.4 \pm 0.1^{\circ}$
32m0206	FeGa 50 ± 3 nm RX 58 nm TEM Au 8 ± 0.3 nm	$C = 0.2903 \pm 0.0005$ nm ($2Q = 64.10 \pm 0.1^{\circ}$)		$C/a = 1.0013 \pm 0.002$ $a = 0.2873 \pm 0.0007$ nm (112, 1-12) = $70.6 \pm 0.1^{\circ}$
32m0210	FeGa 88 ± 3 nm Au $7-8 \pm 0.3$ nm	$C = 0.2904 \pm 0.0005$ nm ($2Q = 64.078 \pm 0.1^{\circ}$)		$C/a = 1.002 \pm 0.002$ $a = 0.2899 \pm 0.0007$ nm (112, 1-12) = $70.6 \pm 0.1^{\circ}$
32m0212	FeGa 88 ± 3 nm Au $7-8 \pm 0.3$ nm	$C = 0.2906 \pm 0.0005$ nm ($2Q = 64.026 \pm 0.1^{\circ}$)	$a_{200} = 0.2895$ ± 0.0005 nm ($2\Theta\gamma =$ $64.3 \pm 0.1^{\circ}$)	$C/a = 1.003 \pm 0.002$ $a = 0.2899 \pm 0.0007$ nm (112, 1-12) = $70.7 \pm 0.1^{\circ}$
32m0269	FeGa 4 ± 3 nm Au $7-8 \pm 0.3$ nm			$C/a = 1.0207 \pm 0.002$ (112, 1-12) = $71.64 \pm 0.1^{\circ}$

Table 3.4: Measured magneto-crystalline anisotropy constants (FMR) and saturation magnetization (VSM). Notations: d-film thickness, K_1 biaxial MCA constant, K_{ip} uniaxial MCA constant.

Name	d (nm)	$(K_1 \pm 0.56) \cdot 10^4$ (J/m ³)	$(K_{ip} \pm 0.10) \cdot 10^4$ (J/m ³)	$M_s \times 10^6$ (A/m)
32m0203	26 ± 3	1.41	-0.43	1.04 ± 0.12
32m0205	44 ± 3	2.01	-0.75	1.01 ± 0.07
32m0206	58 ± 3	2.41	-0.60	1.02 ± 0.05
32m0210	88 ± 3	2.61	-1.30	1.00 ± 0.03

3.5 Conclusion

This chapter summarizes the main structural and magnetic peculiarities of galfenol alloys, used to study the magneto-elastic interactions in this thesis. The choice of the material is based on its enhanced magnetostriction, as compared to pure iron or nickel. Magneto-elastic coupling is enhanced in our samples, as attested by cantilever measurements done in a previous PhD thesis. We briefly discussed the origin of this enhancement, that is more likely attributed to the Ga-induced changes in the electronic structure of the material.

The sample growth by molecular beam epitaxy is well optimized at INSP.

From the magnetic point of view, FeGa thin films exhibit several kinds of magneto-crystalline anisotropy, namely biaxial (or cubic) and uniaxial (UMA). The microscopic origin of the latter is attributed to the interface effects, related to anisotropic interface bonding. Another type of MCA, present in some of our thin films, is perpendicular magnetic anisotropy (PMA). The anisotropy constants were measured by FMR in Baroliche (Argentina).

In the thesis we focus on samples exhibiting in-plane magnetization to consider, from a theoretical point of view (chapter 2, chapter 6), a simpler magnetic structure as compared to PMA.

Chapter 4

Sample Fabrication and Experimental Setup

This chapter is devoted to the description the experimental setup (section 4.1), used in the thesis for the RF measurements, and the sample fabrication procedure (section 4.2). We show several designs, explored to achieve excitation of harmonic and high frequencies of SAW. Also the RF antennas were fabricated to excite spin waves (SWs).

From our experimental point of view, several objectives were set during this thesis:

1. Excitation of surface acoustic waves at harmonic frequencies in order to perform a study of magneto-elastic interactions as a function of frequency, with a single device.
2. Excitation of high frequency SAWs to resonantly couple with spin waves or to explore other possible interactions. Starting from 0.5 GHz the goal was to extend the frequency range up to 5 GHz, at least.
3. Excitation of SWs via RF antennas.

As a very first step of the fabrication process, the samples had to be chemically etched, which was not always possible. Two solutions were considered: deposition of piezo-electric ZnO film on top of the structure and dry etching in collaboration with A. Anane, CNRS/Thales. To excite harmonics and high frequency surfaces acoustic waves we employed several designs of *inter-digital transducers* (IDTs), which were used for all electrical SAW excitation and detection. A lot of progress was done already in the 70s in fabrication of SAW devices, used in filters, delay lines, resonators [118]. A very rich source on the SAW devices can be found in [119]. Note that, this thesis does not have for a goal to develop an IDT. In stead we employ different IDT types, previously developed by others, in particular [120], [121].

4.1 Excitation and detection of SAWs. RF experimental setup

To our knowledge, there are two possible methods to excite surface acoustic waves. First method is an optical excitation via thermoelastic effect [122]. The second method employs an all electrical excitation with inter-digital transducers via piezoelectric effect [123] (ch.2). An IDT consists of an array of electrodes, to which an alternating potential difference, $U(t)$ is applied, as schematically represented in the fig. 4.1. The voltage across the electrodes produces an alternating electric field, as depicted in the fig. 4.2, which by piezoelectric effect causes a series of expansions and compressions near the surface of the material, that propagate in both directions away from the IDT. More precisely, each pair of electrodes will emit a piezo-elastic wave. For sinusoidal supply voltage, these waves will add constructively only if mechanical period, d_m is half of the SAW wave length, i.e. if the excitation frequency is $f_0 = \frac{v_R}{\lambda_{saw}} = \frac{v_R}{2d_m}$. This is a resonance condition and f_0 is referred to as the resonant frequency of the IDTs. From this it can be seen, that the SAW wavelength and frequency are fixed by the geometry of the IDTs and the Rayleigh velocity, v_R of the corresponding propagation medium. To perform the RF measurements we employ a time domain technique, which has its own advantages, as compared to the frequency domain technique (measurements with vector network analyzer (VNA)). These advantages will be discussed later. Two experimental set-ups were used, corresponding to two SAWs detection schemes, namely **rapid sampling** and **synchronous demodulation**.

Figure 4.1: Schematic representation of a bi-directional inter-digital transducer. Notations: **mechanical period**, d_m . **Electrical period**, d_{el} fixes the SAW wavelength, λ_{saw} . **Overlap width** or **aperture**, w corresponds to the SAW emission region.

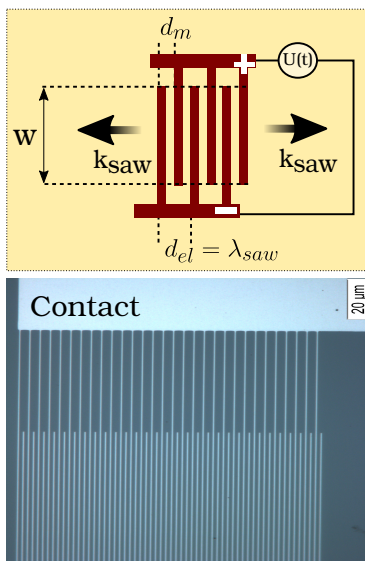


Figure 4.2: A simplified picture of an electric field, generated by alternating voltage, applied on the electrodes (cross section) at different times. As can be seen, the generated stresses add constructively only if the mechanical period, d_m is half of the SAW wave length. Adapted from [123] (p. 59).

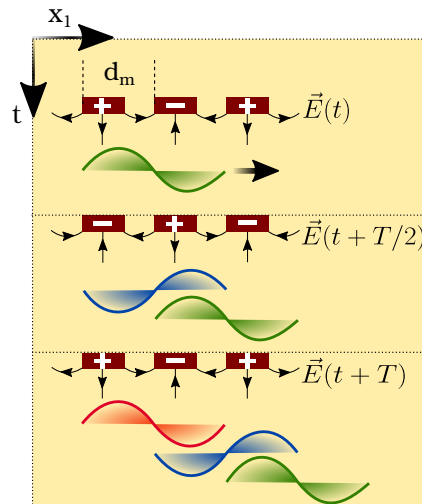
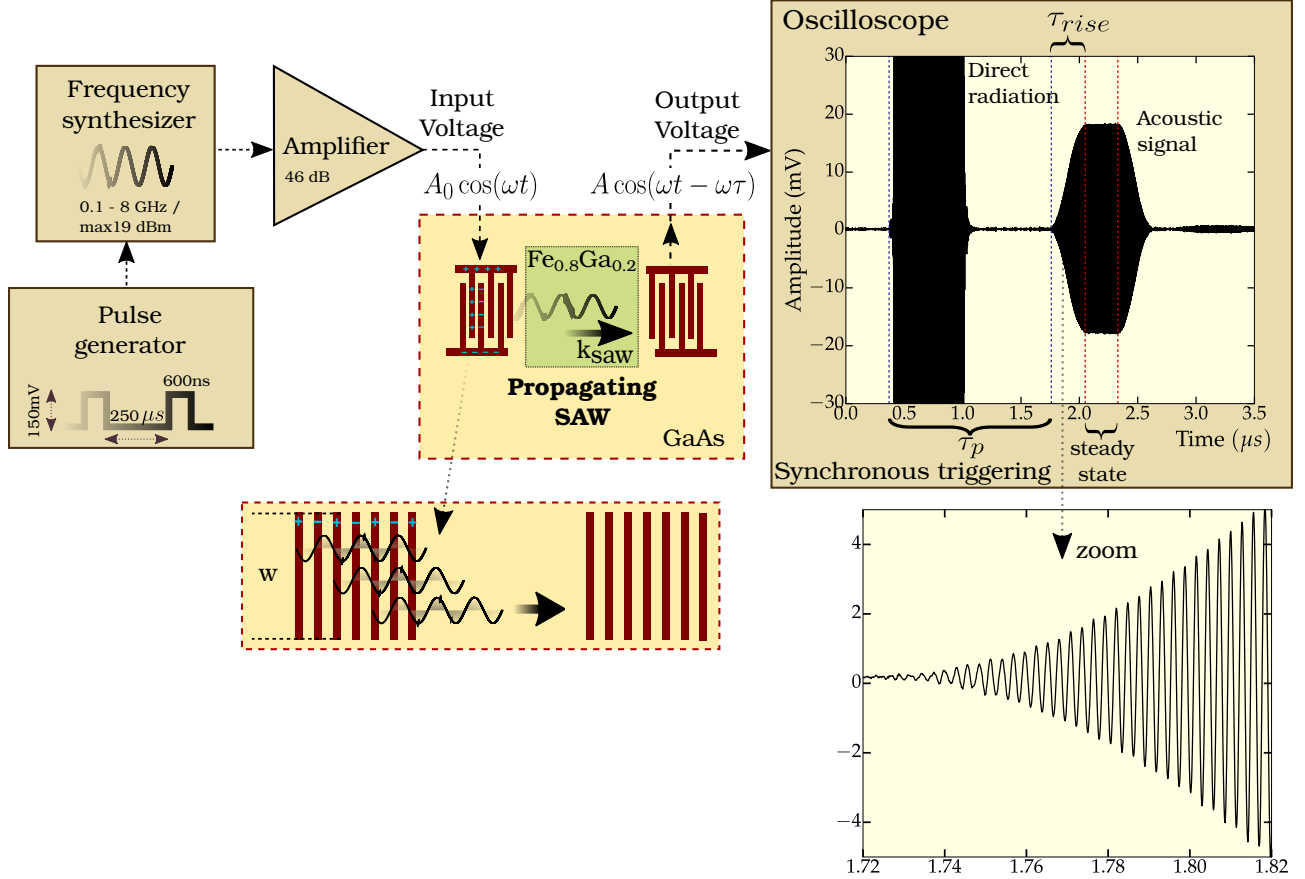


Figure 4.3: Rapid sampling detection scheme. Synchronous triggering implies the simultaneous triggering by the pulse generator and frequency synthesizer.



The figure above schematically represents the rapid sampling detection scheme. An input sinusoidal pulse is generated by a frequency synthesizer and a pulse generator, amplified, $A_0 \cos(\omega t)$ and applied to the emitting IDT, the latter launches a surface acoustic wave, as described above, that propagates in the medium. Inversely, a propagating vibration induces a voltage, $A \cos(\omega t - \omega\tau_p)$ on the receiving IDT, that is detected and sent directly to the oscilloscope. We thus can observe a time real signal. The first burst, represented on the oscilloscope picture is the direct electromagnetic radiation of the emitter to the receiver. The second burst is the real acoustic signal. Note that it is thus possible to measure the SAW propagation time between the IDTs, τ_p , as can be seen from the figure. Knowing the propagation time and the distance between the IDTs, we can experimentally access the phase velocity of SAW within 5-10% error.

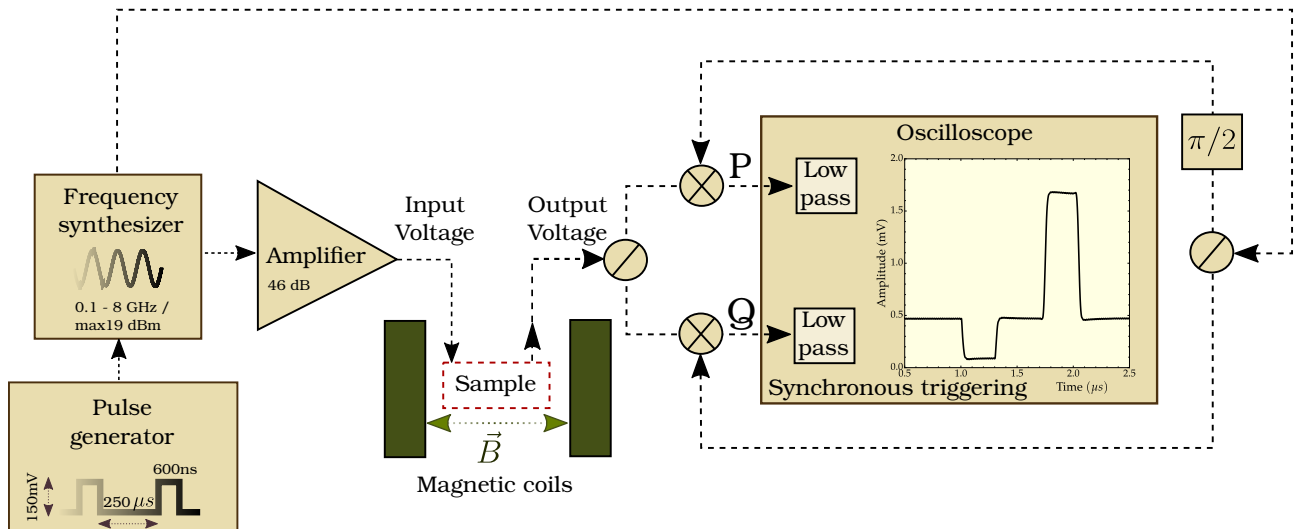
As discussed before, each pair of electrodes emits a wave. A zoom of the SAW emission region in the fig. 4.3 shows such generation of waves, that add constructively. Consequently, these waves propagate slightly different distances between the emitter and receiver. This can be seen in the shape of the acoustic signal, that is the increase in amplitude during some time,

defined as τ_{rise} , up to the steady state, when all the waves are detected by the second IDT. The advantage of the time domain technique is that we can separate the main acoustic signal from the direct electromagnetic radiation, as well as from the acoustic burst reflections or some additional spurious signals. This permits us to experimentally access the *phase*, ϕ (rad) and the *amplitude*, U (mV) of the acoustic signal. The disadvantage of the rapid sampling detection scheme is that it requires a high-performance oscilloscope, especially if one wants to explore high acoustic frequencies above 1GHz. From this point of view, the second detection scheme requires rather a standard oscilloscope, though additional parts, as divider, mixer and phase shifter are required, and it is necessary to calibrate the detection set-up. In this thesis both methods were used (the high-performance oscilloscope was rather late improvement of the experimental setup). The synchronous modulation detection scheme is represented in the fig. 4.4. Note that, the sample is placed into a magnetic field, generated by current carrying coils. For clarity the coils are represented only in the fig. 4.4.

In such a case the output signal from the sample is divided into two, that are in turn mixed with a reference signal, $A_0 \cos(\omega t)$ from the synthesizer, resulting in $P = \frac{AA_0}{4} \left(\cos(2\omega t - \omega\tau_p) + \cos(\omega\tau_p) \right)$ and $Q = \frac{AA_0}{4} \left(\cos(2\omega t - \omega\tau_p) + \sin(\omega\tau_p) \right)$. These two signals, P and Q, are then filtered by low pass within the oscilloscope to yield $P' = \frac{AA_0}{4} \cos(\omega\tau_p)$ and $Q' = \frac{AA_0}{4} \sin(\omega\tau_p)$. The amplitude and the phase of the acoustic signal are then deduced from:

$$\begin{cases} U &= \sqrt{P'^2 + Q'^2} \\ \phi &= \omega\tau_p = \arctan \frac{P'}{Q'} \end{cases}$$

Figure 4.4: Ideal synchronous demodulation detection scheme. Notations: \odot divider; \otimes mixer; $\frac{\pi}{2}$ phase shifter. Synchronous triggering by the pulse generator.



From the measured amplitude and phase we can deduce the *relative change* in the SAW phase velocity, $\frac{\Delta V}{V}$ and *change* in SAW attenuation, $\Delta\Gamma$ as a function of the applied magnetic field, detailed in the appendix H.

$$\begin{cases} \frac{\Delta\phi}{\phi} = -\frac{\Delta V}{V} \\ \Delta\Gamma = -\frac{20}{d_p} \log_{10}\left(\frac{U(B)}{U(B_{ref})}\right) \end{cases} = \frac{1}{V} \left(V(B) - V(B_{ref}) \right) \quad (4.1)$$

where B_{ref} stands for some reference field, d_p is the propagation length.

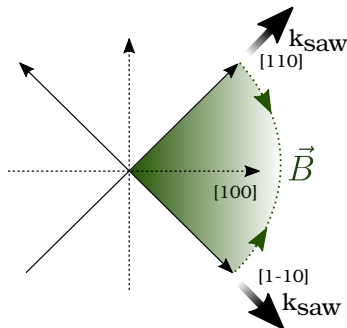
The two measurements schemes permit us to measure the velocity variations of the order of 10^{-6} and the variations in the attenuation of the order of 0.1 dB/cm.

It is also important to note, that such measurement would be impossible without the temperature control of the sample. We are able to stabilize the sample temperature up to 0.001°C .

At this point we should clarify the measurement procedure. The figure below shows the SAW propagation directions, that is $[110]$ and $[1\bar{1}0]$ and the corresponding procedure. Note that the IDTs can excite wave propagation along $[110]$ or $[1\bar{1}0]$, but not along $[100]$. Indeed, in the latter case, due to the symmetry of the piezoelectric tensor, the electric field built in the IDT do not couple to the wave strains. To propagate along $[100]$, we need to deposit on top a piezoelectric ZnO film.

During the measurements magnetic field is applied with respect to the SAW wave vector, \vec{k}_{saw} . In order to compare measurements, performed at different field directions, one should define a **common magnetic reference point**. For this purpose, before any measurement, the sample is saturated in the $\vec{B} \updownarrow \vec{k}_{saw}$ configuration, the magnetic coils are rotated at zero field for some angle, φ_B . Thus, while computing the change in velocity and attenuation, using the eq. (4.1), the reference field, B_{ref} is zero, provided that the sample was saturated in $\vec{B} \updownarrow \vec{k}_{saw}$ configuration.

Figure 4.5: The main crystallographic directions of the sample. SAW can propagate along $[110]$ or $[1\bar{1}0]$ directions, the field is swept at an angle with respect to the SAW wave vector, \vec{k}_{saw} (green shaded region).



Measurement procedure:

1. Saturation at $\vec{B} \updownarrow \vec{k}_{saw}$
2. $B = 0$, remanence
3. Rotation at φ_B with respect to the \vec{k}_{saw} **at remanence**
4. Measurement, field sweeping
 $0 \rightarrow +450\text{mT} \rightarrow -450\text{ mT} \rightarrow +450\text{ mT}$

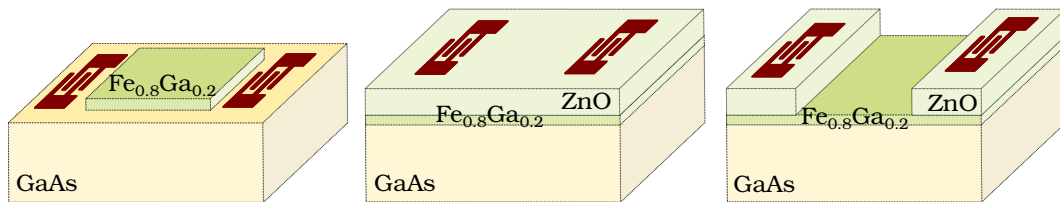
4.2 Fabrication procedure

The fig. 4.6 represents the final result of sample fabrication. Several structures were considered. Most samples were etched (dry or wet). When the etching was an issue, or for wave excitation along [100] (see above), we had to deposit a ZnO piezoelectric layer (200-400nm). Opening a window between the IDTs in such a case results in an unstrained ferromagnetic film. Some samples were dry etched in collaboration with A. Anane, CNRS/Thales.

The main steps in sample fabrication process are the following:

1. Optical lithography is used to protect the central region of the ferromagnetic film
2. The film is wet / dry etched up to the substrate, leaving a central region of the ferromagnetic film untouched
3. OR deposition of the ZnO piezoelectric layer on top of the ferromagnetic film
4. Optical / electron beam lithography are used to fabricate the IDTs. The choice of the lithography technique depends on the IDTs working frequency, as will be explained later

Figure 4.6: Three structures were fabricated. (Left) structure obtained after wet/dry etching, the IDTs are fabricated on top of the GaAs substrate. (Middle) a piezoelectric film of ZnO is deposited on top of the iron gallium thin film, the IDTs are fabricated on top of ZnO. (Right) A window is chemically etched in between the IDTs to have the unstrained ferromagnetic film. Note that, this is a simplified representation, for ZnSe chemical barrier and gold capping layer were omitted. The real structure is: (ZnO)/Au/Fe_{0.8}Ga_{0.2}/ZnSe/GaAs.



4.2.1 Wet etching

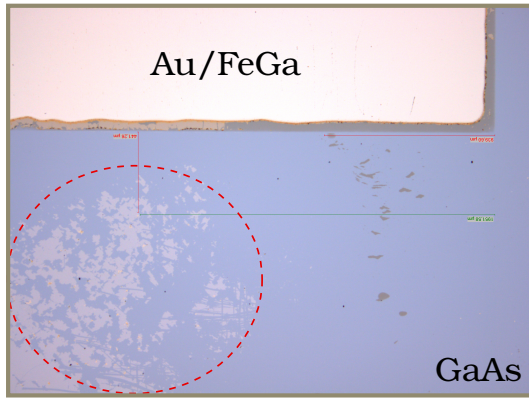
At first, the sample is covered with the *negative* resist AZnLof2035 by *spin coating* technique. This technique allows the creation of a very thin (few μm), smooth and homogeneous resist films¹. The sample is then baked at 150°C for 1 minute. By means of the ultra-violet laser UV (405nm) the central region of the sample surface is illuminated (photo-lithography). Subsequently, the resist around the illuminated region is removed and the sample is chemically (wet) or dry etched, leaving a square of FeGa thin film on the GaAs substrate.

The solution for chemical etching was found in the literature[124]. However, the volume ratio of solvents for a given concentration and etching time were determined experimentally. The main problem arises from the non-uniformity of the etching process, the solution and

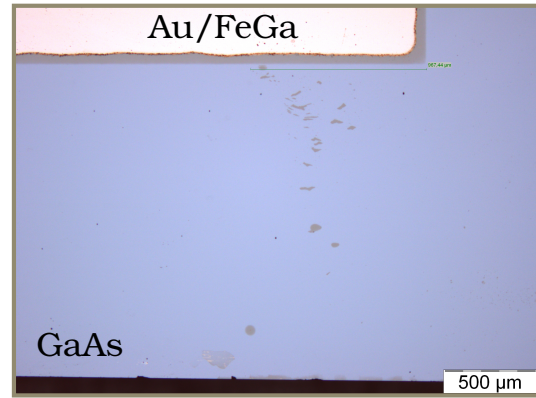
¹The resist film thickness is proportional to the reciprocal square root of the spin speed.

etching time is sample dependent. The disadvantages of this technique is that some residuals of the etched material stick on the surface, close to the border of the protected film in the middle of the structure and thus, the IDTs have to be deposited further from the ferromagnetic film, which implies relatively weaker input signal due to the decay of the propagating wave. Sometimes, these residuals could be mechanically removed with a special cotton swab, moistened in acetone, as represented in fig. 4.7a - fig. 4.7b. Furthermore, the acid eventually attacks below the resist, leaving non-straight borders of the film, resulting in a diffused acoustic wave. The determined solutions and development time for some samples are given in the table below.

Figure 4.7: Result of the wet etching. Red dashed line encircles the residuals of the etched material. As can be seen, the acid attacked under the resist, resulting in a non-straight border of the ferromagnetic film square.



(a) Etching residuals.



(b) The etching residuals are removed mechanically with a cotton swab, moistened in acetone.

Table 4.1: Determined wet etching solution and development time for different samples. Notation: US ultra-sounds.

Name	Thickness (nm)	Solution	Volume ratio	Development time	Comments
32m0100 Fe	55	HCl 25% + HNO ₃ 65%	3:1	40s	-
32m0206 Fe _{0.8} Ga _{0.2}	59	HCl 25% + HNO ₃ 65% HCL 25%	3:1	5s 12s-25s	HCl 25% at 40°C, applying US
32m0210 Fe _{0.8} Ga _{0.2}	70				
32m0212 Fe _{0.8} Ga _{0.2}	90				
32m0215 Fe	88				

4.2.2 Electron beam lithography

To fabricate the IDTs we employed optical and electron-beam lithography techniques, depending on the size of the pattern. The UV lithography was performed by L. Becerra, in charge of the clean room at INSP, while the e-beam lithography was performed by the author in the clean room of ENS (Paris). As discussed, an IDT is composed from an array of electrodes and it is the electrical period, which fixes the working frequency, as discussed in the section 4.1. For most of the cases, we took the electrode width equal to the spacing between the electrodes, that is $\lambda/4$ (μm). The minimal linewidth, that can be fabricated with optical lithography is about $1.2 \mu m$, which fixes the electrical period to be $4.8 \mu m$ and subsequently results in about 570 MHz acoustic frequency. Thus, to excite SAW at higher frequencies the e-beam lithography is necessary.

During the lithography process, a material is covered with a layer of a resist. Basic principle of this technique, either optical or e-beam, is to modify the solubility of the resist due to the exposure to light or electrons [125]. Thus, after the process only the exposed resist is removed² during development in a solvent and this permits to create the nano-patterns. Quality of the process depends on several parameters, among which are the choice of the resist, electron beam energy (acceleration voltage), dosage ($\mu C/cm^2$) and development time. The resolution, pattern quality and proximity (see below) crucially depend on these parameters.

During the exposure, electrons, penetrating the resist/substrate structure, undergo two kinds of scattering processes: forward and backward [125], as depicted in fig. 4.8. The first process is elastic scattering with the resist atoms. As a result the electron beam is broadened (fig. 4.9), depending on the resist thickness, density and acceleration voltage (lower is the energy, more pronounced is the effect). Backward scattering occurs, when most of the electrons pass through the resist into the substrate, undergo collisions and re-emerge back into the resist at some distance from the incident beam. This distance can reach several microns, depending on the beam energy. Thus, writing a feature at one location will affect writing at a nearby location. This can lead to overexposure and destruction of the whole pattern. This undesired effect is referred to as *proximity effect*, which makes it difficult to fabricate dense patterns. To reduce the proximity effects, one can reduce the dimensions in the design, as the actual pattern will be larger. Furthermore, one should determine the correct dose of electrons to obtain a good quality pattern.

²If the resist is positive. On the contrary, if the resist is negative, the exposure lowers its solubility.

Figure 4.8: Forward and backward scattering of electrons, from [126].

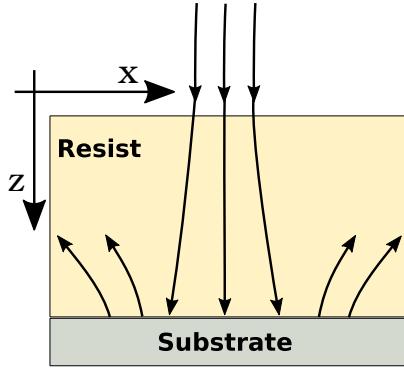
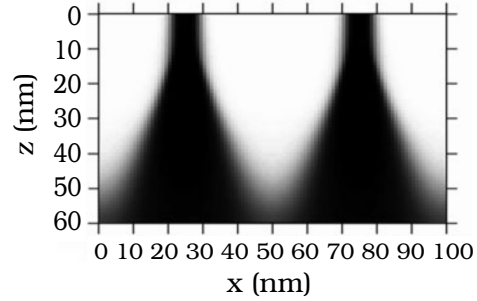
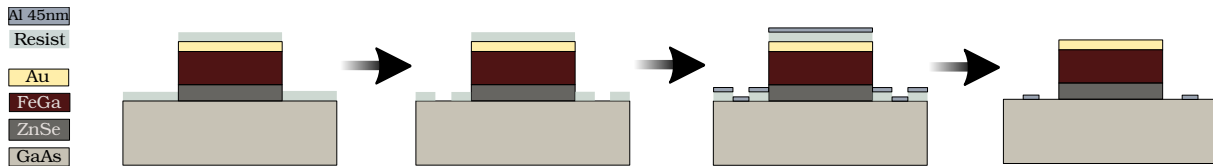


Figure 4.9: E-beam broadening, as electrons penetrate into the resist, from [126].



The main steps on IDT fabrication are illustrated in the fig. 4.10. The sample is covered with a PMMA (poly-methyl methacrylate) resist, after which it is exposed to electrons according to a desired design and developed so that the exposed resist is removed. Finally we deposit by evaporation a thin film of **45nm Al** (metalization) and the rest of the resist is removed in acetone (lift-off).

Figure 4.10: Steps of IDTs fabrication.



The table below summarizes the experimental parameters, used to perform the e-beam lithography. The acceleration voltage and the development time of the resist after the irradiation were respectively, 20keV and 70s in MIBK IPA 3:1 / 30s in IPA. Note that, for the case of the insulating substrate, a thin film of 10nm of Al was deposited on top of the resist to avoid charging effects.

Table 4.2: E-beam lithography parameters, used for sample fabrications. Two different microscope apertures were used to draw patterns for the IDTs electrodes or antennas signal / ground lines ($10\mu m$) and contacts ($120\mu m$).

Material	PMMA thickness (nm)	Backing T°C, time	Dose, $\mu C/cm^2$ (aperture $10\mu m$)	Dose, $\mu C/cm^2$ (aperture $120\mu m$)
GaAs	150	167°C, 15min	240	280
ZnO	150	167°C, 15min	240	280
LiNbO ₃	150	167°C, 15min	190	250
SiO ₂	300	150°C, 15min	228	280

4.3 Excitation of harmonics

The table below summarizes different designs, used to excite the harmonic frequencies. The IDTs dimensions were sufficiently large to use optical lithography. Since the “split-4” design gives access to a larger frequency range, the final samples for RF measurements under the applied magnetic field were fabricated, using this design.

Table 4.3: Different IDT designs, used to excite harmonic frequencies (nominal dimensions).

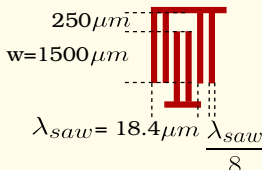
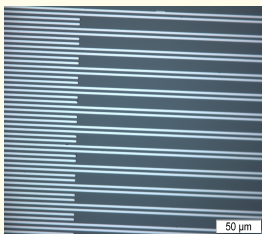
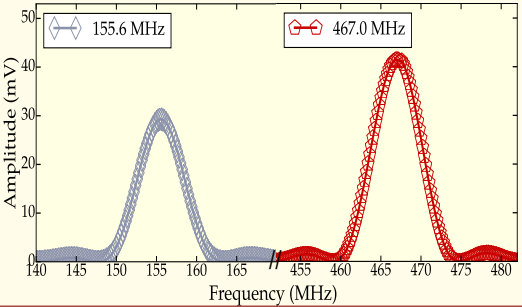
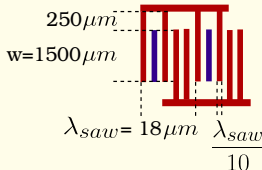
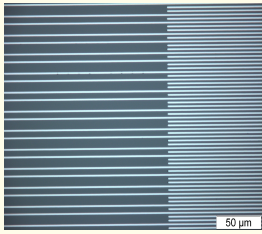
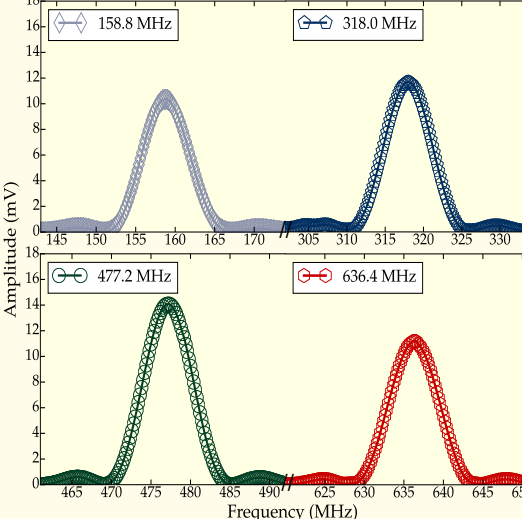
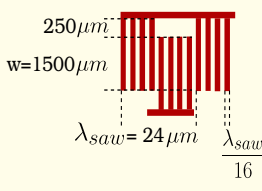
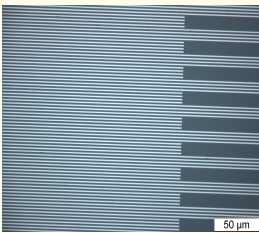
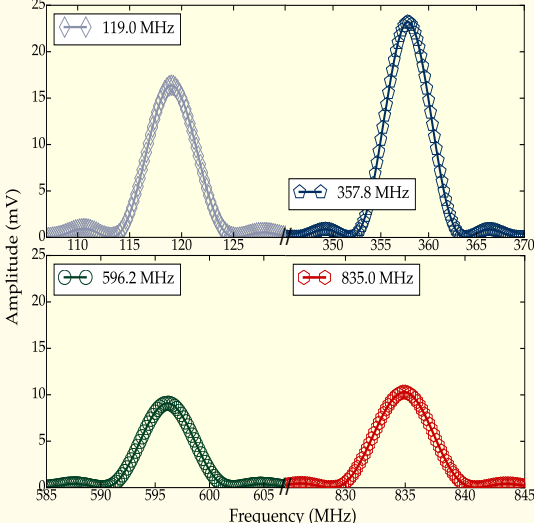
IDT type & Source	Frequency	Optical microscope photo	Measured signal, proportional to the acoustic burst amplitude. ($P=25\text{dBm}=316\text{mW}$)
Split-2 [123] Odd harmonics  $w=1500\mu\text{m}$ $\lambda_{saw}=18.4\mu\text{m} \frac{\lambda_{saw}}{8}$	156 MHz 467 MHz		
Split-52 [120] Even and odd harmonics  $w=1500\mu\text{m}$ $\lambda_{saw}=18\mu\text{m} \frac{\lambda_{saw}}{10}$	159 MHz 318 MHz 477 MHz 636 MHz		

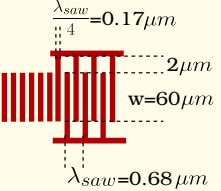
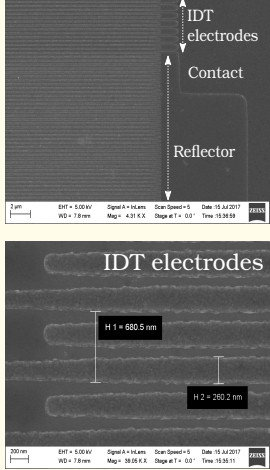
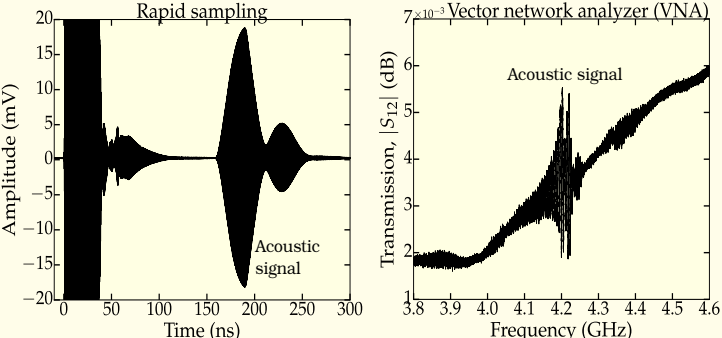
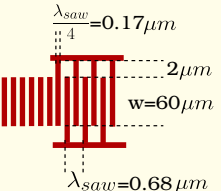
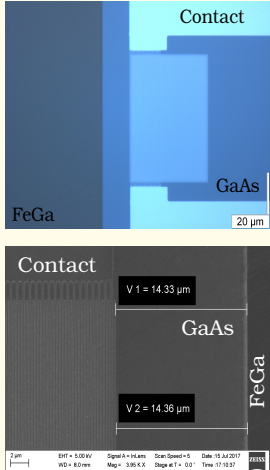
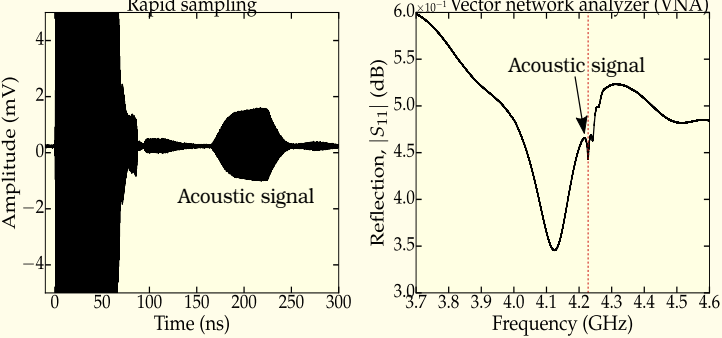
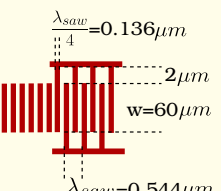
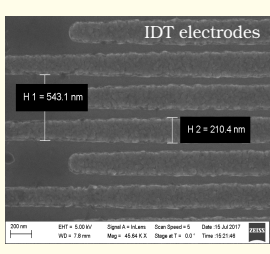
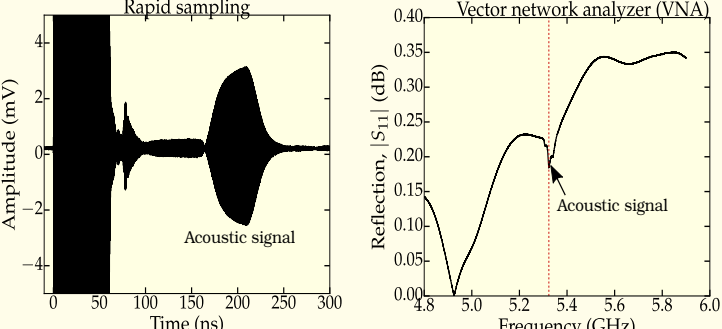
Table 4.4: Different IDT designs, used to excite harmonic frequencies (nominal dimensions).

IDT type & Source	Frequency	Optical microscope photo	Measured signal, proportional to the acoustic burst amplitude. (P=25dBm=316mW)
<p>Split-4 [120] Odd harmonics</p> 	<p>119 MHz 358 MHz 596 MHz 835 MHz 1.07 GHz</p>		

4.4 High frequency range, 4-5 GHz: synchronous IDTs

For excitation of high frequency SAWs, that is 4-5GHz we employed the design, initially created to make a SAW resonator, as described in [121]. In this case a built-in reflector IDT is used. This design is referred to as *synchronous* (SYNCH) IDT and has proved to be the best to excite high frequency SAW. A standard IDT, as described in section 4.1, is a bi-directional, which means that there is a 3dB loss due to SAW excitation in both directions. Placing internal reflector would re-direct the wave, that propagates in another direction and in principle, can double the SAW amplitude. A good source on technical details, that one should take into consideration while designing an IDT is given in [127] (ch.2, sec.2.4). Following this source, for efficient high-frequency SAW excitation we reduced the overlap width (aperture) down to 60 μ m. Figures below show the measured acoustic signal, using the rapid sampling scheme, with a schema of the IDT design and the real images, taken with the e-beam microscope. The table below summarizes the obtained results: test IDTs at 4.2 and 5.2 GHz on pure GaAs and at 4.2 GHz with the FeGa thin film on the SAW propagation path. The acoustic signal was measured using rapid sampling detection scheme, as well as with the vector network analyzer (VNA). The latter permits to measure a transmitted signal in the frequency domain.

Table 4.5: Synchronous IDT (SYNCH) design (nominal dimensions), used to excite high frequency SAW, 4-5GHz. IDTs on pure GaAs (4.2 - 5.2 GHz) and with FeGa film on the SAW propagation path (4.2 GHz).

IDT type & Source	E-beam / Optical microscope photo	Measured signal, proportional to the acoustic burst amplitude. (P=19dBm=79mW)
<p>SYNCH [121], [127] 4.2 GHz Test</p> 		
<p>SYNCH [121], [127] 4.2 GHz Final sample</p> 		
<p>SYNCH [121], [127] 5.2 GHz</p> 		

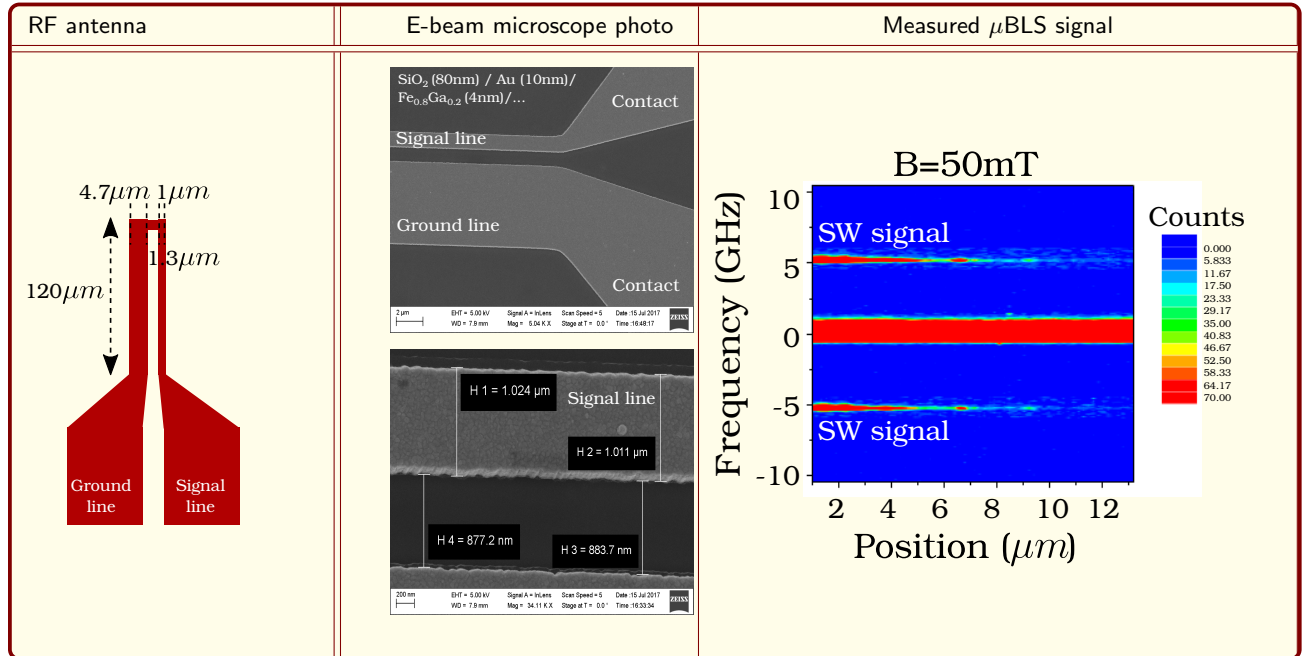
Note that, introducing the ferromagnetic film in the SAW propagation path results in signal amplitude ($\simeq 2\text{mV}$, peak-peak) loss of about 30dB, as compared to pure GaAs ($\simeq 38\text{mV}$, peak-peak).

4.5 Excitation of spin waves with RF antennas

To excite spin waves, radio frequency antennas, or as referred to coplanar waveguide (CWG), are used. There exist several designs, that can be found in the literature, for example symmetric CWG [128], asymmetric CWG [129], [130], broadband antenna (stripe antenna) [131]. Further development in the antennas designs were made to improve the excitation efficiency and reduce the excited wave vector spread, Δk [132], [133]. This leads to a more sophisticated antennas design, namely meander shaped pattern.

To see the excitation of spin waves, we used the micro Brillouin scattering technique³, μBLS . This technique permits to see the excited SWs intensity (counts) as a function of the propagation distance, away from the antenna. As can be seen from the μBLS spectrum, presented in the table below, the SWs attenuation length is of the order of **13 μm** , which is a good result for us, as it opens the possibility to manipulate SWs with SAWs on a reasonable length scale.

Table 4.6: Excitation of SWs with a RF antenna.



³In collaboration with GHOST laboratory, Perugia, Italy.

4.6 Sample connection

Once the samples were fabricated, the next step was to connect them manually, using a silver paste, to integrate in the excitation-detection scheme. Two kind of sample supports were used, depending on the SAW excitation frequencies. First type (fig. 4.11) consists of a copper plate with an insulating plate on top. This type of the support was used for 0.1-1 GHz frequencies. The sample was placed in a chamber (fig. 4.13 - fig. 4.14) and kept at constant temperature (control up to 0.001°C) and in a vacuum ($\approx 10^{-5} - 10^{-6}$ mbar) during the acoustic measurements.

Second type of the sample support (fig. 4.12) is an imprinted circuit with directly welded connectors, that permits to have a better impedance match between the IDTs and excitation source. These supports were employed for the BLS and μBLS measurements (chapter 5, section 5.3).

Figure 4.11: First type of sample support, used for 0.1-1 GHz frequencies. It employs two types of wires to reach the coaxial cable.



Figure 4.13: Chamber, used for the acoustic measurements.

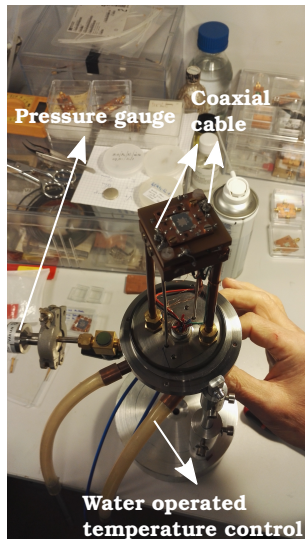


Figure 4.12: Example of a second type of sample support, used for frequencies above 1 GHz. Short wires (4-5mm) of $80\ \mu\text{m}$ diameter are used to connect the IDT terminals to the signal line and the ground.

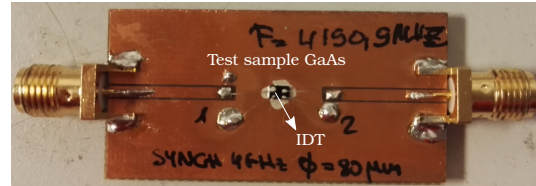
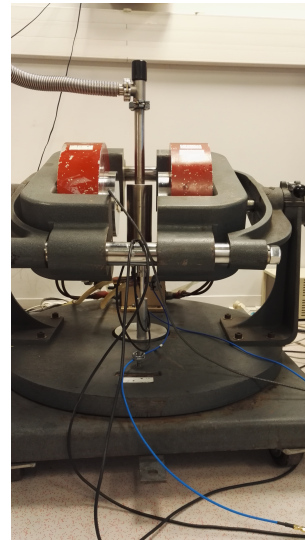


Figure 4.14: Chamber, placed in between current carrying coils.



4.7 Conclusion

To conclude, following developments in the devices fabrication were done during this thesis, based on the information, that could be found in the literature:

1. determining solutions for wet etching
2. design and fabrication of the IDTs in the 0.1-5GHz frequency range, using optical / e-beam lithography
3. preliminary design (in collaboration with GHOST laboratory) and fabrication of the RF antennas, using e-beam lithography.

It must be mentioned, that the efficient SAW excitation at high frequencies can be possible, if one succeeds to achieve a good impedance matching between the IDTs and the excitation source. Such attempts were undertaken, that is addition of variable capacitance and inductance into the excitation circuit, but still require further development.

The results are summarized in the table below:

Table 4.7: Summary of the samples, fabricated during this thesis. Notations: HF high frequency.

Dry / Wet etching, GaAs	Deposition of ZnO	SiO ₂ /Au/FeGa
1) Excitation of harmonics: 0.1-1GHz 2) Excitation of HF SAW: 4.2-5.2GHz	Excitation of SAW along [100] 830MHz	Excitation of spin waves

Chapter 5

RF measurements: Experimental Results

This chapter is devoted to the experimental results and observations. The table below summarizes the samples, studied in this thesis, as well as orders of magnitude of measured variations in the SAW velocity and attenuation¹. The harmonic frequencies were not immediately available, as well as the wet etching solution. Some samples were re-measured, when several frequencies with a single device were available.

Table 5.1: Samples studied via RF measurements. Unless specified otherwise, the composition for all samples is $\text{Fe}_{0.8}\text{Ga}_{0.2}$. Samples are single crystals, except A140. The latter was prepared by Rocio Ranchal (Madrid) by sputtering. We give **maximal values** as the order of magnitude of $\Delta V/V$, $\Delta\Gamma$. Abbreviations: d - film thickness, MS - magnetic structure, IP - in-plane magnetization, CIDT - conventional inter-digital transducer.

Name	d(nm)	MS	Etched / ZnO	IDT	F (MHz)	Direction	$\frac{\Delta V}{V}$ (%)	$\Delta\Gamma$ (dB/cm)
32m0100 Fe	50±3	IP	etched	CIDT	554	[110]	0.004	noise
32m0203-E ₁	26±3	IP	ZnO~178nm	CIDT	300	[1 $\bar{1}$ 0]	noise	noise
32m0206-E ₁	58±3	IP	ZnO	CIDT	306	[1 $\bar{1}$ 0]	0.015	noise
32m0206-E ₂	58±3	IP	etched	split-4	119, 357 595, 833	[1 $\bar{1}$ 0], [110]	0.006	1.2
32m0210-E ₁	88±3	IP	etched	split-4	830	[1 $\bar{1}$ 0], [110]	0.009	3
A 140 polycrystal	55	IP	etched	split-4	119, 357 595, 833	-	0.004	0.7
32m0215-E ₁ Fe	67±3	IP	etched	split-4	830	[1 $\bar{1}$ 0], [110]	0.006	0.2
32m0153-H ₁	92±2	stripes	ZnO ~240nm	CIDT	154	[110], [1 $\bar{1}$ 0]	0.003	0.045
32m0153-H ₃	92±2	stripes	ZnO ~210nm	CIDT	310	-	0.005	0.1
32m0153-S ₁	92±2	stripes	etched	split-4	835	-	0.014	0.7

¹Note that these are maximal measured values.

To be concise in what follows and to avoid cumbersome representation of the experimental data, we focus only on the sample 32m0206 $\text{Fe}_{0.8}\text{Ga}_{0.2}$, as we studied it extensively. In the next chapter we model our system and interpret the observations, which gives more insights into the physics behind the experiment. The results for 32m0215 Fe will then be presented and explained in the chapter 6.

5.1 General remarks

We start with an experimental observation, represented in the fig. 5.1. The plot shows the measured relative change in SAW velocity, $\frac{\Delta V}{V}$ as a function of the external magnetic field, swept from “positive” saturation (circled curve) to “negative” saturation. For the presented measurement the field was applied parallel/anti-parallel to the SAW wave-vector. Firstly, a change in the velocity shows the presence of coupling between SAW and magnetization. For all measurements performed, there are some common features, that can be seen in the fig. 5.1:

- *high field region* exhibits a reversible acoustic behavior
- The *low field region* is defined according to the hysteresis cycle as a region, where both magnetic domains exist and single domain rotation takes place [69] (p.190). This region exhibits a **magneto-elastic hysteresis**.

To give the order of magnitude of the observed phenomena, we define *amplitude of phenomena* as the difference between maximal and minimal change in the velocity or attenuation. For the measurement presented, the variation in velocity is about $6 \cdot 10^{-5}$. The fig. 5.2 represents the change in SAW attenuation vs magnetic field. As can be seen, SAW is mostly attenuated in the low field region, that exhibits magneto-elastic hysteresis, with an amplitude of the phenomena of **0.6 dB/cm**. Let us compare these numerical values with relevant experiments, performed on other materials, found in the literature. An in-exhaustive list of the comparisons is represented in the table 5.2. As an order of magnitude, the value of SAW attenuation can reach even 150dB/cm, as reported previously for MnAs due to giant magneto-caloric effects [134]. It is thus clear that variations we measure are rather small.

Figure 5.1: Relative change in SAW velocity vs the applied magnetic field and magnetic hysteresis for the film of 58nm $\text{Fe}_{0.8}\text{Ga}_{0.2}$. The curve is separated into two main regions, according to the acoustic behavior. The \leftarrow and \rightarrow indicate the field sweeping direction, that is from 200 to -200mT and vice versa, respectively. The inset schematically represents the measurement configuration. Dotted line represents measured hysteresis cycle.

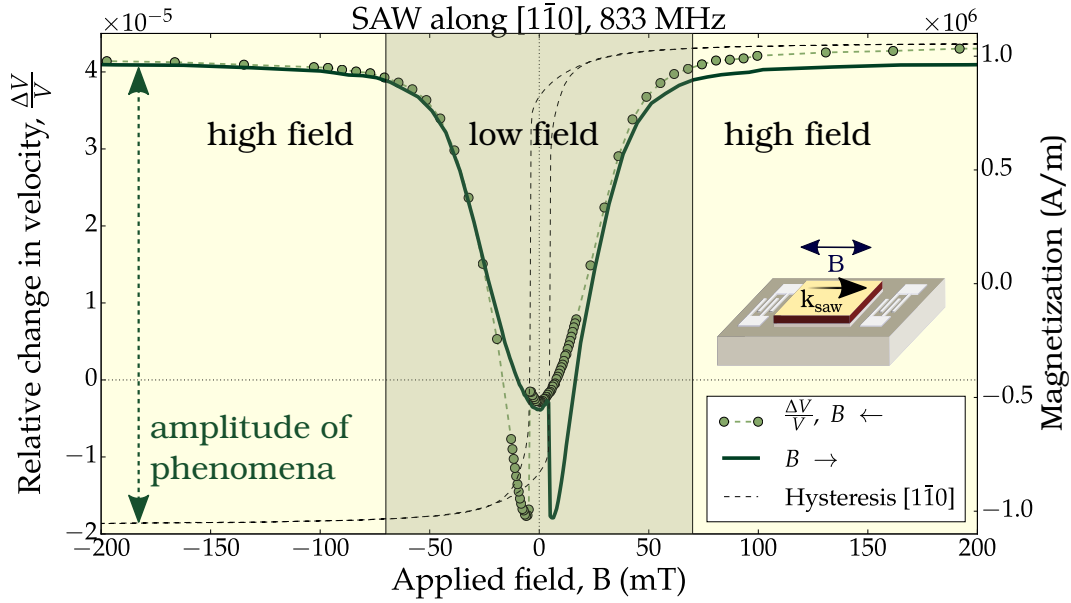


Figure 5.2: Experimental result for change in SAW attenuation vs the applied magnetic field for the film of 58nm $\text{Fe}_{0.8}\text{Ga}_{0.2}$. Dotted line represents measured hysteresis cycle.

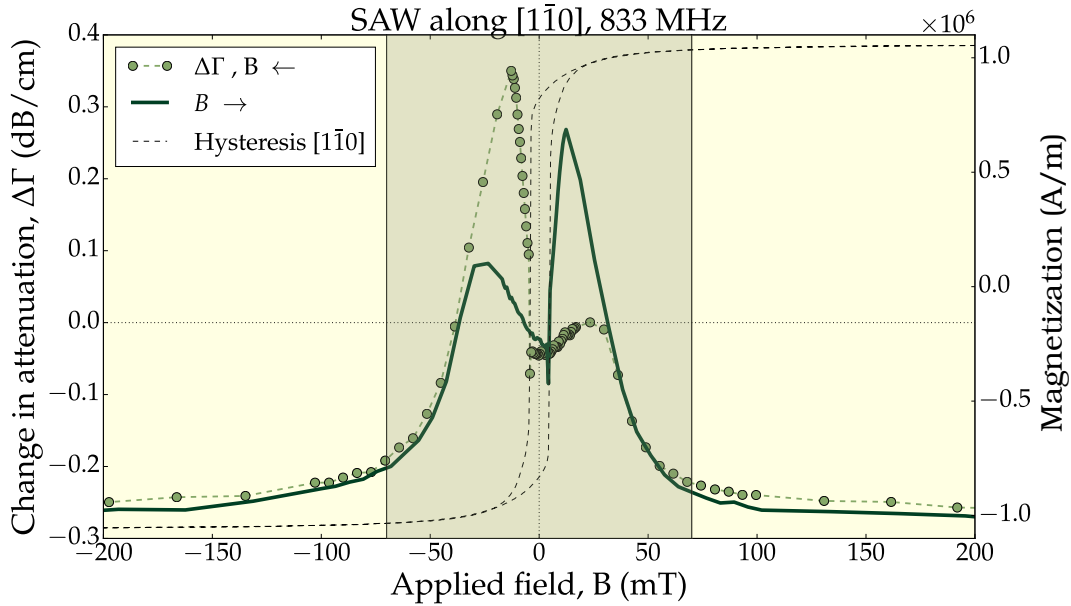


Table 5.2: Order of magnitude of variations in SAW velocity and attenuation, from [135], [86], [136], [18]. Abbreviations: MS - magnetic structure, UMA - uniaxial magneto-crystalline anisotropy, OP - out-of-plane magnetization, IP -in-plane magnetization, HA - hard axis, EA - easy axis.

Material	MS	F(MHz)	$\frac{\Delta V}{V}$ (%)	$\Delta\Gamma$ (dB/cm)	SAW	Field
Ni 850nm [89] (1976)	UMA OP	210 70	0.02	-	HA	HA
Ni 20nm, 37nm [86] (1988)	UMA IP	601	0.01-0.07	25-80	-	$\parallel, \perp,$ at 45° to k_{saw}
TbCo ₂ /FeCo stack 200nm [136] (2014)	UMA IP	232	0.02	-	EA	HA EA
(Ga,Mn)(As,P) 50nm at 5K, resonance [18] (2014)	UMA OP	549	0.01	8.5	HA	HA

5.2 32m0206 Fe_{0.8}Ga_{0.2} 58nm

This section summarizes the main observations for the 58nm sample of Fe_{0.8}Ga_{0.2}, concerning the $\frac{\Delta V}{V}$ measurements. A model of the system is presented in the chapter 6, here we compare the observations with the computed SAW-induced torque, as discussed in the chapter 2. The comparison is indirect, but possible due to the coupling between SAW and magnetization, and it permits to obtain a qualitative explanation of the observed effects.

Note that, the models, presented in the chapter 6 cannot reproduce the variations in the attenuation. We thus, focus only on the the $\frac{\Delta V}{V}$ measurements.

The magnetic structure for this sample is shown in the chapter 2, where we computed the SAW-induced torque. We remind that, the sample is in-plane quasi-isotropic. Biaxial MCA is modified by a uniaxial anisotropy contribution, as can be seen from non-equivalent $[110]$ and $[\bar{1}\bar{1}0]$ directions (section 2.5.3, fig. 2.18).

As mentioned in section 5.1, we can distinguish between two regions, concerning the acoustic behavior, that is high and low field regions. We will start with the description of peculiarities of the first one.

Note that, we measure $\frac{\Delta V}{V}$, that is $\frac{1}{V}[V(B, \varphi) - V(B = 0)]$, meaning that the first point for all measurement configurations is magnetically the same, since before every measurement the sample was saturated in $\vec{B} \uparrow \downarrow \vec{k}$ configuration to have a common reference point. This allows us to compare the measurements, made for different directions of the applied field.

5.2.1 High field region

The following experimental observations can be made:

- (i) When the field is applied parallel or perpendicular to the SAW wave vector, the change in velocity, $\frac{\Delta V}{V}$ is constant, as represented in the fig. 5.3.
- (ii) If the field is applied at some other angle, the acoustic behavior is different. For example, we compare the measurements for the field, applied at 10° and 45° with respect to the SAW wave vector, fig. 5.4. In the first case, the change in velocity tends to a constant value for high fields, approximately above 280 mT, while for the field, applied at 45° , the effect on the SAW velocity is still present at the same field. We refer to this phenomena as different angle dependent acoustic saturation rates.
- (iii) As the field intensity increases, the change in SAW velocity decreases.
- (iv) Since the SAW propagation exhibits a strong angular dependence on the direction of the applied field, we performed measurements at fixed field and frequency, but varied the field angle. The result of these measurements, more proper for SAW propagation along $[1\bar{1}0]$ and at 1.07 GHz, is represented in the fig. 5.5. We observe clearly the sinusoidal variations in the SAW velocity with the applied field direction, the effect decreases with the increasing field.

Figure 5.3: Relative change in SAW velocity, $\frac{\Delta V}{V}$ vs magnetic field, applied parallel and perpendicular to the SAW wave vector, \vec{k}_{saw} .

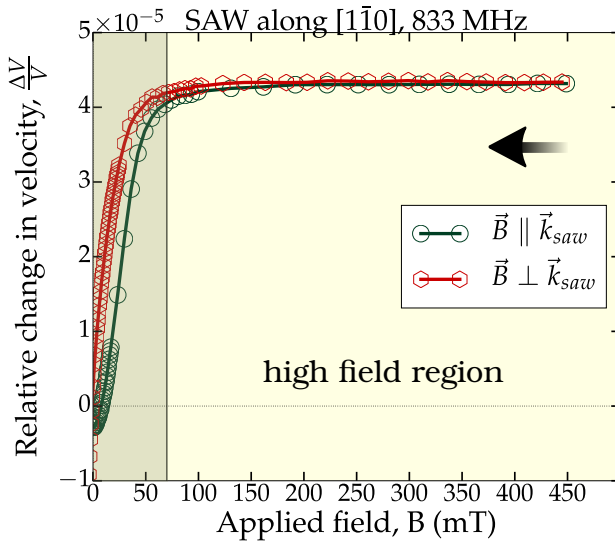


Figure 5.4: Relative change in SAW velocity, $\frac{\Delta V}{V}$ vs magnetic field, applied at 10° and 45° with respect to the SAW wave vector, \vec{k}_{saw} .

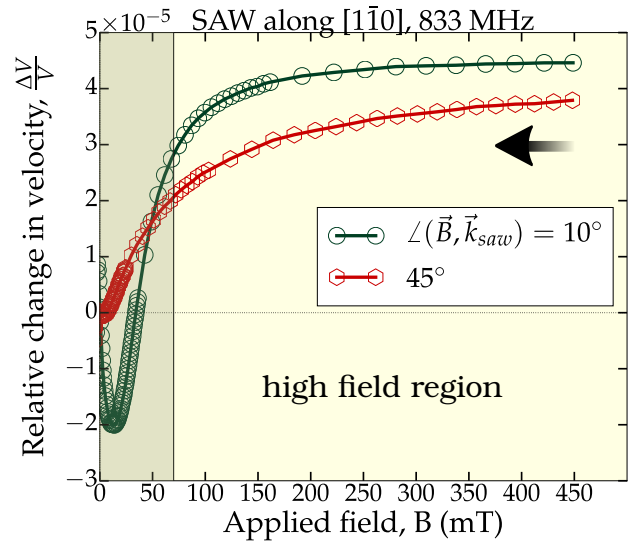
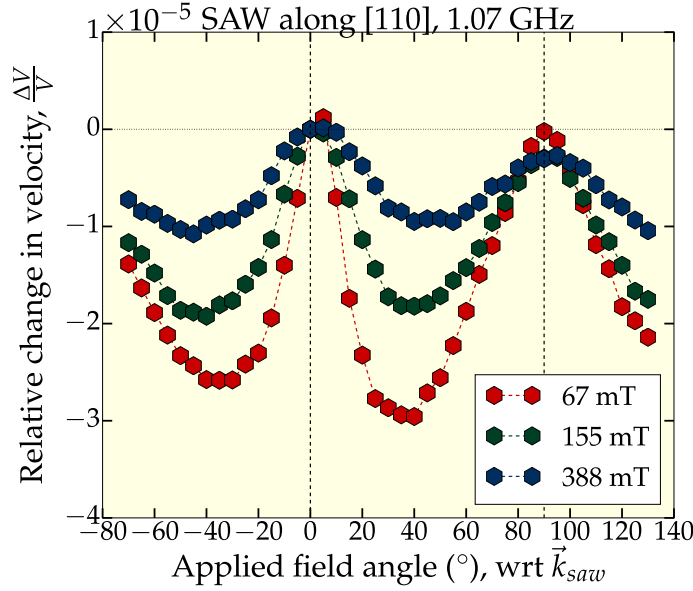


Figure 5.5: Relative change in SAW velocity, $\frac{\Delta V}{V}$ vs magnetic field angle at different intensities.

Let us compare these observations with the computation results, described in the chapter 2. As mentioned earlier, injecting SAW into a ferromagnetic media will result in a torque on the magnetization and in turn, the SAW-induced magnetization dynamics will affect the wave propagation.

First, following the conclusion of the chapter 2, for magnetic field (or saturation magnetization), applied perpendicular or parallel to the SAW wave-vector torque vanishes and thus, there is no effect of SAW on magnetization and vice versa. This can explain, why we observe *no change* in the SAW velocity for parallel and perpendicular configuration in the high field region, i.e. the observation (i). Note that the change in velocity is deduced according to $\frac{\Delta V}{V} = \frac{V(B, \varphi_B) - V(B_{ref})}{V(B, \varphi_B)}$. The reference point is absolutely arbitrary, which results in the curve translation. The constant change in velocity, observed in the fig. 5.3 is due to this reason.

Concerning the (ii)-(iii) observations, the figures below represent the **indirect** comparison between the experimental measurements and the computed torque. As can be seen, torque is non-zero and its amplitude decreases with the increasing field at different rates, that depend on the field direction. Accordingly, in the region, where the torque is active, there is a change in the SAW velocity, that becomes weaker as the field increases. We thus can see a fingerprint of SAW-induced magnetization dynamics on the SAW propagation.

The last observation (iv) requires a proper model of the system (as will be done in the next chapter) for it is difficult to compare the oscillatory torque behavior with the experiment. In the fig. 5.8 we represent the computed torque vs the applied field angle, the latter is defined **with respect to $[1\bar{1}0]$** axis, that coincides with the SAW propagation direction. For relatively low fields the torque dependency on the angle is rather complicated, *because we are sensitive to the magneto-crystalline anisotropy*. At high fields we reproduce the sinusoidal

variations with the applied field angle, that are compatible with the experimental results. There are several similarities to be noticed.

First, the relative change in velocity at a given field is deduced from the phase measurements according to

$$\frac{\Delta V}{V} = \frac{1}{V(\varphi_i)} \left(V(\varphi_i) - V(\varphi = 0) \right)$$

where $\varphi_i \neq 0$ is the applied field angle, the latter is defined with respect to [110]. According to the calculation of the torque we should observe no change in SAW velocity for the parallel and perpendicular configurations (for 0° and 90° , respectively in the fig. 5.5). This is roughly in agreement with the observation.

Both theoretical (torque) and experimental curves show the $\pi/2$ periodicity.

Secondly, when the torque is at its relative maximum, the change in velocity is maximal at high fields. As mentioned previously, the variations in the torque norm with angle decrease with the increasing field, which is (indirectly) in agreement with the experimental observation.

Figure 5.6: Experimental change in SAW velocity and computed norm of the torque density for $\angle(\vec{B}, \vec{k}_{saw}) = 10^\circ$ vs applied field intensity.

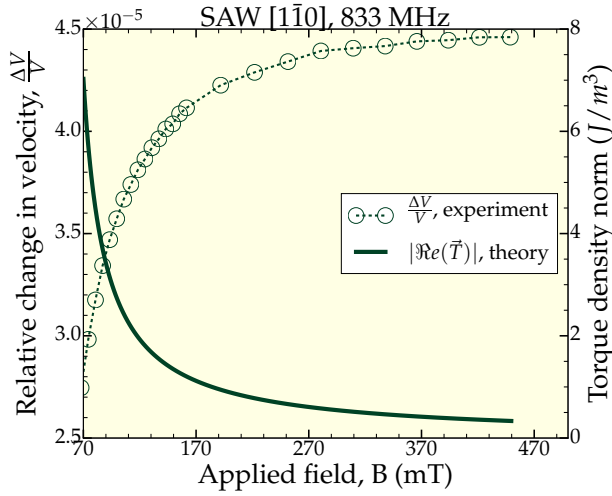


Figure 5.7: Experimental change in SAW velocity and computed norm of the torque density for $\angle(\vec{B}, \vec{k}_{saw}) = 45^\circ$ vs applied field intensity.

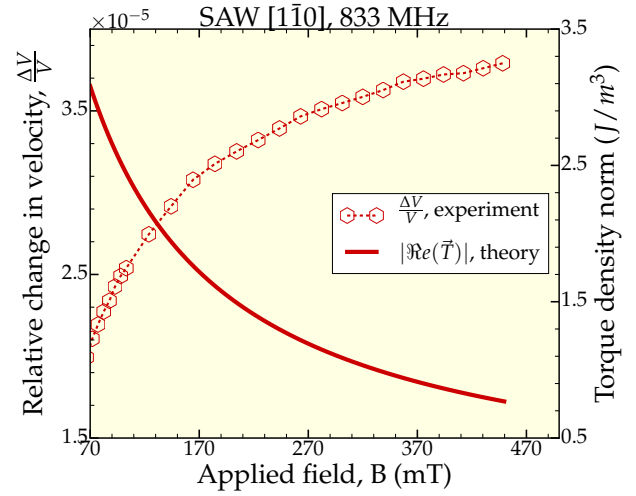
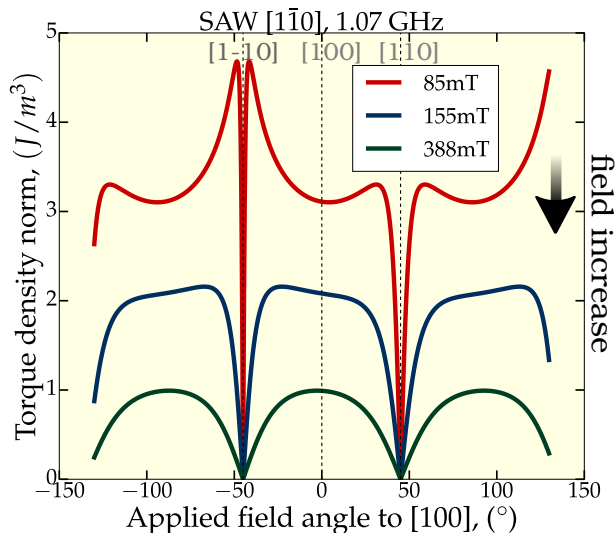


Figure 5.8: Computed norm of the torque density vs the applied field angle for different field intensities.



5.2.2 Low field region

Low field region is more complicated from the analytical point of view, as one should consider the presence of both magnetic domains and single domain rotation. Since in this region magnetic domains are present, we performed the acoustic measurements, combined with the Kerr microscopy imaging in collaboration with L. Thevenard, to observe the domains and the effect of SAW, if any, on the magnetization.

Note that, to explain the low field region, one has to perform the micro-magnetic simulations, taking into account the presence of magnetic domains. Our analytical models within the single domain approximation cannot reproduce these experimental features and the description is beyond the scope of this thesis. In what follows we just report on the experimental observations.

Several features are characteristic for the low field region.

- (i) Presence of **magneto-elastic hysteresis**, as we could already observe in the section 5.1 (fig. 5.1).
- (ii) Dependence of magneto-elastic hysteresis on the applied field angle. This feature is a way more striking than in the high field region, as can be seen from fig. 5.9 - fig. 5.15.

Figure 5.9: Change in SAW velocity for low field region, field is parallel to the SAW wave vector.

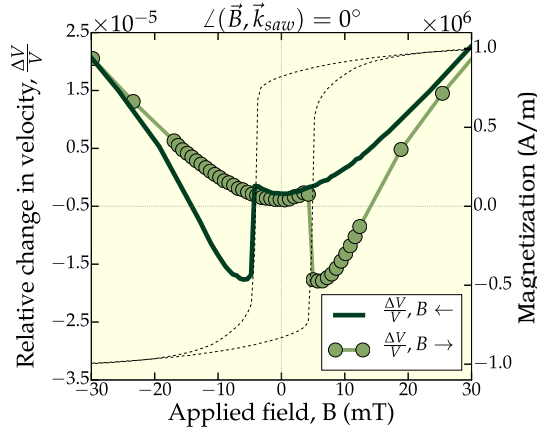


Figure 5.10: Kerr microscopy image of magnetic domains, image taken at 5.4 mT, increasing field.

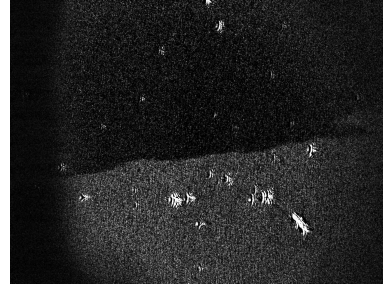


Figure 5.11: Change in SAW velocity for low field region, field is applied at 10° to \vec{k}_{saw} .

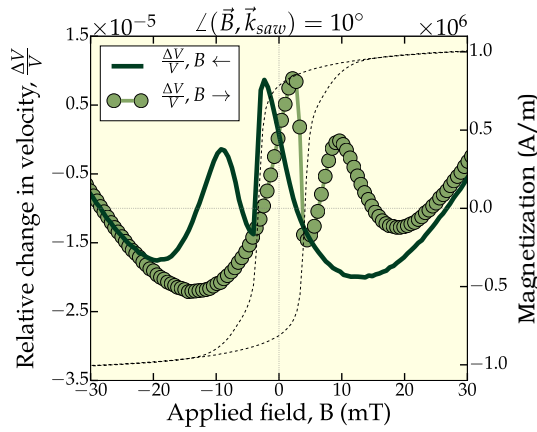


Figure 5.12: Kerr microscopy image of magnetic domains, image taken at -3.9 mT, decreasing field.

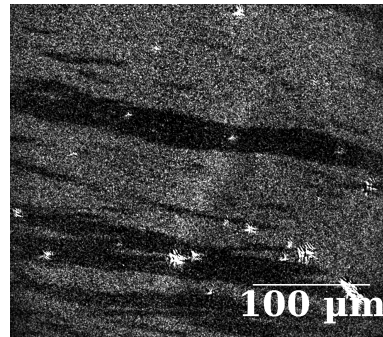


Figure 5.13: Change in SAW velocity for low field region, field is applied at 30° to \vec{k}_{saw} .

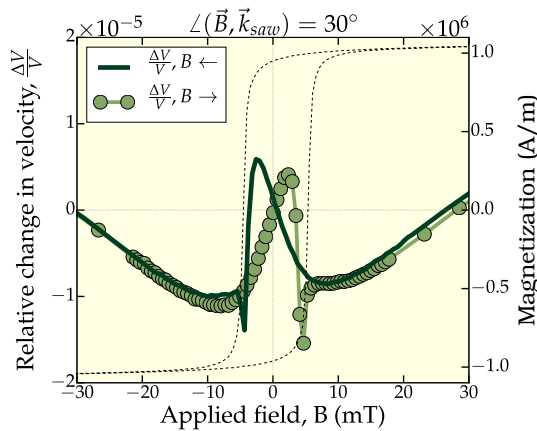


Figure 5.14: Kerr microscopy image of magnetic domains, image taken at -3.9 mT, decreasing field.

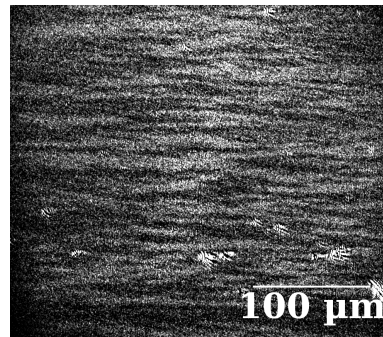
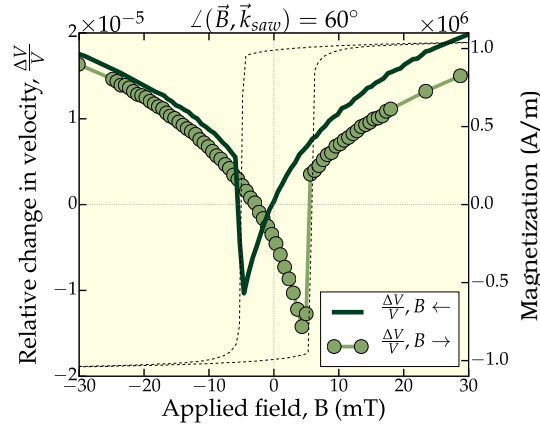


Figure 5.15: Change in SAW velocity for low field region, field is applied at 60° to \vec{k}_{saw} .



(iii) Non-equivalence of positive and negative applied field angles.

Figure 5.16: Change in SAW velocity, field applied at $\pm 5^\circ$ to \vec{k}_{saw} . Black arrow indicates the field sweep direction.

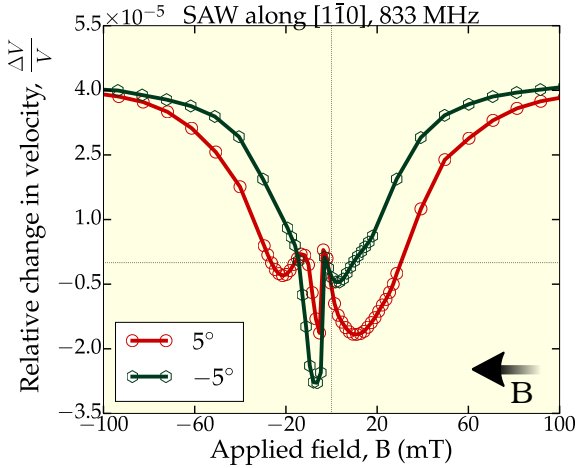


Figure 5.18: Kerr microscopy image taken at -4.6 mT, decreasing field, $\angle(\vec{B}, \vec{k}_{saw}) = 5^\circ$

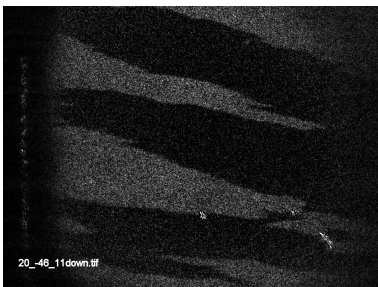


Figure 5.17: Change in SAW attenuation, field applied at $\pm 5^\circ$ to \vec{k}_{saw} .

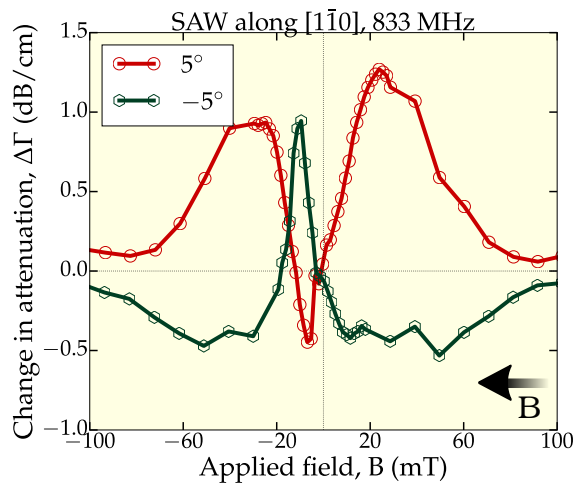


Figure 5.19: Kerr microscopy image taken at 4.2 mT, increasing field, $\angle(\vec{B}, \vec{k}_{saw}) = -5^\circ$



- (iv) Non-equivalence of [110] and [110] directions. This could be already seen from the in-plane hysteresis and is attributed to the contribution of the uniaxial MCA to anisotropy of the system.

Figure 5.20: Change in SAW velocity for different propagation directions.

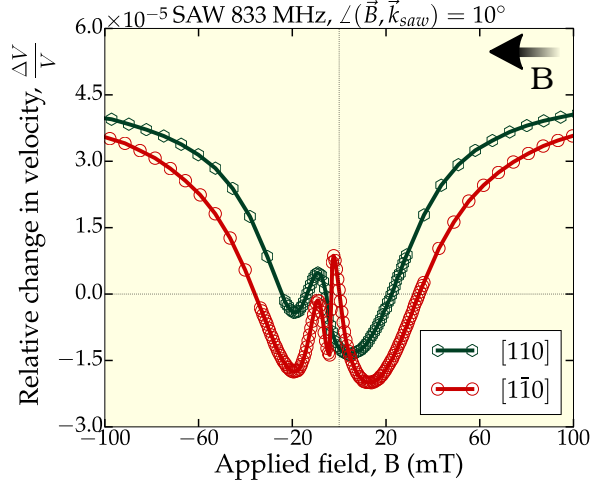
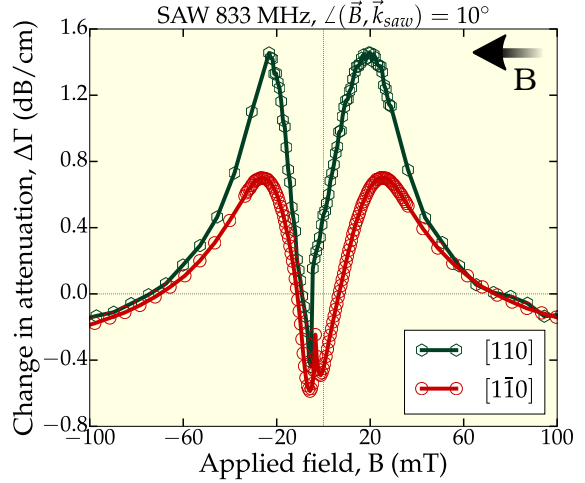


Figure 5.21: Change in SAW attenuation for different propagation directions.



- (v) SAW non-reciprocity, defined as the difference between velocities in forward and backward directions [137], [138]. According to [138] non-reciprocity of the velocity takes its origin in the coupling between Rayleigh and spin waves. The elliptical motion of a particle in the Rayleigh wave is in the same or opposite sense with the precession of the magnetization about the magneto-static field. This might cause the phenomena of non-reciprocity.

Figure 5.22: Change in SAW velocity for $+\vec{k}_{saw}$.

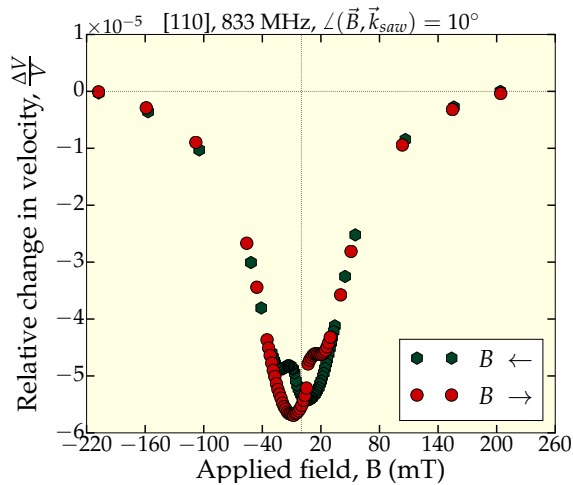
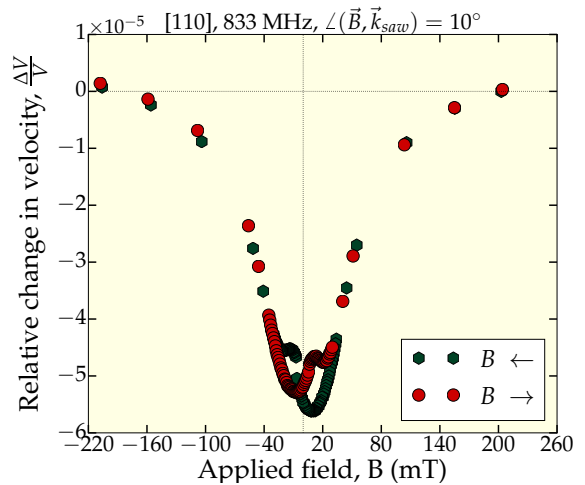


Figure 5.23: Change in SAW velocity for $-\vec{k}_{saw}$.



5.2.3 Effect of frequency

The effect of acoustic frequency can be clearly seen from the whole measurement in terms of amplitude of the phenomena, the latter was defined in section 5.1 (fig. 5.1). *The higher is the acoustic frequency, the larger were the effects observed.* As example, we represent two measurements of velocity, performed at 357 MHz and 833 MHz (fig. 5.24). The fig. 5.25 represents the variations in the SAW velocity with the applied field angle at fixed intensity for different frequencies. In both cases SAW was propagating along the $[1\bar{1}0]$ direction. Note that, the applied field applied is defined with respect to the SAW wave vector.

This can be argued in terms of SAW-induced torque as well, since its norm is inversely proportional to the acoustic frequency:

$$\|\text{Re}(\mathbf{T})\|_{[110]} = \left| \frac{B_2 \cos(2\bar{\varphi})}{2(\omega^2 - \omega_0^2)} \right| \sqrt{A_\theta^2 + A_\varphi^2}$$

More precisely it depends on the difference between acoustic and eigenfrequency of the system, that is $\frac{1}{\omega^2 - \omega_0^2}$. Since ω_0 is much larger than SAW frequency, it is clear that increasing the SAW frequency will decrease the frequency difference and hence, the torque will be larger. This indirect comparison implies larger effects on SAW propagation with increasing frequency.

Figure 5.24: Relative change in velocity for SAW, propagation along $[1\bar{1}0]$, at two different frequencies.

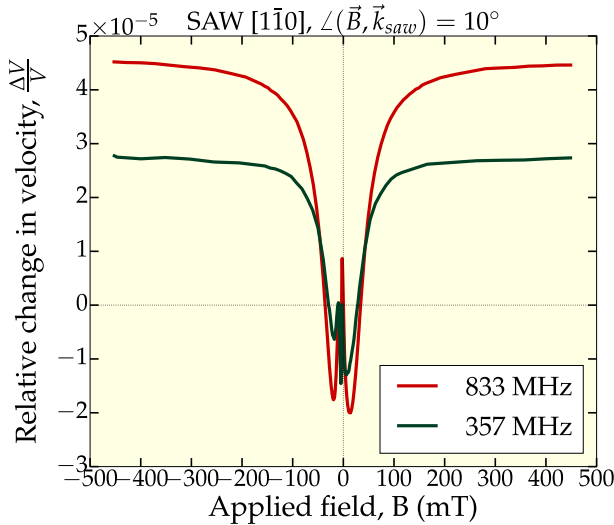
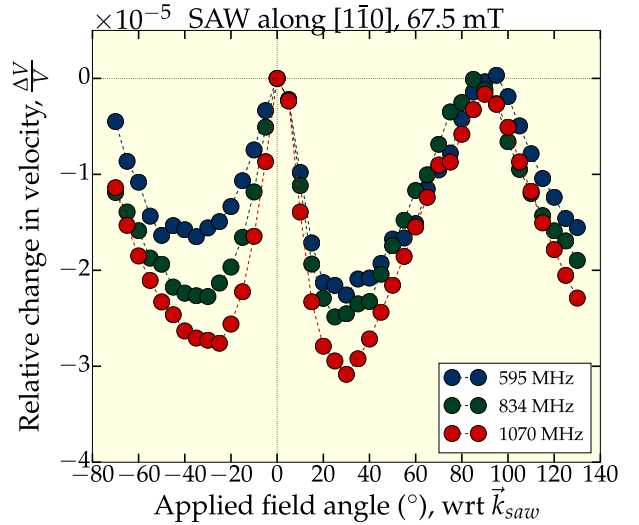


Figure 5.25: Oscillations in the SAW velocity vs applied field angle ($^\circ$) at different frequencies.



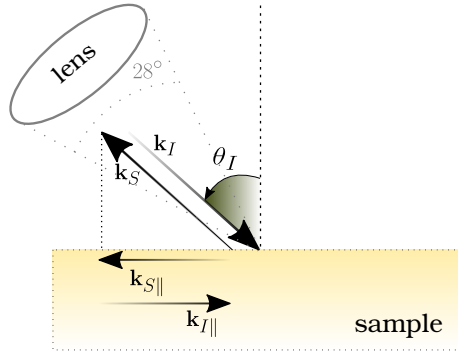
5.3 Preliminary BLS measurements: 32m0279 Fe_{0.8}Ga_{0.2} 4nm

The preliminary conventional BLS measurements were performed in collaboration with S. Tacchi, G. Carlotti and M. Madami (GHOST laboratory, Italy) at the end of this thesis. Here we discuss the experimental results, after giving a brief description [139] of the physical principle behind the BLS. The details of the experimental setup can be found in [139].

Brillouin light scattering technique relies upon the *inelastic scattering* of light by collective excitations of the medium, magnons or phonons. In a BLS experiment, a beam of monochromatic light ($\lambda = 532\text{nm}$) is focused on the surface of the magnetic film under investigation and the light scattered within a solid angle is frequency-analysed using a multi-pass Fabry-Perot interferometer. The incident light of energy $\hbar\omega_I$ and wave vector k_I produces a polarization in the matter, proportional to the susceptibility tensor of the medium. The collective excitation modulates the susceptibility, inducing a change in polarization and thus, resulting in a scattered light. From a quantum-mechanical point of view, the inelastic scattering mechanism can be described as a photon–magnon (photon-phonon) collision in which the total energy and momentum are conserved.

Note that, in the backscattered geometry, used in the conventional BLS setup, the in-plane wave vector component is conserved, as schematically represented in the fig. 5.26.

Figure 5.26: In the backscattered geometry the same lens is used to focus light and to collect the scattered light, the collection angle is $\simeq \pm 14^\circ$.



$$\begin{cases} \omega_S &= \omega_I \pm \omega \\ \mathbf{k}_{S\parallel} &= \mathbf{k}_{I\parallel} \pm \mathbf{q}_{\parallel} \end{cases}$$

$$\{ q_{\parallel} = 2k_I \sin(\theta_I) \quad (5.1)$$

where ω and \mathbf{q}_{\parallel} are the frequency and the in-plane wave vector component of the crystal excitation. Two possible processes may occur: *Stokes*, where $\omega_S < \omega_I$ and *anti-Stokes process*, where $\omega_S > \omega_I$. The first one corresponds to a creation of the excitation, while the second to its annihilation.

In order to observe the resonant interaction between *dipolar* SWs² and SAWs, it was indispensable to have wave length and frequency matching [141]. To reduce the SWs frequency, the film thickness of Fe_{0.8}Ga_{0.2} was reduced down to 4nm. In such a case, the film exhibits a strong in-plane uniaxial anisotropy (whose origin is the interface bonding between Fe and ZnSe, as discussed in [110]), as can be seen from the hysteresis cycle (fig. 5.27). This permits to get a softening of the SW modes and a resonance with the SAW frequency, when the field is applied along the hard axis. On the other hand, from the eq. (5.1) it is clear, that one can “select” a spin wave of a certain wave vector by varying the angle of the incident light. This permitted us to fulfill the resonance condition. A depolarized BLS spectrum taken at remanence, after saturation along the [100] direction, is represented in the fig. 5.28. The incidence angle of light is 20°. The SWs frequency is about 5 GHz, but the peak is rather broad and so it should be possible to match the SAW (dashed blue line) and SWs frequencies. Note, that the lowest SWs frequency is obtained *at remanence*.

To excite high frequency SAWs we employed *synchronous* IDT design, as was described in the chapter 4, section 4.4.

Figure 5.27: Hysteresis of **4nm** film.

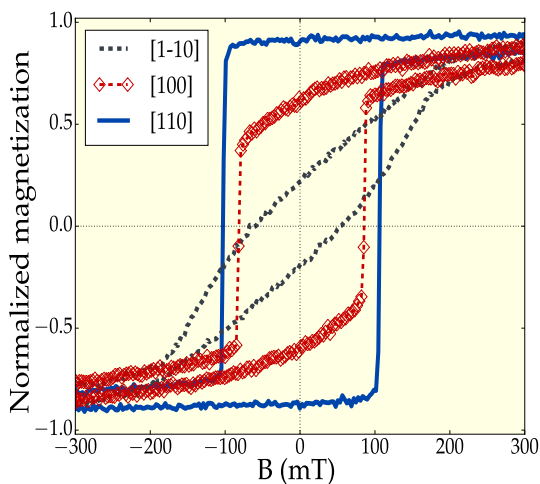
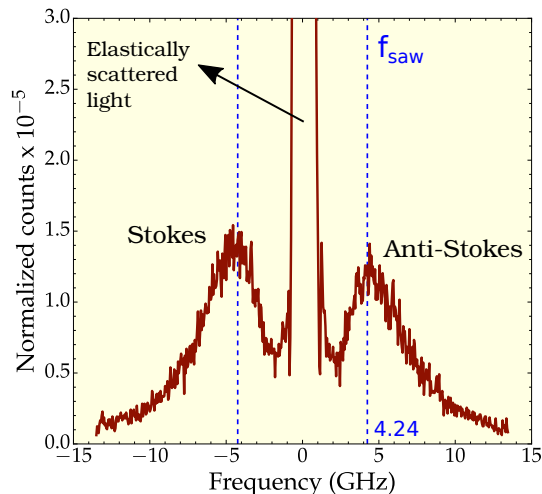


Figure 5.28: BLS spectrum of thermal SWs, centered at the incident light frequency. Dashed blue line represents the SAW frequency.



If we think in terms of a single domain, two configurations to maximize the SAW effect are possible, according to the analysis, performed in the chapter 2. We remind that two angles are important: angle between the equilibrium magnetization and the SAW wave vector and between the equilibrium magnetization and magnetic axis of the film.

²That is spin waves modes, dominated by the dipolar interaction as opposed to the *exchange* SWs [140].

With this in mind, we considered:

- * SAW along $[100]$, measurement at remanence, after saturation along the hard axis, $[\bar{1}10]$
- * SAW along $[110]$, measurement at remanence, after saturation along the medium direction, $[100]$

However, the first solution has not been explored because of the necessity to grow ZnO epilayer on order to make SAW propagate along $[100]$ direction, as explained in the section 4.1

Thus we chose to propagate SAWs along the easy axis, $[110]$. We fabricated the devices to check the resonant interaction both with the thermal SWs and excited with microwave antennas. The final devices are shown in the figures below (fig. 5.29 - fig. 5.30). A polarized

Figure 5.29: Fabricated device: IDTs to excite SAWs at 4.24 GHz, deposited close to the ferromagnetic film, $Fe_{0.8}Ga_{0.2}$ 4nm.

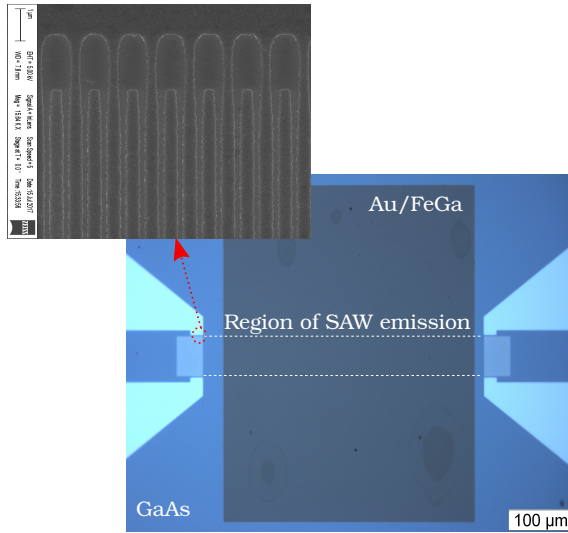
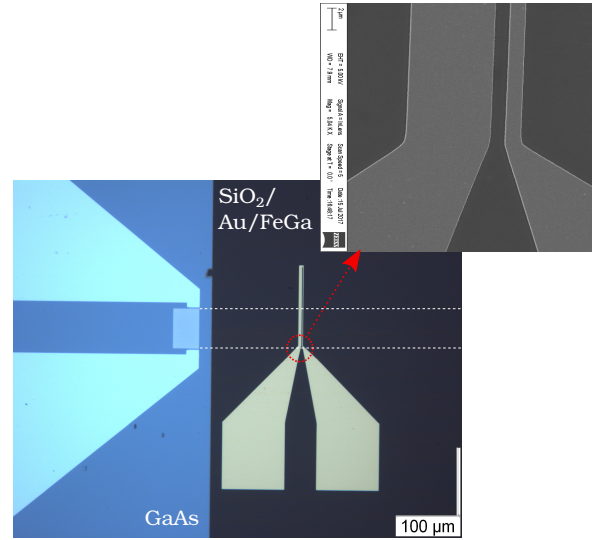


Figure 5.30: Fabricated device: IDTs to excite SAWs and RF antennas to excite SWs, deposited on top of $SiO_2/Au/Fe_{0.8}Ga_{0.2}$ (4nm).



BLS spectrum of continuously emitted SAWs, taken in the FeGa film near the emitting IDT is presented in fig. 5.31. As it can be seen, a large peak associated to propagating SAWs is visible in the anti-Stokes side of the spectrum. The fig. 5.32 shows the depolarized BLS spectrum taken in the same position.

At first, one could think that we do observe an enhancement in the thermal spin wave intensity at the SAW frequency. A straightforward way to check this supposition is to apply a magnetic field of 100mT in order to shift the SWs frequency *out of the resonance condition*. As it can be seen in the fig. 5.33 the **SAW peak did not disappear**.

We attribute this to the fact that the analyzer, used to block the light scattered by phonons (or SAWs), is not ideal, but has a certain extinction ratio. That is, some scattered light due to SAWs-light interaction was detected.

Thus, the “enhancement” in the SWs intensity in the fig. 5.32 is attributed to the excitation of SAW rather than a resonant SAW-SW interaction.

This result is rather puzzling. A possible explanation can be attributed to the fact that, reducing the film thickness, we are more sensitive to the interface effects. In principle, the magneto-elastic constants of thin films differ from those of the bulk material due to the film quality. What could happen in our case, is that the 4 nm thick film is of poor quality from a “magneto-elastic” point of view.

Figure 5.31: BLS spectrum of continuously emitted SAWs.

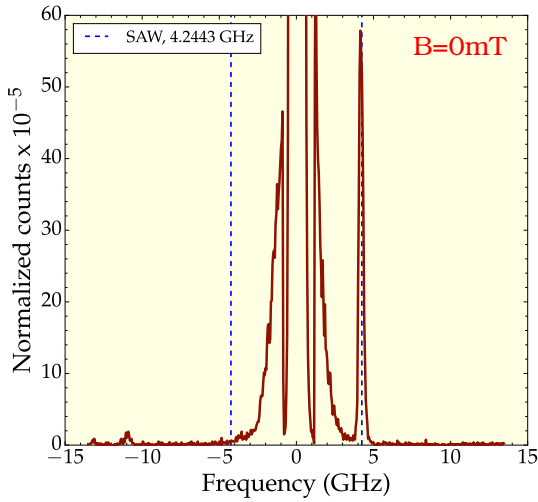


Figure 5.32: BLS spectrum of SWs with continuously emitted SAWs, no applied magnetic field.

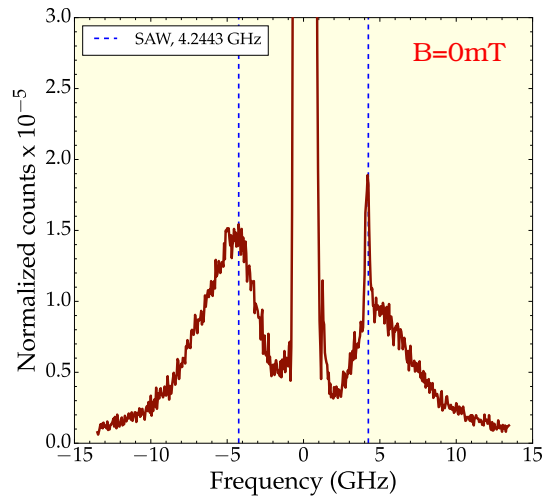
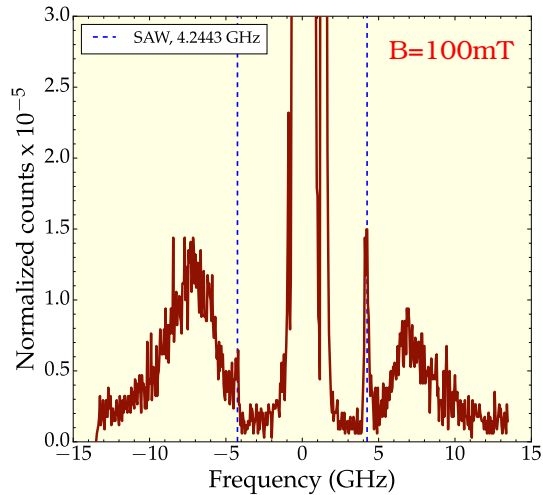


Figure 5.33: BLS spectrum of SWs with continuously emitted SAW at 100mT.



Recall also, that the magneto-elastic energy is a product of *strain* and *magneto-elastic coefficient*. To efficiently modify this energy, even with poor magneto-elastic coefficients of the material, one should be able to apply large strain. Applying such high acoustics it is not an easy task due to the impedance mismatch between the IDTs and the excitation source. Also, as was shown in the chapter 4, section 4.4, introducing a thin film in the SAW propagation path resulted in a 30 dB loss in the signal amplitude.

Since we could not observe the interaction with the thermal spin waves and also due to the lack of time, we did not perform the measurements, using the RF antennas (device, shown in the fig. 5.30). The preliminary measurements were not conclusive and require further investigations.

5.4 Conclusion

Although many samples were studied in this thesis (table 5.1), not to be redundant we focus only on 58nm thick [32m0206](#) $\text{Fe}_{0.8}\text{Ga}_{0.2}$ thin film, that was extensively studied (4 different SAW frequencies, both propagation directions). Several general features could be observed, that are also present in other studied samples. That is, one can distinguish the acoustic behavior at low and high fields.

At low fields both magnetic domains and single domain rotation are present. This regime is characterized by the presence of **magneto-elastic hysteresis** and thus, an irreversible acoustic behavior. Micro magnetic simulations are required to explain the physics and we do not pursue it in this thesis.

Our interest lies in the reversible acoustic behavior at high fields, that shows clear dependence on the direction and intensity of the applied field and could be indirectly compared to the torque, discussed in the chapter 2. This is indeed very relevant for the extraction of the material constants, both magneto-elastic and magneto-crystalline anisotropy coefficients, as will be shown in the chapter 6. The results for a thin film of pure iron, [32m0215](#) Fe will also be presented in the chapter 6 in the frame of comparison between theory and experiment.

We briefly discussed the preliminary measurements, performed with the BLS technique in order to check the resonant interaction between the SWs and SAWs in the thin [32m0279](#) $\text{Fe}_{0.8}\text{Ga}_{0.2}$ film of 4nm. No such interaction was observed. This is attributed to the reduced magneto-elastic coefficients of the material, probably due to the interface effects, and to the small strain amplitude due to inefficient SAW excitation at high frequencies.

Chapter 6

Modeling the System

“Everything should be made as simple as possible, but not simpler”

A. Einstein

6.1 State of art of Theoretical Approaches

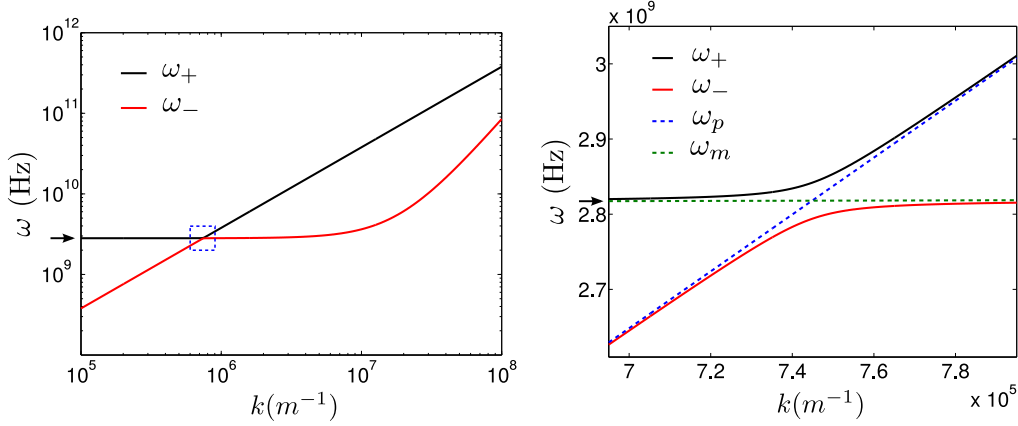
In the chapter 2 we considered the magnetization dynamics, triggered by surface acoustic waves, that is the effect of a propagating SAW *on* magnetization. We will now consider the effect of magnetization dynamics *on* a propagating SAW.

It is important to note that, since both magnetic and elastic systems are coupled, in other words magnons and phonons, a propagating wave in a ferromagnetic medium, possesses a mixed character and should be considered as a hybrid, rather than a purely magnetic or purely elastic wave. That is, in such a wave atomic displacements are accompanied with the precessing spins. The investigation of the *magneto-elastic waves* dates back to 1950s [26], [27]¹. C. Kittel proposed a theoretical treatment [26], based on the classical formalism, and derived the dispersion relation, as well as predicted the non-reciprocity, that is different phase velocity for counter rotating circularly polarized magneto-elastic waves. This effect was later observed experimentally by H. Matthews and R.C. LeCraw [142] and also seen in our experiments, as discussed in the chapter 5, section 5.2.2. Following Kittel, A. Kamra *et al.* revisited and extended further the calculations [141]. The authors derive the dispersion relation for a bulk ferromagnetic material, in which elastic waves are injected by means of a non-magnetic transducer. The obtained dispersion is represented in the figure below².

¹The source in english is available on <http://www.jetp.ac.ru/cgi-bin/e/index/e/8/1/p157?a=list>. The authors propose a phenomenological treatment of coupled magneto-elastic waves in ferromagnets and ferrites.

²Note that, for the configurations considered in the article, the coupling occurs, even when the saturation magnetization is perpendicular or parallel to the propagation wave vector. But this is true only in the case of *shear elastic waves*, as discussed in the chapter 2 and noted by the authors.

Figure 6.1: Calculated dispersion curve for magneto-elastic waves, from [141].



As can be seen from the figure, the coupling manifests itself strongly only *at resonance*, that is when wavelengths and frequencies match, resulting in the *anti-crossing* of the dispersion curve. In this region the phononic and magnonic excitations hybridize. Far away from the resonance, the branches correspond more to pure dispersions of phonons and magnons. From a theoretical point of view this implies, that working below the resonance, we can consider a propagating SAW as being purely Rayleigh wave, that possesses the corresponding strain components, ε_{11} , ε_{13} , ε_{33} , as described in the chapter 1, section 1.1. In principle, being at resonance implies the existence of all strain components, some non-existing in the Rayleigh wave. Such theoretical treatment for a magneto-elastic wave propagation was proposed by A.K. Ganguly *et al.* [89], [135], as will be discussed later. In our calculations, we thus assume, that a propagating SAW is modified by the magneto-elasticity of the medium, but keeps its purely “elastic character”.

In what follows we discuss the existing theoretical approaches, that treat the propagation of SAWs in a ferromagnetic medium. We do not intend to give an exhaustive state of the art of the literature. The following description rather shows possible ways to treat the problem.

We start with a simpler approach, coined by Dreher *et al.* as a “backaction approach” [17], used to study the elastically driven ferromagnetic resonance. Backaction in the sense, that a propagating SAW triggers magnetization dynamics and as a consequence, its propagation is modified. Thus, in this approach authors keep the “elastic character” of the wave, even at resonance. To track the modification, one should consider a system of coupled equations, that is displacement components, $u_i(t)$ and dynamic magnetization components, $m_i(t)$. The displacement components are coupled to the magnetization through stress, that can be expressed as a derivative of the total energy density, F with respect to strain:

$$\rho \frac{\partial^2 u_i}{\partial t^2} = \frac{\partial \sigma_{ij}}{\partial x_j} \quad (6.1)$$

with

$$\begin{cases} \sigma_{ii} &= \frac{\partial F}{\partial \varepsilon_{ii}} \\ \sigma_{ij} &= \frac{1}{2} \frac{\partial F}{\partial \varepsilon_{ij}} \quad i \neq j \end{cases} \quad (6.2)$$

Thus, *magneto-elastic terms* will enter the displacement expressions. Dynamic magnetization components are, in turn, expressed in terms of SAW strain components (as was shown in chapter 2, in our case in spherical coordinates, so for angular variations $\delta\theta(t)$, $\delta\varphi(t)$). Obtaining coupled equations, the subsequent procedure would be described in the chapter 1, section 1.1.3 or in the appendix B, including the dynamic magnetization components. This necessarily increases the complexity of the approach. For simplicity the authors of [17] treat the acoustic modes, described by eq. (6.1), separately. Furthermore, the following assumptions are made:

- (i) The elastic wave is assumed to be purely *longitudinal*. The obtained expression, that permits to calculate the dispersion of the perturbed longitudinal wave, reads:

$$\left(\omega^2 - v_1^2 k^2 \left[1 - F \cdot \underbrace{\frac{b_1^2}{v_1^2 \mu_0 \rho} \cdot f(B_{app}, \theta_0, \phi_0)}_{\text{magneto-elastic contribution}} \right] \right) u_x = 0$$

where $v_1^2 = \frac{c_{11}}{\rho}$ is the sound velocity in the absence of magneto-elastic coupling, b_1 magneto-elastic constant, ρ material density, $f(B_{app}, \theta_0, \phi_0)$ a function of the applied field intensity, direction and magnetization equilibrium orientation and F is described below.

- (ii) To take into account film-on-substrate structure, the authors introduced a *dilution factor*³, $F = \frac{d}{\lambda_{saw}}$, where d is the film thickness. The dilution factor reduces the magneto-elastic contribution to correspond to the real physical picture, in which only a small fraction of the total volume, penetrated by SAW, is ferromagnetic.

This approach was also employed by L. Thevenard *et al.* where a more rigorous calculation was undertaken [18]. The authors follow the same procedure, as described in chapter 1, section 1.1.3, taking into account the magneto-elasticity, which enters via eq. (6.2). They determine solutions for the penetration depth and wave vector and from the mechanical boundary conditions, they obtain:

$$\left(c_{44} - \rho \frac{\omega^2}{k^2} \right) \left(c'_{11} c'_{33} - c'^2_{13} - c'_{33} \rho \frac{\omega^2}{k^2} \right) = c'_{33} c_{44} \left(c'_{11} - \rho \frac{\omega^2}{k^2} \right) \left(\rho \frac{\omega^2}{k^2} \right)^2$$

where the primed elastic constants, c'_{ij} are modified by *the magneto-elastic contribution*.

³The term in the original article is “filling” factor. We rephrase it to represent the physical meaning, from our view point, in a more appropriate way.

Solving this equation for the wave vector k numerically yields the solution, the real part of which is used to compute the relative change in SAW velocity, $\frac{\Delta V}{V}$ and imaginary part to compute the change in the attenuation, $\Delta\Gamma$.

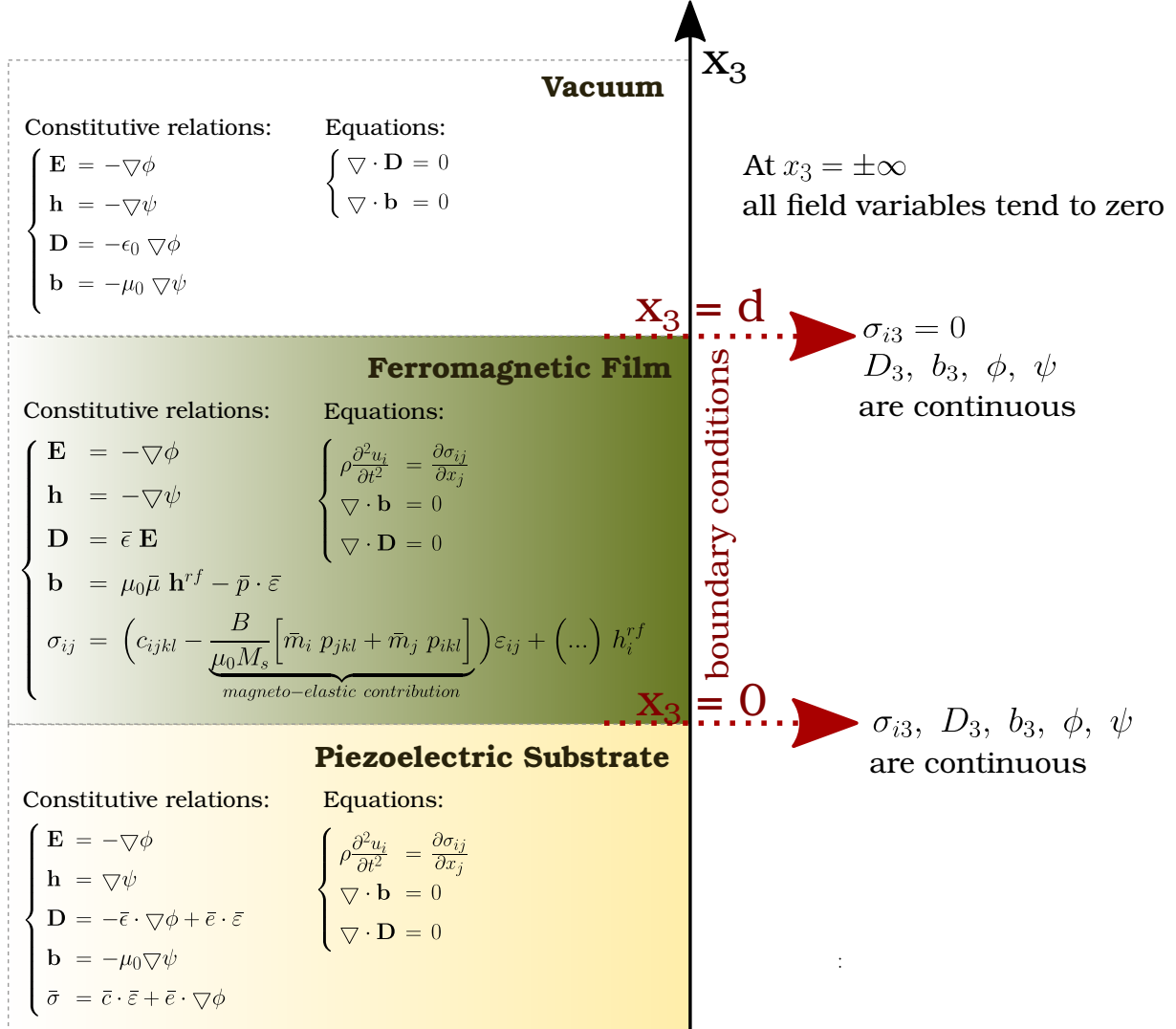
So the essence of the “backaction approach” is to consider an elastic wave, that is modified by the magneto-elastic coupling, i.e. modification of the *elastic constants* of the medium. To account for the real physical structure, that is film-on-substrate, a dilution factor is needed. Note that the drawback of the dilution factor is that it *depends* on the SAW frequency.

A way more rigorous approach was proposed by A.K. Ganguly *et al.* [89], [135]. The essence of this approach is represented in the fig. 6.2. The authors consider a layered stack in vacuum, that includes both ferromagnetic film and a piezoelectric substrate. There are several equations to be solved for each layer, i.e. Maxwell’s equations and the equations of motion, subject to mechanical and electro-magnetic boundary conditions. The constitutive relations give the expressions for electric \mathbf{E} , magnetic \mathbf{h} fields, dielectric displacement \mathbf{D} , magnetic induction \mathbf{b} and stress $\bar{\sigma}$. These quantities are coupled through magneto-elasticity in the ferromagnetic medium and piezoelectricity in the substrate, as can be seen from the expressions. To compute the dispersion relation for a wave, propagating in such a layered medium, the authors employ a transfer matrix method, proposed by Fahmy and Adler [143], [144]. This method was developed for general multi-layered structures by A.H. Fahmy, during his PhD [145] (1973). In this approach the system of equations together with the boundary conditions is written as a first-order matrix differential equation. Numerically each layer is characterized by a transfer matrix, containing the material characteristics (i.e. elastic, magneto-elastic, MCA constants etc.). The stack of layers is represented by one matrix, obtained by multiplying the matrices of the successive layers [146]. As can be seen, this approach is very rigorous, as it takes into account the real physical structure. Furthermore, both electromagnetic and mechanical boundary conditions are satisfied.

This approach was further extended by O. Bou Matar *et al.* [147], where the authors considered N-stack layered structure and the goal was to improve the method against numerical instabilities. A good review on the matrix techniques, used for modeling the ultrasonic waves propagation in multi-layers can be found in [148].

Another method, was presented by P.G. Gowtham *et al.*, which considers film-on-substrate structure, where ferromagnetic thin film is considered as a perturbation, that modifies boundary conditions on the SAW [149].

Figure 6.2: A schematic representation of the approach, used in [89], [135]. Notations: h^{rf} radio frequency applied h-field, \bar{p} magneto-elastic tensor, $\bar{\epsilon}$ dielectric tensor, \bar{e} piezoelectric tensor, \bar{c} elastic constants tensor, d film thickness.



The table below summarizes some of the existing approaches and their pros and cons to study the SAW propagation in a ferromagnetic media.

In this thesis three theoretical/phenomenological approaches were considered, based on [52] (“anelastic approach”), [150] (“film-on-substrate” approach, simplified) and [135] (“film-on-substrate” approach, rigorous). Due to the lack of time, we could conclude only the first two, while we are still working on the third approach. It is very useful when one cannot ignore the piezoelectricity, for example in the case of LiNbO_3 , which is a strongly piezoelectric material, or a stack of layers is considered.

In what follows we present the approaches, used to model our system.

Table 6.1: In-exhaustive list of different theoretical approaches, that study the problematics of the SAW propagation in a ferromagnetic medium. Notations: electro-magnetic boundary conditions, EM bc.

Approach	Source	Cons	Pros
"Backaction"	[17], [18]	Frequency dependent dilution factor	A simpler qualitative modeling
Perturbative	[149]	-	Simplified, rigorous
Film-on-substrate	[89], [135], [147]	Heavy	Rigorous: - Real physical structure - Mechanical and EM bc are satisfied - Piezoelectricity is taken into account - All strain components are taken into account

6.2 Anelastic approach

We start with a very approximate approach that gives a simpler physical picture. It comes from the fact, that in reality applied external stress might result in a non-instantaneous strain (the effect being linear), that is the system takes time to respond. Such behavior is referred to as *anelastic*. For illustration, we present different types of mechanical behavior, classified according to stress-strain relation, as summarized in [52] (p.3):

Table 6.2: Classification of different mechanical behaviors according to stress-strain relation, from [52].

Behaviour	Unique equilibrium (complete recoverability)	Instantaneous	Linear
Ideal elasticity	Yes	Yes	Yes
Non linear elasticity	Yes	Yes	No
Instantaneous plasticity	No	Yes	No
Anelasticity	Yes	No	Yes
Linear viscoelasticity	No	No	Yes

where unique equilibrium means that, for each level of an applied stress there exists a *unique* equilibrium value of strain.

In this frame, consider⁴ a simple time-dependent deformation, for example a uniaxial stress, $\sigma = \sigma_0 e^{i\omega t}$. The resulting strain would be of the form $\varepsilon = \varepsilon_0 e^{i(\omega t - \phi(\omega))}$, where $\phi(\omega)$ is defined as the *phase lag*. Taking the stress-strain ratio yields:

$$\frac{\sigma}{\varepsilon} = \frac{\sigma_0}{\varepsilon_0} e^{i\phi(\omega)} = M^*(\omega) = M_{\text{Re}} + iM_{\text{Im}} \simeq M_{\text{Re}}(1 + i\phi) \quad (6.3)$$

where $M^*(\omega)$ is *complex elastic modulus*. The phase lag can be expressed as the ratio of imaginary and real parts, $\phi \simeq \frac{M_{\text{Im}}}{M_{\text{Re}}}$, provided that $\phi \ll 1$. Consider now an elastic wave,

⁴The following description is based on [52], ch.1, sections 1.3 and 1.6.

propagating along the x direction , the one-dimensional wave equation is given by (see section 1.1.2):

$$\rho \frac{\partial^2 u}{\partial t^2} = M^* \frac{\partial^2 u}{\partial x^2} \quad (6.4)$$

where the real elastic modulus is replaced by a complex one to account for anelasticity, as justified in [52] (p.25).

Solution of the above equation can be given in a form of a damped plane wave, that is $u = u_0 e^{-\Gamma x} e^{i\omega(t - \frac{x}{v})}$, where Γ stands for attenuation and has units of reciprocal length. Plugging the solution into eq. (6.4) yields:

$$-\rho\omega^2 = M^* \left(\Gamma^2 + 2i \frac{\omega\Gamma}{v} - \frac{\omega^2}{v^2} \right) \simeq M^* \left(2i \frac{\omega\Gamma}{v} - \frac{\omega^2}{v^2} \right)$$

Since we consider the attenuation to be small, the Γ^2 term should be negligible with respect to the ratio $\frac{\omega^2}{v^2}$. Using the relation, given by eq. (6.3), we re-arrange the above equation:

$$-\rho\omega^2 = -M_{\text{Re}} \left(\frac{\omega^2}{v^2} + \frac{2\phi\omega\Gamma}{v} \right) + iM_{\text{Re}} \left(\frac{2\omega\Gamma}{v} - \frac{\phi\omega^2}{v^2} \right)$$

Equating the real and imaginary parts yields: $(\frac{\omega^2}{v^2} \gg \frac{2\phi\Gamma\omega}{v})$

$$\begin{cases} v^2 = \frac{1}{\rho} M_{\text{Re}} \\ \Gamma = \frac{\phi\omega}{2v} = \frac{\pi\phi}{\lambda} \simeq \frac{\pi}{\lambda} \frac{M_{\text{Im}}}{M_{\text{Re}}} \end{cases} \quad (6.5)$$

From this it is possible to relate the velocity and attenuation of a propagating plane wave to the complex elastic modulus of the medium. We thus need to show, that in the case of a propagating Rayleigh wave, the stress can be expressed in terms of *complex elastic constants* and if it does, we can employ the above relations to compute the change in velocity and attenuation of the SAW, as will be shown later.

Let us thus consider a ferromagnetic film on a semi-infinite elastic substrate, as represented in the fig. 6.3. In our experiments, as described in chapter 5, SAW is propagation along $[110]$ or $[1\bar{1}0]$ direction. To describe our system we define a new set of coordinates, $(x'_1 \parallel [110], x'_2 \parallel [1\bar{1}0], x'_3 \parallel [001])$, obtained by rotating the old coordinate system around x_3 by $\frac{\pi}{4}$ (fig. 6.4). The “'” sign stands for the new basis.

We now *assume*, that the film experiences strain, imposed by SAW, identical to the one, when SAW propagates in a pure elastic semi-infinite solid, that is

$$(e'_{ij})(t) = \begin{pmatrix} e'_{11}(t) & 0 & e'_{13}(t) \\ 0 & 0 & 0 \\ e'_{13}(t) & 0 & e'_{33}(t) \end{pmatrix}$$

Figure 6.3: SAW propagation in film /substrate structure.

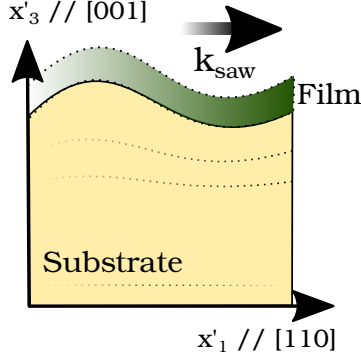
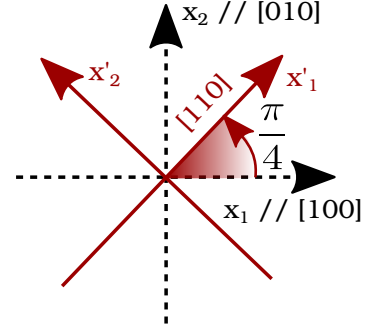


Figure 6.4: New coordinate system is obtained by rotation of the old one by $\frac{\pi}{4}$ around the [001] direction.



Thus at the surface, as discussed in the section 1.1.2, shear strain component vanishes, $e'_{13}(t) = 0$ and from the boundary conditions on σ'_{i3} , we have:

$$\sigma'_{33} = c'_{33kl} e'_{kl}(t) = c'_{31} e'_{11}(t) + c_{33} e'_{33}(t) = 0$$

where we use the c' notation to represent **the elastic constants of the substrate in the new basis**. Under this assumption, the transverse and shear strain components can be related via elastic constants. As discussed in the section 2.3 of the chapter 2, shear component vanishes at the surface in the case of a wave, propagating in a semi-infinite elastic solid. For a thin film of a nanometer thickness our assumption, can thus be re-formulated as follows:

Assumption №1
Following holds for the film

$$e'_{33}(t) = -\frac{c'_{13}}{c'_{33}} e'_{11}(t)$$

In order to express the elastic constants for a **ferromagnetic film**, we compute the stress components, using the derivative of the total energy density (appendix C) with respect to strain ⁵ [84]:

$$\sigma_{ii} = \frac{\partial F}{\partial \varepsilon_{ii}}, \quad \sigma_{ij} = \frac{1}{2} \frac{\partial F}{\partial \varepsilon_{ij}} \quad i \neq j \quad (6.6)$$

⁵Note that, in [84] a $\frac{1}{2}$ factor is missing for σ_{ij} . Stress components can be computed either from the Hooke's law (eq. (1.7)) or from the derivative of the elastic energy density with respect to strain. The $\frac{1}{2}$ is necessary to obtain the same expression in both cases.

We obtain in the standard basis:

$$\left\{ \begin{array}{l} \sigma_{11} = B_1(\sin^2 \theta \cos^2 \varphi - \frac{1}{3}) + \widehat{c}_{11} \varepsilon_{11} + \widehat{c}_{12} (\varepsilon_{22} + \varepsilon_{33}) \\ \sigma_{22} = B_1(\sin^2 \theta \sin^2 \varphi - \frac{1}{3}) + \widehat{c}_{11} \varepsilon_{22} + \widehat{c}_{12} (\varepsilon_{11} + \varepsilon_{33}) \\ \sigma_{33} = B_1(\cos^2 \theta - \frac{1}{3}) + \widehat{c}_{11} \varepsilon_{33} + \widehat{c}_{12} (\varepsilon_{11} + \varepsilon_{22}) \\ \sigma_{12} = \frac{B_2}{4} \sin^2 \theta \sin(2\varphi) + 2\widehat{c}_{44} \varepsilon_{12} \\ \sigma_{13} = \frac{B_2}{4} \sin(2\theta) \cos(\varphi) + 2\widehat{c}_{44} \varepsilon_{13} \\ \sigma_{23} = \frac{B_2}{4} \sin(2\theta) \sin(\varphi) + 2\widehat{c}_{44} \varepsilon_{23} \end{array} \right.$$

The stress and strain components can be expressed in the new basis, following the transformation rules, where γ is the transformation matrix⁶ :

$$\left\{ \begin{array}{l} \varepsilon_{ij} = \gamma_{\mu i} \gamma_{\nu j} \varepsilon'_{\mu\nu} \\ \sigma'_{\mu\nu} = \gamma_{\mu i} \gamma_{\nu j} \sigma_{ij} \end{array} \right. \quad \gamma = \begin{pmatrix} \frac{1}{\sqrt{2}} & \frac{1}{\sqrt{2}} & 0 \\ -\frac{1}{\sqrt{2}} & \frac{1}{\sqrt{2}} & 0 \\ 0 & 0 & 1 \end{pmatrix} \quad (6.7)$$

We obtain after some algebra:

$$\left\{ \begin{array}{l} \sigma'_{11} = \widehat{c}'_{11} \varepsilon'_{11} + \widehat{c}'_{12} \varepsilon'_{12} + \widehat{c}'_{13} \varepsilon'_{33} + \frac{B_1}{2} (\sin^2 \theta - \frac{2}{3}) + \frac{B_2}{4} \sin^2 \theta \sin(2\varphi) \\ \sigma'_{22} = \widehat{c}'_{12} \varepsilon'_{11} + \widehat{c}'_{11} \varepsilon'_{22} + \widehat{c}'_{13} \varepsilon'_{33} + \frac{B_1}{2} (\sin^2 \theta - \frac{2}{3}) - \frac{B_2}{4} \sin^2 \theta \sin(2\varphi) \\ \sigma'_{33} = \widehat{c}'_{33} \varepsilon'_{33} + \widehat{c}'_{13} (\varepsilon'_{11} + \varepsilon'_{22}) + B_1 (\cos^2 \theta - \frac{1}{3}) \\ \sigma'_{12} = 2\widehat{c}'_{66} \varepsilon'_{12} - \frac{B_1}{2} \sin^2 \theta \cos(2\varphi) \\ \sigma'_{13} = \frac{B_2}{4} \sin(2\theta) \sin(\varphi + \frac{\pi}{4}) + 2\widehat{c}'_{44} \varepsilon'_{13} \\ \sigma'_{23} = \frac{B_2}{4} \sin(2\theta) \sin(\varphi - \frac{\pi}{4}) + 2\widehat{c}'_{44} \varepsilon'_{23} \end{array} \right. \quad (6.8)$$

with \widehat{c}'_{ij} elastic constants **of the ferromagnetic film** in the new basis:

$$\left\{ \begin{array}{l} \widehat{c}'_{11} = \frac{1}{2}\widehat{c}_{11} + \frac{1}{2}\widehat{c}_{12} + \widehat{c}_{44} \\ \widehat{c}'_{12} = \frac{1}{2}\widehat{c}_{11} + \frac{1}{2}\widehat{c}_{12} - \widehat{c}_{44} \\ \widehat{c}'_{13} = \widehat{c}_{12} \\ \widehat{c}'_{33} = \widehat{c}_{11} \\ \widehat{c}'_{44} = \widehat{c}_{44} \\ \widehat{c}'_{66} = \frac{1}{2}\widehat{c}_{11} - \frac{1}{2}\widehat{c}_{12} \end{array} \right. \quad (6.9)$$

As discussed in the chapter 2, SAW triggers magnetization dynamics and the deviations from the equilibrium position are assumed to be small. We thus can Taylor-expand the stress components (eq. (6.8)) up to the first order around the equilibrium position, $(\bar{\theta}, \bar{\varphi}, \bar{\varepsilon}_{ij})$. Taking

⁶Rows represent the coordinates in the old basis.

$\bar{\theta} = \frac{\pi}{2}$, i.e. in-plane magnetization and noticing that, at equilibrium the *static* part of the stress vanishes for it is the energy minimum ($\left. \frac{\partial F}{\partial \varepsilon_{ij}} \right|_{\bar{\varepsilon}_{ij}} = 0$), we can express

$$\left\{ \begin{array}{l} \sigma'_{11}(t) = \left(\frac{\hat{c}_{11}}{2} + \frac{\hat{c}_{12}}{2} + \hat{c}_{44} - \hat{c}_{12} \frac{c_{12}}{c_{11}} \right) e'_{11}(t) + \frac{B_2}{2} \cos(2\bar{\varphi}) \delta\varphi(t) \\ \sigma'_{22}(t) = \left(\frac{\hat{c}_{11}}{2} + \frac{\hat{c}_{12}}{2} + \hat{c}_{44} - \hat{c}_{12} \frac{c_{12}}{c_{11}} \right) e'_{11}(t) - \frac{B_2}{2} \cos(2\bar{\varphi}) \delta\varphi(t) \\ \sigma'_{33}(t) = \left(\hat{c}_{12} - \hat{c}_{11} \frac{c_{12}}{c_{11}} \right) e'_{11}(t) \\ \sigma'_{12}(t) = B_1 \sin(2\bar{\varphi}) \delta\varphi(t) \\ \sigma'_{13}(t) = 2\hat{c}_{44} e'_{13}(t) - \frac{B_2}{2} \sin(\bar{\varphi} + \frac{\pi}{4}) \delta\theta(t) \\ \sigma'_{23}(t) = -\frac{B_2}{2} \sin(\bar{\varphi} - \frac{\pi}{4}) \delta\theta(t) \end{array} \right. \quad (6.10)$$

where we used the assumption №1 to replace the transverse strain term, $e'_{33}(t)$. From the equations above it is clear, that the stress components are *modified* by the magneto-elastic coupling terms, proportional to angular variations of magnetization. The latter are expressed in terms of the SAW strain components, $e'_{ij}(t)$ and are, a priori, complex numbers. Thus, one can express the stress components in terms of *complex* elastic constants and this is what we were looking for. To proceed further another assumption should be made.

Following the assumption №1, a ferromagnetic film experiences the same strain, that exists in SAW, propagating in a semi-infinite elastic medium. In such a case, at the surface the shear strain component vanishes, as already discussed in the section 2.3. Thus, in order to correlate the SAW velocity and the complex elastic constant, it is sufficient to consider only longitudinal strain. Therefore, the next assumption is the following

Assumption №2
Change in SAW velocity is related to the σ_{11} component

Justification of this assumptions is possible, however, a posteriori, using a more sophisticated model, as will be seen from the next section (section 6.3).

From the above, we need to express the σ_{11} in terms of a complex elastic constant. The in-plane angular variation, $\delta\varphi(t)$ is given by:

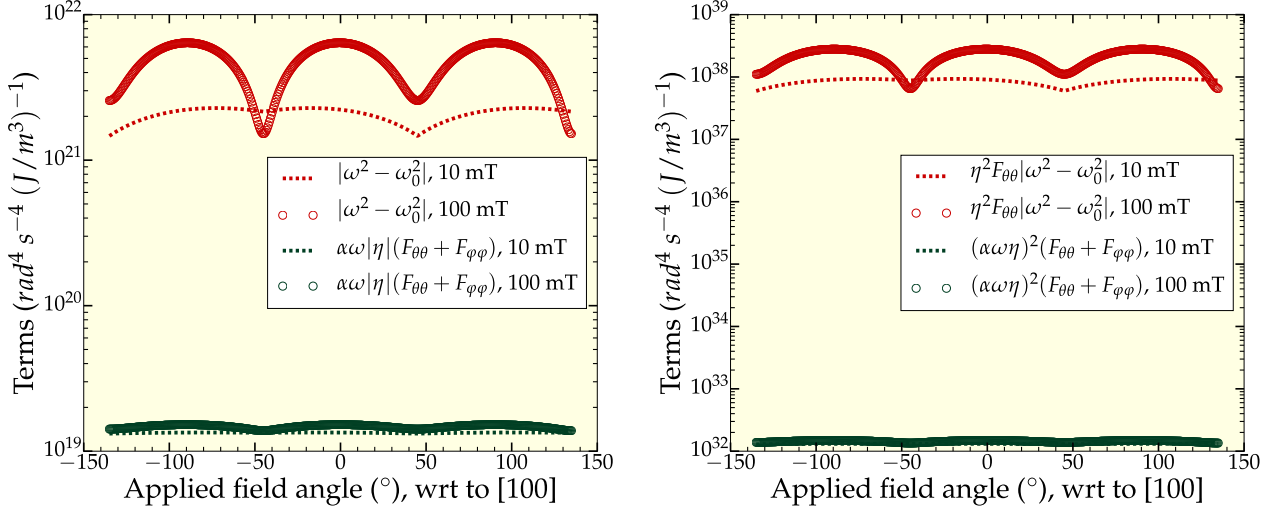
$$\delta\varphi(t) = \frac{1}{2} \frac{(\eta^2 F_{\theta\theta} + i\alpha\omega\eta) B_2 \cos(2\bar{\varphi})}{(\omega^2 - \omega_0^2) - i\alpha\omega \eta (F_{\theta\theta} + F_{\varphi\varphi})} e'_{11}(t)$$

Re-arranging yields:

$$\delta\varphi(t) = \left[\frac{\eta^2 F_{\theta\theta} (\omega^2 - \omega_0^2) - (\alpha\omega\eta)^2 (F_{\theta\theta} + F_{\varphi\varphi})}{(\omega^2 - \omega_0^2)^2 + (\alpha\omega\eta)^2 (F_{\theta\theta} + F_{\varphi\varphi})^2} \frac{B_2}{4} \cos(2\bar{\varphi}) + \right. \\ \left. i \frac{\alpha\omega\eta (\omega^2 + \eta^2 F_{\theta\theta}^2)}{(\omega^2 - \omega_0^2)^2 + (\alpha\omega\eta)^2 (F_{\theta\theta} + F_{\varphi\varphi})^2} \frac{B_2}{2} \cos(2\bar{\varphi}) \right] e'_{11}(t) \quad (6.11)$$

In the section 2.3.2 of the chapter 2 we showed that $\alpha\omega\eta(F_{\theta\theta} + F_{\varphi\varphi})$ term in the denominator of the above expression is negligible with respect to $(\omega^2 - \omega_0^2)$ (fig. 6.5a). Also the term, containing $(\alpha\omega\eta)^2$, in the numerator of the real part of the expression is negligible with respect to its counterpart, as can be seen from the fig. 6.5b.

Figure 6.5: Different terms of the eq. (6.11) vs the applied field angle, at different field intensity. Numerical values of the damping parameter and SAW frequency are 0.01 and 0.833 MHz, respectively.



(a) Terms in the denominator of eq. (6.11).

(b) Terms in the numerator of the real part of eq. (6.11).

We thus can simplify:

$$\delta\varphi(t) = \underbrace{\left[\frac{\eta^2 F_{\theta\theta}}{(\omega^2 - \omega_0^2)} \frac{B_2}{4} \cos(2\bar{\varphi}) \right]}_{\delta\varphi_{\text{Re}}} + i \underbrace{\left[\frac{\alpha\omega\eta(\omega^2 + \eta^2 F_{\theta\theta}^2)}{(\omega^2 - \omega_0^2)} \frac{B_2}{2} \cos(2\bar{\varphi}) \right]}_{\delta\varphi_{\text{Im}}} e'_{11}(t) \quad (6.12)$$

Given eq. (6.12), the longitudinal stress component can be expressed as:

$$\sigma'_{11}(t) = \underbrace{\left[\left(\frac{\hat{c}_{11}}{2} + \frac{\hat{c}_{22}}{2} + \hat{c}_{44} - \hat{c}_{12} \frac{c_{12}}{c_{11}} + \frac{B_2}{2} \cos(2\bar{\varphi}) \delta\varphi_{\text{Re}} \right)}_{\hat{C}'_{\text{Re}}} + i \underbrace{\left[\frac{B_2}{2} \cos(2\bar{\varphi}) \delta\varphi_{\text{Im}} \right]}_{\hat{C}'_{\text{Im}}} \right]}_{\left(\hat{C}'_{\text{Re}} + i \hat{C}'_{\text{Im}} \right)} e'_{11}(t) = \left(\hat{C}'_{\text{Re}} + i \hat{C}'_{\text{Im}} \right) e'_{11}(t) \quad (6.13)$$

Therefore σ'_{11} is complex, as expected, and this is the case of *retarded elasticity*. Note that, if damping is neglected, the stress components can no longer be expressed in terms of complex elastic constants. It is thus the magnetic damping, that accounts for *anelastic* behavior.

Using eq. (6.12) we can explicitly express the real, \widehat{C}'_{Re} and imaginary, \widehat{C}'_{Im} parts of the elastic constant of the ferromagnetic medium:

$$\widehat{C}'_{\text{Re}} = \frac{\widehat{c}_{11}}{2} + \frac{\widehat{c}_{22}}{2} + \widehat{c}_{44} - \widehat{c}_{12} \frac{c_{12}}{c_{11}} + \underbrace{B_2^2 \cos^2(2\bar{\varphi}) \frac{\eta^2 F_{\theta\theta}}{4(\omega^2 - \omega_0^2)}}_{\text{magneto-elastic contribution}} \quad (6.14)$$

$$\widehat{C}'_{\text{Im}} = B_2^2 \cos^2(2\bar{\varphi}) \frac{\alpha\omega\eta(\omega^2 + \eta^2 F_{\theta\theta}^2)}{4(\omega^2 - \omega_0^2)} \quad (6.15)$$

Furthermore, the obtained expression, eq. (6.14) shows, that the elastic constants of the ferromagnetic film are modified by the magneto-elastic coupling with a very clear dependency on the field direction and intensity.

Note that, as in the case of the computation of the torque density (section 2.4) for SAW propagating along [110], we also find the sensitivity to the B_2 magneto-elastic coefficient. This point is very important and will be discussed in the section 6.4.

After obtaining the expression for the longitudinal stress component in terms of complex elastic constants of the film, the last assumption is to be made to account for the film-on-substrate structure, that is to take the film thickness into account, since the change of the SAW velocity originates within the film. We define **effective elastic constants of the structure** as the sum of the elastic constants of the substrate and the film, taking into account film thickness and SAW penetration depth:

* **Substrate**, GaAs: elastic constants

$$C' = C'_{\text{Re}} + i C'_{\text{Im}} = C'_{\text{Re}} \quad (6.16)$$

* **Ferromagnetic film**, $\text{Fe}_{0.8}\text{Ga}_{0.2}$: complex elastic constants, given by eq. (6.13)

$$\widehat{C}' = \widehat{C}'_{\text{Re}} + i \widehat{C}'_{\text{Im}} \quad (6.17)$$

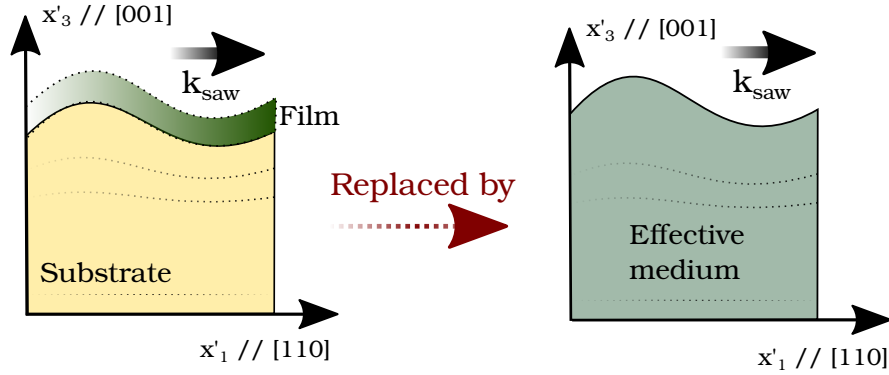
* **Film-on-substrate: effective elastic constants**

Assumption №3

$$C'^{eff} = \frac{(\lambda - d)C' + d\widehat{C}'}{\lambda} \simeq C' + \frac{d}{\lambda}\widehat{C}' = (C' + \frac{d}{\lambda}\widehat{C}'_{\text{Re}}) + i \frac{d}{\lambda}\widehat{C}'_{\text{Im}}$$

where d , λ are the film thickness and SAW wave length, respectively. Under this assumption the medium is transformed into an effective medium with *effective* elastic constants, as illustrated in the figure below.

Figure 6.6: Original and assumed structures.



The ratio $\frac{d}{\lambda}$ is referred to as a *dilution factor*, as discussed in the section 6.1, and takes into account the film thickness with respect to the SAW penetration depth, which is of the order of one wavelength.

6.2.1 Expressions for $\frac{\Delta V}{V}$

Let us go back to the assumption N°2. As discussed previously, since the shear strain component vanishes, we only consider the velocity changes related to the longitudinal strain component. From the assumption N°3 we have for the real part of the effective elastic constant, $C'_{\text{Re}}{}^{\text{eff}} = C' + \frac{d}{\lambda} \widehat{C}'_{\text{Re}}$:

$$C'_{\text{Re}}{}^{\text{eff}} = C' + \frac{d}{\lambda} \widehat{C}'_{\text{Re}}$$

The velocity of a longitudinal wave in the effective medium is given by:

$$\rho V_L^2 = C'_{\text{Re}}{}^{\text{eff}}$$

where ρ is the effective medium density. Thus:

$$d(\ln V_L^2) = d\left(\frac{\ln C'_{\text{Re}}{}^{\text{eff}}}{\rho}\right)$$

or

$$\frac{\Delta V_L}{V_L} = \frac{1}{2} \frac{\Delta C'_{\text{Re}}{}^{\text{eff}}}{C'_{\text{Re}}{}^{\text{eff}}} \quad (6.18)$$

Note that the substrate elastic constant, C' is independent of the applied field, thus $\Delta C'_{\text{Re}}{}^{\text{eff}} = \frac{d}{\lambda} \Delta \widehat{C}'_{\text{Re}}$. Since $\frac{d}{\lambda}$ is small, we have $C'_{\text{Re}}{}^{\text{eff}} \approx C'$, so we obtain:

$$\frac{\Delta V_L}{V_L} = \frac{d}{2\lambda} \frac{\Delta \widehat{C}'_{\text{Re}}}{C'} \quad (6.19)$$

Note that, these are velocity variations of a *longitudinal wave*, propagating in an effective medium. A priori, we cannot identify them with the velocity variations of the Rayleigh wave. However, a more sophisticated approach, presented in the section 6.3.3 shows, that *the variation of the Rayleigh velocity are dominated by the longitudinal velocity*. Furthermore the computed variations, using both approaches, are of the same order of magnitude, as will be seen in the section 6.4.1.

Analytically it is possible to compute the SAW attenuation, using eq. (6.5). However, we could not reproduce our experimental data with this analysis. As could be seen in the chapter 5, fig. 5.2 SAW is mostly attenuated in the low field region, that is where the magnetic domains are present.

6.3 Film-on-Substrate Approach

The approach, explored in this section is based on the previous work of G.W. Farnell and E.L. Adler, that considered propagation of elastic waves in a film-on-substrate structure [150]. As discussed in the section 1.1.2, to find the Rayleigh velocity, the general search procedure is the following:

- (i) We assume solutions of the equations of motion in terms of plane waves, exponentially decaying with depth.
- (ii) Plugging the assumed solutions into the equations of motion, we obtain a new equation, solving which yields the solutions for the penetration depth and wave vector.
- (iii) Linear combination of the obtained solutions should satisfy the boundary conditions for a certain value of the Rayleigh velocity. It is thus possible to deduce the latter from boundary conditions.

For a general case of a anisotropic film on a piezoelectric⁷ substrate, there exist a linear combination of four solutions for the substrate and of eight for the film [150]. That is, particle displacement, u_i and electric potential⁸, ϕ are written as a linear combination of partial waves with corresponding penetration depth and amplitude.

The calculations are greatly simplified, if one considers an *isotropic* film on an *isotropic* substrate, thus both being *non-piezoelectric*. In this case, following the above procedure, Farnell and Adler arrive to the system of linear equations, solvable iff determinant of the matrix, M represented below, vanishes. The Rayleigh velocity is thus a solution of the

⁷Piezoelectric materials lack center of symmetry and are by nature anisotropic [47], ch.2, p.110.

⁸Note that piezoelectric wave is the wave with four components: three mechanical displacements, u_i and electric potential, ϕ , that originates from the electric field, accompanying the elastic wave due to the piezoelectric effect.

equation $\det M = 0$.

$$M = \begin{pmatrix} b_5 & -1 & -b_5 & -1 & -b_c & 1 \\ -1 & -b_6 & -1 & b_6 & 1 & b_d \\ 1 - b_5^2 & 2b_6 & 1 - b_5^2 & -2b_6 & -r(1 - b_c^2) & -2rb_d \\ 2b_5 & -1 + b_5^2 & -2b_5 & -1 + b_5^2 & -2rb_c & r(1 - b_c^2) \\ 1 - b_5^2 e^{ikb_5h} & 2b_6 e^{ikb_6h} & (1 - b_5^2) e^{-ikb_5h} & -2b_6 e^{-ikb_6h} & 0 & 0 \\ 2b_5 e^{ikb_5h} & (-1 + b_5^2) e^{ikb_6h} & -2b_5 e^{-ikb_5h} & (-1 + b_5^2) e^{-ikb_6h} & 0 & 0 \end{pmatrix} \quad (6.20)$$

where h is the film thickness and $b_{i \in [5,6,c,d]}$ terms are defined as:

$$\begin{cases} b_5 = i\sqrt{1 - (v/\widehat{v}_T)^2} \\ b_6 = i\sqrt{1 - (v/\widehat{v}_L)^2} \\ b_c = -i\sqrt{1 - (v/v_T)^2} \\ b_d = -i\sqrt{1 - (v/v_L)^2} \\ r = c_{44}/\widehat{c}_{44} \end{cases} \quad (6.21)$$

where the “ $\widehat{}$ ” notation is used to distinguish between parameters of the *film* and the substrate:

- * \widehat{v}_T velocity of a bulk transverse plane wave in the film material
- * \widehat{v}_L velocity of a bulk longitudinal plane wave in the film material
- * \widehat{c}_{44} elastic constant of the film
- * v_T velocity of a bulk transverse plane wave in the substrate material
- * v_L velocity of a bulk longitudinal plane wave in the substrate material
- * c_{44} elastic constant of the substrate

F&A calculations assume isotropic elastic film and isotropic elastic substrate. In principal, their approach could be extended to elastic cubic film and elastic cubic substrate. However, not to render the calculations heavier, we will employ their expressions. The eq. (6.20) is thus a starting point for us. We assume, that SAWs propagate in

Assumption №1
Isotropic film / Isotropic (non-piezoelectric) substrate

as represented in the fig. 6.7.

Justifications of this assumption can be discussed on the physical grounds. Neglecting piezo-electricity and considering isotropic media will definitely modify the absolute value of the Rayleigh velocity. But what we are interested in, is the *change* in velocity as a function of the magnetic field. We assume the field-induced *change* in velocity is *the same* for isotropic and anisotropic systems.

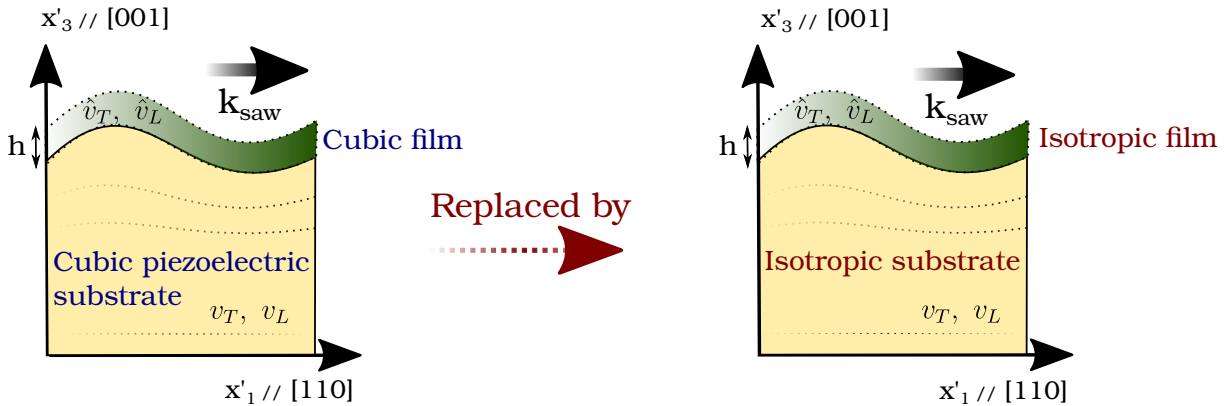
We thus need to compute the transverse, \hat{v}_T , v_T and longitudinal, \hat{v}_L , v_L velocities in the bulk film and bulk substrate materials, respectively. Since the film is ferromagnetic, we consider a *magneto-elastic wave*, that is the elastic wave, accompanied by a time-varying magnetic field, originating from the precessing magnetization. The transverse and longitudinal velocities of the film material are modified by the magneto-elastic coupling, as was already discussed in the previous section. Furthermore, we saw that, damping does not play a role in the variation of the velocity. Thus, for simplicity of the calculation we *assume* it can be neglected.

Assumption №2
Damping is neglected, $\alpha = 0$

Note that, the assumption that the medium is *elastically isotropic*, does not imply that it is *magnetically isotropic*. As an example, a ferromagnetic crystal can possess a cubic symmetry as a crystalline structure, but exhibits uniaxial magneto-crystalline anisotropy, that does not exhibit the four fold symmetry. We thus simplify the problem from the elastic point of view, while keeping the symmetry of the magnetic anisotropy intact.

We will now present the search procedure to obtain the transverse and longitudinal velocities in the bulk film material.

Figure 6.7: “Isotropisation” of the structure.



6.3.1 Ferromagnetic Film: Transverse Wave Velocity, \widehat{v}_T

To compute the **transverse wave** velocity, \widehat{v}_T in the film bulk material we employ the results, already presented in the chapter 2 and section 6.2. We consider a magneto-elastic wave, polarized along [001] and propagating along [110] (fig. 6.7), that has five components, assumed to be of the form:

$$\begin{cases} u'_1 = 0 \\ u'_2 = 0 \\ u'_3 = U_t e^{i(\omega t - kx'_1)} \\ \delta\theta = \Theta e^{i(\omega t - kx'_1)} \\ \delta\varphi = \Phi e^{i(\omega t - kx'_1)} \end{cases} \quad (6.22)$$

Since the components of such a wave exhibit the dependence on x_1 only, the strain matrix assumes the following values

in the new basis:

$$(e'_{ij}) = \begin{pmatrix} 0 & 0 & e'_{13} \\ 0 & 0 & 0 \\ e'_{13} & 0 & 0 \end{pmatrix} \quad (6.23)$$

in the standard basis:

$$(e_{ij}) = \begin{pmatrix} 0 & 0 & \frac{1}{\sqrt{2}}e'_{13} \\ 0 & 0 & \frac{1}{\sqrt{2}}e'_{13} \\ \frac{1}{\sqrt{2}}e'_{13} & \frac{1}{\sqrt{2}}e'_{13} & 0 \end{pmatrix} \quad (6.24) \quad \text{and}$$

the equations of motion give

$$\begin{cases} \widehat{\rho} \frac{\partial^2 u'_1}{\partial t^2} = \frac{\partial \sigma'_{11}}{\partial x'_1} \\ \widehat{\rho} \frac{\partial^2 u'_2}{\partial t^2} = \frac{\partial \sigma'_{12}}{\partial x'_1} \\ \widehat{\rho} \frac{\partial^2 u'_3}{\partial t^2} = \frac{\partial \sigma'_{13}}{\partial x'_1} \end{cases} \quad (6.25)$$

First, we need to explicitly express the strain components. This is done by deriving the total energy density of a ferromagnet with respect to strain (eq. (6.6)). Then we re-write the obtained expression in the new basis (eq. (6.8)) and make a Taylor expansion around the equilibrium position (eq. (6.10)). Using strain matrix, eq. (6.23) for this type of wave, we finally obtain:

$$\begin{cases} \widehat{\rho} \omega^2 u'_1 = ik \frac{B_2}{2} \cos(2\bar{\varphi}) \delta\varphi \\ \widehat{\rho} \omega^2 u'_2 = ik B_1 \sin(2\bar{\varphi}) \delta\varphi \\ \widehat{\rho} \omega^2 u'_3 = k^2 c_{44} u'_3 - \frac{ik}{2} B_2 \sin(\bar{\varphi} + \frac{\pi}{4}) \delta\theta \end{cases} \quad (6.26)$$

It follows, that $u'_1 \neq 0$, $u'_2 \neq 0$, that is in contradiction with what we assumed in the beginning. However, as will be seen further, $u'_3 \gg u'_1, u'_2$ and thus, the assumption is self-consistent.

The expressions for angular variations, $\delta\varphi$, $\delta\theta$ were previously derived in appendix D and using the eq. (6.23), (also eq. (6.24), so that the expressions for angular variations can be employed) we finally obtain

$$\begin{cases} \delta\theta = ik \frac{B_2}{2} \frac{\eta^2 F_{\varphi\varphi}}{\omega^2 - \omega_0^2} \sin\left(\bar{\varphi} + \frac{\pi}{4}\right) u'_3 \\ \delta\varphi = k\omega \frac{B_2}{2} \frac{\eta}{\omega^2 - \omega_0^2} \sin\left(\bar{\varphi} + \frac{\pi}{4}\right) u'_3 \end{cases} \quad (6.27)$$

Plugging eq. (6.27) into eq. (6.26) we find:

$$\hat{\rho}\omega^2 = k^2 \tilde{c}'_{44} \quad (6.28)$$

where \tilde{c}'_{44} is the *effective elastic constant*, modified by the magneto-elastic contribution:

$$\tilde{c}'_{44} = c'_{44} + \underbrace{\frac{B_2^2}{4} \frac{\eta^2 F_{\varphi\varphi}}{(\omega^2 - \omega_0^2)} \sin^2\left(\bar{\varphi} + \frac{\pi}{4}\right)}_{\text{magneto-elastic contribution}} \quad (6.29)$$

and finally the transverse velocity, $\hat{v}_T^2 = \left(\frac{\omega}{k}\right)^2$ can be expressed in terms of the modified elastic constant:

$$\hat{v}_T^2 = \frac{\tilde{c}'_{44}}{\hat{\rho}} \quad (6.30)$$

Self-consistency of the assumption

Following the obtained expression for the modified elastic constant, \tilde{c}'_{44} and using the eq. (6.27), we can explicitly express the displacement amplitude ratios:

$$\begin{cases} \frac{u'_1}{u'_3} = \frac{i}{\tilde{c}'_{44}} \frac{\omega\eta}{4(\omega^2 - \omega_0^2)} B_2^2 \cos(2\bar{\varphi}) \sin\left(\bar{\varphi} + \frac{\pi}{4}\right) \\ \frac{u'_2}{u'_3} = \frac{i}{\tilde{c}'_{44}} \frac{\omega\eta}{2(\omega^2 - \omega_0^2)} B_1 B_2 \sin(2\bar{\varphi}) \sin\left(\bar{\varphi} + \frac{\pi}{4}\right) \end{cases}$$

In the figures below we plot the numerical values of the ratios modulus, $\left|\frac{u'_1}{u'_3}\right|$, $\left|\frac{u'_2}{u'_3}\right|$ vs applied field angle for different values of the field intensity. As can be seen, the latter are of the order 10^{-5} , that is $u'_3 \gg u'_1, u'_2$ and thus, $u'_1 = u'_2 \simeq 0$. Therefore the assumption on the wave components, i.e. eq. (6.22) is approximately verified.

Figure 6.8: Modulus of the displacement amplitude ratio $\left|\frac{u'_1}{u'_3}\right|$ vs applied field angle, for different field intensities.

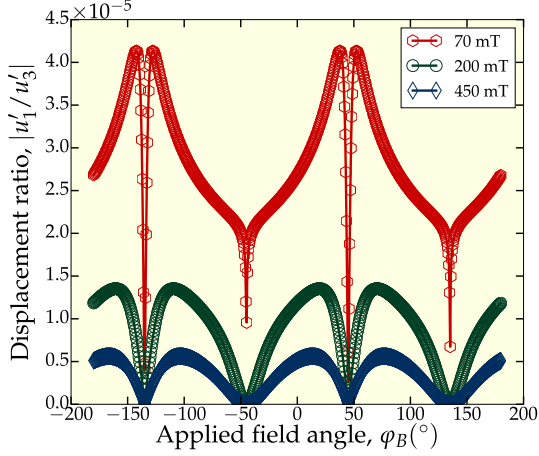
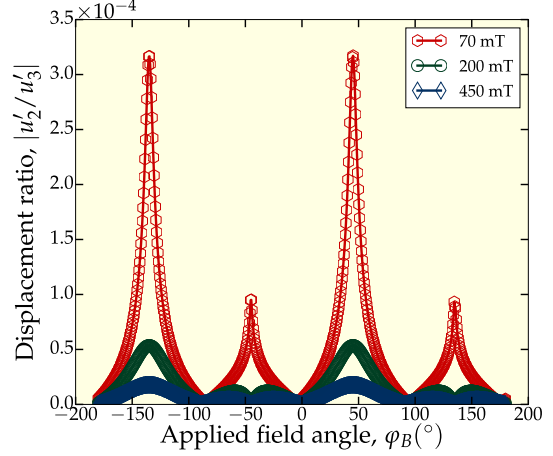


Figure 6.9: Modulus of the displacement amplitude ratio $\left|\frac{u'_2}{u'_3}\right|$ vs applied field angle, for different field intensities.



6.3.2 Ferromagnetic Film: Longitudinal Wave Velocity, \hat{v}_L

Following the same procedure, described above, we compute the velocity of the **longitudinal wave**, \hat{v}_L , polarized along [110], propagating in the bulk ferromagnetic materials, assuming the wave components:

$$\begin{cases} u'_1 &= U_l e^{i(\omega t - kx'_1)} \\ u'_2 &= 0 \\ u'_3 &= 0 \\ \delta\theta &= \Theta e^{i(\omega t - kx'_1)} \\ \delta\varphi &= \Phi e^{i(\omega t - kx'_1)} \end{cases}$$

We thus find:

$$\hat{v}_L^2 = \frac{\tilde{c}'_{11}}{\rho} \quad (6.31)$$

with the effective elastic constant:

$$\tilde{c}'_{11} = \frac{c_{11}}{2} + \frac{c_{12}}{2} + c_{44} + \frac{B_2^2}{4} \frac{\eta^2 F_{\theta\theta}}{\omega^2 - \omega_0^2} \cos^2(2\bar{\varphi}) \quad (6.32)$$

The self-consistency of the assumption on the wave components can also be verified numerically, as it was in the previous case.

6.3.3 Longitudinal velocity, \hat{v}_L vs transverse velocity, \hat{v}_T

Let us now compute the velocity variations of longitudinal and transverse waves in the ferromagnetic bulk material with the applied magnetic field, at different field angles. The result is shown in the figures below. Computations are carried out using the values, given in the chapter 2, table 2.1. As can be seen, the variations of the transverse velocity are 100 times smaller than those of the longitudinal one. This means that the change in the Rayleigh velocity is mostly due to the longitudinal strain component. This proves a posteriori, that the assumption №2 we took in the “anelastic” approach (change in SAW velocity is related to σ_{11} component) is reasonable.

Figure 6.10: Computed velocity of the transverse wave, \hat{v}_T in the bulk ferromagnetic material. Field applied at 15° with respect to $[100]$ direction.

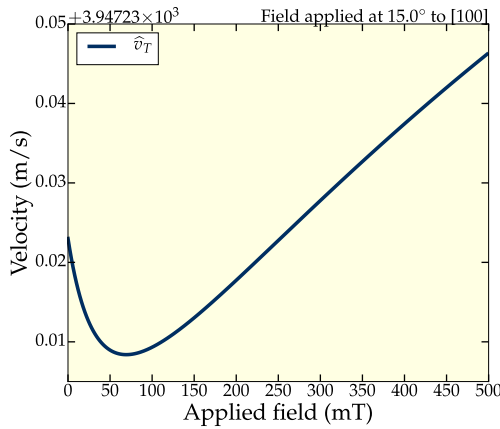


Figure 6.12: Computed velocity of the transverse wave, \hat{v}_T in the bulk ferromagnetic material. Field applied at 65° with respect to $[100]$ direction.

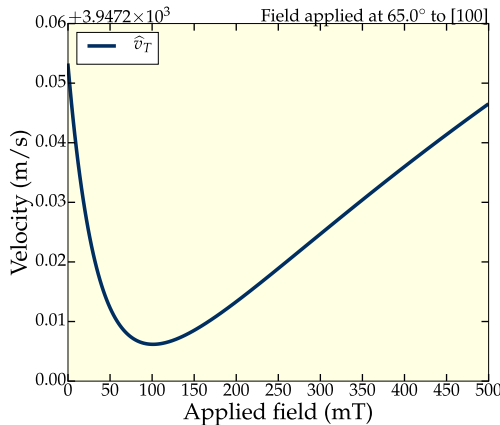


Figure 6.11: Computed velocity of the longitudinal wave, \hat{v}_L in the bulk ferromagnetic material. Field applied at 15° with respect to $[100]$ direction.

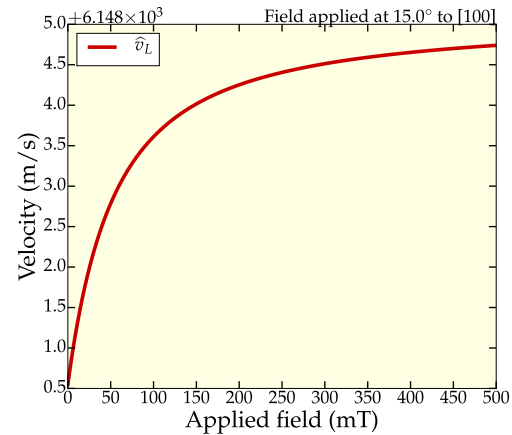
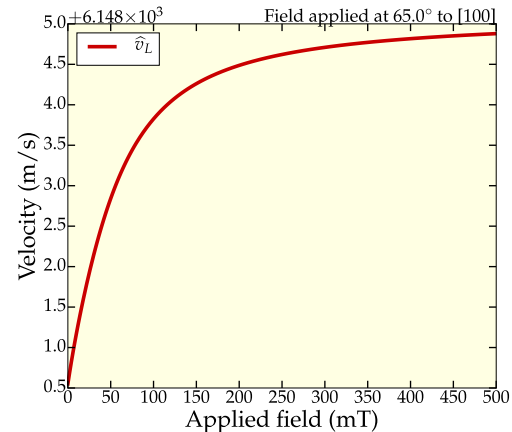


Figure 6.13: Computed velocity of the longitudinal wave, \hat{v}_L in the bulk ferromagnetic material. Field applied at 65° with respect to $[100]$ direction.

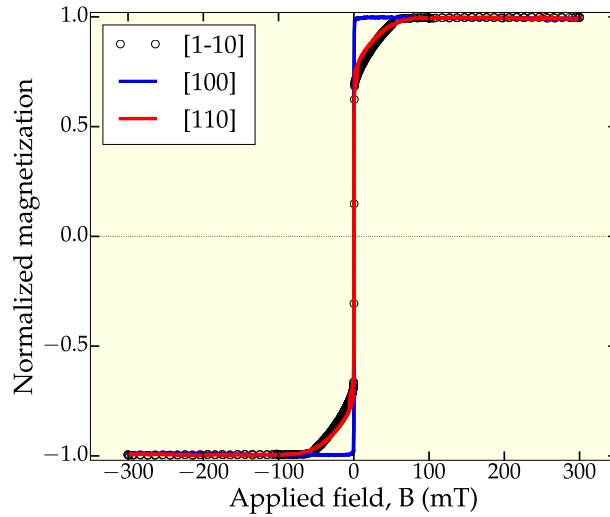


6.4 Interpretation and Fits of the Experimental Data

In the next sections we will employ the developed theoretical models to fit our experimental data in order to extract the material parameters, namely the magneto-elastic coefficient B_2 (SAW along [110]) and MCA constants, K_1 , K_{ip} . As was described in the chapter 5, we performed two kind of measurements, in which the variations in SAW velocity, $\frac{\Delta V}{V}$ were measured vs field *at fixed angle* and vs angle, *at fixed field*, for different acoustic frequencies. From the following discussion, it will be clear that the best fitting procedure is to fit the velocity versus the applied field angle, starting first from measurements, taken at high fields.

Let us make an observation of the sample of pure iron, [32m0215 Fe 67nm](#). This sample exhibits biaxial-uniaxial MCA, the latter due to the interface effects in case of a thin film on a substrate, as was discussed in the chapter 3. A typical hysteresis for pure iron thin film is represented in the figure below (fig. 6.14).

Figure 6.14: Typical hysteresis for pure Fe ([32m0100](#)).

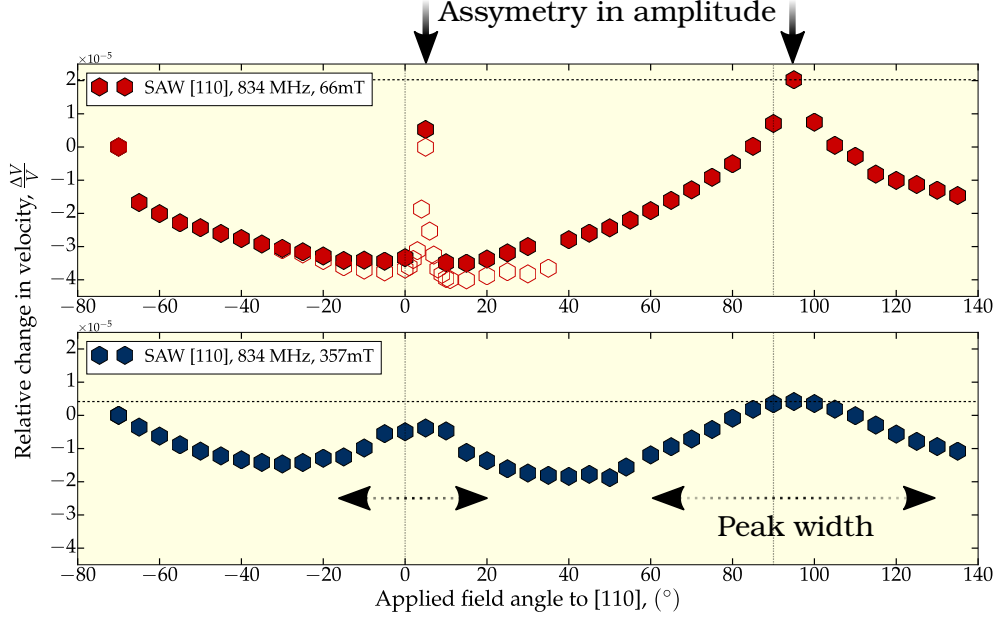


The measured variations in the SAW velocity, $\frac{\Delta V}{V}$ vs applied field angle at fixed frequency, 834 MHz for different field intensities, 66mT and 357mT are represented in the fig. 6.15.

The following striking features can be observed:

- (i) Asymmetry in the “peaks” amplitudes
- (ii) The “peaks” width is different, the effect being much more pronounced at lower field, 66mT

Figure 6.15: 32m0215 Fe 67nm. Relative change in velocity, $\frac{\Delta V}{V}$ vs applied field angle at 834MHz, at 66mT and 357mT.



At first, to discuss these results, we can reason in terms of the SAW-induced torque. The fig. 6.16 summarizes previous computation results, derived in the chapter 2. Note that, the computation was carried out for the material constants (K_1 , K_{ip} , B_2) of Fe_{0.8}Ga_{0.2} 58nm sample.

Nevertheless, we can employ the results to discuss the physics. Let us note few important points:

- (i) In the section 6.2 we derived the expression for the real part of the elastic constant of the film, modified by the magneto-elastic contribution. The latter is *always* negative, for so is the difference in frequencies⁹ $\omega^2 - \omega_0^2$. It follows that, the modification of the elastic constants of the material by magneto-elastic contribution results in the *softening* of the elastic constants and thus, **the SAW velocity is smaller, when coupled.**

$$\widehat{C}'_{\text{Re}} = \frac{\widehat{c}_{11}}{2} + \frac{\widehat{c}_{22}}{2} + \widehat{c}_{44} - \widehat{c}_{12} \frac{c_{12}}{c_{11}} + \underbrace{B_2^2 \cos^2(2\varphi) \frac{\eta^2 F_{\theta\theta}}{4(\omega^2 - \omega_0^2)}}_{\text{magneto-elastic contribution, } <0}$$

- (ii) As discussed, the parallel, $\mathbf{m} \parallel \mathbf{k}_{\text{saw}}$ or perpendicular configuration, $\mathbf{m} \perp \mathbf{k}_{\text{saw}}$ results in the zero torque or in other words, there is *no coupling*. However, zero torque for the first configuration is a consequence of the neglected shear strain component, e_{13} (section 2.3.1). In reality, *there is* a coupling in such configuration, though small.

⁹The proper frequency increases with the field, so for a fixed acoustic frequency either the difference is zero, that is *resonance*, either it is negative.

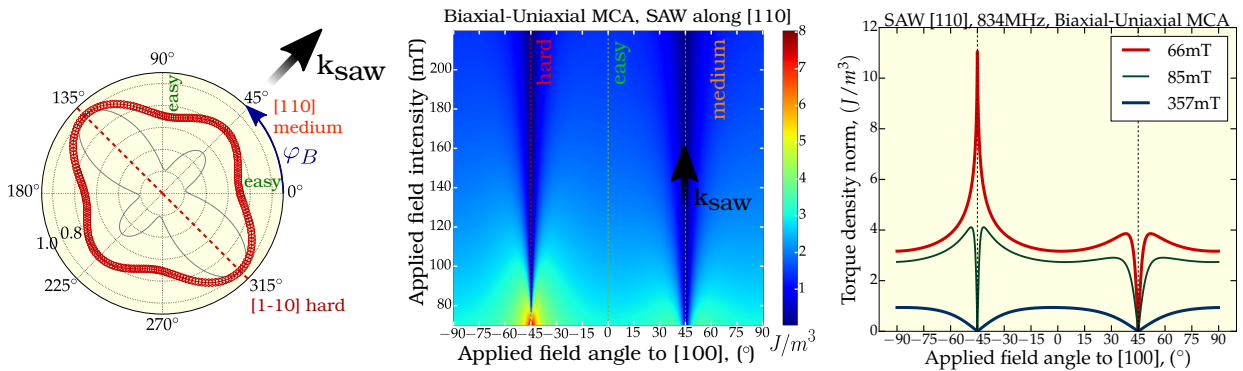
- (iii) As can be seen from the torque norm variations with the applied field angle (fig. 6.16, left), for a low field value, as 66mT (85mT) we are still *sensitive* to the magneto-crystalline anisotropy (MCA) of the system¹⁰. This is a fingerprint of the eigenfrequency of the system, ω_0 as can be seen from fig. 6.17, where we compare biaxial and biaxial-uniaxial MCA systems. When magnetization is along a hard axis, the eigenfrequency drops down and thus, torque is larger. This is an important point and we can reformulate it as: **when we approach the resonance condition, $\omega_0 = \omega$ the magneto-elastic coupling is stronger.**
- (iv) As the field increases, we are no longer sensitive to the MCA, but only to the oscillatory term, $|B_2 \cos(2\bar{\varphi})|$ in the torque expression (eq. (2.20), chapter 2), that is proportional to the magneto-elastic coefficient.

Following these points, we can now interpret our results (fig. 6.15).

The asymmetry in “peaks” amplitude is clearly related to the small coupling at 0° (field parallel to the SAW wave vector) and the absence of the latter at 90° (field is perpendicular to the SAW wave vector). We are sensitive enough to measure it.

On the other hand, the SAW velocity is higher in the decoupled state and as a consequence, the “peak” amplitude is higher¹¹ at 90° .

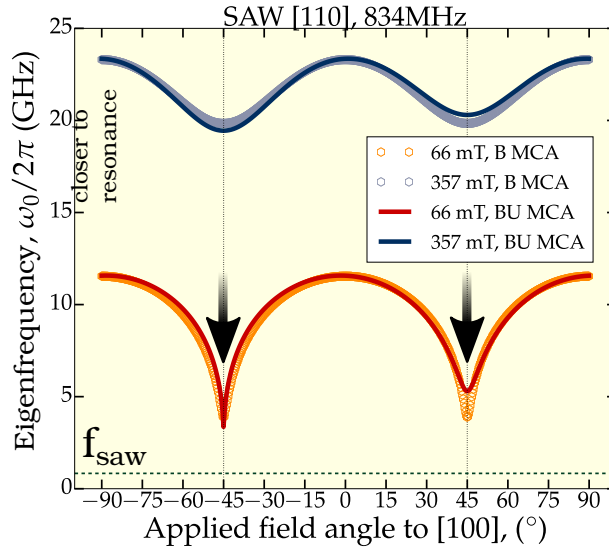
Figure 6.16: Polar plot of MCA energy density (left). Colorplot of the torque density norm (middle). Torque density norm vs applied field angle at different field intensities (left).



¹⁰Note that for this set of parameters, used in calculation, at 66mT the magnetization is not completely aligned with the applied field at -45° . This is why the torque is not zero, from the other hand 85mT is enough to result in the perpendicular configuration, $\mathbf{m} \perp \mathbf{k}_{saw}$ and thus, torque vanishes.

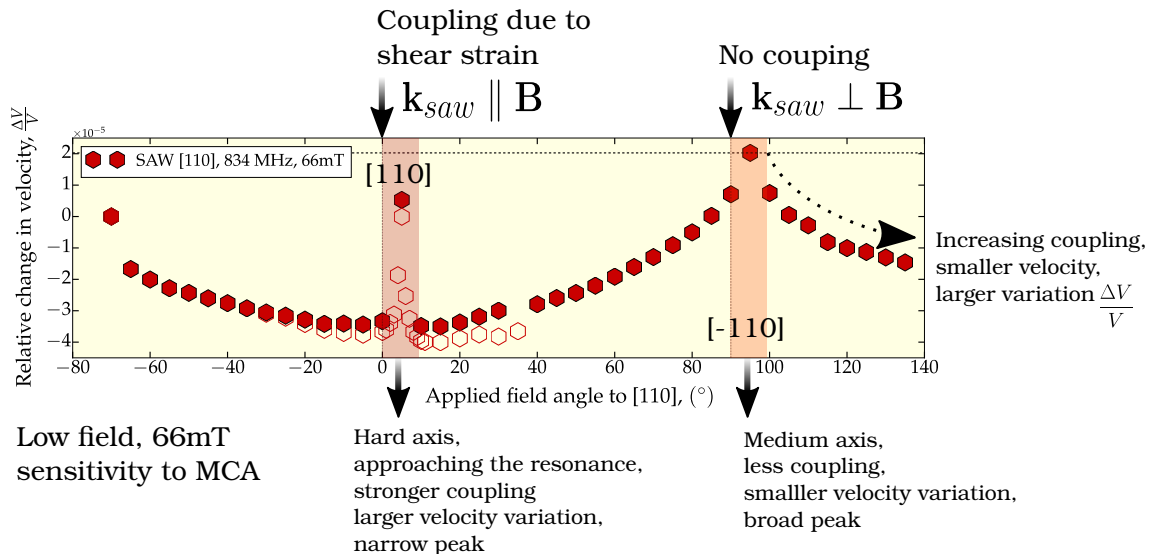
¹¹Note that, when we treat experimental data, the change in the SAW velocity is deduced according to $\frac{\Delta V}{V} = \frac{V(\varphi_B) - V(\varphi_{Bref})}{V(\varphi_B)}$. The reference angle is absolutely arbitrary, so what counts is the peak height at different angle and not its zero value.

Figure 6.17: Computed eigenfrequency, $\omega_0/2\pi$ vs the applied field angle for different field intensities and different MCA systems. Notation: B MCA biaxial MCA, BU MCA biaxial-uniaxial MCA.



At low field we are sensitive to the MCA. For the field, applied along the hard axis, the coupling is stronger. This results in large variations of the velocity, that results in a “narrow” peak at 0° . As the field is increased, we become less and less sensitive to the MCA on one hand and the coupling decreases, on the other. This results in the “peak broadening”, as velocity variations become smaller. Note that it is **at high field we are sensitive to the B_2 coefficient**. This discussion is summarized in the figure below (fig. 6.18). This one curve can tell us so much about the physics behind the magneto-elastic interaction!

Figure 6.18: Summary of the interpretation.



However, there are two features of this curve that must be discussed.

First, if we look at the polar plot of the biaxial-uniaxial energy density (fig. 6.16, left), it is clear that the medium and hard axes are along $[110]$ and $[1\bar{1}0]$ directions, respectively. The direction, however, depends on the sign of the MCA constant (section 1.2.4). When the field is applied along hard axis, at 90° the coupling should be larger and we would expect a narrow peak.

This is not what we observe. This implies, in the frame of this reasoning, that *the medium and hard axes are reversed*. The latter is possible if the K_{ip} constant is *positive*.

The negative value of the uniaxial MCA constant is related to the anisotropic interface bonding and should be negative $[109]$ $[110]$. Further investigation is needed to understand this observation.

Secondly we observe, that the peaks are slightly shifted with respect to the main crystallographic directions. Since the indicated angles are *measured*, we attribute this effect to a measurement error.

Based on the discussion above, we propose the following fitting procedure. First, the high field measurements are considered to extract B_2 values then we can extract K_1 , K_{ip} by fitting the variations $\frac{\Delta V}{V}$ at low fields. Note that, it is possible to distinguish between the biaxial and uniaxial MCA contributions due to the width of the “peaks”.

It is also clear, that the film-on-substrate approach is more appropriate, since it takes into account both longitudinal and shear strain components, and thus can reproduce the asymmetry in the “peaks” height.

6.4.1 32m0215 Fe 67nm

We now proceed with fitting the data. Some of the experimental results for this sample were discussed in the section above. SAW propagation direction is $[110]$. As discussed, the fitting procedure is the following:

1. We set the MCA constants to zero, $K_1 = K_{ip} = 0$ and fit the amplitude of the variations, choosing the appropriate value of the B_2 constant. The corresponding fit is represented with a red solid curve in the fig. 6.19.
2. Having determined the magneto-elastic coefficient, B_2 , we adjust K_1 and then K_{ip} . The corresponding fit is represented with a dashed blue line.

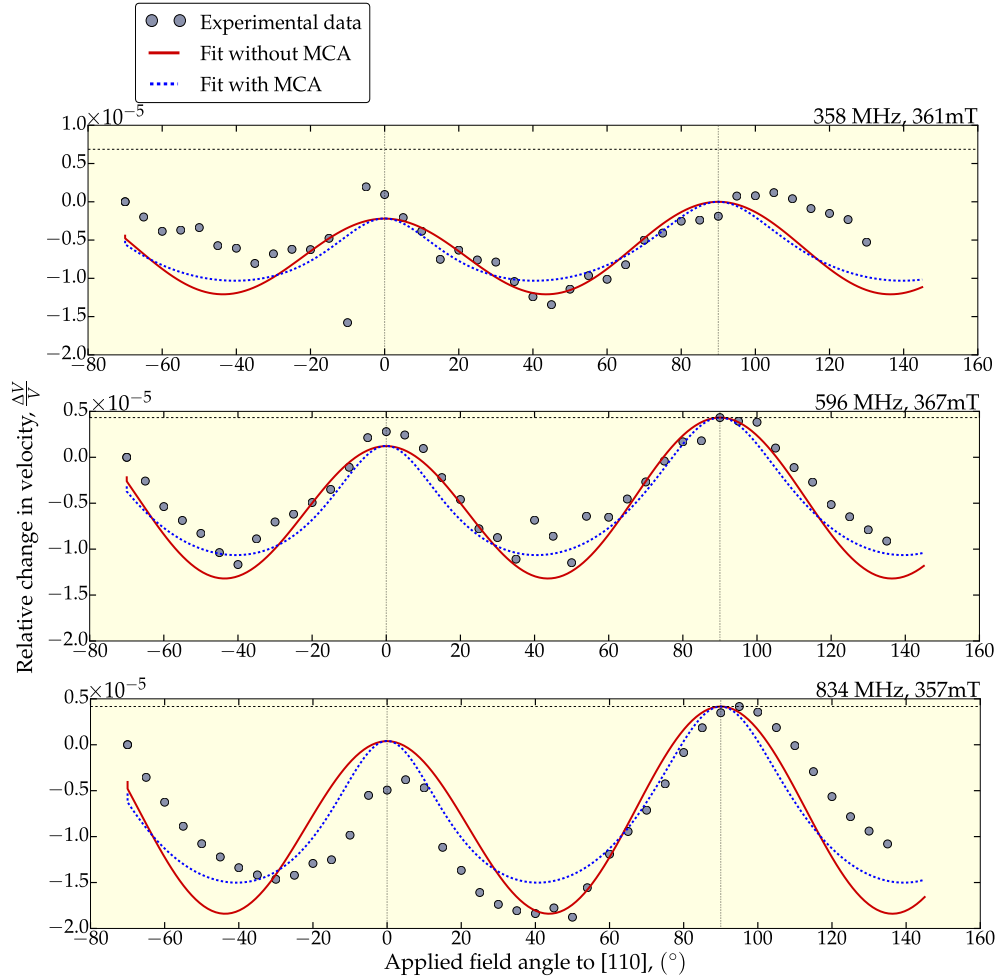
Note that, in the previous section we gave an interpretation in terms of torque. In the figures below, we compute the change in velocity at two different frequencies for low, 60mT and high, 400mT fields to see the effect of the MCA on the SAW velocity at low field.

The fig. 6.19 represents the velocity variations, $\frac{\Delta V}{V}$ with the applied field angle for three different frequencies, 358MHz, 596MHz and 834MHz at high field. The table 6.3 summarizes the materials constants, used to obtain the best fits. Note, that K_{ip} is taken to be *positive*.

Table 6.3: Film-on-substrate approach (section 6.3), fitting parameters B_2 , K_1 , K_{ip} .

MCA	Best fit value
without MCA	$ B_2 = 2.4 \cdot 10^7$, $K_1 = K_{ip} = 0$ (J/m^3)
with MCA	$ B_2 = 2.4 \cdot 10^7$ (J/m^3) $K_1 = 6 \cdot 10^3$ $K_{ip} = 10^4$

Figure 6.19: Fit of the experimental data for different frequencies.



Low field features: close to the resonance?

The peculiar features for velocity variations at low field, as discussed at the beginning of this section (fig. 6.15), require a special attention. We cannot fit them with our model. However, we tried to change the parameters to see whether these features can be reproduced. We found numerically that this is the case for a system, exhibiting only uniaxial anisotropy MCA with an enhanced value $2.5 \cdot 10^4 \text{ J/m}^3$, since we could reproduce *the shape of the experimental curve* (fig. 6.20): a narrow peak when the field is parallel to [110], surrounded by well defined minima structures.

We also calculated the difference of the acoustic and eigenfrequencies, $\omega_0^2 - \omega^2$ (fig. 6.21) for different acoustic frequencies and fields.

The striking observation is that for $\omega = 1\text{GHz}$ and 50mT , the $\omega_0^2 - \omega^2$ term is almost zero (when a uniaxial anisotropy of $2.5 \cdot 10^4$ is artificially considered), which implies the *resonance*. Increasing the field or frequency, we shift up the term, which is an expected behavior.

Since for this simulated system we could reproduce *the shape* of the experimental curve and we are close to resonance, **we speculate that experimentally this might be the case.**

We recall that our approach is no longer valid when the value of SAW angular frequency, ω is close to ω_0 , as it implies non-linear magnetization dynamics. Thus we cannot fit these experimental values.

Figure 6.20: Computed $\frac{\Delta V}{V}$ vs applied field.

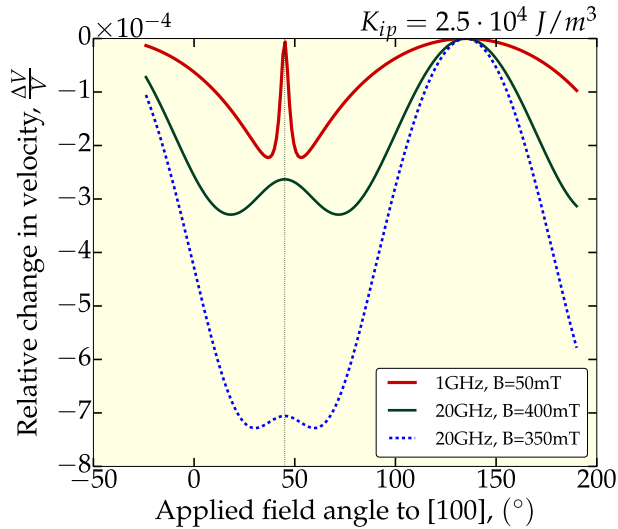
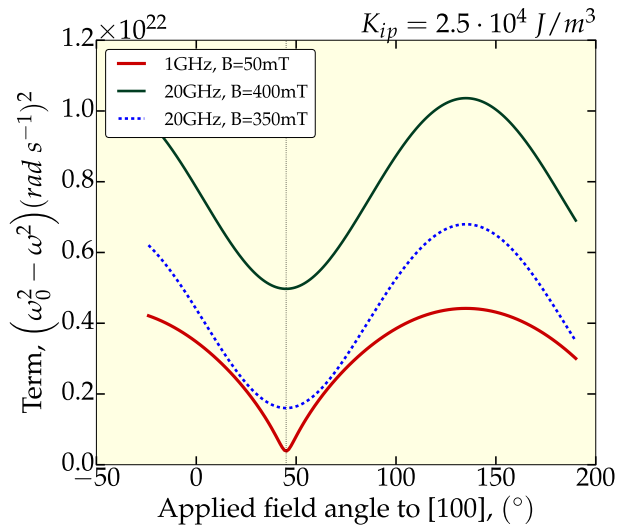


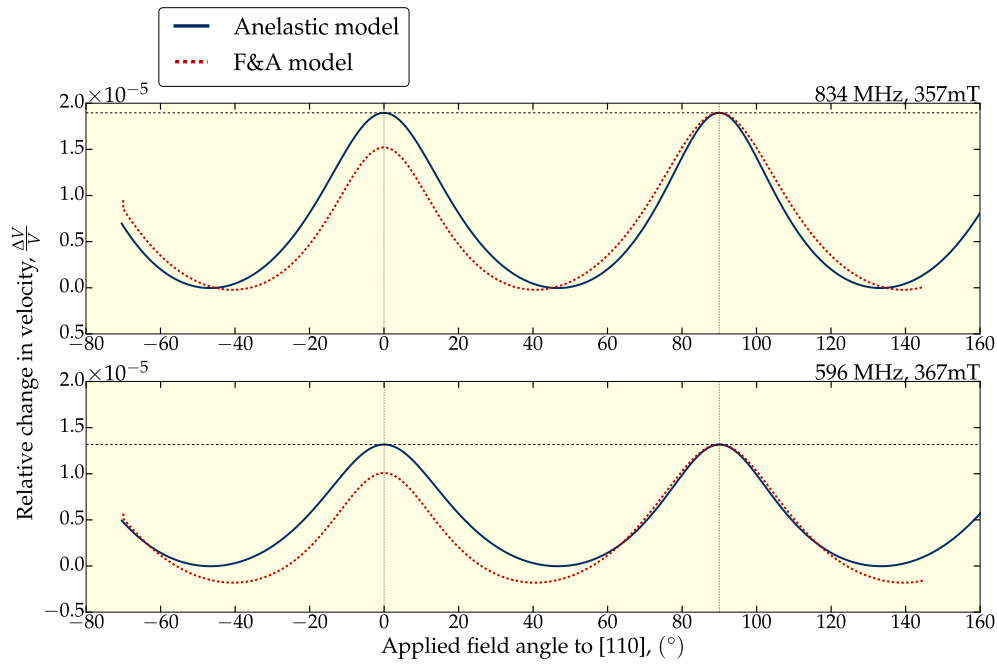
Figure 6.21: Computed $\omega_0^2 - \omega^2$ vs applied field.



Film-on-substrate vs anelastic approach

The last point to address to in this discussion is the comparison between two theoretical approaches, explored in this chapter. The figure below (fig. 6.22) represents the computed velocity variations vs field angle, using two approaches. We took the same parameters for the anisotropy constants, that we obtained from the fits with the film-on-substrate approach (table 6.3). The magneto-elastic constant, B_2 was adjusted to the fit the data at 834MHz with the “anelastic” approach, $|B_2| = 2.85 \cdot 10^7 (J/m^3)$, which is not bad, given the approximations we made. As discussed before, the anelastic model cannot reproduce the asymmetry in the peaks height for it does not take into account the shear strain contribution. But also the frequency dependent dilution factor comes into play: for the same value of the magneto-elastic constant we cannot fit perfectly the data at two different frequencies. Nevertheless, the advantage of the anelastic approach is in its simplicity, that does give the insights into physics.

Figure 6.22: Computation of the velocity oscillations, using two models, for 834MHz and 596MHz.



6.4.2 32m0206 Fe_{0.8}Ga_{0.2} 58nm

Many experimental results for this sample were presented in the chapter 5. The fig. 6.24 - fig. 6.23 represent the experimental data and fits for different fields and frequencies. The following table summarizes the fitting parameters, obtained using the film-on-substrate model, as well as the measured values. Note that as in the case with pure iron, the uniaxial MCA constant is positive from the fit.

If we compare the fits at high field, 389mT, it is clear that the MCA does not play any role. At relatively low field, 155mT we are much more sensitive to the MCA, as can be seen from the peaks' width. It is thus possible to distinguish between the two contributions to the MCA of the system (biaxial and uniaxial) and to extract the constants.

Table 6.4: Film-on-substrate approach (section 6.3), fitting parameters B_2 , K_1 , K_{ip} .

MCA	Best fit value	Measured value (table 2.1, table 3.4)
without MCA	$ B_2 = 1.2 \cdot 10^7$, $K_1 = K_{ip} = 0$ (J/m^3)	
with MCA	$ B_2 = 1.2 \cdot 10^7$ (J/m^3) $K_1 = 2 \cdot 10^4$ $K_{ip} = 0.7 \cdot 10^4$	$B_2 = -1.0 \cdot 10^7$ (J/m^3) $K_1 = 2.41 \cdot 10^4$ $K_{ip} = -0.6 \cdot 10^4$

Figure 6.23: Fit of the experimental data for different frequencies at a fixed field, 389mT.

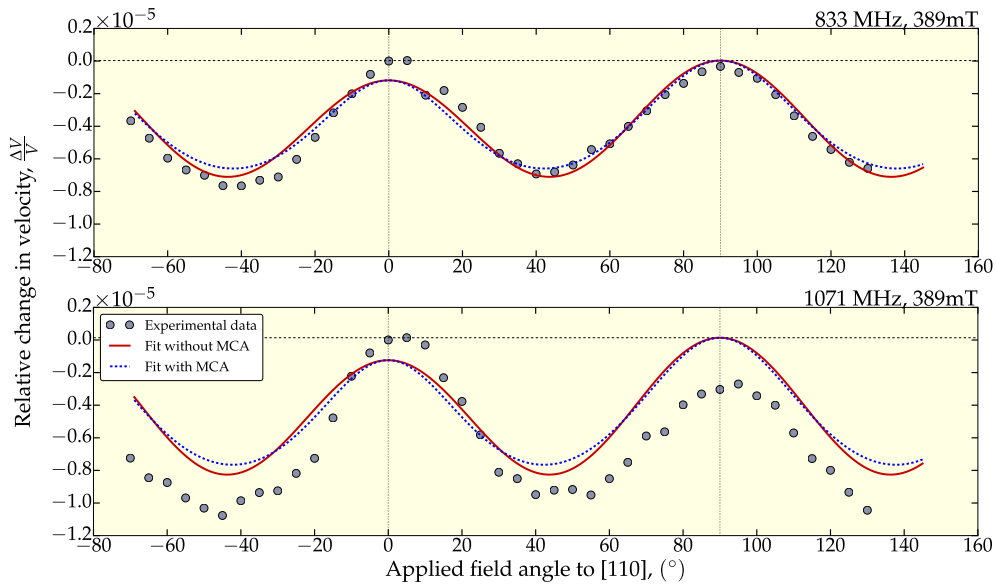
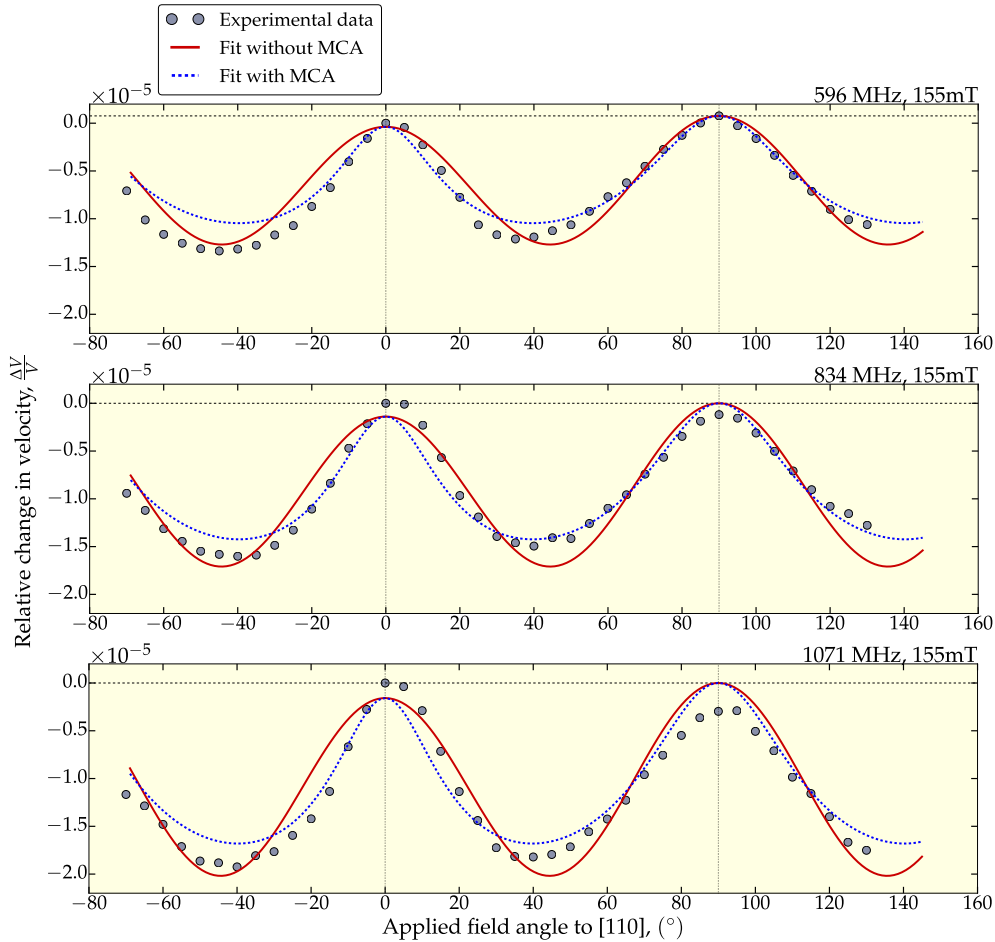


Figure 6.24: Fit of the experimental data for different frequencies at a fixed field, 155mT.



6.5 Conclusion

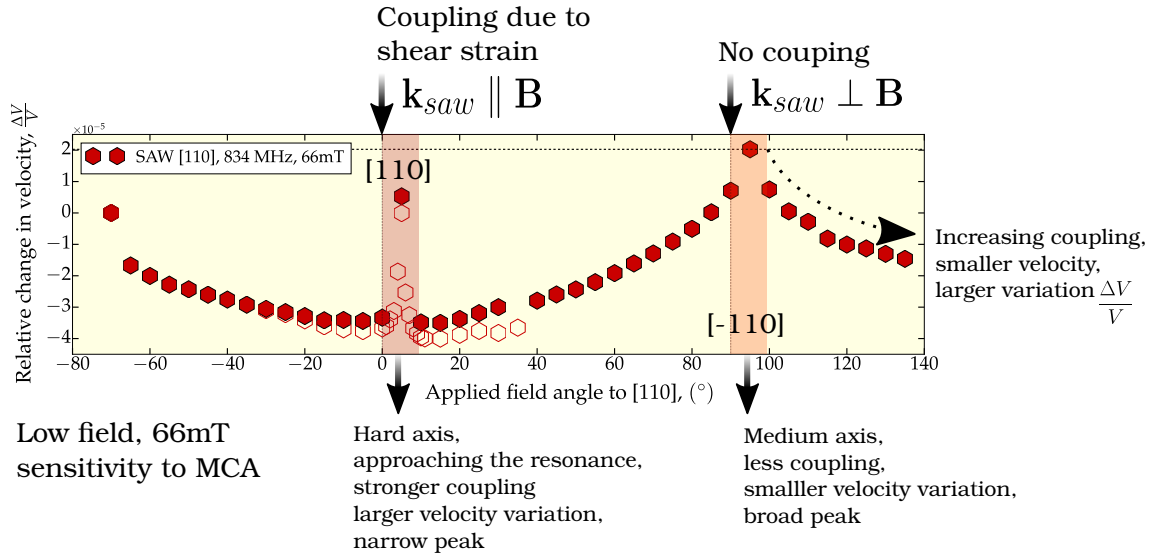
This chapter was devoted to the modeling of the system. After giving an in-exhaustive state of the art of the theoretical approaches, existing in the literature, we considered two approaches.

The first approach is based on the theory of anelasticity and is very approximate. Within this approach we derive the expression for an effective elastic constant of the medium. The real part of the expression is used to compute the change in the Rayleigh velocity. The main drawbacks of this approach is the introduction of a “dilution factor” to account for the real film-on-substrate structure, and the approximation that the change in the velocity is due to the longitudinal strain component only.

In the second approach we adapt the calculation of Farnell and Adler, describing the propagation of SAWs in a film-on-substrate structure, by including the magneto-elasticity. This approach is more rigorous, as it take into account both longitudinal and shear strain component of SAW, which is crucial for fitting the experimental data. Furthermore the film

thickness parameter enters naturally in the calculation and so no dilution factor is needed. Having established the theoretical framework, we pass to the numerical analysis and data interpretation. The result of the interpretation is concluded in the figure below, that represents the velocity variations with the applied field angle at low field (32m0215 Fe).

Figure 6.25: Summary of the interpretation.



We then proceed with our data analysis. We propose a fitting procedure to extract the material constants, namely magneto-elastic, B_2 and MCA, K_1, K_{ip} parameters. This can be done by fitting the velocity variations vs the applied field angle. Fitting the data first, taken at high fields, permits to extract the B_2 , while at lower field we are sensitive to the MCA. It is also possible to distinguish between K_1 and K_{ip} contribution. We thus propose *a new method to extract material parameters, employing SAWs.*

Conclusion & Perspectives

In this PhD thesis, I carried out a study in order to obtain a better understanding of physics behind the magneto-elastic interaction between magnetization and surface acoustic waves (SAWs), in epitaxied ferromagnetic thin films. This was done by a systematic investigation of SAW propagation versus magnetic field, in devices working at different frequencies, thanks to a time-consuming technological development of inter-digital transducers (frequencies up to 5GHz were attained in GaAs substrates). This was accompanied by the development of two phenomenological models that permitted the description of the SAW velocity variations versus magnetic field, in terms of intrinsic parameters of the thin films, i.e. the magnetic anisotropy and the magneto-elastic coefficients. Our aim was to write equations as simple as we could, compatible with LLG equations and SAW propagation laws. This was done in the single domain approximation and without taking into account the piezoelectric properties of the substrate. In particular, we carried out a study of the directionality of the magneto-elastic coupling as a function of the direction and the intensity of the magnetic field and of the SAW frequency in Fe and FeGa thin films epitaxied on GaAs(001). Samples of different magnetic structure, that is with in-plane, out-of-plane or in-plane isotropic and of different thicknesses were studied, using a high sensitivity RF acoustic setup. Based on our experimental findings and theoretical approach (for the moment only in-plane magnetized samples were considered), we could propose a new method to extract the material parameters, namely magneto-elastic coupling coefficients and magneto-crystalline anisotropy (MCA) constants.

It turns out that the SAW induced torque on the thin film magnetization can be regarded as the main player of the magneto-elastic coupling game. It was shown how the coupling strongly depends on the direction of the applied field, more precisely on the equilibrium orientation of magnetization with respect to the SAW wave vector. This permits us to put forward two important points of our work:

- First, SAW propagation along the in-plane [100] or [110] family directions of a cubic crystal, exhibits a sensitivity to different magneto-elastic coefficients, i.e. B_1 and B_2 , respectively. By a fitting procedure, exploiting the analytical models, we succeeded to extract the B_2 coefficient of Fe and FeGa thin films. Furthermore, by varying the

field, we showed that the acoustic measurement are well sensitive to biaxial and uniaxial anisotropies present in the epitaxied thin films. All these values were compared with magnetic anisotropy and magneto-elastic coefficients measured by more traditional means, like FMR and cantilever method. A good agreement was found, corroborating our phenomenological models. If FMR is a widely used and reliable technique to extract magnetic anisotropy coefficients, the cantilever method remains incipient in actual nanomagnetism research. *We believe that obtaining a complete set of measurement of both parameters (magneto-elastic and anisotropic), by a unique acoustic experiment is a successful novelty.*

- Secondly, it was seen that the coupling strongly depends on the direction of the applied field, more precisely on the equilibrium orientation of magnetization with respect to the SAW wave vector. In particular, two angles are important: the first one is between the SAW wave vector and the equilibrium magnetization and the second one is between the equilibrium magnetization and the magnetic axis of the film. From one hand, when magnetization is perpendicular to the SAW wave vector, no coupling is possible; when it is parallel, a slight coupling is possible only because of the shear strain component, present in the SAW (precisely, Rayleigh wave). On the other hand, when magnetization is pulled towards the hard axes, because of the energy barrier for the magnetization, the proper frequency of the system drops down. This is a smart way to approach SAW-SW resonance: spin waves and elastic waves hybridize, coupling is stronger and dynamic magnonic applications can be envisaged. *These considerations permit us to conclude that the largest magneto-elastic coupling is found when the magnetic field is applied at 45° (hard axis) with respect to the SAW propagation direction, that coincides with an easy axis of the system.* This has a direct consequence on the choice of the material, in which the Spin Wave - SAW interactions are considered. Ideally, such material should have strong magneto-elastic coupling coefficient for the SAW propagation directions and strong magneto-crystalline anisotropy.

The perspectives are the following:

In order to verify our concept of “torque maximization” experimentally, we should consider the appropriate SAW excitation configuration for our samples, that is along [100] direction. Uniaxial anisotropy favoring [110] direction is expected to maximize the coupling. Since uniaxial anisotropy in these systems is due to interface effects and scales with the inverse of the film thickness, very thin film should be prepared. The fabrication of such device is a more difficult process, since the symmetry of the GaAs piezo-electric tensor does not allow a coupling between the wave strains and the IDT electric field. A possible solution is to cap the thin film with a layer of piezoelectric ZnO. Such a device was recently fabricated, but was broken at the end of the fabrication process.

It would be interesting to consider other type of surface acoustic waves, for example Love waves (shear horizontal) and different MCA systems to see, if further improvement in the coupling optimization can be achieved.

From the point of view of possible applications in magnonics, new acoustic driven phenomenas can be envisaged, once magneto-elastic coupling is well modeled and understood. Typical examples are: remote controlled opening of gaps in dynamical magnonic crystal [38], Doppler shift [151], acoustically driven spin pumping “acoustic spin pumping” [152], [153]. As was mentioned in the introduction, the preliminary steps in this direction were made during the thesis. Many efforts were devoted to the optimization of RF antenna, a new technique for INSP, for efficient excitation of spin waves. Antennas were fabricated by myself at INSP and tested by μ BLS in collaboration with the GHOST group in Perugia, Italy. **It was found that the propagation distance for the spin waves in our samples of $\text{Fe}_{1-x}\text{Ga}_x$ is about $13\mu\text{m}$.** It was important to verify that the SWs propagation distance is reasonable enough to proceed any further. Furthermore, the preliminary measurements were done with conventional BLS to check the *resonant interaction* in a 4nm thick film of $\text{Fe}_{0.8}\text{Ga}_{0.2}$. The thickness was chosen in such a way as to reduce the SWs frequency down up to 4GHz, by applying the field along the hard axis [1-10]. The interaction was checked, but unfortunately did not yield a positive result, which is rather puzzling. This work is probably too recent and preliminary to be presented in this manuscript. However, a possible explanation can be attributed to the fact, that reducing the film thickness makes the interface effects due to the growth dominant. A complication for ultra-thin films is the value of the magneto-elastic coefficients which could be different from the bulk ones, maybe correlated to the crystalline quality. Recall also, that the magneto-elastic energy is a product of strain and magneto-elastic coefficient. To modify this energy, even with poor magneto-elastic coefficients of the material, one should be able to apply a large strain amplitude. At such high acoustic frequencies it is difficult to achieve due to the impedance mismatch between the IDTs and the excitation source. Several solutions are possible. To improve the film quality, we would have to increase the film thickness. We have to find the optimum balance between high uniaxial anisotropy values (low thickness and low SAW frequencies) and good crystalline quality (higher thickness and consequent higher SAW frequencies). The task is challenging, but is worth pursuing.

Appendix A

Local rotations

Consider only the asymmetric part of the displacement gradient:

$$\xi(\mathbf{r}, t_0) = \frac{1}{2} \begin{pmatrix} 0 & \Omega_{12} & \Omega_{13} \\ -\Omega_{12} & 0 & \Omega_{23} \\ -\Omega_{13} & -\Omega_{23} & 0 \end{pmatrix}$$

Using eq. (1.3), the differential displacement can be expressed as follows:

$$\begin{cases} du_1 & = & \Omega_{12}dx_2 + \Omega_{13}dx_3 \\ du_2 & = & -\Omega_{12}dx_1 + \Omega_{23}dx_3 \\ du_3 & = & -\Omega_{13}dx_1 - \Omega_{23}dx_2 \end{cases}$$

then the scalar product of $\mathbf{du} \cdot \mathbf{dr}$ yields zero:

$$\mathbf{du} \cdot \mathbf{dr} = \sum_i du_i dx_i = (\Omega_{12}dx_2 + \Omega_{13}dx_3)dx_1 - (\Omega_{12}dx_1 - \Omega_{23}dx_3)dx_2 - (\Omega_{13}dx_1 + \Omega_{23}dx_2)dx_3 = 0$$

This implies that differential displacement vector \mathbf{du} and \mathbf{dr} are orthogonal. This result holds for rotations (fig. 1.4c), *provided* that the rotation angle ϕ is **infinitesimally small**, so that $\mathbf{du} \cdot \mathbf{dr} \approx 0$. Therefore the asymmetric part of the displacement gradient matrix represents infinitesimal rotations, rigid or local (fig. 1.6). However local rotations do not contribute to the propagation of the elastic waves [50].

Appendix B

Propagation along [100] direction: detailed calculation

The starting point of the calculation are the equations of motion, as expressed in the section 1.1.3:

$$\begin{cases} \rho \frac{\partial u_1^2}{\partial t^2} = c_{11} \frac{\partial^2 u_1}{\partial x_1^2} + c_{12} \frac{\partial^2 u_3}{\partial x_1 \partial x_3} + c_{44} \left(\frac{\partial^2 u_1}{\partial x_3^2} + \frac{\partial^2 u_3}{\partial x_1 \partial x_3} \right) \\ \rho \frac{\partial u_2^2}{\partial t^2} = c_{44} \left(\frac{\partial^2 u_2}{\partial x_1^2} + \frac{\partial^2 u_2}{\partial x_3^2} \right) \\ \rho \frac{\partial u_3^2}{\partial t^2} = c_{12} \frac{\partial^2 u_1}{\partial x_1 \partial x_3} + c_{11} \frac{\partial^2 u_3}{\partial x_3^2} + c_{44} \left(\frac{\partial^2 u_1}{\partial x_1 \partial x_3} + \frac{\partial^2 u_3}{\partial x_1^2} \right) \end{cases}$$

The assumed solutions are of the form:

$$\begin{cases} u_1 = U e^{-\alpha x_3} e^{i(\omega t - k x_1)} \\ u_2 = V e^{-\alpha x_3} e^{i(\omega t - k x_1)} \\ u_3 = W e^{-\alpha x_3} e^{i(\omega t - k x_1)} \end{cases}$$

By plugging the above expressions into the equations of motion and regrouping terms, we obtain:

$$\begin{cases} [-k^2 c_{11} + \alpha^2 c_{44} + \rho \omega^2] U + ik\alpha (c_{12} + c_{44}) W = 0 \\ ([-\alpha^2 + k^2] c_{44} + \rho \omega^2) V = 0 \\ ik\alpha (c_{12} + c_{44}) U + [-k^2 c_{44} + \alpha^2 c_{11} + \rho \omega^2] W = 0 \end{cases} \quad (\text{B.1})$$

which yields a system of equations solvable iff:

$$\begin{vmatrix} -k^2 c_{11} + \alpha^2 c_{44} + \rho \omega^2 & ik\alpha (c_{12} + c_{44}) \\ ik\alpha (c_{12} + c_{44}) & -k^2 c_{44} + \alpha^2 c_{11} + \rho \omega^2 \end{vmatrix} = 0$$

Thus:

$$\alpha^4 c_{11} c_{44} + \alpha^2 \left(k^2 \left[(c_{12} + c_{44})^2 - c_{11}^2 - c_{44}^2 \right] + (c_{11} + c_{44}) \rho \omega^2 \right) + \left[k^4 c_{11} c_{44} - k^2 \rho \omega^2 (c_{11} + c_{44}) + \rho^2 \omega^4 \right] = 0$$

Dividing by k^4 and using the relation $k = \frac{\omega}{V_r}$, where V_r being the Rayleigh velocity, we introduce after some algebra a variable $\mathbf{q} = \frac{\alpha}{\mathbf{k}}$ and obtain a quadratic equation in q^2 :

$$q^4 + q^2 \frac{(c_{12} + c_{44})^2 - c_{11}^2 - c_{44}^2 + (c_{11} + c_{44}) \rho V_r^2}{c_{11} c_{44}} + \frac{(c_{11} - \rho V_r^2)(c_{44} - \rho V_r^2)}{c_{11} c_{44}} = 0 \quad (\text{B.2})$$

Consequently the quadratic equation has two roots q_1^2 and q_2^2 , that satisfy:

$$\begin{cases} q_1^2 + q_2^2 &= \frac{c_{11}^2 + c_{44}^2 - (c_{12} + c_{44})^2 - (c_{11} + c_{44}) \rho V_r^2}{c_{11} c_{44}} \\ q_1^2 \cdot q_2^2 &= \frac{(c_{11} - \rho V_r^2)(c_{44} - \rho V_r^2)}{c_{11} c_{44}} \end{cases} \quad (\text{B.3})$$

To reflect the decrease of wave amplitude with depth, α should be either real positive or complex with real part positive, thus among four solutions, q obtained only two are retained, q_1 and q_2 , yielding two penetration depths:

$$\begin{cases} \alpha_1 &= \frac{q_1}{k} \\ \alpha_2 &= \frac{q_2}{k} \end{cases} \quad (\text{B.4})$$

Since the solid is *finite*, boundary conditions should be satisfied, which relate mechanical (and electrical in the case of piezoelectric solids) variables at the interface between the two media, that is:

† material displacement is continuous at the interface between two rigidly bound solids;

† in the absence of an external force stress is continuous or vanishes, if the second medium is vacuum;

Having found two solutions, we can show that choosing only one does not satisfy the zero-stress condition, $\sigma_{i3} = 0 \quad i \in [1, 2, 3]$ at the surface ($x_3 = 0$):

$$\begin{cases} \sigma_{13} &= c_{44} \left(\frac{\partial u_1}{\partial x_3} + \frac{\partial u_3}{\partial x_1} \right) &= 0 \\ \sigma_{23} &= c_{44} \frac{\partial u_2}{\partial x_3} &= 0 \\ \sigma_{33} &= c_{12} \frac{\partial u_1}{\partial x_1} + c_{11} \frac{\partial u_3}{\partial x_3} &= 0 \end{cases} \Leftrightarrow \begin{cases} \alpha u_1 + i k u_3 &= 0 \\ \alpha u_2 &= 0 \\ i k c_{12} u_1 + \alpha c_{11} u_3 &= 0 \end{cases} \quad \text{and} \quad \alpha^2 c_{11} + k^2 c_{12} \neq 0$$

Thus a linear combination of the two solutions should be considered, α_i given by eq. (B.4):

$$\begin{cases} u_1 = (U_1 e^{-\alpha_1 x_3} + U_2 e^{-\alpha_2 x_3}) e^{i(\omega t - k x_1)} \\ u_2 = 0 \\ u_3 = (W_1 e^{-\alpha_1 x_3} + W_2 e^{-\alpha_2 x_3}) e^{i(\omega t - k x_1)} \end{cases}$$

In such a case the boundary conditions are expressed as follows:

$$\begin{cases} (\alpha_1 U_1 + ikW_1) e^{-\alpha_1 x_3} + (\alpha_2 U_2 + ikW_2) e^{-\alpha_2 x_3} = 0 \\ (\alpha_1 c_{11} W_1 + ikc_{12} U_1) e^{-\alpha_1 x_3} + (\alpha_2 c_{11} W_2 + ikc_{12} U_2) e^{-\alpha_2 x_3} = 0 \end{cases} \quad (\text{B.5})$$

From eq. (B.1), the polarizations are related by:

$$\begin{cases} \frac{W_1}{U_1} = \frac{ik\alpha_1(c_{12}+c_{44})}{k^2 c_{44} - \alpha_1^2 c_{11} - \rho\omega^2} = \frac{iq_1(c_{12}+c_{44})}{c_{44} - q_1^2 c_{11} - \rho V_r^2} = r_1 \\ \frac{W_2}{U_2} = \frac{ik\alpha_2(c_{12}+c_{44})}{k^2 c_{44} - \alpha_2^2 c_{11} - \rho\omega^2} = \frac{iq_2(c_{12}+c_{44})}{c_{44} - q_2^2 c_{11} - \rho V_r^2} = r_2 \end{cases} \quad (\text{B.6})$$

Thus the boundary conditions are satisfied iff:

$$\begin{vmatrix} \alpha_1 + ikr_1 & \alpha_2 + ikr_2 \\ \alpha_1 r_1 c_{11} + ikc_{12} & \alpha_2 r_2 c_{11} + ikc_{12} \end{vmatrix} = 0$$

Plugging the expressions for amplitudes ratios r_1 , r_2 from eq. (B.6) we obtain after some simplification:

$$\begin{vmatrix} q_1^3 c_{11} + q_1(c_{12} + \rho V_r^2) & q_2^3 c_{11} + q_2(c_{12} + \rho V_r^2) \\ q_1^2 c_{11} c_{44} + c_{12}(c_{44} - \rho V_r^2) & q_2^2 c_{11} c_{44} + c_{12}(c_{44} - \rho V_r^2) \end{vmatrix} = 0$$

which yields:

$$(c_{44} - \rho V_r^2) \left(q_1^2 q_2^2 \frac{c_{11}^2 c_{44}}{(c_{44} - \rho V_r^2)} + (q_1^2 + q_2^2) c_{11} c_{12} + c_{12}(c_{12} + \rho V_r^2) \right) = q_1 q_2 c_{11} (c_{12} + c_{44}) \rho V_r^2$$

Squaring the above expression and making use of eq. (B.3) we have:

$$(c_{44} - \rho V_r^2) (c_{11}^2 - c_{12}^2 - c_{11} \rho V_r^2)^2 = c_{11} c_{44} (c_{11} - \rho V_r^2) (\rho V_r^2)^2$$

which can be put into the final dimensionless form:

$$\left(1 - \frac{c_{11}}{c_{44}} x\right) \left(1 - \frac{c_{12}^2}{c_{11}^2} - x\right)^2 = (1 - x) x^2 \quad (\text{B.7})$$

with $x = \frac{\rho V_r^2}{c_{11}}$.

Thus, if there exist a real solution of eq. (B.7), i.e. if boundary conditions are satisfied, we can calculate velocity of the Rayleigh wave. Furthermore, the particle displacement in such a wave can be expressed as:

$$u = \left[\begin{pmatrix} U_1 \\ 0 \\ W_1 \end{pmatrix} e^{-q_1 x'_3} + \begin{pmatrix} U_2 \\ 0 \\ W_2 \end{pmatrix} e^{-q_2 x'_3} \right] e^{i(\omega t - kx_1)}$$

where $x'_3 = kx_3$ is the normalized coordinate. Using eq. (B.6) we can re-write the above expression to obtain a normalized displacement:

$$\frac{u}{U_1} = \left[\begin{pmatrix} 1 \\ 0 \\ r_1 \end{pmatrix} e^{-q_1 x'_3} + \gamma \begin{pmatrix} 1 \\ 0 \\ r_2 \end{pmatrix} e^{-q_2 x'_3} \right] e^{i(\omega t - kx_1)} \quad (\text{B.8})$$

where γ is defined as the amplitude ratio following the expression eq. (B.5):

$$\frac{U_2}{U_1} = -\frac{\alpha_1 + ikr_1}{\alpha_2 + ikr_2} = -\frac{q_1 + ir_1}{q_2 + ir_2} = \gamma \quad (\text{B.9})$$

We now can use the analytical expressions eq. (B.2), eq. (B.7) and eq. (B.8) to determine the Rayleigh velocity, strain and displacements components for a wave, propagating in an anisotropic solid. We take the material constants of GaAs [154]:

$$\begin{cases} c_{11} &= 118.4 \text{ GPa} \\ c_{12} &= 53.7 \text{ GPa} \\ c_{44} &= 59.1 \text{ GPa} \\ \rho &= 5317 \text{ kg/m}^3 \end{cases}$$

Solving eq. (B.7) numerically, we obtain the Rayleigh velocity along [100] direction equal to 2711 m/s, as can be seen in the appendix B.

The eq. (B.2) does not yield real solutions, as can be visualized in (appendix B), but complex with real part positive: $q \simeq 0.402 \pm i0.561$. We thus express:

$$\begin{cases} q_1 &= q_R + iq_I \\ q_2 &= q_R - iq_I = \bar{q}_1 \end{cases}$$

Figure B.1: Determining the Rayleigh velocity from the eq. (B.7). The smallest solution is Rayleigh velocity, the other two correspond to the mode, we do not excite experimentally.

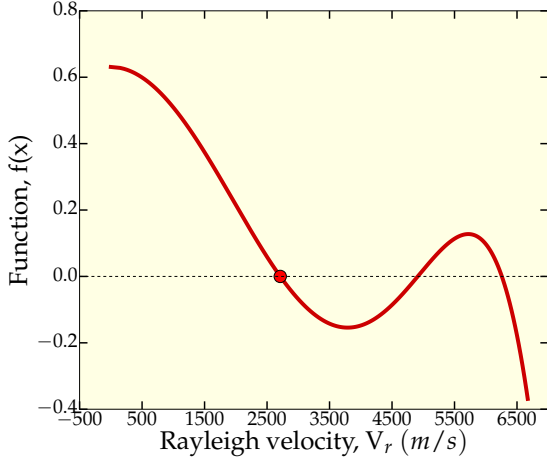
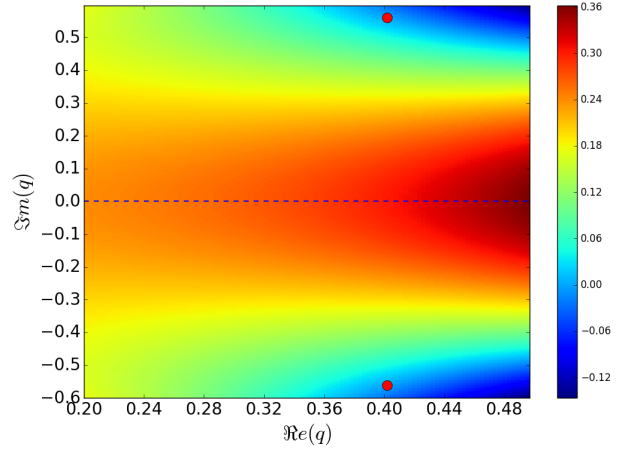


Figure B.2: Colorplot of the function eq. (B.2), function vanishes at $q = 0.402 \pm i0.561$ (red dots).



It follows from eq. (B.6) that $r_2 = -\bar{r}_1$. Furthermore, $\gamma = -\frac{q_1 + ir_1}{q_2 + ir_2}$ and $\bar{\gamma} = -\frac{q_2 + ir_2}{q_1 + ir_1}$, so that $|\gamma| = 1$. Ratios r_1 , r_2 and γ are conveniently expressed as:

$$\begin{cases} r_1 &= r e^{i\psi} \\ r_2 &= r e^{i(\pi - \psi)} \\ \gamma &= e^{i\phi} \end{cases} \quad (\text{B.10})$$

Phases ψ and ϕ can be evaluated using the eq. (B.6) and eq. (B.9), respectively. Given the eq. (B.10), we can express the normalized displacements:

$$\frac{u}{U_1} = e^{-q_R x'_3} e^{i(\omega t - kx_1)} \begin{pmatrix} e^{i(q_I x'_3 + \phi)} + e^{-i q_I x'_3} \\ 0 \\ -r(e^{i(q_I x'_3 - \psi + \phi)} - e^{-i(q_I x'_3 - \psi)}) \end{pmatrix}$$

or

$$\frac{u}{U_1} = 2 e^{i\frac{\phi}{2}} e^{-q_R x'_3} e^{i(\omega t - kx_1)} \begin{pmatrix} \cos\left(q_I x'_3 + \frac{\phi}{2}\right) \\ 0 \\ -ir \sin\left(q_I x'_3 - \psi + \frac{\phi}{2}\right) \end{pmatrix} \quad (\text{B.11})$$

and consequently taking the real part of the above expression yields:

$$\begin{cases} u_x = \operatorname{Re}\left(\frac{u_1}{U_1}\right) = 2 \cos\left(\frac{\phi}{2} + \omega t - kx\right) \cos\left(q_I x'_3 + \frac{\phi}{2}\right) e^{-q_R x'_3} \\ u_y = \operatorname{Re}\left(\frac{u_2}{U_1}\right) = 0 \\ u_z = \operatorname{Re}\left(\frac{u_3}{U_1}\right) = 2r \sin\left(\frac{\phi}{2} + \omega t - kx\right) \sin\left(q_I x'_3 - \psi + \frac{\phi}{2}\right) e^{-q_R x'_3} \end{cases} \quad (\text{B.12})$$

Strain components can be found from the obtained expressions for the normalized displacement components:

$$\begin{cases} \varepsilon_{xx} = \operatorname{Re}\left(\frac{\varepsilon_{11}}{kU_1}\right) = 2 \sin\left(\frac{\phi}{2} + \omega t - kx_1\right) \cos\left(q_I x'_3 + \frac{\phi}{2}\right) e^{-q_R x'_3} \\ \varepsilon_{xz} = \operatorname{Re}\left(\frac{\varepsilon_{13}}{kU_1}\right) = -\cos\left(\frac{\phi}{2} + \omega t - kx_1\right) \left\{ q_R \cos\left(q_I x'_3 + \frac{\phi}{2}\right) + q_I \sin\left(q_I x'_3 + \frac{\phi}{2}\right) + r \sin\left(q_I x'_3 - \psi + \frac{\phi}{2}\right) \right\} e^{-q_R x'_3} \\ \varepsilon_{zz} = \operatorname{Re}\left(\frac{\varepsilon_{33}}{kU_1}\right) = 2r \sin\left(\frac{\phi}{2} + \omega t - kx_1\right) \left\{ -q_R \sin\left(q_I x'_3 - \psi + \frac{\phi}{2}\right) + q_I \cos\left(q_I x'_3 - \psi + \frac{\phi}{2}\right) \right\} e^{-q_R x'_3} \end{cases} \quad (\text{B.13})$$

To summarize, we find:

$$\begin{cases} q_1 = 0.402 - i 0.561 \\ q_2 = 0.402 + i 0.561 \\ r_1 = 1.1224 - i 0.3826 = 1.186 e^{-0.328 i} \\ r_2 = -1.1224 - i 0.3826 = 1.186 e^{-2.81 i} \\ \gamma = -0.3228 - i 0.9465 = e^{-1.899 i} \end{cases}$$

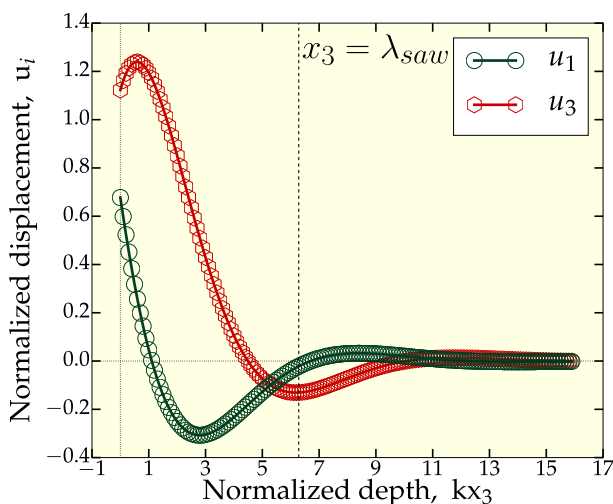


Figure B.3: Normalized displacement components vs normalized depth, eq. (B.12)

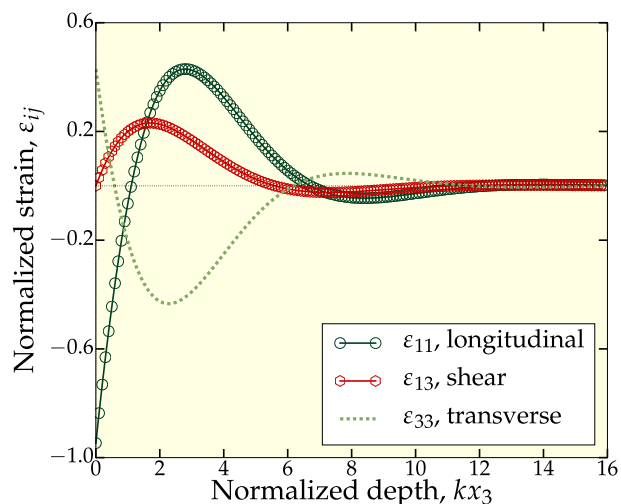


Figure B.4: Normalized strain components vs normalized depth, eq. (B.13)

Appendix C

Expression for free energy density

Free energy density for a **cubic system** is expressed in terms of θ , φ angles and strain components. Note that, as explained in chapter 3, our samples exhibit both biaxial and uniaxial in-plane anisotropy and thus, this uniaxial MCA term appears in the final expression. \mathbf{H} stands for the applied H-field, θ_H and φ_H are the applied field angles, M_s saturation magnetization.

$$\begin{aligned}
 F = F_Z + F_d + F_{biax} + F_{uni} + F_{mel} + F_{el} = & \\
 & \underbrace{-\mu_0 H M_s \left(\cos \theta \cos \theta_H + \sin \theta \sin \theta_H \cos(\varphi - \varphi_H) \right)}_{F_Z} + \underbrace{\frac{1}{2} \mu_0 M_s^2 \cos^2 \theta}_{F_d} + \\
 & \underbrace{\frac{K_1}{4} \left(\sin^4 \theta \sin^2(2\varphi) + \sin^2(2\theta) \right)}_{F_{biax}} + \underbrace{K_{ip} \sin^2 \theta \cos^2 \left(\varphi - \frac{\pi}{4} \right)}_{F_{uni}} + \\
 & B_1 \left(\varepsilon_{11} \left(\sin^2 \theta \cos^2 \varphi - \frac{1}{3} \right) + \varepsilon_{22} \left(\sin^2 \theta \sin^2 \varphi - \frac{1}{3} \right) + \varepsilon_{33} \left(\cos^2 \theta - \frac{1}{3} \right) \right) + \\
 & + \underbrace{\frac{B_2}{2} \left(\varepsilon_{12} \sin^2 \theta \sin(2\varphi) + \sin(2\theta) \left[\varepsilon_{13} \cos \varphi + \varepsilon_{23} \sin \varphi \right] \right)}_{F_{mel}} + \\
 & \underbrace{\frac{c_{11}}{2} \left(\varepsilon_{11}^2 + \varepsilon_{22}^2 + \varepsilon_{33}^2 \right) + 2c_{44} \left(\varepsilon_{12}^2 + \varepsilon_{13}^2 + \varepsilon_{23}^2 \right) + c_{12} \left(\varepsilon_{11}\varepsilon_{22} + \varepsilon_{11}\varepsilon_{33} + \varepsilon_{22}\varepsilon_{33} \right)}_{F_{el}}
 \end{aligned} \tag{C.1}$$

Appendix D

Expressions for angular variations

$$\delta\theta(t), \delta\varphi(t)$$

In eq. (2.6), chapter 2 we defined the equation for torque density:

$$\mathbf{T} = i\omega \frac{M_s}{\gamma} \left(\delta\theta \mathbf{e}_\theta + \sin\bar{\theta} \delta\varphi \mathbf{e}_\varphi \right)$$

To express $\delta\theta$, $\delta\varphi$ we will make use of LLG equation:

$$\frac{d\mathbf{m}(t)}{dt} = \gamma_0 \mathbf{m}(t) \times \mathbf{H}_{eff}(t) + \alpha \mathbf{m}(t) \times \frac{d\mathbf{m}(t)}{dt}$$

We express effective field as the gradient of the total energy density, $\mathbf{H}_{eff} = -\frac{1}{\mu_0} \nabla f$ in spherical coordinates:

$$\nabla f = \frac{\partial f}{\partial r} \mathbf{e}_r + \frac{1}{r} \frac{\partial f}{\partial \theta} \mathbf{e}_\theta + \frac{1}{r \sin \theta} \frac{\partial f}{\partial \varphi} \mathbf{e}_\varphi$$

Since $r = |\mathbf{m}| = |\mathbf{e}_r| = 1$ is conserved, we have:

$$\nabla f = \frac{\partial f}{\partial \theta} \mathbf{e}_\theta + \frac{1}{\sin \theta} \frac{\partial f}{\partial \varphi} \mathbf{e}_\varphi \tag{D.1}$$

The terms of LLG-equation can be expressed as:

(i)

$$\frac{d\mathbf{m}}{dt} = \frac{d\theta}{dt} \mathbf{e}_\theta + \sin \theta \frac{d\varphi}{dt} \mathbf{e}_\varphi$$

(ii)

$$\gamma_0 \mathbf{m}(t) \times \mathbf{H}_{eff}(t) = |\gamma| \frac{\partial f}{\partial \theta} \mathbf{e}_\varphi - \frac{|\gamma|}{\sin \theta} \frac{\partial f}{\partial \varphi} \mathbf{e}_\theta$$

(iii)

$$\alpha \mathbf{m}(t) \times \frac{d\mathbf{m}(t)}{dt} = \alpha \frac{d\theta}{dt} \mathbf{e}_\varphi - \frac{\alpha}{\sin \theta} \frac{d\varphi}{dt} \mathbf{e}_\theta$$

That can be split into two equations:

$$\begin{cases} \frac{d\theta}{dt} = -\frac{|\gamma|}{\sin\theta} \frac{\partial f}{\partial\varphi} - \alpha \sin\theta \frac{d\varphi}{dt} \\ \frac{d\varphi}{dt} = \frac{|\gamma|}{\sin\theta} \frac{\partial f}{\partial\theta} + \frac{\alpha}{\sin\theta} \frac{d\theta}{dt} \end{cases}$$

Regrouping yields two separate equations for $\delta\theta$ and $\delta\varphi$:

$$\begin{cases} \frac{d\theta}{dt} = -\frac{\alpha|\gamma|}{(1+\alpha^2)} \frac{\partial f}{\partial\theta} - \frac{|\gamma|}{(1+\alpha^2)} \frac{1}{\sin\theta} \frac{\partial f}{\partial\varphi} \\ \frac{d\varphi}{dt} = \frac{|\gamma|}{(1+\alpha^2)} \frac{1}{\sin\theta} \frac{\partial f}{\partial\theta} - \frac{\alpha|\gamma|}{(1+\alpha^2)} \frac{1}{\sin^2\theta} \frac{\partial f}{\partial\varphi} \end{cases} \quad (\text{D.2})$$

The right hand side of the eq. (D.2) can be Taylor-expanded about the equilibrium position $(\bar{\theta}, \bar{\varphi}, \bar{\varepsilon}_{ij})$:

$$\left\{ \begin{array}{l} \frac{\partial f}{\partial\theta} \simeq \frac{\partial f}{\partial\theta}|_{eq} + \frac{\partial^2 f}{\partial\theta^2}|_{eq} \delta\theta + \frac{\partial^2 f}{\partial\varphi\partial\theta}|_{eq} \delta\varphi + \frac{\partial^2 f}{\partial\varepsilon_{ij}\partial\theta}|_{eq} \delta\varepsilon_{ij} \\ \frac{1}{\sin\theta} \frac{\partial f}{\partial\varphi} \simeq \frac{1}{\sin\bar{\theta}} \frac{\partial f}{\partial\varphi}|_{eq} + \left[\frac{1}{\sin\bar{\theta}} \frac{\partial^2 f}{\partial\theta\partial\varphi}|_{eq} - \frac{\cos\bar{\theta}}{\sin^2\bar{\theta}} \frac{\partial f}{\partial\varphi}|_{eq} \right] \delta\theta + \frac{1}{\sin\bar{\theta}} \frac{\partial^2 f}{\partial\varphi^2}|_{eq} \delta\varphi + \frac{1}{\sin\bar{\theta}} \frac{\partial^2 f}{\partial\varepsilon_{ij}\partial\varphi}|_{eq} \delta\varepsilon_{ij} \\ \frac{1}{\sin\theta} \frac{\partial f}{\partial\theta} \simeq \frac{1}{\sin\bar{\theta}} \frac{\partial f}{\partial\theta}|_{eq} + \left[\frac{1}{\sin\bar{\theta}} \frac{\partial^2 f}{\partial\theta^2}|_{eq} - \frac{\cos\bar{\theta}}{\sin^2\bar{\theta}} \frac{\partial f}{\partial\theta}|_{eq} \right] \delta\theta + \frac{1}{\sin\bar{\theta}} \frac{\partial^2 f}{\partial\varphi\partial\theta}|_{eq} \delta\varphi + \frac{1}{\sin\bar{\theta}} \frac{\partial^2 f}{\partial\varepsilon_{ij}\partial\theta}|_{eq} \delta\varepsilon_{ij} \\ \frac{1}{\sin^2\theta} \frac{\partial f}{\partial\varphi} \simeq \frac{1}{\sin^2\bar{\theta}} \frac{\partial f}{\partial\varphi}|_{eq} + \left[\frac{1}{\sin^2\bar{\theta}} \frac{\partial^2 f}{\partial\theta\partial\varphi}|_{eq} - \frac{2\cos\bar{\theta}}{\sin^3\bar{\theta}} \frac{\partial f}{\partial\varphi}|_{eq} \right] \delta\theta + \frac{1}{\sin^2\bar{\theta}} \frac{\partial^2 f}{\partial\varphi^2}|_{eq} \delta\varphi + \frac{1}{\sin^2\bar{\theta}} \frac{\partial^2 f}{\partial\varepsilon_{ij}\partial\varphi}|_{eq} \delta\varepsilon_{ij} \end{array} \right.$$

First derivatives in the expansion should vanish at equilibrium, thus only second order terms are retained:

$$\left\{ \begin{array}{l} \frac{\partial f}{\partial\theta} \simeq f_{\theta\theta} \delta\theta + f_{\theta\varphi} \delta\varphi + f_{\theta\varepsilon_{ij}} \delta\varepsilon_{ij} \\ \frac{1}{\sin\theta} \frac{\partial f}{\partial\varphi} \simeq \frac{1}{\sin\bar{\theta}} f_{\theta\varphi} \delta\theta + \frac{1}{\sin\bar{\theta}} f_{\varphi\varphi} \delta\varphi + \frac{1}{\sin\bar{\theta}} f_{\varphi\varepsilon_{ij}} \delta\varepsilon_{ij} \\ \frac{1}{\sin\theta} \frac{\partial f}{\partial\theta} \simeq \frac{1}{\sin\bar{\theta}} f_{\theta\theta} \delta\theta + \frac{1}{\sin\bar{\theta}} f_{\theta\varphi} \delta\varphi + \frac{1}{\sin\bar{\theta}} f_{\theta\varepsilon_{ij}} \delta\varepsilon_{ij} \\ \frac{1}{\sin^2\theta} \frac{\partial f}{\partial\varphi} \simeq \frac{1}{\sin^2\bar{\theta}} f_{\theta\varphi} \delta\theta + \frac{1}{\sin^2\bar{\theta}} f_{\varphi\varphi} \delta\varphi + \frac{1}{\sin^2\bar{\theta}} f_{\varphi\varepsilon_{ij}} \delta\varepsilon_{ij} \end{array} \right. \quad (\text{D.3})$$

where we adapted a compact notation $\frac{\partial^2 h}{\partial x \partial y} = h_{xy}$. Plugging the eq. (D.3) into the eq. (D.2) we obtain:

$$\begin{cases} \frac{d\theta}{dt} = \zeta_1 \delta\theta + \zeta_2 \delta\varphi + \sum_{i \leq j} \zeta_{ij} \delta\varepsilon_{ij} \\ \frac{d\varphi}{dt} = \kappa_1 \delta\theta + \kappa_2 \delta\varphi + \sum_{i \leq j} \kappa_{ij} \delta\varepsilon_{ij} \end{cases} \quad (\text{D.4})$$

where:

$$\begin{cases} \zeta_1 = -\frac{\alpha|\gamma|}{1+\alpha^2} f_{\theta\theta} - \frac{|\gamma|}{1+\alpha^2} \frac{1}{\sin\bar{\theta}} f_{\theta\varphi} \\ \zeta_2 = -\frac{\alpha|\gamma|}{1+\alpha^2} f_{\theta\varphi} - \frac{|\gamma|}{1+\alpha^2} \frac{1}{\sin\bar{\theta}} f_{\varphi\varphi} \\ \zeta_{ij} = -\frac{\alpha|\gamma|}{1+\alpha^2} f_{\theta\varepsilon_{ij}} - \frac{|\gamma|}{1+\alpha^2} \frac{1}{\sin\bar{\theta}} f_{\varphi\varepsilon_{ij}} \end{cases} \quad (\text{D.5})$$

$$\begin{cases} \kappa_1 = \frac{|\gamma|}{1+\alpha^2} \frac{1}{\sin\bar{\theta}} f_{\theta\theta} - \frac{\alpha|\gamma|}{1+\alpha^2} \frac{1}{\sin^2\bar{\theta}} f_{\theta\varphi} \\ \kappa_2 = \frac{|\gamma|}{1+\alpha^2} \frac{1}{\sin\bar{\theta}} f_{\theta\varphi} - \frac{\alpha|\gamma|}{1+\alpha^2} \frac{1}{\sin^2\bar{\theta}} f_{\varphi\varphi} \\ \kappa_{ij} = \frac{|\gamma|}{1+\alpha^2} \frac{1}{\sin\bar{\theta}} f_{\theta\varepsilon_{ij}} - \frac{\alpha|\gamma|}{1+\alpha^2} \frac{1}{\sin^2\bar{\theta}} f_{\varphi\varepsilon_{ij}} \end{cases} \quad (\text{D.6})$$

Assuming the exponential time-dependence of $\delta\theta$, $\delta\varphi$, the eq. (D.4) yields:

$$\begin{cases} \delta\theta = \sum_{i \leq j} \frac{(\kappa_2 \zeta_{ij} - \zeta_2 \kappa_{ij} - i\omega \zeta_{ij}) \delta\varepsilon_{ij}}{\zeta_2 \kappa_1 - \zeta_1 \kappa_2 + \omega^2 + i\omega(\zeta_1 + \kappa_2)} \\ \delta\varphi = \sum_{i \leq j} \frac{(\zeta_1 \kappa_{ij} - \kappa_1 \zeta_{ij} - i\omega \kappa_{ij}) \delta\varepsilon_{ij}}{\zeta_2 \kappa_1 - \zeta_1 \kappa_2 + \omega^2 + i\omega(\zeta_1 + \kappa_2)} \end{cases}$$

Appendix E

First and second order derivatives of free energy density

1. First order derivative with respect to θ , $\frac{\partial F}{\partial \theta}$

$$\begin{aligned} \frac{\partial F}{\partial \theta} = & \mu_0 H M_s \left(\sin \theta \cos \theta_H - \cos \theta \sin \theta_H \cos(\varphi - \varphi_H) \right) - \frac{1}{2} \mu_0 M_s^2 \sin(2\theta) + \\ & \frac{K_1}{2} \sin(2\theta) \left(\sin^2 \theta \sin^2(2\varphi) + 2 \cos(2\theta) \right) + K_{ip} \sin(2\theta) \cos^2\left(\varphi - \frac{\pi}{4}\right) + \\ & B_1 \sin(2\theta) \left(\varepsilon_{11} \cos^2 \varphi + \varepsilon_{22} \sin^2 \varphi - \varepsilon_{33} \right) + \\ & B_2 \left(\frac{1}{2} \varepsilon_{12} \sin(2\theta) \sin(2\varphi) + \cos(2\theta) (\varepsilon_{13} \cos \varphi + \varepsilon_{23} \sin \varphi) \right) \end{aligned} \quad (\text{E.1})$$

2. First order derivative with respect to φ , $\frac{\partial F}{\partial \varphi}$

$$\begin{aligned} \frac{\partial F}{\partial \varphi} = & \mu_0 H M_s \sin \theta \sin \theta_H \sin(\varphi - \varphi_H) + \frac{K_1}{2} \sin^4 \theta \sin(4\varphi) - K_{ip} \sin^2 \theta \sin\left(2\varphi - \frac{\pi}{2}\right) + \\ & B_1 \sin(2\varphi) \sin^2 \theta (\varepsilon_{22} - \varepsilon_{11}) + B_2 \left(\varepsilon_{12} \sin^2 \theta \cos(2\varphi) + \frac{\sin(2\theta)}{2} (\varepsilon_{23} \cos \varphi - \varepsilon_{13} \sin \varphi) \right) \end{aligned} \quad (\text{E.2})$$

3. Second order derivative with respect to θ , $\mathbf{F}_{\theta\theta}$

$$\begin{aligned} \frac{\partial^2 F}{\partial \theta^2} = & \mu_0 H M_s \left(\cos \theta \cos \theta_H + \sin \theta \sin \theta_H \cos(\varphi - \varphi_H) \right) - \mu_0 M_s^2 \cos(2\theta) + \\ & K_1 \left(\sin^2(2\varphi) \left[\cos(2\theta) \sin^2 \theta + \frac{1}{2} \sin^2(2\theta) \right] + 2 \cos(4\theta) \right) + 2K_{ip} \cos(2\theta) \cos^2\left(\varphi - \frac{\pi}{4}\right) + \\ & 2B_1 \cos(2\theta) \left(\varepsilon_{11} \cos^2 \varphi + \varepsilon_{22} \sin^2 \varphi - \varepsilon_{33} \right) + \\ & B_2 \left(\varepsilon_{12} \cos(2\theta) \sin(2\varphi) - 2 \sin(2\theta) \left[\varepsilon_{13} \cos \varphi + \varepsilon_{23} \sin \varphi \right] \right) \end{aligned}$$

4. Second order derivative with respect to φ , $\mathbf{F}_{\varphi\varphi}$

$$\begin{aligned} \frac{\partial^2 F}{\partial \varphi^2} = & \mu_0 H M_s \sin \theta \sin \theta_H \cos(\varphi - \varphi_H) + 2K_1 \sin^4 \theta \cos(4\varphi) - 2K_{ip} \sin^2 \theta \cos\left(2\varphi - \frac{\pi}{2}\right) + \\ & 2B_1 \cos(2\varphi) \sin^2 \theta (\varepsilon_{22} - \varepsilon_{11}) - 2B_2 \left(\varepsilon_{12} \sin^2 \theta \sin(2\varphi) + \frac{\sin(2\theta)}{4} (\varepsilon_{13} \cos \varphi + \varepsilon_{23} \sin \varphi) \right) \end{aligned}$$

5. Second order derivative with respect to θ , φ , $\mathbf{F}_{\theta\varphi}$

$$\begin{aligned} \frac{\partial^2 F}{\partial \theta \partial \varphi} = & \mu_0 H M_s \cos \theta \sin \theta_H \sin(\varphi - \varphi_H) + K_1 \sin^2 \theta \sin(2\theta) \sin(4\varphi) - K_{ip} \sin(2\theta) \sin\left(2\varphi - \frac{\pi}{2}\right) + \\ & B_1 \sin(2\theta) \sin(2\varphi) (\varepsilon_{22} - \varepsilon_{11}) + B_2 \left(\varepsilon_{12} \sin(2\theta) \cos(2\varphi) + \cos(2\theta) \left[\varepsilon_{23} \cos \varphi - \varepsilon_{13} \sin \varphi \right] \right) \end{aligned}$$

6. Second order derivative with respect to θ , ε_{ij} , $\mathbf{F}_{\theta\varepsilon_{ij}}$ and φ , ε_{ij} , $\mathbf{F}_{\varphi\varepsilon_{ij}}$

$$\begin{cases} F_{\theta\varepsilon_{11}} = B_1 \sin(2\theta) \cos^2 \varphi \\ F_{\theta\varepsilon_{22}} = B_1 \sin(2\theta) \sin^2 \varphi \\ F_{\theta\varepsilon_{33}} = -B_1 \sin(2\theta) \\ F_{\theta\varepsilon_{12}} = \frac{B_2}{2} \sin(2\theta) \sin(2\varphi) \\ F_{\theta\varepsilon_{13}} = B_2 \cos(2\theta) \cos \varphi \\ F_{\theta\varepsilon_{23}} = B_2 \cos(2\theta) \sin \varphi \end{cases} \quad \begin{cases} F_{\varphi\varepsilon_{11}} = -B_1 \sin^2 \theta \sin(2\varphi) \\ F_{\varphi\varepsilon_{22}} = B_1 \sin^2 \theta \sin(2\varphi) \\ F_{\varphi\varepsilon_{33}} = 0 \\ F_{\varphi\varepsilon_{12}} = B_2 \sin^2 \theta \cos(2\varphi) \\ F_{\varphi\varepsilon_{13}} = -\frac{B_2}{2} \sin(2\theta) \sin \varphi \\ F_{\varphi\varepsilon_{23}} = \frac{B_2}{2} \sin(2\theta) \cos \varphi \end{cases}$$

Appendix F

Strain and magnetization orientation at equilibrium

To find the equilibrium strain and magnetization orientation, $\bar{\varepsilon}_{ij}$, $\bar{\theta}$, $\bar{\varphi}$ we minimize the energy density, eq. (C.1):

$$\frac{\partial F}{\partial \theta} \Big|_{eq} = \frac{\partial F}{\partial \varphi} \Big|_{eq} = \frac{\partial F}{\partial \varepsilon_{ij}} \Big|_{eq} = 0$$

First, we search for the equilibrium strain values. We express the corresponding derivatives in terms of the magnetization directional cosines (section 1.2.4, fig. 1.15) as:

$$\begin{cases} \frac{\partial F}{\partial \varepsilon_{12}} = B_2 m_1 m_2 + 4c_{44} \varepsilon_{12} \\ \frac{\partial F}{\partial \varepsilon_{13}} = B_2 m_1 m_3 + 4c_{44} \varepsilon_{13} \\ \frac{\partial F}{\partial \varepsilon_{23}} = B_2 m_2 m_3 + 4c_{44} \varepsilon_{23} \end{cases}$$

At equilibrium derivatives vanish for $\varepsilon_{ij} = -\frac{B_2}{4c_{44}} m_i m_j$, $i \neq j$ and thus we obtain:

$$\boxed{\bar{\varepsilon}_{ij} = -\frac{B_2}{4c_{44}} \bar{m}_i \bar{m}_j} \quad i \neq j$$

On the other hand,

$$\begin{cases} \frac{\partial F}{\partial \varepsilon_{11}} \Big|_{eq} = B_1 \left(m_1^2 - \frac{1}{3} \right) + c_{11} \varepsilon_{11} + c_{12} (\varepsilon_{22} + \varepsilon_{33}) = 0 \\ \frac{\partial F}{\partial \varepsilon_{22}} \Big|_{eq} = B_1 \left(m_2^2 - \frac{1}{3} \right) + c_{11} \varepsilon_{22} + c_{12} (\varepsilon_{11} + \varepsilon_{33}) = 0 \\ \frac{\partial F}{\partial \varepsilon_{33}} \Big|_{eq} = B_1 \left(m_3^2 - \frac{1}{3} \right) + c_{11} \varepsilon_{33} + c_{12} (\varepsilon_{11} + \varepsilon_{22}) = 0 \end{cases}$$

or

$$\underbrace{\begin{pmatrix} c_{11} & c_{12} & c_{12} \\ c_{12} & c_{11} & c_{12} \\ c_{12} & c_{12} & c_{11} \end{pmatrix}}_C \cdot \underbrace{\begin{pmatrix} \varepsilon_{11} \\ \varepsilon_{22} \\ \varepsilon_{33} \end{pmatrix}}_E = -B_1 \underbrace{\begin{pmatrix} m_1^2 - \frac{1}{3} \\ m_2^2 - \frac{1}{3} \\ m_3^2 - \frac{1}{3} \end{pmatrix}}_M$$

which yields:

$$\mathbf{E} = -B_1 C^{-1} \mathbf{M}$$

with $\det C = (c_{12} - c_{11}) [2c_{12}^2 - c_{11}(c_{11} + c_{12})]$ and

$$C^{-1} = \frac{1}{2c_{12}^2 - c_{11}(c_{11} + c_{12})} \begin{pmatrix} -(c_{11} + c_{12}) & c_{12} & c_{12} \\ c_{12} & -(c_{11} + c_{12}) & c_{12} \\ c_{12} & c_{12} & -(c_{11} + c_{12}) \end{pmatrix}$$

Using $m_1^2 + m_2^2 + m_3^2 = 1$ (the magnetization norm is conserved), we after some algebra obtain:

$$\begin{pmatrix} \varepsilon_{11} \\ \varepsilon_{22} \\ \varepsilon_{33} \end{pmatrix} = \frac{B_1}{2c_{12}^2 - c_{11}(c_{11} + c_{12})} \begin{pmatrix} (m_1^2 - \frac{1}{3})(c_{11} + 2c_{12}) \\ (m_2^2 - \frac{1}{3})(c_{11} + 2c_{12}) \\ (m_3^2 - \frac{1}{3})(c_{11} + 2c_{12}) \end{pmatrix}$$

Proportionality constant can be simplified:

$$\frac{B_1(c_{11} + 2c_{12})}{2c_{12}^2 - c_{11}(c_{11} + c_{12})} = \frac{B_1(c_{11} + 2c_{12})}{(c_{12} - c_{11})(2c_{12} + c_{11})} = \frac{B_1}{(c_{12} - c_{11})} = -\frac{B_1}{2c'_{66}}$$

where c'_{66} is defined as $c'_{66} = \frac{(c_{11} - c_{12})}{2}$. Finally we obtain:

$$\boxed{\bar{\varepsilon}_{ii} = -\frac{B_1}{2c'_{66}} \bar{m}_i^2 + \frac{B_1}{6c'_{66}}}$$

It follows immediately that the trace of the strain matrix vanishes

$$\sum_i \bar{\varepsilon}_{ii} = -\frac{B_1}{2c'_{66}} + 3 \cdot \frac{B_1}{6c'_{66}} = 0$$

This implies the volume conservation.

To deduce the equilibrium magnetization orientation we use the obtained expressions for strain, $\bar{\varepsilon}_{ij}$. At **zero field**, from the eq. (E.1) we have:

$$\begin{aligned} \frac{\partial F_{tot}}{\partial \theta} \Big|_{eq} &= -\frac{1}{2}\mu_0 M_0^2 \sin(2\theta) + \left(\frac{K_1}{2} + \frac{B_2^2}{16c_{44}}\right) \sin(2\theta) \left[\sin^2 \theta \sin^2(2\varphi) + 2 \cos(2\theta)\right] + \\ &K_{ip} \sin(2\theta) \cos^2\left(\varphi - \frac{\pi}{4}\right) + \frac{B_1^2}{2c'_{66}} \left[\cos^2 \theta - \sin^2 \theta (\cos^4 \varphi + \sin^4 \varphi)\right] \sin(2\theta) \end{aligned} \quad (F.1)$$

It follows that for any value of $\bar{\varphi}$ the derivative vanishes, if $\bar{\theta} = \frac{\pi}{2}$ or $\bar{\theta} = 0$. This results in the in-plane and out-of-plane magnetization orientation, respectively. Since for $\bar{\theta} = 0$ the in-plane angle $\bar{\varphi}$ is undefined, $\bar{\theta}$ should be necessary $\frac{\pi}{2}$, setting the in-plane magnetization orientation. We also notice that the first term, resulting from the demagnetizing energy, is independent of the in-plane orientation, $\bar{\varphi}$. Given the above argument, this term vanishes when $\bar{\theta} = \frac{\pi}{2}$. Physically this means, that the demagnetizing field keeps the magnetization in-plane.

The situation is different when a magnetic field is applied out-of-plane, but we do not consider such cases here. We thus assume the in-plane magnetization orientation and search numerically for the equilibrium angle, that is $\frac{\partial F}{\partial \varphi} \Big|_{\bar{\varphi}} = 0$ and $\frac{\partial^2 F}{\partial \varphi^2} \Big|_{\bar{\varphi}} > 0$, given:

$$\left\{ \begin{aligned} \frac{\partial F}{\partial \varphi} \Big|_{\bar{\varphi}} &= \mu_0 H M_s \sin(\bar{\varphi} - \varphi_H) - K_{ip} \sin\left(2\bar{\varphi} - \frac{\pi}{2}\right) + \left(\frac{K_1}{2} + \frac{B_1^2}{4c'_{66}} - \frac{B_2^2}{16c'_{44}}\right) \sin(4\bar{\varphi}) \\ \frac{\partial^2 F}{\partial \varphi^2} \Big|_{\bar{\varphi}} &= \mu_0 H M_s \cos(\bar{\varphi} - \varphi_H) + 2K_1 \cos(4\bar{\varphi}) - 2K_{ip} \cos\left(2\bar{\varphi} - \frac{\pi}{2}\right) + \frac{B_1^2}{c'_{66}} \cos^2(2\bar{\varphi}) + \frac{B_2^2}{4c_{44}} \sin^2(2\bar{\varphi}) \end{aligned} \right. \quad (F.2)$$

Several solutions are possible, as represented in fig. F.1 - fig. F.2. At zero field there exist four possible equilibrium orientations along the easy axes. Due to the uniaxial MCA, the easy axes are slightly shifted with respect to main crystallographic directions. With the increasing field, only one possible set of solutions remains. To compute the equilibrium angle, we follow the experimental protocol, i.e. we start at high field and reduce it progressively to zero. In such a case, the magnetization will rotate towards the closest easy axis. For example, close to [100] or [010] for the field applied at 35° (fig. F.1) or 65° (fig. F.2), respectively.

Figure F.1: Evolution of equilibrium angle, $\bar{\varphi}$ with the intensity of the applied field (left). Polar plot of the MCA energy density and the direction of the applied field, $\varphi_H = 35^\circ$ (right). At zero field four equilibrium orientations are possible along the easy axes. The latter are slightly shifted from the main crystallographic directions due to the uniaxial MCA.

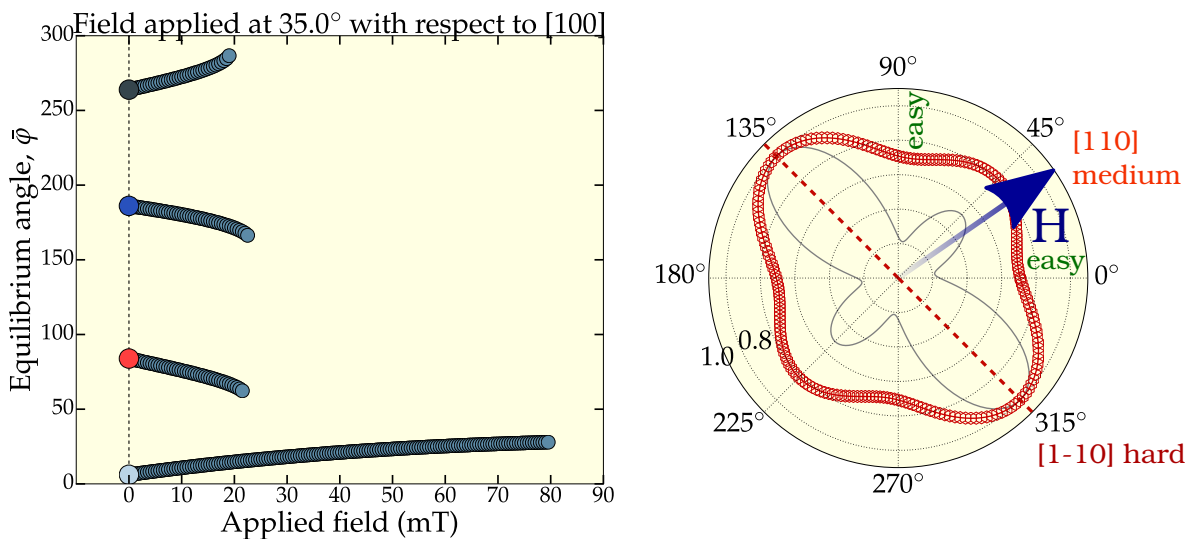
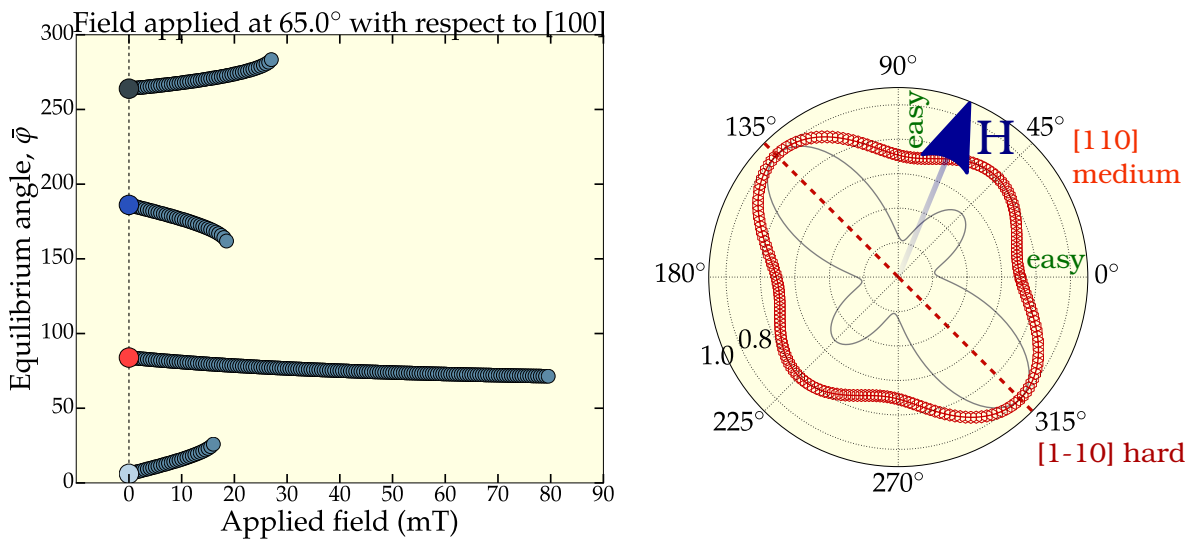


Figure F.2: Evolution of the equilibrium angle, $\bar{\varphi}$ with the intensity of the applied field (left). Polar plot of the MCA energy density and the direction of the applied field, $\varphi_H = 65^\circ$ (right).



Appendix G

Kappa, κ_i , κ_{ij} and zeta, ζ_i , ζ_{ij} terms

For the in-plane equilibrium orientation of the magnetization, $\bar{\theta} = \frac{\pi}{2}$ the eq. (D.5) and the eq. (D.6) can be simplified (given the second order derivatives in the appendix E):

$$\begin{cases} \kappa_1 &= |\eta| F_{\theta\theta}|_{eq} \\ \kappa_2 &= -\alpha|\eta| F_{\varphi\varphi}|_{eq} = \alpha\zeta_2 \\ \zeta_1 &= -\alpha|\eta| F_{\theta\theta}|_{eq} = -\alpha\kappa_1 \\ \zeta_2 &= -|\eta| F_{\varphi\varphi}|_{eq} \end{cases}$$

$$\begin{cases} \zeta_{11} &= |\eta|B_1 \sin(2\bar{\varphi}) \\ \zeta_{22} &= -|\eta|B_1 \sin(2\bar{\varphi}) = -\zeta_{11} \\ \zeta_{12} &= -|\eta|B_2 \cos(2\bar{\varphi}) \\ \zeta_{13} &= \alpha|\eta|B_2 \cos \bar{\varphi} = -\alpha\kappa_{13} \\ \zeta_{23} &= \alpha|\eta|B_2 \sin \bar{\varphi} = -\alpha\kappa_{23} \\ \zeta_{33} &= 0 \end{cases} \quad \begin{cases} \kappa_{11} &= \alpha|\eta|B_1 \sin(2\bar{\varphi}) = \alpha\zeta_{11} \\ \kappa_{22} &= -\alpha|\eta|B_1 \sin(2\bar{\varphi}) = -\alpha\zeta_{11} \\ \kappa_{12} &= -\alpha|\eta|B_2 \cos(2\bar{\varphi}) = \alpha\zeta_{12} \\ \kappa_{13} &= -|\eta|B_2 \cos \bar{\varphi} \\ \kappa_{23} &= -|\eta|B_2 \sin \bar{\varphi} \\ \kappa_{33} &= 0 \end{cases}$$

Appendix H

Relative change in velocity $\frac{\Delta V}{V}$ and change in attenuation $\Delta\Gamma$

The SAW phase velocity is calculated from the obtained phase (rad) $\phi = kd_p = \omega\tau_p$, where d_p , τ_p are the propagation distance and time, respectively:

$$\phi = \omega\tau_p = \frac{\omega d_p}{V}$$

and thus, for fixed propagation distance and time, the change in phase as a function of the applied magnetic field is expressed as

$$\Delta\phi = \omega d_p \Delta\left(\frac{1}{V}\right) = -\frac{\omega d_p}{V(B_{ref} = 0)} \cdot \frac{\Delta V}{V(B)} = -\phi_0 \frac{\Delta V}{V(B)}$$

or

$$\frac{\Delta V}{V(B)} = -\frac{\Delta\phi}{\phi_0}$$

In order calculate the attenuation of the wave, we measure the amplitude of the output signal, U at different applied magnetic fields. This measured amplitude of the electric signal can be related to the SAW attenuation via:

$$U(B) = U_0 e^{-\alpha(B)d_p}$$

where α stands for the SAW attenuation, U_0 is an amplitude factor, proportional to the amplitude of the emitted wave. The amplitude ratio with respect to the reference magnetic field, B_{ref} yields:

$$\frac{U}{U_{ref}} = e^{-\Delta\alpha d_p}$$

or expressed in neper per cm (Np/cm):

$$\Delta\alpha = -\frac{1}{d_p} \ln\left(\frac{U}{U_{ref}}\right)$$

Then we convert to dB/cm:

$$\Delta\Gamma = -\frac{1}{d_p} \ln\left(\frac{U}{U_{ref}}\right) \frac{Np}{cm} = -\frac{1}{d_p} \log_{10}\left(\frac{U}{U_{ref}}\right) \ln(10) \frac{Np}{cm} = -\frac{20}{d_p} \log_{10}\left(\frac{U}{U_{ref}}\right) \frac{dB}{cm}$$

Bibliography

- [1] J. W. Lu, E. Chen, M. Kabir, M. R. Stan, and S. A. Wolf. Spintronics technology: past, present and future. *International Materials Reviews*, 61(7):456–472, 2016.
- [2] V. K. Joshi. Spintronics: A contemporary review of emerging electronics devices. *Engineering Science and Technology, an International Journal*, 19(3):1503 – 1513, 2016.
- [3] E. Beaurepaire, J-C. Merle, A. Daunois, J-Y. Bigot. Ultrafast spin dynamics in ferromagnetic nickel. *PRL*, 76(22):4250–4253, 1996.
- [4] J. Kim, M. Vomir, and J-Y. Bigot. Ultrafast magnetization dynamics induced by acoustic pulses in nickel thin films. *Optical Society of America*, 2013.
- [5] J. V. Jäger and A. V. Scherbakov and B. A. Glavin and A. S. Salasyuk and R. P. Campion and A. W. Rushforth and D. R. Yakovlev and A. V. Akimov and M. Bayer. Resonant driving of magnetization precession in a ferromagnetic layer by coherent monochromatic phonons. *PRB*, 92(2), 2015.
- [6] C. D. Stanciu, F. Hansteen, A. V. Kimel, A. Kirilyuk, A. Tsukamoto, A. Itoh, and Th. Rasing. All-optical magnetic recording with circularly polarized light. *PRL*, 99(4), 2007.
- [7] J. A. de Jong, I. Razdolski, A. M. Kalashnikova, R. V. Pisarev, A. M. Balbashov, A. Kirilyuk, Th. Rasing, A. V. Kimel. Coherent control of the route of an ultrafast magnetic phase transition via low-amplitude spin precession. *PRL*, 108(15), 2012.
- [8] S. Alebrand, M. Gottwald, M. Hehn, D. Steil, M. Cinchetti, D. Lacour, E. E. Fullerton, and S. Mangin M. Aeschlimann. Light-induced magnetization reversal of high-anisotropy TbCo alloy films. *APL*, 101(16):162408, 2012.
- [9] M. O. A. Ellis, E. E. Fullerton, and R. W. Chantrell. All-optical switching in granular ferromagnets caused by magnetic circular dichroism. *Scientific Reports*, 6(1), 2016.
- [10] J. Lindner. Current-driven magnetization switching and domain wall motion in nanostructures: survey of recent experiments. *Superlattices and Microstructures*, 47(4):497–521, 2010.

- [11] K. Uchida, S. Takahashi, K. Harii, J. Ieda, W. Koshibae, K. Ando, S. Maekawa, and E. Saitoh. Observation of the spin seebeck effect. *Nature*, 455(7214):778–781, 2008.
- [12] H. Ohno. Bridging semiconductor and magnetism. *Journal of Applied Physics*, 113(13):136509, 2013.
- [13] M. Cormier, V. Jeudy, T. Niazi, D. Lucot, M. Granada, J. Cibert, and A. Lemaître. Electric-field-induced magnetization reorientation in a (Ga,Mn)As/(Ga,Mn)(As,P) bilayer with out-of-plane anisotropy. *PRB*, 90:174418, 2014.
- [14] A.J. Schellekens, A. van den Brink, J.H. Franken, H.J.M. Swagten, and B. Koopmans. Electric-field control of domain wall motion in perpendicularly magnetized materials. *Nature Communications*, 3:847, 2012.
- [15] K. Roy, S. Bandyopadhyay, and J. Atulasimha. Hybrid spintronics and straintronics: a magnetic technology for ultra low energy computing and signal processing. *APL*, 99(6):063108, 2011.
- [16] K. Roy. Ultralow energy analog straintronics using multiferroic composites. *IEEE Transactions on Nanotechnology*, 16(2):333–346, 2017.
- [17] L. Dreher, M. Weiler, M. Pernpeintner, H. Huebl, R. Gross, M. S. Brandt, and S. T. B. Goennenwein. Surface acoustic wave driven ferromagnetic resonance in nickel thin films: theory and experiment. *PRB*, 86:134415, 2012.
- [18] L. Thevenard, C. Gourdon, J.-Y. Prieur, H. J. von Bardeleben, S. Vincent, L. Becerra, L. Largeau, and J.-Y. Duquesne. Surface-acoustic-wave-driven ferromagnetic resonance in (Ga,Mn)(As,P) epilayers. *PRB*, 90:094401, 2014.
- [19] L. Thevenard, J.-Y. Duquesne, E. Peronne, H. J. von Bardeleben, H. Jaffres, S. Ruttala, J.-M. George, A. Lemaître, and C. Gourdon. Irreversible magnetization switching using surface acoustic waves. *PRB*, 87:144402, 2013.
- [20] L. Thevenard, I. S. Camara, S. Majrab, M. Bernard, P. Rovillain, A. Lemaître, C. Gourdon, and J.-Y. Duquesne. Precessional magnetization switching by a surface acoustic wave. *PRB*, 93:134430, 2016.
- [21] L. Thevenard, I. S. Camara, J.-Y. Prieur, P. Rovillain, A. Lemaître, C. Gourdon, and J.-Y. Duquesne. Strong reduction of the coercivity by a surface acoustic wave in an out-of-plane magnetized epilayer. *PRB*, 93:140405, 2016.
- [22] W. Li, B. Buford, A. Jander, and P. Dhagat. Acoustically assisted magnetic recording: A new paradigm in magnetic data storage. *IEEE Transactions on Magnetism*, 50(3):37–40, 2014.

- [23] J. Dean, M. T. Bryan, J. D. Cooper, A. Virbule, J. E. Cunningham, and T. J. Hayward. A sound idea: manipulating domain walls in magnetic nanowires using surface acoustic waves. *APL*, 107(14):142405, 2015.
- [24] E. du Tremolet de Lacheisserie. *Magnetostriction Theory and Applications of Magnetoelasticity*. CRC Press, 1993.
- [25] S. Bhuktare A. Bose H. Singh A.A. Tulapurkar. Gyration based on magneto-elastic coupling at a ferromagnetic/piezoelectric interface. *Scientific Reports*, 2017.
- [26] C. Kittel. Interaction of spin waves and ultrasonic waves in ferromagnetic crystals. *Phys. Rev.*, 110:836–841, 1958.
- [27] A.I. Akhiezer, V.G. Bar'iakhtar, and S.V. Peletminskii. Coupled magnetoelastic waves in ferromagnetic media and ferroacoustic resonance. *Journal of Experimental and Theoretical Physics*, vol.8, no.1, p. 157 (Russian original - *ZhETF*, Vol. 35, No. 1, p. 228, January 1959), 1958.
- [28] E. G. Spencer and R. C. LeCraw. Magnetoacoustic resonance in yttrium iron garnet. *PRL*, 1:241–243, 1958.
- [29] H. Bömmel and K. Dransfeld. Excitation of hypersonic waves by ferromagnetic resonance. *PRL*, 3:83–84, 1959.
- [30] M. Pomerantz. Excitation of spin-wave resonance by microwave phonons. *PRL*, 7:312–313, 1961.
- [31] R. J. Ikola. New excitation mechanism for magnetoacoustic resonance in YIG. *Journal of Applied Physics*, 36(10):3260–3263, 1965.
- [32] V. V. Kruglyak and S. O. Demokritov and D. Grundler. Magnonics. *Journal of Physics D: Applied Physics*, 43(26):260301, 2010.
- [33] S. Neusser and D. Grundler. Magnonics: spin waves on the nanoscale. *Advanced Materials*, 21:2927 – 2932, 07 2009.
- [34] A. Chumak, V. Vasyuchka, A. Serga, and B. Hillebrands. Magnon spintronics. *Nature Physics*, 11:453–461, 06 2015.
- [35] T. Fischer, M. Kewenig, D. A. Bozhko, A. A. Serga, I. I. Syvorotka, F. Ciubotaru, C. Adelmann, B. Hillebrands, and A. V. Chumak. Experimental prototype of a spin-wave majority gate. *APL*, 110(15):152401, 2017.
- [36] A.V. Chumak, A. A. Serga and B. Hillebrands. Magnon transistor for all-magnon data processing. *Nature Communications*, 2014.

- [37] A. Anane. Nanomagnonics with ultra-thin YIG films. *Habilitation a diriger les recherches*, 2017.
- [38] A. V. Chumak, A. A. Serga and B. Hillebrands. Magnonic crystals for data processing. *Journal of Physics D: Applied Physics*, 50(24):244001, 2017.
- [39] J. Topp, D. Heitmann, M. P. Kostylev, and D. Grundler. Making a reconfigurable artificial crystal by ordering bistable magnetic nanowires. *PRL*, 104:207205, 2010.
- [40] A. V. Chumak, T. Neumann, A. A. Serga, B. Hillebrands and M. P. Kostylev. A current-controlled, dynamic magnonic crystal. *Journal of Physics D: Applied Physics*, 42(20):205005, 2009.
- [41] J. Atulasimha and A. B. Flatau. A review of magnetostrictive iron-gallium alloys. *Smart Materials and Structures*, 20(4):043001, 2011.
- [42] Thomas D. Rossing, editor. *Handbook of Acoustics*. Springer, 2007.
- [43] Allan D. Pierce. *Acoustics: An Introduction to Its Physical Principles and Applications*. McGraw-Hill Book Company, 1981.
- [44] Lord Rayleigh. On waves propagated along the plane surface of an elastic solid. *Proceedings of the London Mathematical Society*, s1-17(1):4–11, 1885.
- [45] Lord Rayleigh. The problem of the whispering gallery. *Philosophical Magazine Series 6*, 20(120):1001–1004, 1910.
- [46] P. Hess. Surface acoustic waves in materials science. *Physics Today*, 55(3):42–47, 2002.
- [47] D. Royer, E. Dieulesaint. *Elastic Waves in Solids I*. Springer-Verlag GmbH, 1999.
- [48] J. Pedrós, L. García-Gancedo, C. J. B. Ford, C. H. W. Barnes, J. P. Griffiths, G. A. C. Jones, and A. J. Flewitt. Guided propagation of surface acoustic waves and piezoelectric field enhancement in ZnO/GaAs systems. *Journal of Applied Physics*, 110(10):103501, 2011.
- [49] Jin-Chen Hsu, Tsung-Tsong Wu. Bleustein-Gulyaev-Shimizu surface acoustic waves in two-dimensional piezoelectric phononic crystals. *IEEE Transactions on Ultrasonics, Ferroelectrics, and Frequency Control*, 53(6):1169–1176, 2006.
- [50] B. A. Auld. *Acoustic Fields and Waves in Solids. Volume I*. Wiley, 1973.
- [51] L. D. Landau. *Theory of Elasticity*. Elsevier LTD, Oxford, 2004.
- [52] A. S. Nowick. *Anelastic Relaxation in Crystalline Solids*. Academic Press, 2012.

- [53] D. Sander. The correlation between mechanical stress and magnetic anisotropy in ultrathin films. *Reports on Progress in Physics*, 62(5):809–858, 1999.
- [54] G. Verschuur. *Hidden Attraction: The Mystery and History of Magnetism*. Oxford University Press, 1996.
- [55] U. Häfeli, W. Schütt, J. Teller, M. Zborowski, editor. *Scientific and Clinical Applications of Magnetic Carriers*. Springer Us, 2013.
- [56] S. Blundell. *Magnetism in Condensed Matter*. Oxford University Press, 2001.
- [57] J. M. D. Coey. *Magnetism and Magnetic Materials*. Cambridge University Press, 2010.
- [58] A. Reisenegger. Magnetic fields of neutron stars. *arXiv*, 2013.
- [59] W. Heisenberg. Zur theorie des ferromagnetismus. *Zeitschrift für Physik*, 49(9-10):619–636, 1928.
- [60] N. A. Spaldin. *Magnetic materials : Fundamentals and Applications*. Cambridge University Press, 2011.
- [61] N. W. Ashcroft, N. D. Mermin. *Solid State Physics*. Harcourt College, 1976.
- [62] L. D. Landau and E. Lifshitz. On the theory of the dispersion of magnetic permeability in ferromagnetic bodies. *Phys. Z. Sowjet.*, 8:153, 1935.
- [63] C. Kittel. Physical theory of ferromagnetic domains. *Reviews of Modern Physics*, 21(4):541–583, 1949.
- [64] A. Hubert, R. Schäfer. *Magnetic Domains*. Springer Berlin Heidelberg, 1998.
- [65] R. C. O’Handley. *Modern Magnetic Materials: Principles and Applications*. Wiley-Interscience, 1999.
- [66] M. Getzlaff. *Fundamentals of Magnetism*. Springer Berlin Heidelberg, 2007.
- [67] M. Barturen, J. Milano, M. Vásquez-Mansilla, C. Helman, M. A. Barral, A. M. Llois, M. Eddrief, and M. Marangolo. Large perpendicular magnetic anisotropy in magnetostrictive FeGa thin films. *PRB*, 92(5), 2015.
- [68] D-S. Wang, R. Wu, and A.J. Freeman. Magnetocrystalline anisotropy of interfaces: first-principles theory for Co-Cu interface and interpretation by an effective ligand interaction model. *Journal of Magnetism and Magnetic Materials*, 129(2-3):237–258, 1994.
- [69] E. W. Lee. Magnetostriction and magnetomechanical effects. *Reports on Progress in Physics*, 18(1):184–229, 1955.

- [70] L. Néel. Anisotropie magnétique superficielle et surstructures d'orientation. *Journal de Physique et le Radium*, 15(4):225–239, 1954.
- [71] E. du Tremolet de Lacheisserie, D. Gignoux, M. Schlenker, editor. *Magnetism. Fundamentals*. Springer, 2005.
- [72] B. Hillebrands and K. Ounadjela, editors. *Spin Dynamics in Confined Magnetic Structures I*. Springer Berlin Heidelberg, 2001.
- [73] B. Heinrich J. Anthony, C. Bland, editor. *Ultrathin Magnetic Structures I*. Springer Berlin Heidelberg, 1994.
- [74] A. G. Gurevich, G. A. Melkov. *Magnetization Oscillations and Waves*. CRC Press, 2000.
- [75] C. Bilzer. *Microwave susceptibility of thin ferromagnetic films: metrology and insight into magnetization dynamics*. Theses, Université Paris Sud - Paris XI, 2007.
- [76] H. Suhl. Theory of the magnetic damping constant. *IEEE Transactions on Magnetics*, 34(4):1834–1838, 1998.
- [77] H. Maier-Flaig, S. Klingler, C. Dubs, O. Surzhenko, R. Gross, M. Weiler, H. Huebl, and S. T. B. Goennenwein. Temperature-dependent magnetic damping of yttrium iron garnet spheres. *PRB*, 95(21), 2017.
- [78] M. W. Wu and J. H. Jiang and M. Q. Weng. Spin dynamics in semiconductors. *Physics Reports*, 493(2-4):61–236, 2010.
- [79] N. S. Almeida and D. L. Mills. Eddy currents and spin excitations in conducting ferromagnetic films. *PRB*, 53(18):12232–12241, 1996.
- [80] B. Heinrich, R. Urban, and G. Woltersdorf. Magnetic relaxation in metallic films: Single and multilayer structures. *Journal of Applied Physics*, 91(10):7523, 2002.
- [81] K. Lenz, H. Wende, W. Kuch, K. Baberschke, K. Nagy, and A. Jánossy. Two-magnon scattering and viscous gilbert damping in ultrathin ferromagnets. *PRB*, 73(14), 2006.
- [82] T. L. Linnik, A. V. Scherbakov, D. R. Yakovlev, X. Liu, J. K. Furdyna, and M. Bayer. Theory of magnetization precession induced by a picosecond strain pulse in ferromagnetic semiconductor (Ga,Mn)As. *PRB*, 84:214432, 2011.
- [83] A. V. Scherbakov, A. S. Salasyuk, A. V. Akimov, X. Liu, M. Bombeck, C. Brüggemann, D. R. Yakovlev, V. F. Sapega, J. K. Furdyna, M. Bayer. Coherent magnetization precession in ferromagnetic (Ga,Mn)As induced by picosecond acoustic pulses. *PRL*, 105:117204, 2010.

- [84] A. K. Ganguly, K. L. Davis, D. C. Webb, C. Vittoria, and D. W. Forester. Magnetically tuned surface-acoustic-wave phase shifter. *Electronics Letters*, 11(25-26):610, 1975.
- [85] D. C. Webb, K. L. Davis, N. C. Koon, and A. K. Ganguly. Magneto-elastic surface wave propagation in a low-anisotropy rare-earth-iron compound at 80MHz. *APL*, 31(4):245–247, 1977.
- [86] R. F. Wiegert and M. Levy. Magnetic field dependence of surface acoustic wave velocity and attenuation in nickel thin films. *Journal of Applied Physics*, 64(10):5411–5413, 1988.
- [87] A. Clark, M. Wun-Fogle, J. B. Restorff, and T. A. Lograsso. Magnetostrictive properties of galfenol alloys under compressive stress. *MATERIALS TRANSACTIONS*, 43(5):881–886, 2002.
- [88] M. Weiler, L. Dreher, C. Heeg, H. Huebl, R. Gross, M. S. Brandt, and S. T. B. Goennenwein. Elastically driven ferromagnetic resonance in nickel thin films. *PRL*, 106:117601, 2011.
- [89] A. K. Ganguly, K. L. Davis, D. C. Webb, and C. Vittoria. Magnetoelastic surface waves in a magnetic film–piezoelectric substrate configuration. *Journal of Applied Physics*, 47(6):2696–2704, 1976.
- [90] M. Barturen. Magneto-elastic coupling coefficients in epitaxied FeGa thin films. (*Unpublished*).
- [91] R. A. Kellogg. Mechanical properties of magnetostrictive iron-gallium alloys. *Ames Laboratory Conference Papers, Posters, and Presentations*, 2003.
- [92] Mariana Barturen. *Magnetic anisotropy and magneto-elastic coupling in epitaxial FeGa thin films grown over ZnSe/GaAs(001)*. Theses, Université Pierre et Marie Curie - Paris VI, 2014.
- [93] G. Petculescu, R. Wu, and R. McQueeney. Magnetoelasticity of bcc Fe-Ga alloys. In *Handbook of Magnetic Materials*, pages 123–226. Elsevier, 2012.
- [94] A.G. Olabi and A. Grunwald. Design and application of magnetostrictive materials. *Materials & Design*, 29(2):469–483, 2008.
- [95] R. A. Kellogg. Development and modeling of iron-gallium alloys. 2003.
- [96] Y. Du, M. Huang, S. Chang, D. L. Schlagel, T. A. Lograsso, and R. J. McQueeney. Relation between Ga ordering and magnetostriction of Fe-Ga alloys studied by X-ray diffuse scattering. *PRB*, 81(5), 2010.

- [97] A. E. Clark, K. B. Hathaway, M. Wun-Fogle, J. B. Restorff, T. A. Lograsso, V. M. Keppens, G. Petculescu, and R. A. Taylor. Extraordinary magnetoelasticity and lattice softening in bcc Fe-Ga alloys. *Journal of Applied Physics*, 93(10):8621–8623, 2003.
- [98] O. Ikeda, R. Kainuma, I. Ohnuma, K. Fukamichi, and K. Ishida. Phase equilibria and stability of ordered bcc phases in the Fe-rich portion of the Fe-Ga systems. *Journal of Alloys and Compounds*, 347(1-2):198–205, 2002.
- [99] R. Wu. Origin of large magnetostriction in FeGa alloys. *Journal of Applied Physics*, 91(10):7358, 2002.
- [100] S. Bhattacharyya, J. R. Jinschek, A. Khachaturyan, H. Cao, J. F. Li, and D. Viehland. Nanodispersed DO₃-phase nanostructures observed in magnetostrictive Fe-19% Ga galfenol alloys. *PRB*, 77(10), 2008.
- [101] A.G. Khachaturyan and D. Viehland. Structurally heterogeneous model of extrinsic magnetostriction for Fe-Ga and similar magnetic alloys: Part I. decomposition and confined displacive transformation. *Metallurgical and Materials Transactions A*, 38(13):2308–2316, 2007.
- [102] A.G. Khachaturyan and D. Viehland. Structurally heterogeneous model of extrinsic magnetostriction for Fe-Ga and similar magnetic alloys: Part II. giant magnetostriction and elastic softening. *Metallurgical and Materials Transactions A*, 38(13):2317–2328, 2007.
- [103] H. Wang, Y. N. Zhang, Teng Yang, Z. D. Zhang, L. Z. Sun, and R. Q. Wu. Ab initio studies of the effect of nanoclusters on magnetostriction of FeGa alloys. *APL*, 97(26):262505, 2010.
- [104] Y. Du, M. Huang, T. A. Lograsso, and R. J. McQueeney. X-ray diffuse scattering measurements of chemical short-range order and lattice strains in a highly magnetostrictive Fe_{0.813}Ga_{0.187} alloy in an applied magnetic field. *PRB*, 85(21), 2012.
- [105] Y. N. Zhang, J. X. Cao, and R. Q. Wu. Rigid band model for prediction of magnetostriction of iron-gallium alloys. *APL*, 96(6):062508, 2010.
- [106] H. Wang, Y. N. Zhang, R. Q. Wu, L.Z. Sun, D. S. Xu, and Z. D. Zhang. Understanding strong magnetostriction in Fe-Ga alloys. *Scientific Reports 3*, 3521, 2013.
- [107] J. J. Krebs, B. T. Jonker, and G. A. Prinz. Properties of Fe single-crystal films grown on (100)GaAs by molecular-beam epitaxy. *Journal of Applied Physics*, 61(7):2596–2599, 1987.

- [108] F. Gustavsson, E. Nordström, V. H. Etgens, M. Eddrief, E. Sjöstedt, R. Wäppling, and J.-M. George. Magnetic moment and anisotropy at the Fe/ZnSe(001) interface studied by conversion electron mössbauer spectroscopy. *PRB*, 66(2), 2002.
- [109] E. Sjöstedt, L. Nordström, F. Gustavsson, and O. Eriksson. Uniaxial magnetocrystalline anisotropy of metal/semiconductor interfaces: Fe/ZnSe(001). *PRL*, 89(26), 2002.
- [110] M. Marangolo, F. Gustavsson, G. M. Guichar, M. Eddrief, J. Varalda, V. H. Etgens, M. Rivoire, F. Gendron, H. Magnan, D. H. Mosca, and J. M. George. Structural and magnetic anisotropies of Fe/ZnSe (001) thin films. *PRB*, 70(13), 2004.
- [111] L.B. Steren, J. Milano, M. Eddrief, and V.H. Etgens. Magnetic properties of Fe/ZnSe/Fe trilayers. *Physica B: Condensed Matter*, 320(1-4):162–164, 2002.
- [112] M. Eddrief, Y. Zheng, S. Hidki, B. Rache Salles, J. Milano, V. H. Etgens, and M. Marangolo. Metastable tetragonal structure of Fe100-epitaxial thin films on ZnSe/GaAs(001) substrate. *PRB*, 84(16), 2011.
- [113] M. Barturen, B. Rache Salles, P. Schio, J. Milano, A. Butera, S. Bustingorry, C. Ramos, A. J. A. de Oliveira, M. Eddrief, E. Lacaze, F. Gendron, V. H. Etgens, and M. Marangolo. Crossover to striped magnetic domains in FeGa magnetostrictive thin films. *APL*, 101(9):092404, 2012.
- [114] M. Barturen, M. Sacchi, M. Eddrieff, J. Milano, S. Bustingorry, H. Popescu, N. Jaouen, F. Sirotti, and M. Marangolo. Rotatable anisotropy of epitaxial FeGa thin films. *The European Physical Journal B*, 86(4), 2013.
- [115] S. Tacchi, S. Fin, G. Carlotti, G. Gubbiotti, M. Madami, M. Barturen, M. Marangolo, M. Eddrief, D. Bisero, A. Rettori, and M. G. Pin. Rotatable magnetic anisotropy in a FeGa thin film with stripe domains: dynamics versus statics. *PRB* 89, 024411, 2014.
- [116] M. Marangolo, F. Gustavsson, M. Eddrief, Ph. Sainctavit, V. H. Etgens, V. Cros, F. Petroff, J. M. George, P. Bencok, and N. B. Brookes. Magnetism of the Fe/ZnSe(001) interface. *PRL*, 88(21), 2002.
- [117] V. H. Etgens, B. Capelle, L. Carbonell, and M. Eddrief. The use of thickness graded samples to investigate the elastic to plastic relaxation in ZnSe/GaAs(001). *APL*, 75(14):2108–2110, 1999.
- [118] L. Bo, C. Xiao, C. Hualin, M. A. Mohammad, and T. Xiangguang. Surface acoustic wave devices for sensor applications. *Journal of semiconductors*, 2016.
- [119] D.P. Morgan. *Surface wave devices for signal processing*. North Holland, 1985.

- [120] F. J. R. Schülein, E. Zallo, P. Atkinson, O. G. Schmidt, R. Trotta, A. Rastelli, A. W. Hubert, and J. Krenner. Fourier synthesis of radiofrequency nanomechanical pulses with different shapes. *Nature nanotechnology*, 2015.
- [121] G. Avitabile, L. Roselli, C. Atzeni, and G. Manes. Surface acoustic wave resonators. *European Transactions on Telecommunications*, 2(5):547–554, 1991.
- [122] A. Karabutov. Laser excitation of surface acoustic waves: a new direction in opto-acoustic spectroscopy of a solid. *IOP Science*, 1985.
- [123] D. Royer, E. Dieulesaint. *Elastic Waves in Solids II*. Springer-Verlag GmbH, 1999.
- [124] *Handbook of Metal Etchants*. CRC Press, 1990.
- [125] M. A. Mohammad. *Investigation of electron beam nanolithography processes, mechanisms, and applications*. PhD thesis, University of Alberta, 2011.
- [126] M. A. Mohammad, M. Muhammad, S. K. Dew, and M. Stepanova. Fundamentals of electron beam exposure and development. In *Nanofabrication*, pages 11–41. Springer Vienna, 2011.
- [127] R. Mathew. *Creating and imaging Surface Acoustic Waves on GaAs*. PhD thesis, Department of Physics, Engineering Physics and Astronomy, Queen’s University, Kingston, Ontario, Canada, 2009.
- [128] M. Bailleul, D. Olligs, C. Fermon, and S. O. Demokritov. Spin waves propagation and confinement in conducting films at the micrometer scale. *Europhysics Letters*, 56(5):741, 2001.
- [129] M. Bailleul, D. Olligs, and C. Fermon. Propagating spin wave spectroscopy in a permalloy film: a quantitative analysis. *APL*, 83(5):972–974, 2003.
- [130] Y. Khivintsev, Y. Filimonov, and S. Nikitov. Spin wave excitation in yttrium iron garnet films with micron-sized antennas. *APL*, 106:052407, 2015.
- [131] V. E. Demidov, M. P. Kostylev, K. Rott, P. Krzysteczko, G. Reiss, and S. O. Demokritov. Excitation of microwaveguide modes by a stripe antenna. *APL*, 95(11):112509, 2009.
- [132] V. Vlaminck and M. Bailleul. Spin-wave transduction at the submicrometer scale: experiment and modeling. *PRB*, 81:014425, 2010.
- [133] M. Haidar. *Role of surfaces in magnetization dynamics and spin polarized transport: a spin wave study*. PhD thesis, Institut de Physique et Chimie des Matériaux de Strasbourg, 2012.

- [134] M. Marangolo, W. Karboul-Trojet, J.-Y. Prieur, V. H. Etgens, M. Eddrief, L. Becerra, and J.-Y. Duquesne. Surface acoustic wave triggering of giant magnetocaloric effect in MnAs/GaAs devices. *APL* 105, 162403, 2014.
- [135] A. K. Ganguly, K. L. Davis, and D. C. Webb. Magnetoelastic surface waves on the (110) plane of highly magnetostrictive cubic crystals. *Journal of Applied Physics*, 49(2):759–767, 1978.
- [136] H. Zhou, A. Talbi, N. Tiercelin, and O. Bou Matar. Multilayer magnetostrictive structure based surface acoustic wave devices. *APL*, 104(11):114101, 2014.
- [137] Y. Shimizu, K. Hasegawa, and R. Members. Nonreciprocity in saw velocity on a magnetized ferrite substrate. *Electronics and Communications in Japan, Vol. 63-A, No.3*, 1980.
- [138] M.F. Lewis and E. Patterson. Acoustic-surface-wave isolator. *APL* 20, 276, 1972.
- [139] G. Carlotti and G. Gubbiotti. Brillouin scattering and magnetic excitations in layered structures. *La Rivista del Nuovo Cimento*, 22(12):1–60, 1999.
- [140] D. D. Stancil, A. Prabhakar. *Spin Waves. Theory and Applications*. Springer Science+Business Media, LLC, 2009.
- [141] A. Kamra, H. Keshtgar, P. Yan, Peng, and G. Bauer. Coherent elastic excitation of spin waves. *PRB*, 91:104409, 2015.
- [142] H. Matthews and R. C. LeCraw. Acoustic wave rotation by magnon-phonon interaction. *PRL*, 8:397–399, 1962.
- [143] A.H. Fahmy and E. L. Adler. Propagation of acoustic surface waves in multilayers: A matrix description. *APL*, 22(10):495–497, 1973.
- [144] E. L. Adler. Matrix methods applied to acoustic waves in multilayers. *IEEE Transactions on Ultrasonics, Ferroelectrics, and Frequency Control*, 37(6):485–490, 1990.
- [145] A.H. Fahmy. *Acoustic wave propagation and amplification in multilayers*. PhD thesis, Department of Electrical Engineering, McGill University, Montreal, Canada., 1973.
- [146] E. L. Adler, J. K. Slaboszewicz, G. W. Farnell, and C. K. Jen. PC software for saw propagation in anisotropic multilayers. *IEEE Transactions on Ultrasonics, Ferroelectrics, and Frequency Control*, 37(3):215–223, 1990.
- [147] O. B.Matar, N. Gasmi, H. Zhou, M. Goueygou, and A. Talbi. Legendre and laguerre polynomial approach for modeling of wave propagation in layered magneto-electro-elastic media. *The Journal of the Acoustical Society of America*, 133(3):1415–1424, 2013.

- [148] M. J. S. Lowe. Matrix techniques for modeling ultrasonic waves in multilayered media. *IEEE Transactions on Ultrasonics, Ferroelectrics, and Frequency Control*, 42(4):525–542, July 1995.
- [149] P. G. Gowtham, D. Labanowski, and S. Salahuddin. Mechanical back-action of a spin-wave resonance in a magnetoelastic thin film on a surface acoustic wave. *PRB*, 94:014436, 2016.
- [150] G.W. Farnell and E.L. Adler. Elastic wave propagation in thin layers. In *Physical Acoustics*, pages 35–127. Elsevier, 1972.
- [151] A. V. Chumak, P. Dhagat, A. Jander, A. A. Serga, and B. Hillebrands. Reverse doppler effect of magnons with negative group velocity scattered from a moving bragg grating. *PRB*, 81:140404, 2010.
- [152] K. Uchida, H. Adachi, T. An, T. Ota, M. Toda, B. Hillebrands, S. Maekawa, and E. Saitoh. Long-range spin seebeck effect and acoustic spin pumping. *Nature materials*, 2011.
- [153] M. Weiler, H. Huebl, F. S. Goerg, F. D. Czeschka, R. Gross, and S. T. B. Goennenwein. Spin pumping with coherent elastic waves. *PRL*, 108:176601, 2012.
- [154] R. I. Cottam and G. A. Saunders. The elastic constants of GaAs from 2K to 320K. *Journal of Physics C: Solid State Physics*, 6(13):2105, 1973.